

**Characterization of Internal Flow, Spray Evolution and
Mixture Formation of Multi-Hole Nozzle
for Diesel Engine**

(ディーゼル機関用多噴孔ノズルの内部流れ，噴霧挙動，混合気
形成に関する研究)

by

Pengbo Dong

Dissertation

Submitted to the Graduate School of Engineering

of Hiroshima University

in Partial Fulfillment of the Requirements

for the Degree of

Doctor of Engineering

Hiroshima University

August, 2016

ABSTRACT

Multi-hole nozzles have a wide range of application in fuel supply system of modern diesel engines, although single-hole nozzles dominate the basic internal flow and spray research. Parameters of nozzle geometry are crucial factors that can alter nozzle internal flow dynamics and the consequent spray behaviors. The novelty of this study lies in the implementation of applying the practical prototype mini-sac multi-hole diesel nozzles in the experimental and numerical study. Specifically, the high-speed video observation method (Mie scattering and laser absorption-scattering technique) was applied to visualize the injection processes and the spray evolution of different nozzles inside a high-pressure and high-temperature vessel. Meanwhile, aiming to understand the mechanism behind the multi-hole nozzle spray behaviors better, the numerical simulation (Two-phase Flow and Discrete Droplet Model methods) was conducted to reveal the three-dimensional nature of the internal flow and spray under the same conditions with that in experiments.

Comparisons of the spray and internal flow characteristics between the traditional single-hole nozzles and the modern practice multi-hole nozzles (10 holes) were conducted firstly under the evaporating and non-evaporating conditions. The injection pressure, injection quantity, and the micro orifice effects were also taken into the consideration.

Furthermore, the characteristics of spray morphology, evolution processes, and evaporation characteristics emerging from the practical diesel multi-hole nozzles were compared and analyzed during the transient injection processes in detail from a variety of views, including different engine dynamic operation conditions and various nozzle geometrical conditions. The effect of rail pressure (80, 120, 180 MPa) and injection quantity (0.3, 2.0mm³/hole) were paid attention to firstly, and then the multi-hole nozzles with different orifice diameter (0.07, 0.10, 0.133 mm), and different hole length (0.4, 0.6, 0.8 mm) were selected to pursuing a better understanding about the nozzle geometrical design effect on the spray behaviors.

Moreover, the relationship between different multi-hole nozzle internal flow properties and the corresponding spray behaviors was investigated by the numerical simulation method systematically under the same conditions with that in experiments. Additionally, the effect of multiple fuel injection, nozzle hole inlet roundness (0, 8, 16, 32 μm), and K factor of the hole (-0.13, 0, 0.15) on the multi-hole nozzle internal flow properties was discussed deeply as well.

The spray modeling processes under engine operation conditions and the optimized design of diesel multi-hole nozzles can get some clue and benefit from the results presented in this study.

TABLE OF CONTENTS

ABSTRACT	i
TABLE OF CONTENTS	ii
NOMENCLATURES.....	vi
CHAPTER 1 INTRODUCTION	1
1.1 BACKGROUND AND MOTIVATION	1
1.2 OBJECTIVES AND APPROACHES	8
1.3 OUTLINES.....	8
1.4 STUDIES REVIEW.....	9
1.4.1 Internal Flow Investigation for Diesel Nozzles.....	9
1.4.2 Investigation about Effect of Nozzle Internal Flow on Near-field Spray	16
1.4.3 Diesel Spray Evolution, Mixture Formation and Combustion Processes	22
1.4.4 Optical Diagnostic Technique for Diesel Spray.....	32
1.5 SUMMARY.....	36
CHAPTER 2 EXPERIMENTAL APPARATUS AND MEASUREMENT METHOD	38
2.1 HIGH PRESSURE AND HIGH TEMPERATURE AMBIENT CONDITON ACQUIRING SYSTEM	38
2.2 HIGH PRESSURE INJECTION SYSTEM AND INJECTION RATE MEASUREMENT SYSTEM	39
2.3 ELECTRICAL CONTROLLING SYSTEM	43
2.4 OPTICAL MEASUREMENT SYSTEMS	44
2.4.1 Mie Scattering Method	44
2.4.2 Laser Absorption-Scattering Technique	46
2.5 SUMMARY.....	54
CHAPTER 3 MODELS AND THEORETICAL BASIS APPLIED IN NUMERICAL STUDY	55
3.1 MULTI-PHASE FLOW COMPUTATION METHOD APPLIED IN NOZZLE INTERNAL FLOW STUDY	55
3.1.1 Basic Description for Multi-Phase Flow Models.....	56
3.1.2 Analysis about Multi-Phase Flow Models	59
3.1.3 Numerical Solution Method for Multi-Phase Flow Model	60
3.2 MATHEMATICAL MODELS APPLIED IN NOZZLE INTERNAL FLOW STUDY	61
3.2.1 Turbulence Model	61
3.2.2 Cavitation Model.....	62

3.3 NUMERICAL METHOD APPLIED IN SPRAY SIMULATION STUDY	64
3.3.1 Spray Sub-models.....	64
3.4 SUMMARY	67
CHAPTER 4 SPRAY EVOLUTION OF MULTI-HOLE NOZZLES UNDER NON-EVAPORATION CONDITIONS	68
4.1 VISUALIZATION OF SPRAY BY MIE-SCATTERING	68
4.1.1 Experimental Condition.....	68
4.1.2 Image Processing and Analysis Method	69
4.2 CHARACTERISTICS OF INJECTION PROCESSES AND SPRAY BEHAVIORS OF SINGLE- HOLE AND MULTI-HOLE NOZZLES.....	70
4.2.1 Injection Rate of Single-hole and Multi-hole Nozzles.....	71
4.2.2 Far-field and Near-field Spray Images	78
4.2.3 Comparison of Time-resolved Spray Characteristics.....	90
4.3 NON-EVAPORATING SPRAY EVOLUTION OF MULTI-HOLE NOZZLES	104
4.3.1 Under Different Engine Dynamic Operation Conditions.....	105
4.3.2 Relationship between Nozzle Geometrical Structure and Spray Characteristics	105
4.4 CORRELATION OF EXPERIMENTAL RESULT AND EMPIRICAL PREDICTED MODEL FOR SPRAY TIP PENETRATION.....	117
4.4.1 Comparison between Experimental Result and Classic Predicted Model.....	117
4.4.2 Correction of Spray Tip Penetration Prediction Equations	119
4.5 Summary.....	124
CHAPTER 5 INTERNAL FLOW CHARACTERISTICS OF MULTI-HOLE NOZZLES.....	125
5.1 MESH BUILDING PROCESS, BOUNDARY CONDITIONS AND SIMULATION VALIDATION	125
5.2 CHARACTERISTICS OF INTERNAL FLOW INSIDE SINGLE-HOLE AND MULTI-HOLE NOZZLES.....	129
5.2.1 Computational Results via Full and Partial Mesh of Multi-hole Nozzle Geometry	130
5.2.2 Global Comparison of Internal Flow between Single-hole and Multi-hole Nozzles	131
5.2.3 Under Tiny and Normal Injection Quantity Conditions	136
5.2.4 Effect of Micro Nozzle Hole Diameter.....	142
5.2.5 Internal Flow and Spray Transient around the End and Start of Injection	147
5.3 INTERNAL FLOW VARIATION OF MULTI-HOLE NOZZLES	149
5.3.1 Under Different Dynamic Operation Conditions.....	149

5.3.2 Relationship between Nozzle Geometrical Structure and Internal Flow Properties	153
5.4 CORRELATING NOZZLE GEOMETRICAL DESIGN AND INTERNAL FLOW WITH SPRAY BEHAVIORS	166
5.5 SUMMARY	169
CHAPTER 6 NUMERICAL COMPUTATIONAL STUDY OF MULTI-HOLE NOZZLE SPRAY	171
6.1 MESH BUILDING PROCESS, BOUNDARY CONDITIONS, AND SIMULATION VALIDATION	171
6.2 COUPLING OF MULTI-HOLE NOZZLE INTERNAL FLOW RESULTS WITH SPRAY SIMULATION	174
6.3 COMPARISON OF SPRAY SIMULATION RESULT BETWEEN SINGLE-HOLE AND MULTI-HOLE NOZZLES.....	176
6.4 CHARACTERISTICS OF MULTI-HOLE NOZZLE SPRAY	178
6.4.1 Ambient Flow and Spray Interaction of Multi-Hole Nozzle Spray	178
6.4.2 Under Different Rail Pressure Conditions	179
6.4.3 Sensitivity of Spray Properties to Nozzle Hole Diameter Variation	181
6.5 SUMMARY	183
CHAPTER 7 SPRAY EVOLUTION AND MIXTURE FORMATION OF MULTI-HOLE NOZZLES UNDER EVAPORATION CONDITIONS.....	184
7.1 INTRODUCTION.....	184
7.1.1 Experimental Conditions.....	184
7.1.2 Image Processing and Technical Validation	184
7.2 EVAPORATING SPRAY CHARACTERISTICS OF SINGLE-HOLE AND MULTI-HOLE NOZZLES.....	188
7.2.1 Global comparison in the evaporation spray between different nozzles.....	189
7.2.2 Effect of Micro Nozzle Hole Diameter on Mixture Formation Process.....	192
7.3 EVAPORATING SPRAY EVOLUTION AND MIXTURE FORMATION PROCESSES OF MULTI-HOLE NOZZLES.....	195
7.3.1 Liquid and Vapor Phase Distribution under Different Dynamic Operation Conditions	195
7.3.2 Effect of Multi-hole Nozzle Geometrical Design on Evaporating Spray Characteristics.....	201
7.4 DISCUSSION ON RELATIONSHIP OF NOZZLE GEOMETRICAL DESIGN, INTERNAL FLOW, NEAR-FIELD SPRAY AND MIXTURE FORMATION CHARACTERISTICS.....	210
7.5 SUMMARY	212

CHAPTER 8 CONCLUSIONS	214
8.1 FINDINGS OF THE CURRENT STUDY	214
8.1.1 Comparison between Single-hole and Multi-hole Nozzles.....	214
8.1.2 Non-evaporating Spray Evolution of Multi-Hole Nozzles.....	216
8.1.3 Internal Flow Characteristics inside Multi-Hole Nozzle	217
8.1.4 Computational Study of Multi-Hole Nozzle Sprays	218
8.1.5 Mixture Formation Characteristics of Multi-Hole Nozzle Sprays	219
8.1.6 Correlation of Nozzle Geometrical Design, Internal Flow, and Spray Behaviors	220
8.2 RECOMMENDATIONS FOR FUTURE WORKS	221
REFERENCES	222

NOMENCLATURES

A	Theoretical flow area
ASOI	After start of injection
C_a	Coefficient of area contraction
C_v	Velocity coefficient
C_n	Droplet number density
C_d	Discharge coefficient
CH	methylidyne
C/R	Compression ratio
CCD	Charge-coupled device
CFD	Computational fluid dynamic
CO	Carbon monoxide
D	Nozzle hole diameter
DDM	Discrete Droplet Model
DME	Dimethyl ether
DMN	Dimethyl naphthalene
ECU	Electronic control unit
EOI	End of injection
Eq_a	Equivalence ratio of liquid
Eq_v	Equivalence ratio of vapor
fps	Frames per second
HC	Hydrocarbon
HCCI	Homogeneous charge compression ignition
K	Nozzle hole K factor
l	Eddy size
L	Nozzle hole length
L_0	Lift-off-length
LAS	Laser absorption-scattering
LDA	Laser doppler anemometer
LDV	Laser doppler velocimetry
LIEF	Laser induced exciplex fluorescence

LIF	Laser induced fluorescence
LII	Laser induced incandescence
LRS	Laser rayleigh scattering
LTO	Low temperature oxidation
M_o	Initial jet flow momentum flux
NO _x	Oxides of nitrogen
P_a	Ambient pressure
PAH	Polycyclic aromatic hydrocarbons
PCCI	Premixed charge compression ignition
PDA	Phase dopper anemometry
PDPA	Phase doppler particle analysis
PIV	Particle image velocimetry
PLIF	Planar laser-induced fluorescence
PM	Particulate matters
PREDIC	Premixed lean diesel combustion
Q_{ext}	Extinction efficiency
Q_f	Injection rate
RoHR	Rate of heat release
R	Nozzle hole inlet roundness
S	Spray tip penetration
SCR	Selective catalytic reduction
SMD	Sauter mean diameter
SOI	Start of injection
SRS	Spontaneous Raman Scattering
t	Times after start of injection
T	Temperature
T_a	Ambient temperature
TDC	Top dead center
TKE	Turbulence kinetic energy
UHC	Unburnt hydrocarbon
UV	Ultra-violet
\bar{V}	Effective injection velocity

V_r	Velocity component on the hole axis direction
V_i	Velocity component on the hole radial direction
Vis	Visible
We	Weber number
θ_s	Spray angle
θ_c	Spray cone angle
α	Sound velocity
ε	Molar absorption coefficient
μ	Mixture viscosity
λ	Wavelength
σ	Liquid surface tension
ϕ	Equivalence ratio
u_{rel}	Relative velocity between droplets and gas
ρ_a	Ambient density (Kg/m ³)
ρ_f	Fuel density
τ_i	Transmittance of neutral filter
ΔP	Difference of injection pressure and the ambient pressure (MPa)
3-D	Three dimensional

CHAPTER 1 INTRODUCTION

1.1 BACKGROUND AND MOTIVATION

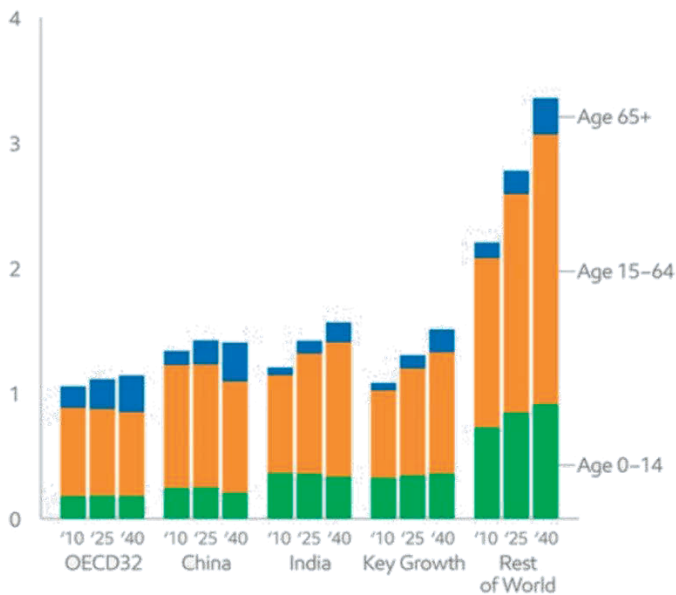
The Dutch physicist, Christiaan Huygens, firstly linked the combustion to piston mechanical structure in 1673--1680, which implemented the “internal combustion” in the history of human beings for the first time. Beau de Rochas proposed the four-stroke cycle principle of constant volume combustion firstly in 1862. After that, the first spark-ignition engine came out in 1876. The Diesel engine was first invented by Rudolf Diesel in 1892 [Heywood 1988]. As one of the most important inventions in 19 century, in recent hundred years of human history, every major technological breakthrough in the field of internal combustion engines are driving the progress of human. By its own high thermal efficiency, wide range of power and speed, and high reliability and flexibility, internal combustion engines have now become the most widely used power machinery in industrial, agricultural production, and transportation fields [Lentinello 2000].

However, as an important bridge between the humans, the living environment, and natural resources, the development of internal combustion engine technology will undoubtedly affect major changes in environment, oil, gas, and other natural resources on the Earth. Human beings enjoy the development and achievements brought by the internal combustion engine technology, meanwhile have to face the negative issues, such as the environmental degradation, energy depletion and so on. The traditional internal combustion engine provides the inexhaustible power, whilst consumes non-renewable resources, and exhausts a large number of emissions, which are harmful to the environment. Energy supply and environmental health and safety are becoming major challenges for the development of human society. In the next half century, the main power equipment relied by the human is still the internal combustion engine, and oil will still be the main fuel [Arcoumanis, C., et al, 2009]. Thus, as the main power source of power machinery, overall performance of the internal combustion engine is attracting more and more attentions.

The world energy demand is increasing with the booming of the population. Based on the research from ExxonMobil [Colton, 2014], as shown in Figure 1.1, the population of world will reach approximate 9 billion in 2040, and the aged tendency of population will be more serious. At the time, energy demand will rise to 1200 quadrillion BTUs (British thermal unit) following the tendency of the last two decades. Even it is believed that the energy conservation and efficient energy implement can be conducted further and better, the energy demand in 2040 will reach about at least 700 quadrillion BTUs.

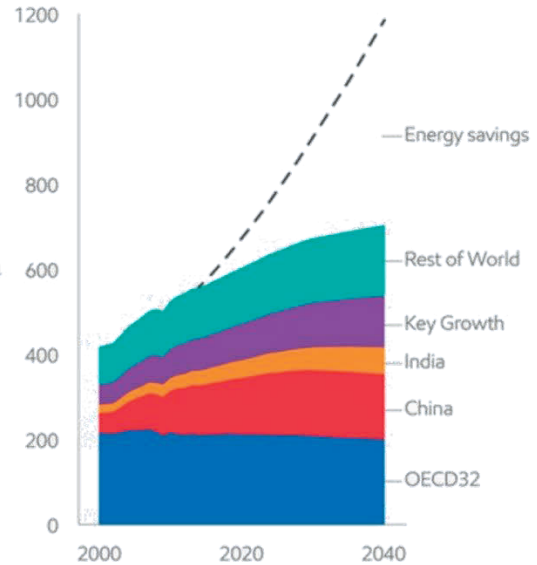
Demographics

Billion people



Energy demand

Quadrillion BTUs



*OECD (Organization for Economic Co-operation and Development), Mexico and Turkey included in key Growth countries.

Figure 1.1 Global population and energy demand forecast [Colton, 2014]

When the attention is paid to the category of the energy demand in the following half of the century, the prediction is shown in Figure 1.2 [Roger Cracknell 2015]. It is conceivable that the energy consumption will bring a series of problems, and the fossil fuel will be exploited excessively, because the mainly energy is still acquired from coal and oil in the future decades, although the renewable energy and clear energy is expected to be developed further and more. As a result, the energy crisis is threatening the development of the human, and a lot of researchers spare no effort to find new ways to solve this imminent danger.

According to the research from BP Corporation, as shown in Figure 1.3, among the whole energy demand, the growth in the global consumption of liquid fuels is driven by transport and industry. The transport will account for over 60% of the whole demand. The growth in transport demand reflects rapid increases in vehicle ownership in emerging economies, partially offset by sustained gains in vehicle efficiency. Transport fuel continues to be dominated by oil (88% in 2035). Non-oil alternatives will only increase to 12% in 2035.

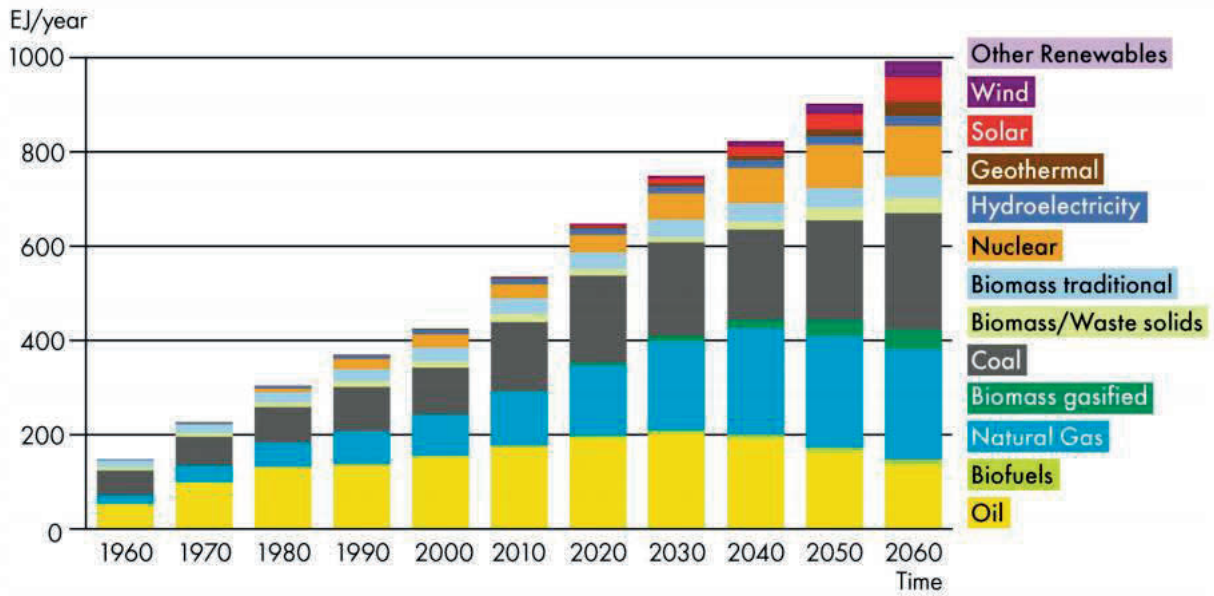
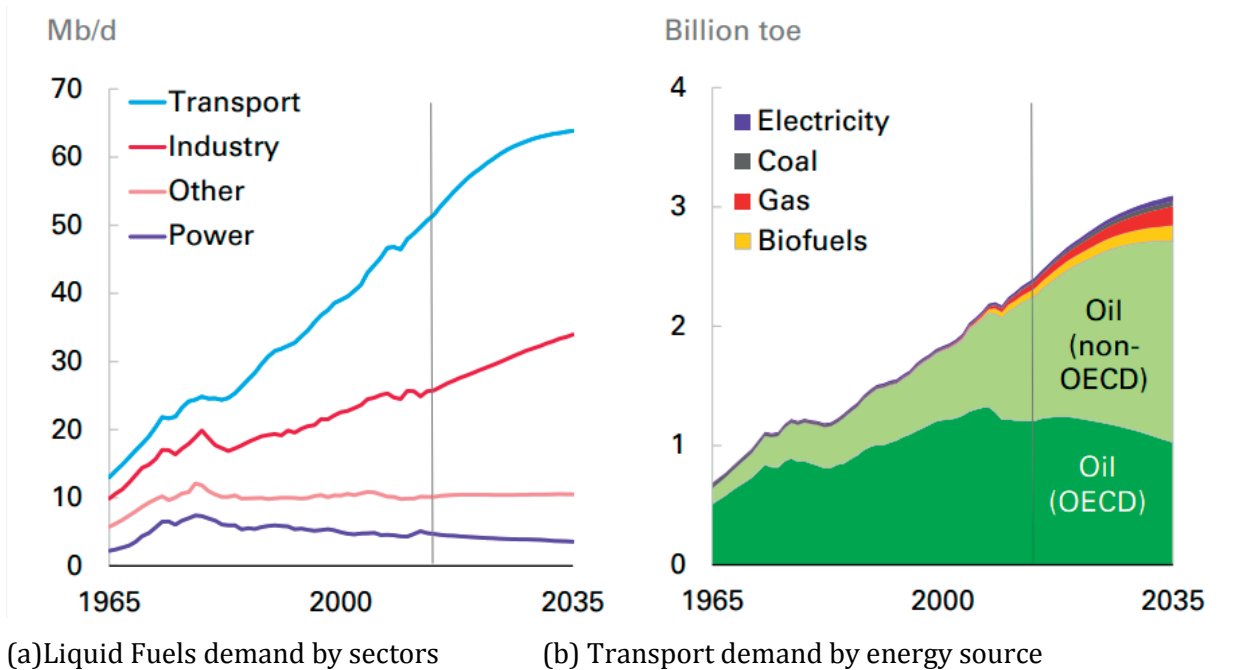


Figure 1.2 Global total primary energy demand forecast [Roger Cracknell 2015]



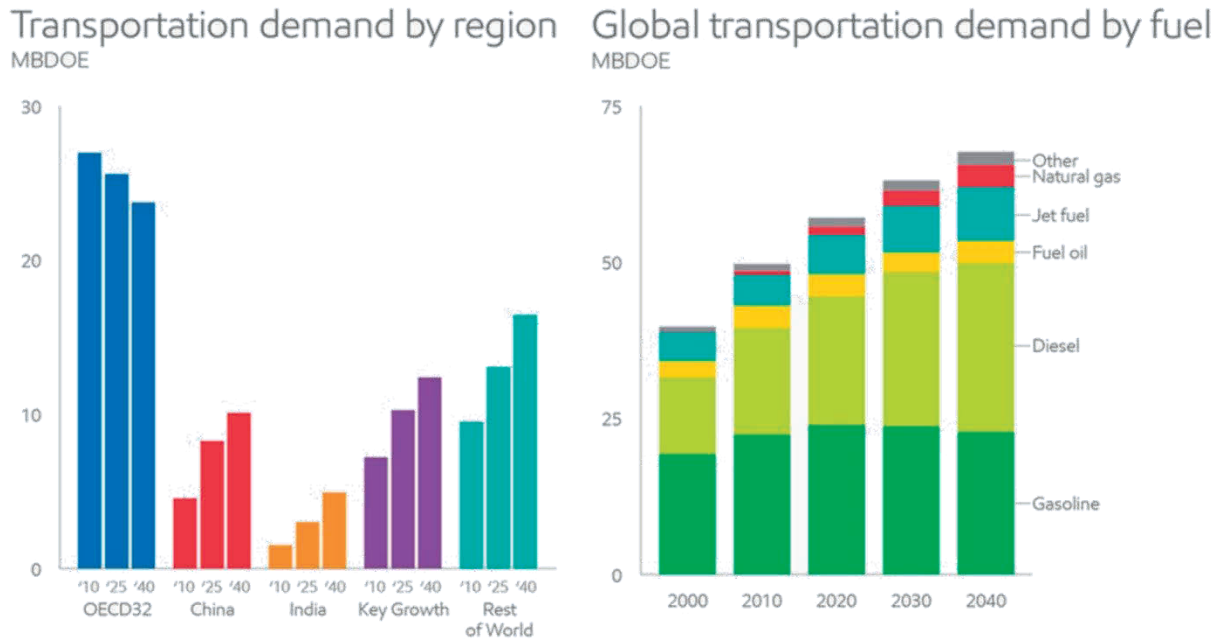
(a) Liquid Fuels demand by sectors

(b) Transport demand by energy source

Figure 1.3 Global consumption of liquid fuels and transport demand by energy source [BP Energy Outlook, 2016]

The transportation demand by region and fuel is shown in Figure 1.4 [Colton, 2014]. Except for the OECD countries, the demand of transportation in all of the other regions will

continuous to increase dramatically. As for the fuel types which contribute to the transportation demand, the oil accounts for about 95% of the total consumption even in 2040, when vehicle fuel economy improves a lot. Moreover, the demand for diesel will grow 45%, which indicates the diesel cars, trucks, and marine will expand further. Therefore, as the most widely used engines in commercial vehicle and marines, diesel engine should enhance fuel economy performance, which can relieve the pressure caused by the shortage of the resources effectively.

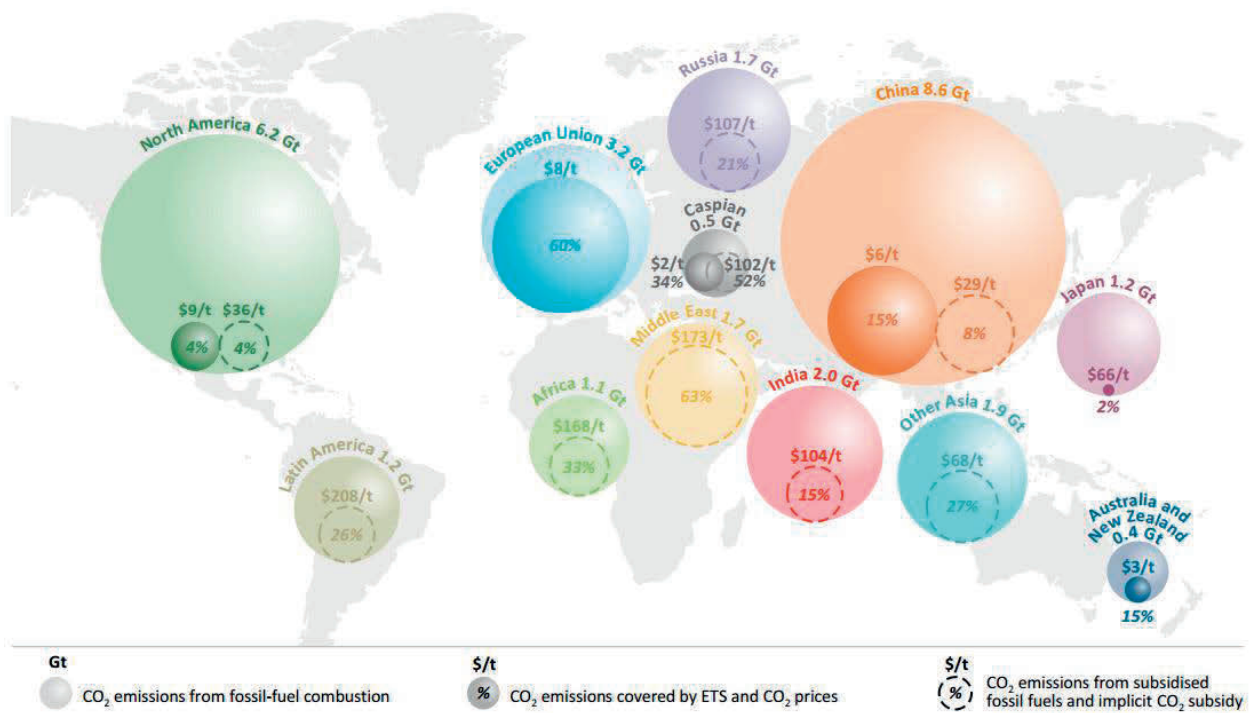


*OECD (Organization for Economic Co-operation and Development), Mexico and Turkey included in key Growth countries.

Figure 1.4 Global transportation demand by region and fuel [Colton, 2014]

However, in recent years, because of the climate change, more and more attentions are paid to environmental protection. In fact, the consumption of the fossil fuel is one of the main indisputable sources of the pollutions, which causes up the climate warming, fog, and haze. It has been presented by researchers [Lacis et al, 2013; Dillon et al, 2010] that the greenhouse gas emission is the immediate reason of the world warming. The greenhouse gases and harmful gases are polluting the earth, and threatening the eco-system and the health of human beings. The energy related CO₂ emissions, especially caused by the fossil-fuel combustion in 2014 all around the world is published by International Energy Agency and shown in Figure 1.5 [Maria van der Hoeven, 2015]. China, North America, and European Union are the first three largest carbon market in the world. The technology improvement, such as optimizing the methods of combustion, enhancing the energy

efficiency, and reducing the harmful gases emission substantially, becomes very significant subject for the sustainable development of the human being.



Notes: The implicit CO₂ subsidy is calculated as the ratio of the economic value of those subsidies to the CO₂ emissions released from subsidised energy consumption. ETS = emissions trading scheme.

Figure 1.5 Energy-related CO₂ emissions in selected regions [Maria van der Hoeven, 2015]

The drive to reduce diesel automotive emissions such as NO_x, particulates, CO has led to the introduction of compliance standards, such as the European Euro-1 to -6 standards [European Commission, 2016] or the US Tier-1 to -3 standards [Environmental Protection Agency, 2016]. The historical global emission regulation of diesel engine is exhibited in Figure 1.6, which mainly contains 3 kinds of system (Japan, North America, and European Union) [Peter, W., 2003]. The internal combustion engine emission control laws of the world's major countries are according to the Europe, the United States is. The Europe, Japanese, and the United States systems have different focused points, while all of the trend are toward stringent increasingly, eventually tending to zero emissions.

Moreover, there are also targets for vehicle efficiency and tail-pipe greenhouse gas emissions. For example, the automobile makers' voluntary agreement [European Commission, 2014], the Corporate Average Fuel Economy (CAFE) [National Highway Traffic Administration, 2016], emission regulation in Europe [European Commission, 2009], and vehicle greenhouse gas standards in the USA [Environmental Protection Agency, 2012] are all play very significant roles in

the control of the emission and promotion of the advanced engine technology. Implementation of emission regulations are also paralleled by regulations about fuel properties, such as the European Fuel Quality Directive [European Commission, 1998] and US regional Low-Carbon Fuel Standards [California Air Resources Board, 2006].

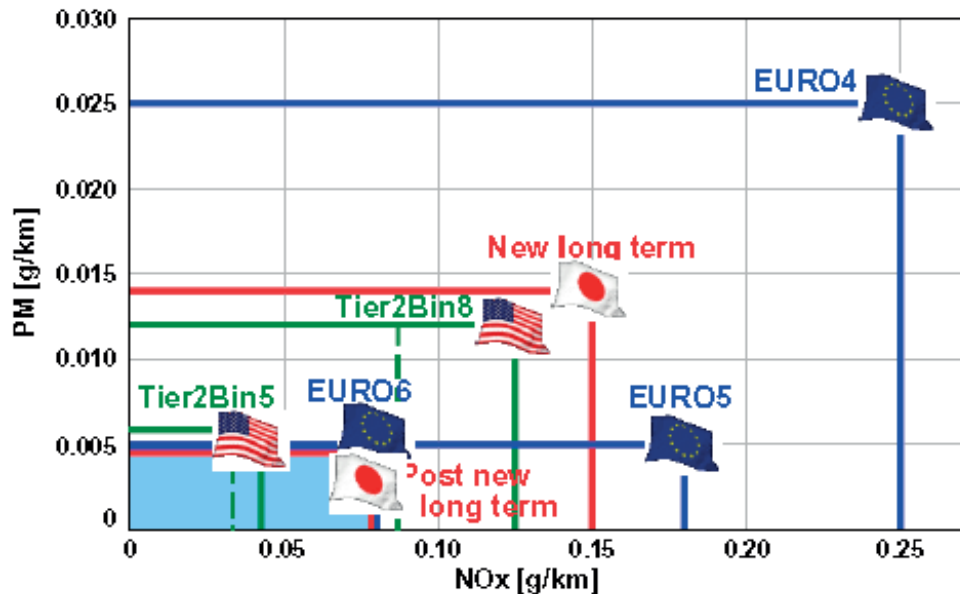


Figure 1.6 Global regulation of NOx and PM emissions for diesel engines [Peter, W., 2003]

A lot of new techniques were developed out for diesel engines to satisfy the more and more serious emission laws. However, without doubt that the engine cost will be forced to raise up. In fact, more attentions should be paid to improve the diesel engine performance without increasing engine cost too much. As it is known that the traditional diesel combustion mode, which is called diffusive combustion, has its deficient that the NO_x and PM emissions cannot be reduced simultaneously, which attributes to the formation mechanisms of NO_x and PM. As a result, the researchers begin the new generation research about the advanced concept of combustion in the diesel engines to break out the limitation of emission. For example, PCCI (Premixed Charge Compression Ignition), HCCI (Homogeneous Charge Compression Ignition), and HCPC (Homogenous Charge Progressive Combustion) and son on, in which the theories are all forcing on the optimization of fuel air mixture formation and the control of equivalence ratio and temperature inside the chamber. These processes and parameters mainly depend on the fuel spray evolution inside the chamber. Therefore, the injector is regarded as one of the most important components in the diesel engines that can affect the injection quantity, injection times, injection timing, spray

quality, the consequent combustion performance, and the whole engine performance. It is really worthwhile to pay more attention to the diesel spray emerging from different kinds of injectors.

In fact, the diesel sprays have been drawing extensive attentions of researchers for several decades, because the combustion process, the resulting engine performance, and the emission formation of the Diesel engine are well known to be governed mainly by the spray evolution, in terms of the breakup, atomization, air entrainment, and mixture formation processes. Further, one of the determining factors that can greatly influence the quality of the fuel atomization and mixture homogeneity is the nozzle geometry, since it can directly affect the characteristics of the complicated turbulent and cavitation flow patterns inside the nozzle. As a result, over the past decades scholars have spared no effort to investigate the internal flow [Bergwerk, 1959; Hiroyasu et al., 1991; Koo and Martin, 1995] and spray behaviors [Hiroyasu and Arai, 1990; Siebers, 1998; Araneo et al., 1999], which provided many classic and fundamental theories for later generations. Originally, the injectors, that firstly held the vision of researchers, were mainly the single-hole ones due to their simple configuration and the easiness of arranging instruments and applying diagnostic techniques around the single spray plume. A lot of spray and combustion models applied in the computational study were conceivable to be developed from the single-hole nozzles studies.

However, multi-hole nozzles, which simultaneously inject several spray plumes, are generally applied in modern real Diesel engines. Furthermore, the recent trend of the diesel injectors assembled in the high-pressure common rail injection system is to use larger number of smaller holes, which inevitably results in the orifices being aligned around the sac symmetrically and normally located off-axis to the centre of the nozzle [Lai et al. 2011]. As a result, the difficulties in the optical access into the complex configuration and the mutual interference between the spray plumes injected from the multi-hole nozzle presented a major challenge for researchers to get thorough understanding about the mechanism of the internal flow and spray evolution of the multi-hole nozzles.

Until now the different effects of single-hole and multi-hole nozzles on the internal flow and spray behaviours have not yet been agreed upon; furthermore, there is rarely research that focuses on the spray properties emerging from realistic multi-hole nozzle injectors. Therefore, it is worthwhile to conduct a systematic study on this issue to provide references for engine design and modeling in the future.

1.2 OBJECTIVES AND APPROACHES

The target of this study is to investigate the Diesel multi-hole nozzle internal flow, spray evolution, and mixture formation characteristics numerically and experimentally. The specific objectives of this study are shown as follows:

Analyze the effects of multi-hole nozzle geometry on nozzle internal flow and spray evolution characteristics comparing with the criterion which belongs to the single-hole nozzle under the non-evaporation and evaporation conditions.

Illustrate the influence of dynamic factors (injection pressure and injection quantity) and geometrical factor (hole diameter) on the difference in the internal flow and spray behaviors between the single-hole and multi-hole nozzles.

CFD numerical study of the spray was conducted with the consideration of internal flow properties to provide an insightful understanding of the spray injected by different nozzles from the macroscopic and microscopic views.

Focus on the multi-hole nozzle and investigate the properties of internal flow, spray evolution, and mixture formation of the multi-hole nozzles which is characterized by different dynamic operation and nozzle geometrical factors.

Correlate the nozzle geometrical design and nozzle internal flow with the spray evolution and mixture formation characteristics of diesel multi-hole nozzles.

In this study, the Mie Scattering technique was implemented to obtain the information of Diesel spray emerging from different kinds of nozzles under the non-evaporation condition. In addition, the Laser Absorption-Scattering (LAS) technique was adopted to analyze the mixture formation process of Diesel spray qualitatively and quantitatively under the evaporation condition. Moreover, the nozzle internal flow and spray were reproduced by the CFD simulation method under the corresponding conditions with the aim of providing integrated explanations and speculations for the mechanism behind the phenomenon observed in the experiments.

1.3 OUTLINES

To present this work, the thesis is organized as follows: First of all, a review of previous work, such as study on diesel nozzle internal flow, relationship between the nozzle internal flow and the near-field spray, mixture formation characteristics and combustion concepts of Diesel spray, and optical diagnostic techniques for spray and combustion, is presented in Chapter 1. Chapter 2 introduces the experimental apparatus implemented in this study, such as injection rate meter, fuel injection

system, high pressure and high temperature constant volume vessel, and the observation techniques applied in this investigation. The theoretical basis and computational model applied in the numerical study is described in Chapter 3. After that, the spray evolution of multi-hole nozzles under non-evaporation conditions is shown in Chapter 4. To correlate the nozzle internal flow with the spray behaviors, Chapter 5 illuminates the internal flow characteristics of multi-hole nozzles under different conditions. And then, the nozzle spray will be investigated numerically from the unique view in chapter 6. Furthermore, the characteristics of the spray evolution and mixture formation of multi-hole nozzles will be discussed under the evaporation conditions in Chapter 7 by applying LAS technique. Finally, general conclusions on characteristics of internal flow, spray evolution, and mixture formation of multi-hole nozzles for diesel engine are summarized in Chapter 8.

1.4 STUDIES REVIEW

1.4.1 Internal Flow Investigation for Diesel Nozzles

1.4.1.1 Mechanism of Cavitation Appearance

The nozzle internal flow cavitation is regarded as one of the main factors that alter the spray atomization. It is known that under the high injection pressure and stable temperature conditions, when the nozzle internal flow velocity is high enough, the cavitation can occur, which is because that the liquid phase vaporizes instantaneously when the local static pressure (decreases with velocity increasing) is lower than the saturated vapor pressure (critical pressure). Hence a two-phase flow forms inside the nozzles. The following figure (Figure 1.7) can be used to give a lively explanation about the cavitation flow. The low enough pressure and vapor nucleation are two key factors that generate the two-phase flow [Huang Jianchuan et al., 1992]. The heterogeneous nucleation mainly attributes to the diesel nozzle internal flow [Brennen E.P., 1995; Delale C.F., 2005]. The occurrence and development of the cavitation flow is very sensitive to the initial nucleation density, and some researchers [Keller, 1972; Katz and Acosta, 1982; Meryer, 1992; Liu and Brennen, 1998; Arora et al., 2007;] have tried to correlate the initial nucleation density with the cavitation development mathematically, while it did not work very well because of the limitation of nucleation density measurement inside the liquid. That is the reason why the cavitation flow prediction still has a long way to go, and until now it just can be reproduced with some model under some assumption.

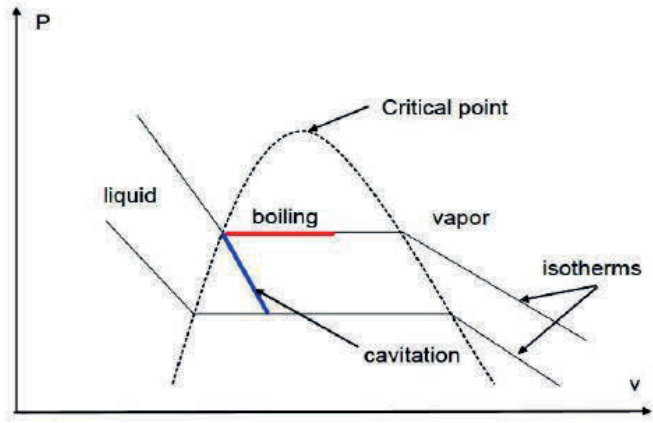


Figure 1.7 schematic of cavitation formation within the phase changing processes [Lecoffre Y., 1999]

When the two-phase flow is paid attention to under the nozzle fuel injection condition, the initial cavitation and pressure distribution inside the nozzle internal flow is presented in Figure 1.8 schematically. This kind of two phase flow is mainly caused by the hydraulic factors. The sudden change of the nozzle geometric on the hole inlet can generate the vena contracta, and with the increasing of the flow velocity, the local pressure is reduced to the critical vapor pressure, where the cavitation bubbles will appear in the downstream. Specially, there is usually 4 kinds of cavitation, which is shown in Figure 1.9. There are film-type, string type, hydraulic flip type, and multi-type cavitated flow. These kinds of flow can alter the fuel jet first stage break up directly, and during the past several decades, a lot of scholars tried their best to reveal the nature behind them.

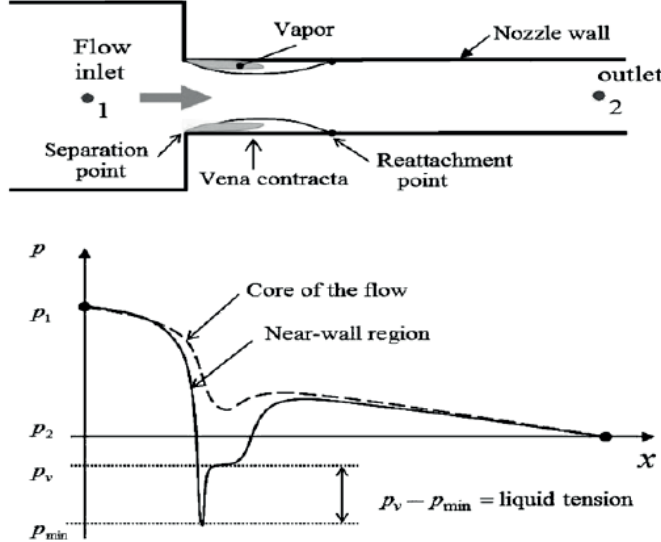


Figure 1.8 Initial cavitation and pressure distribution inside the nozzle internal flow

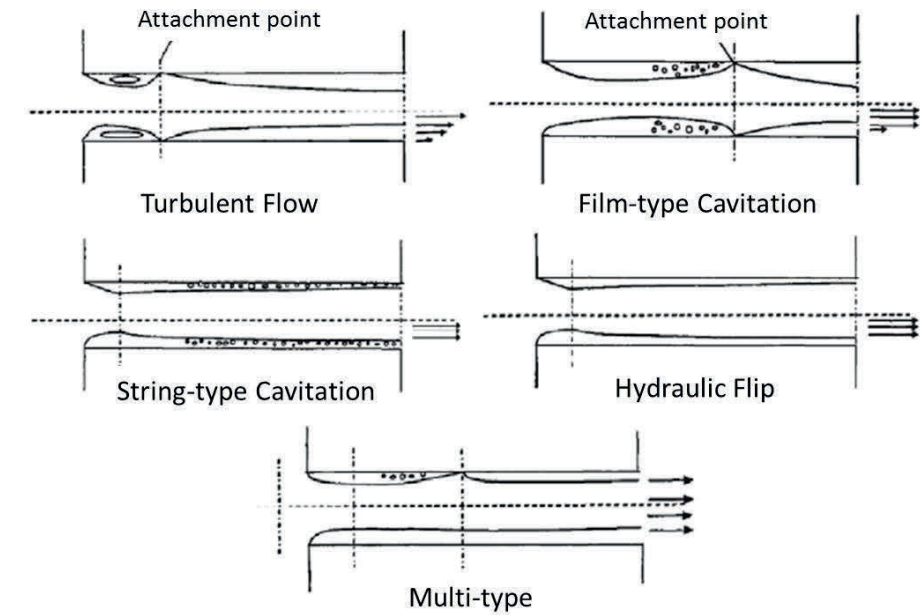


Figure 1.9 Five kinds of flow state inside the nozzle

1.4.1.2 Experimental Investigation about Nozzle Internal Flow

As introduced before, the researchers mainly paid attention to the single-hole nozzles, because of the simple geometric and convenience for observation. The enlarged [Soteriou, 1995; Afzal et al., 1999; Roth et al., 2002;] and real-size models [Chaves et al., 1995; Badock et al., 1999] were conducted to observe the nozzle internal, and the cavitation structure and the relationship between the nozzle geometry, cavitation flow, and nozzle discharge coefficient were understood by the researchers, and some classic theory was concluded out gradually. However, limited by the experimental apparatus at that time, the experiments could not be conducted under the real engine operation conditions.

With the development of materials science and measurement technologies, scholars began to investigate the properties of internal flow of multi-hole injectors. Arcoumanis et al. took photographs for a scaled (20×) injector tip, which showed that there were asymmetric film-type cavitation inside the hole and even string-type cavitation inside the sac of the multi-hole nozzle, and the needle eccentricity could cause a strong asymmetric effect on the flow and cavitation location in different holes of the multi-hole injector. After that, Arcoumanis et al. used detailed photographs of a real-size multi-hole nozzle to demonstrate the effect of cavitation number on the behaviours of cavitation within the hole [Arcoumanis et al., 2000]. They found that there were large differences in the cavitation structure and type. The typical photos are shown in Figure 1.10 and Figure 1.11, respectively. These phenomena had never been found under the single-hole condition.

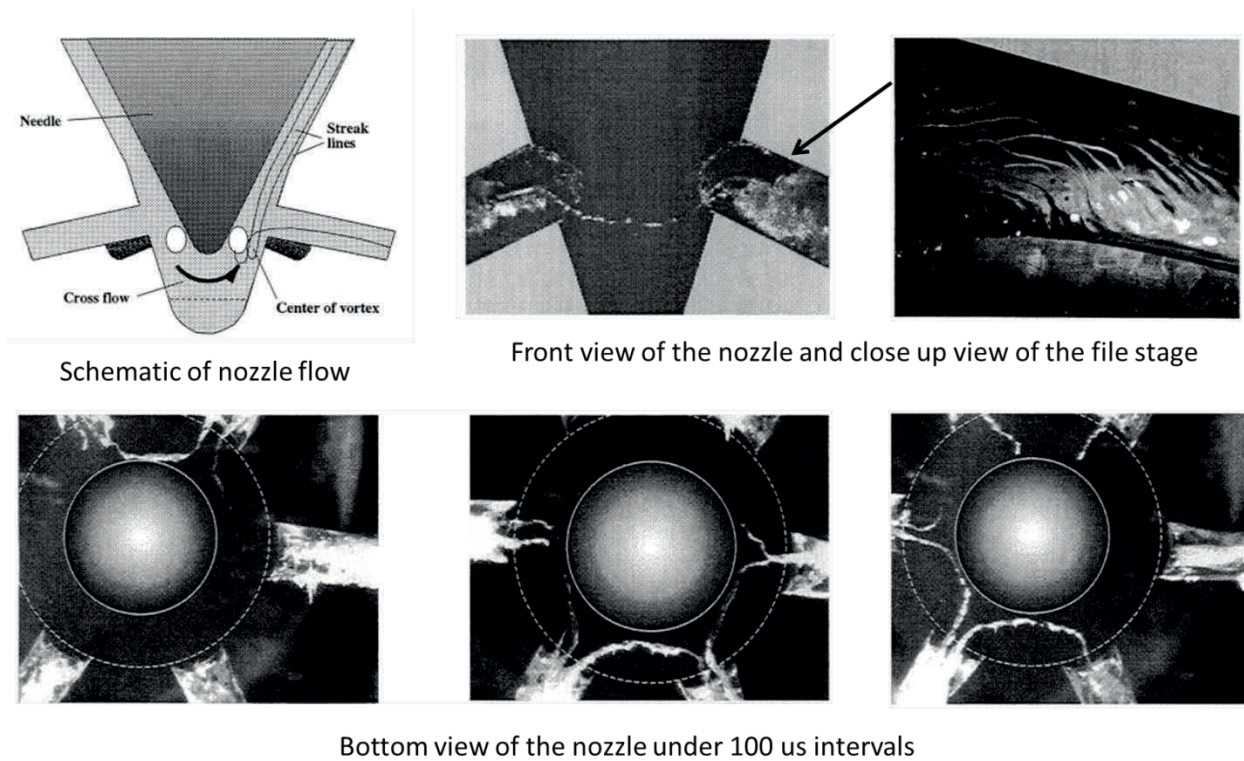


Figure 1.10 Film-type and string-type cavitation inside the nozzle [Arcoumanis et al., 1999]

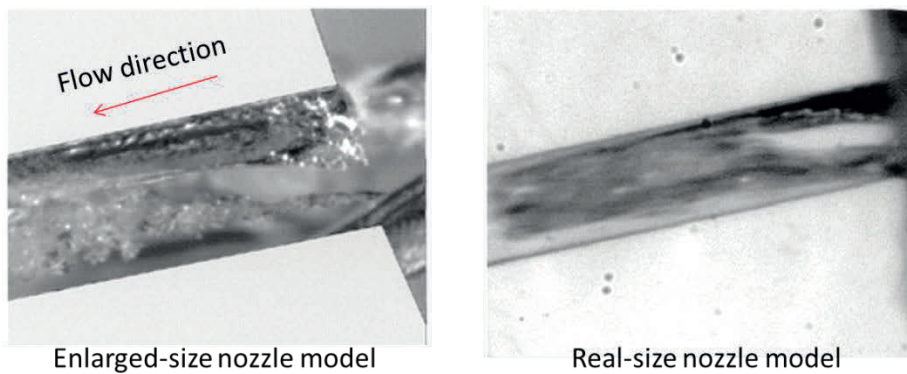


Figure 1.11 Comparison of cavitation under enlarged- and real-size nozzle model conditions [Arcoumanis et al, 2000]

Researchers had also been concentrating about the internal flow properties under different nozzle geometry conditions. For example, the effect of hole number, inlet roundness [Bergwerk, W., 1959; Nurick, W.H., 1976;], ratio of length to diameter [Lichtarowicz & Pearce, 1974], taper ratio [Winklhofer, 2001; Benajes, 2004;], and the roughness of the holewall [Lecoffre, 1999] and so on, a lot of geometrical factors can alter the internal flow characteristics. Originally, the simple structure single-hole models were mainly applied to get a fundamental understanding about the effect of nozzle configuration. However, the research conducted by Schmidt et al. showed that there was

asymmetrical cavitation inside asymmetrical-hole nozzle, and it was easy to observe the partial hydraulic flip phenomenon [Schmidt et al., 1999]. Therefore, the researchers wanted to control the cavitation and turbulent inside the nozzle by adjusting the geometrical design [Kim et al., 1997; Laonual, 2001; Blessing, 2003;]. The relationship between the nozzle internal flow of the multi-hole nozzle and the nozzle geometry will be discussed in detail in Chapter 5.

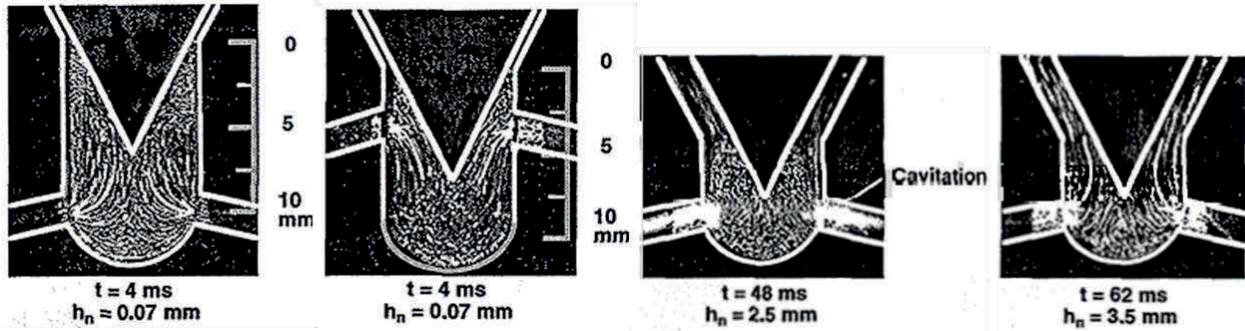


Figure 1.12 Flow trend inside multi-hole nozzle with different geometry [Kim et al., 1997]

Moreover, when concerning the internal flow quantitatively, the discharge coefficient is still an important parameter, that attracting the attention of the researchers. With the increasing of the cavitation level, the effective flow area should be reduced, and the discharge coefficient is also reduced. As a result, this parameter is a good reflection of the cavitation level inside the hole. It is concluded that under no-cavitation condition, the discharge coefficient mainly depends on the Reynolds number [Lichtarowicz et al., 1965], while under the cavitation condition, the discharge coefficient mainly depends on the cavitation number (CN) i.e. $CN = (P_{injection} - P_v) / (P_{injection} - P_{back})$ [Payri, 2004]. The specific relationship is shown in Figure 1.13. However, all these experiments were conducted under the quasi-steady conditions.

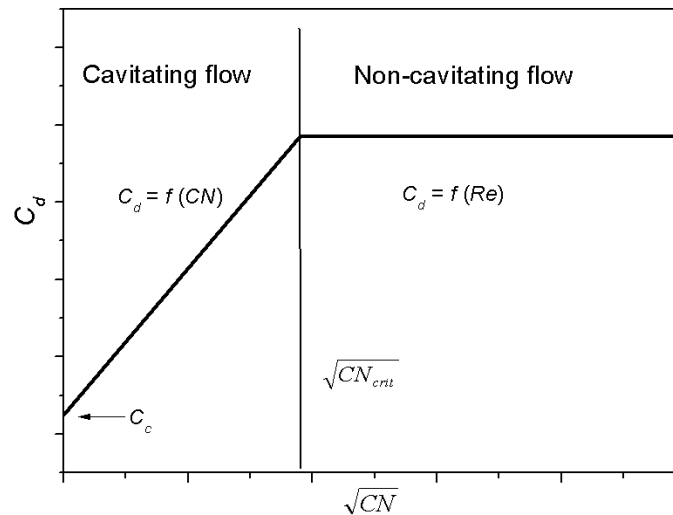


Figure 1.13 Relationship between cavitation number and discharge coefficient [Lichtarowicz, 1965]

In a word, until now it is still difficult to get the accurate quantitative data from the realistic diesel injector transient internal flow (high pressure, high velocity and micro size).

1.4.1.3 Numerical Investigation about Nozzle Internal Flow

As it is known that the principal properties of diesel fuel spray that affects the combustion and engine performance are droplet size, spray angle, spray cone angle, and spray tip penetration. These characteristics are mainly governed by the internal flow inside the nozzle. Under the realistic operation condition, the Reynolds number of the internal flow normally ranges from 10^4 to 10^7 , which can result in the flow becoming super complicated, including the turbulent flow, mass transfer process, compressible flow, and unsteady fluid dynamics. [Ramamurthi & Nandakumar, 1999]. Albeit many studies have revealed that the cavitation and vortices generated in the nozzle hole could play a significant role in the spray characteristics, it is indeed difficult to directly observe the extremely transient high-speed flow in the minute space of the nozzle and holes for both enlarged transparent nozzles and real-size nozzles. With the development of numerical simulation techniques, it has launched a new era for researchers to investigate the internal flow in real-size nozzles under realistic operating conditions. It has been proven that CFD techniques can provide a good correlation of the nozzle design to the spray performances [Mulemane, A., 2004].

The continuum method is the most popular concept applied in the simulation of the internal flow, which has a very wide range of application. It has some advantages when applied in the models, such as reflecting the whole mechanism of the cavitation appearance, structure of the two-phase flow, bubble dynamics, turbulence, and the interaction between them. The calculation time is also acceptable under the framework of RANS (Reynold-Averaged Navier-Stokes). There is an assumption that inside the two-phase flow, the liquid phase and vapor phase can be interinfiltration, and the two-phase can be treated as continuum, respectively.

As a result, when the two-phase flow is treated as a whole continuum to conduct the simulation and calculation, it is called the single-phase flow model [Schmidt, 1999; Qin, 2001; Dumont, 2001;]. The vapor and liquid mixture in infinitesimal control volume is assumed as completely uniform compressible flow medium. Its density is usually treated as a function of the density of each phase and sub-phase volume fraction in the local flow field. The mixture pressure and velocity field satisfy the Navier-Stokes equations, while the governing equations are not closed, because the volume fraction of each phase needs to be solved. Single-fluid model has been developed to take full advantage of mature single-phase flow solver without a heavy calculation, and very suitable for many irregular three-dimensional basin. Thus, the single-fluid model has been

very widely used. However, the single-fluid model assumes that there is no slip between different phases, and generally applied in the case under a strong phase coupling condition.

When the vapor phase and liquid phase are treated as two kinds of continuum, and the equations about the two phases are solved separately, it is called the multi-phase flow model [Alajbegovic, 1999; Von Berg, 2005;]. Under this assumption, gas-liquid two-phase cavitation flow is continuous independent media, and the movement of both the flow field is controlled by the conservation equations, respectively, which can allow the slip between different kinds of phase. The mass, momentum, and energy exchange of liquid and gas phase flow can be more easily presented by the corresponding transport equations of different kinds of phase. Thus, the two-phase fluid model can reflect more details of the flow field than the single-phase fluid model.

For super small gas core inside the liquid, which can be assumed to be suspended bubble in liquid spherical, the balance between the force is $P = P_B - 2S / R$, where P_B and R are the pressure and the gas core radius, respectively, and S is the surface tension coefficient, P is the pressure of out of the gas core. As can be seen, in order to develop into cavitation bubbles, the balance of the above relation must be destroyed, namely pressure outside the core should be much lower than the pressure inside the gas core, which means that the liquid must have a low pressure field to generate the presence of cavitation. According to the cavitation formation mechanism, it shows that the cavitation occurrence and development under the critical conditions and different tension conditions mainly depends on gas core size and density in the local liquid flow field.

Thus, a generic cavitation flow model must eliminate scale effect caused by the gas core, so as to apply for different fluids and different flow conditions. Unfortunately, the handling of core size and distribution inside the cavitation flow is still is the most difficult part, and the progress is very slow. Therefore, both of the two kinds of models are just the simplest way to describe the effect of the gas core, and the initial radius and gas core number density in the flow field are processed into the adjustable model constants.

In general, the cavitation flow model mentioned above can reproduce the two phase internal flow inside the diesel nozzle, and predict the macroscopic cavitation flow properties successfully relatively, such as the corresponding flow structure and cavitation exhibition characteristics under different orifice geometries and injection pressure conditions. Such programs can reflect the characteristics of diesel nozzle internal flow, and it is also easy to implement relatively. Therefore, this method will be applied in this article and make a systematic research on the nozzle internal flow under different conditions.

1.4.2 Investigation about Effect of Nozzle Internal Flow on Near-field Spray

So far, many scholars have been using experiments and numerical simulation models and to extensively investigate the effect of nozzle internal flow characteristics on the near-field jet break up processes. The effect of cavitation and the turbulence on inside the nozzle the jet atomization process is the focus of most research. The main developments are summarized and discussed on the aspects of experiments and numerical simulations, respectively.

1.4.2.1 Introduction of the Experimental Investigation

In recent years, with the development progress of the experimental methods, including the science and technology, researchers can not only measure the macro spray nozzle near-field structure (such as spray cone angle, penetration distance, and Sauter mean diameter, etc.) , but also can observe the nozzle cavitation process inside the hole, and even the jet liquid nucleus and surface. This helps scientists to delve into the interior of the nozzle flow associated cavitation, turbulence, and jet atomization process in some extent.

The importance of cavitation flow on the fuel jet atomization has been well proved very early by Arai et al., Hiroyasu et al., Bode and Soteriou et al. They all applied the transparent nozzle and the nozzle size ranged from enlarged size to real size, but the injection pressure was not high enough as the modern common rail system. For example, the experiments conducted by Arai et al. and Hiroyasu et al. showed that the inception of cavitation can change the spray behavior obviously. The spray angle can be enhanced and the break up length and spray tip penetration can be shortened. The upper half of the Figure 1.14 shows photographs of cavitating nozzle flow. Flow is from the top of the figure to the bottom. The lower half of the figure shows quantitative measurements of spray quantities.

The internal flow cavitation and the near-field spray could be observed more clearly and in more detail from the beginning of this century. The development of the light source, camera, and material of the transparent nozzle mainly attributed to this issue. The result shown in Figure 1.15 is some typical research conducted by high speed observation method. And the relationship between the internal flow and the near-filed spray was investigated from different views under different conditions, including the type of injectors, nozzle hole geometry factors, injection pressure, and needle lift height and so on.

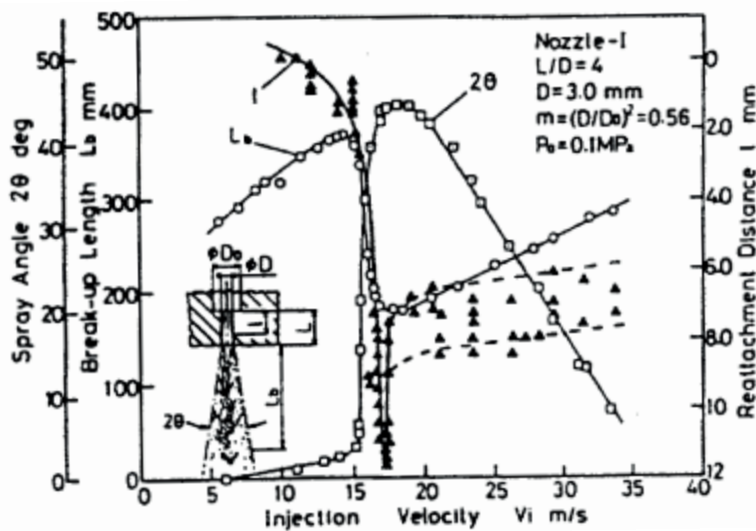
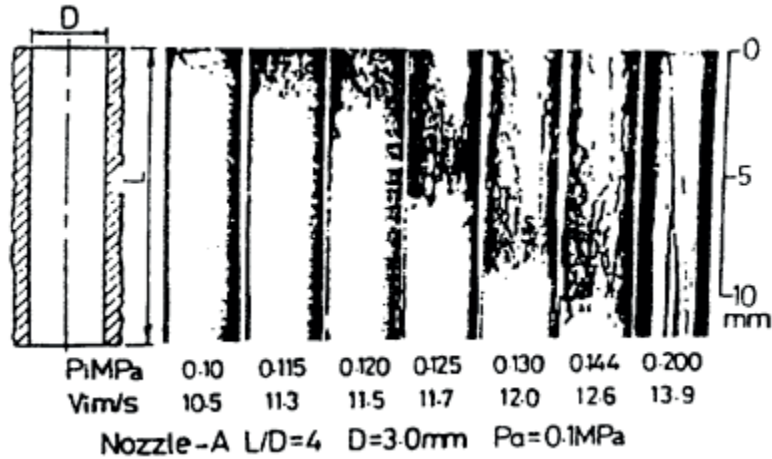
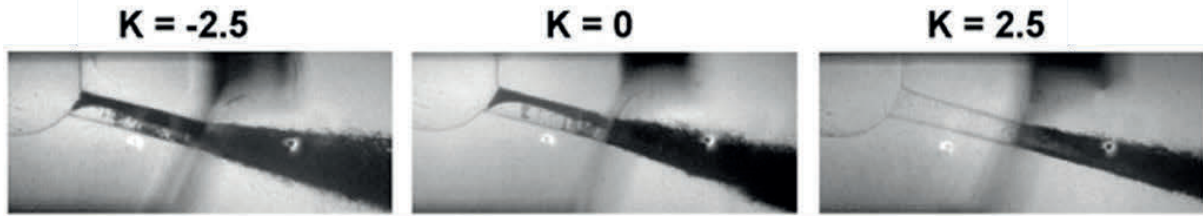
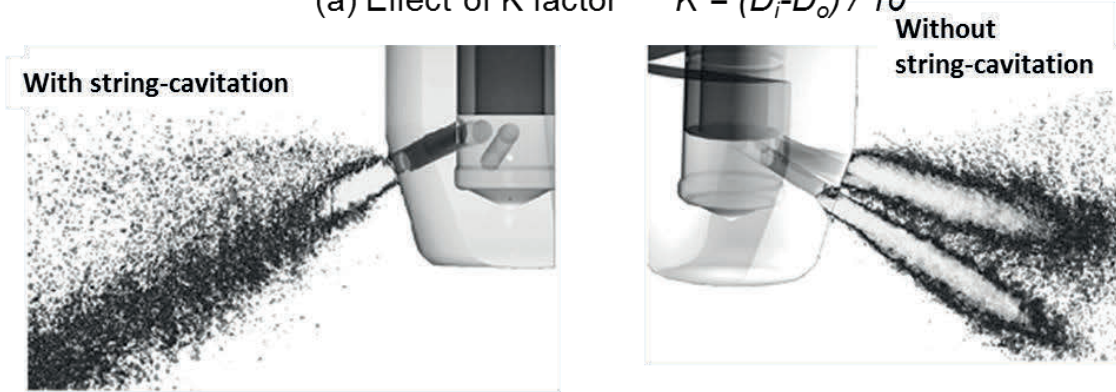


Figure 1.14 Observations of cavitating nozzles. [Arai et al., 1991; Hiroyasu et al.,1991;]

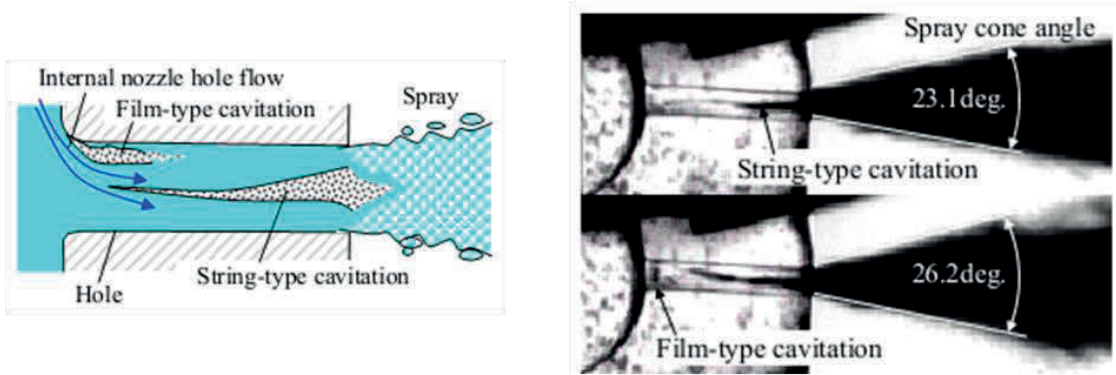
According to the result in Figure 1.15, the spray first break up process mainly depends on the nozzle internal two-phase flow. Unfortunately, the inability to obtain quantitative data cavitation bubbles collapse, they were unable to assess how the cavitation bubbles collapse process in the nozzle affect the near field of the jet nebulizer quantitatively. As a result, some other researchers began to pay attention to the effect of the nozzle internal flow on the spray momentum [Payri, R., 2005], evaporation [Yuhei Matsumoto, 2007], combustion [Bergstrand, P., 2001; Payri, F., 2006; Wu, Z., 2011;], and engine performance directly [Kim, B.K.,2005; Kuhnert, S., 2010; Montgomery, D.T., 1996;], and it also has been proved that the nozzle interflow of different nozzle geometry and conditions can alter the injection rate [Benajes, J., 2004], spray propagation, evaporation, combustion, and engine performance obviously, while it is still necessary to investigate more.



(a) Effect of K factor $K = (D_i - D_o) / 10$



(b) Effect of string-type cavitation type



(c) cavitation type

Figure 1.15 Visualization of the internal flow and near-field spray simultaneously [M. Blessing et al., 2003; M. Gavaises and A. Andriotis, 2006; Tomohiro Hayashi, 2012;]

Recently, the application of synchrotron x-ray sources with high energy pulses has been extended to the study of fuel sprays during the last decade. Lai et al. applied ultra-fast phase-contrast X-ray imaging technique to observe the spray structure near the orifice exits of single-hole and multi-hole nozzles, and the result revealed that compared with the single-hole nozzle, multi-hole nozzles produced much more unstable jet structure [Lai et al., 2011]. Moreover, as shown in Figure 1.16, Moon et al. concluded from the X-ray images that the needle lift curve, needle moving speed, fuel velocity distribution at the orifice exit, and the jet flow breakup of the multi-hole nozzle are quite different from those of the single-hole nozzle [Moon et al., 2015].

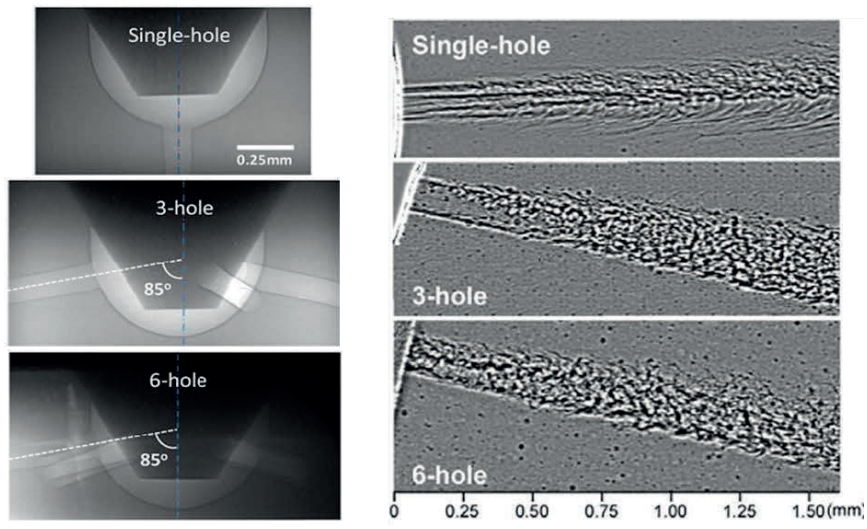
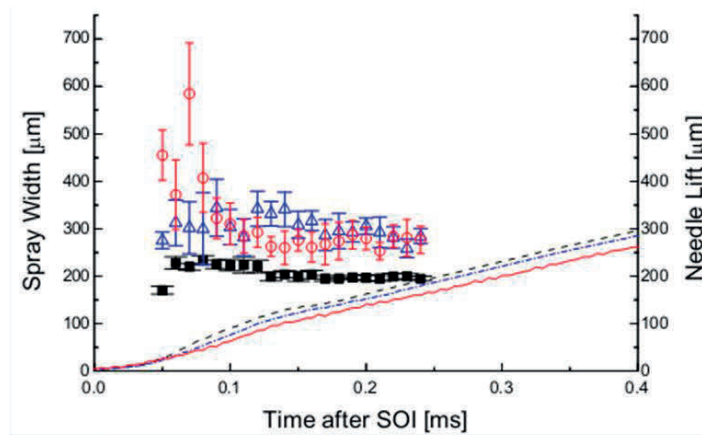


Figure 1.16 X-ray image of internal flow and near-field spray [Moon et al., 2015]

It should be noted that all the recent research was conducted under the multi-hole nozzle condition, which is more closed to the real option condition, and a lot of interesting phenomenon were published by these researches. However, the nozzle are all specially design to increase the visualization of the experiment, and the observation was mostly conducted under the constant operation conditions, which still had large differences from the real injection conditions. The limited multi-hole injector types and experimental conditions hindered a more satisfied situation in understanding the flow dynamics of real multi-hole nozzles under practical operating conditions thoroughly. That is also the reason why this research focuses more on the practical multi-hole nozzles.

1.4.2.2 Introduction of the Numerical Investigation

After recognizing the important role played by nozzle cavitation and turbulence on the jet atomization, the researchers began trying to build physical sub-cavitation disturbance and

turbulence disturbance models to couple with the atomization model for multidimensional simulations, whilst examining the impact of nozzle internal flow on jet atomization.

Huh & Gosman [1991] and Bianchi, et al. [1999], developed a phenomenological model, in which the spray atomization is induced by turbulence, and the initial disturbance and spray angle of the jet could be corrected by turbulence intensity on the nozzle outlet. In the specific processes, the researchers associated the wavelength characteristic of instability wave with the integration of turbulence length scale linearly to obtain atomization length scales, and the same methods of linear association was used to get the atomization time scale, thereby the radial velocity of the atomization processes can be obtained. After that, the radial velocity and axial velocity of the atomized spray were compared to determine the spray angle. The model is currently popular for Star-CD, Fire, KIVA, and other commercial programs, while the presence of cavitation inside the nozzle is not included in its forecast for turbulence parameters.

Arcoumanis, et al. [1997] proposed an atomization model which could take the nozzle cavitation and turbulence simultaneously. To link the spray atomization to nozzle hole flow, the model used a series of rough approximations. First, discharge coefficient formula is corrected to calculate the effective velocity and effective radius of the liquid jet. Nozzle exit flow parameters were estimated using the empirical formula. The model assumes that the characteristic radius of cavitation bubbles is equal to the difference between the pore radius of the nozzle hole and the effective radius of the liquid column. Combined with the characteristic radius and Rayleigh equation, collapse time of cavitation bubbles was calculated out. At the same time, the model also defined the characteristic burst time for the bubbles diffusion from the center to the surface of the jet, which is caused by the turbulence in the jet, and then the minimum value of both the two kinds of time was set as the atomization characteristic time scale. In theory, this is an atomization model with relatively complete physical concept, which includes a one-dimensional simulation of the oil supply system and the multidimensional simulation of the jet atomization, while because too many empirical formulas were introduced, the forecast inaccuracies of model were increased somehow.

Nishimura & Assanis [2000] developed a primary atomization model based on the energy of cavitation bubble collapse. The core idea of this model is to assume that the energy provided by the cavitation bubbles collapse inside and outside the nozzle was all converted into the turbulent kinetic energy in the flow field. When the liquid jet was injected out of the nozzle, the turbulent kinetic energy, the average speed, cavitation bubble volume fraction, and bubbles size were all

determined by a phenomenological model. The first break up was regarded to be controlled by the air force, surface tension, and turbulence induced crushing force. And the same with Arcoumanis, et al.'s model, this model mainly processed the internal flow, cavitation, and the scrambled force of the jet atomization based on experience equations and simple assumptions, thus the mechanism of nozzle turbulence and cavitation reflected by this model was also limited.

In recent years, with the improvement of the three-dimensional two-phase flow simulation methods for the internal flow inside the nozzles, some researchers try to use the three-dimensional simulation of flow field to predict orifice outflow conditions. Von Berg et al. [2005], and Tatschl, et al. [2000] coupled Eulerian two-phase flow model, which could describe the three-dimensional cavitation flow, with the spray primary break up model, which could consider cavitation and turbulence in the Eulerian- Lagrangian framework. The key of the coupling is the implementation of transferring the detailed flow parameters at the nozzle exit to the downstream flow field numerically. The calculations show that the method of introducing the nozzle orifice flow parameters calculated by the two-phase flow model into the first break model as the primary boundary conditions is possible to predict the impact of various changes in the microscopic flow conditions on the macro atomization characteristics. Baumgarten, et al. [2002] used a similar approach to examine the impact of the turbulence and cavitation on the nozzle atomization, and the difference is only about the processing details for the two-phase flow nozzle cavitation model and spray primary break up model.

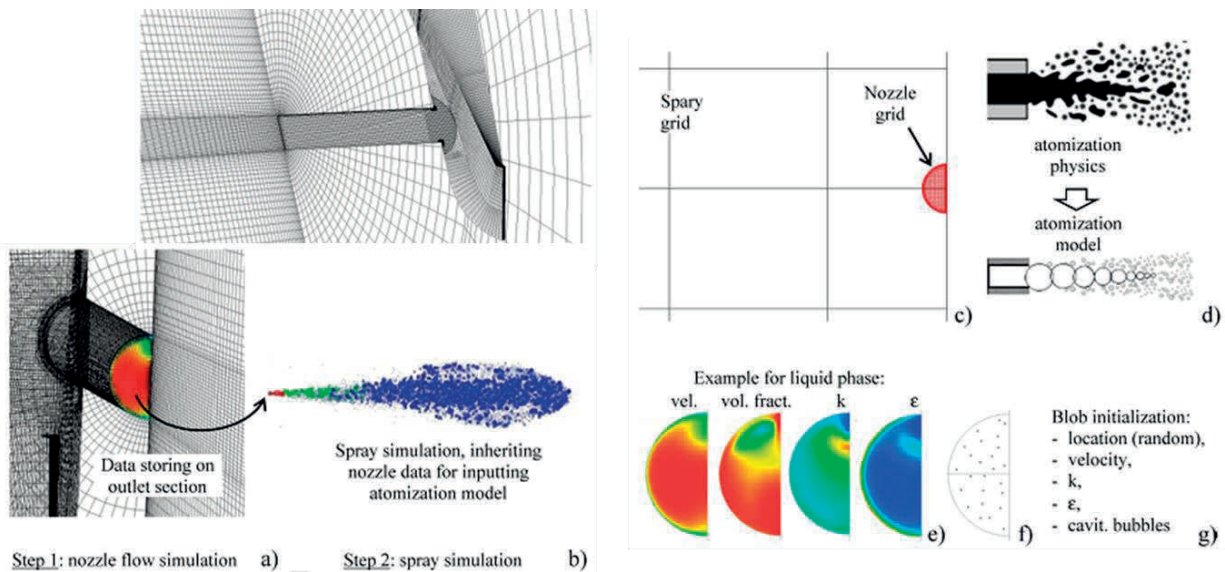


Figure 1.17 Calculation with internal flow coupled spray model [Michele Battistoni et al., 2012]

The example of the calculation steps is shown in Figure 1.17, and it including seven stages. Specifically, nozzle flow results (a) transferred to the spray computation (b); comparison of nozzle hole grid and spray grid (c); blob method for primary atomization (d); examples of spatial (and temporal) distributions inside the hole area stored to file (e); random location of blob centroids (f); blob initialization (g).

Clearly, these methods can be to better to reflect the physical processes, and thus it has the most promising. This method will also adopted in this method and more detail introduction will be presented in Chapter 6. In general, whether the experimental method or numerical simulation model, when applied to investigate the mechanism of the effect of the internal flow on the nozzle jet, analyzing the physical processes inside the nozzle and near-field (such as the growth and collapse of cavitation bubbles, turbulence evolution of field, etc.) in-depth is the key to the interpretation of such a mechanism.

1.4.3 Diesel Spray Evolution, Mixture Formation and Combustion Processes

1.4.3.1 Spray Evolution and Mixture Formation

As introduced before, the spray evolution and mixture formation process are thought as the most important key factors for the subsequent combustion process. Therefore, it is necessary to understand the spray evolution process deeply, which can make a contribution to improve the combustion and emission performance. Plenty of researches focused on spray atomization, and as shown in Figure 1.18, the internal turbulent [DeJuhasz, 1931; Schweitzer, 1937], cavitation [Bergwerk, 1959], mutation of the boundary condition at nozzle exit [Rupe, 1953], and surface wave caused by aerodynamic interference [Castleman, 1931] were proved to be the determinants during the atomization process separately. Recently, the fundamental experiments, especially for the visualization of the spray evolution, have made great processes. It was found that the spray atomization could not be explained by each determinant described above, individually. In fact, the atomization processes were affected by the combined factors, in which the internal flow turbulence, cavitation instability, and aerodynamic forces are paramount [Arcoumanis et al., 1970; Smallwood and Gülder, 2000;]. Therefore, the previous works mainly concentrated on those three paramount factors, which are introduced in this review emphatically.

It is known that the phenomenon of coherent liquid disintegrating into ligaments and large droplets is defined as primary break-up, and this process usually happens during the internal flow stage even the spray does not emerging from the nozzle hole, which is attributed by the turbulence

and cavitation, simultaneously. Wu et al. [1995] found that the droplets form from turbulent eddies when the surface energy is lower than the radial fluctuations of kinetic energy of the eddy, which is described as follow,

$$C_l(4\pi l^2)\sigma \leq \rho_f v_l^2(\pi l^3/6)/2 \quad (1.1)$$

where σ is the liquid surface tension, l is the eddy size, C_l is an empirical factor, v_l is the radial fluctuation velocity, and ρ_f is the liquid density. The turbulent effect highly depends on the flow velocity. The specific introduction is presented in the previous sections. When the spray emerges from the nozzle orifice, aerodynamic-induced break-up plays a role in mixture formation, gradually.

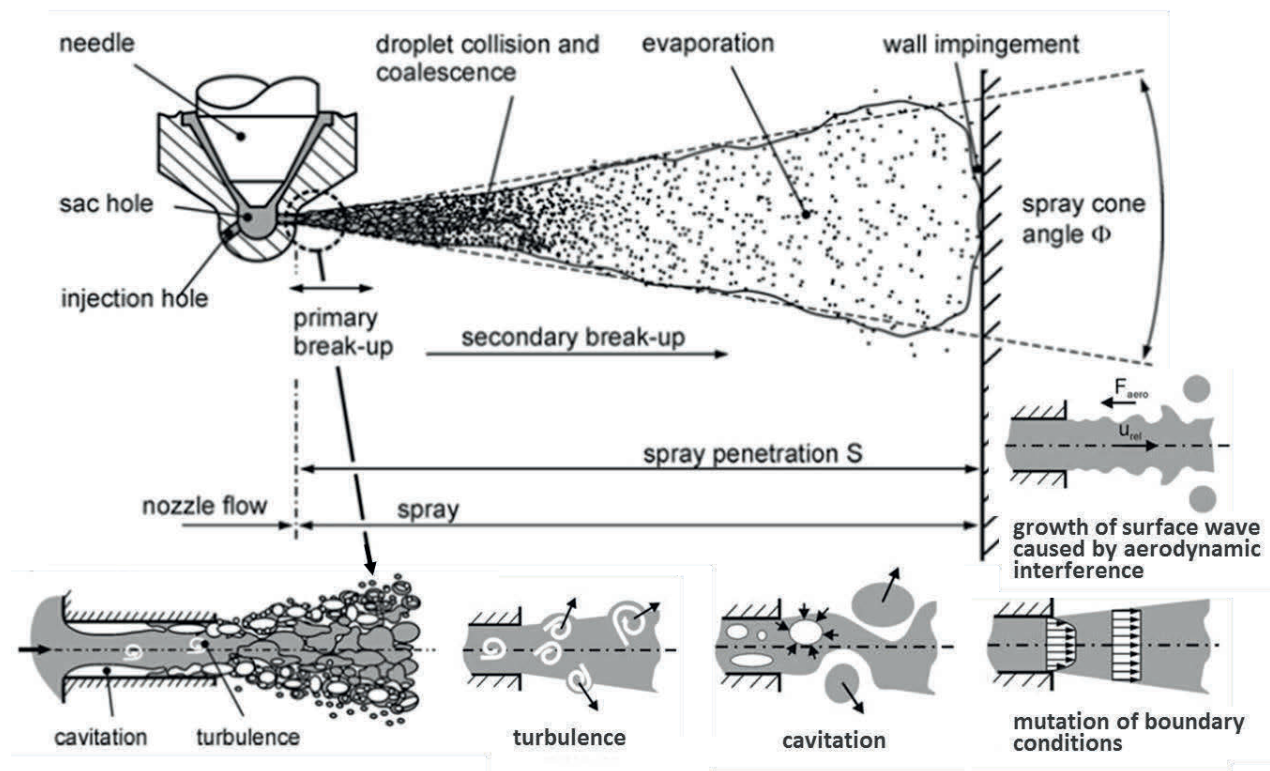


Figure 1.18 Spray break-up process from hole-injector [Baumgarten, C., 2006]

Previs Studies [Hiroyasu et al., 1990 and 1991;] indicated that the coherent liquid does not disintegrate into small droplets immediately, and there is a region closed to nozzle exit with ligaments and dense large droplets. This process should also be included into the primary break-up process because the internal turbulence and cavitation exert more decisive effect than aerodynamic forces on fuel disintegration during this process. Hiroyasu and Arai [1990] calculated the axial length of the external break-up region by Equation 1.2.

$$L_b = 7 \cdot D \cdot \left(1 + 0.4 \frac{r}{D}\right) \cdot \left(\frac{P_a}{\rho_l u^2}\right)^{0.05} \cdot \left(\frac{L}{D}\right)^{0.13} \cdot \left(\frac{\rho_l}{\rho_a}\right)^{0.5} \quad (1.2)$$

where r is the radius of the nozzle hole inlet, L and D are the length and diameter of the nozzle hole, u is the initial jet velocity, ρ_l and ρ_a mean liquid and gas density, and P_a represents the ambient pressure density. When the spray extends the break-up length, aerodynamic force leads to the formation of smaller droplets, which is called the secondary break-up. This process highly depends on the ratio of aerodynamic to surface tension, which is defined as gas phase Weber number,

$$We_a = (\rho_a \cdot u_{rel}^2 \cdot d) / \sigma \quad (1.3)$$

in which d is droplet diameter, and u_{rel} is the relative velocity between droplets and gas. It is well known that different break-up models exist according to different Weber numbers. According to different Weber numbers, different break-up models are classified. [Pilch and Erdman, 1987].

All of these break-up mechanisms works on diesel engine sprays, and the disintegration process contributed by high Weber number takes place in upstream. On the other hand, the break-up process belonging to low Weber number appears in downstream correspondingly.

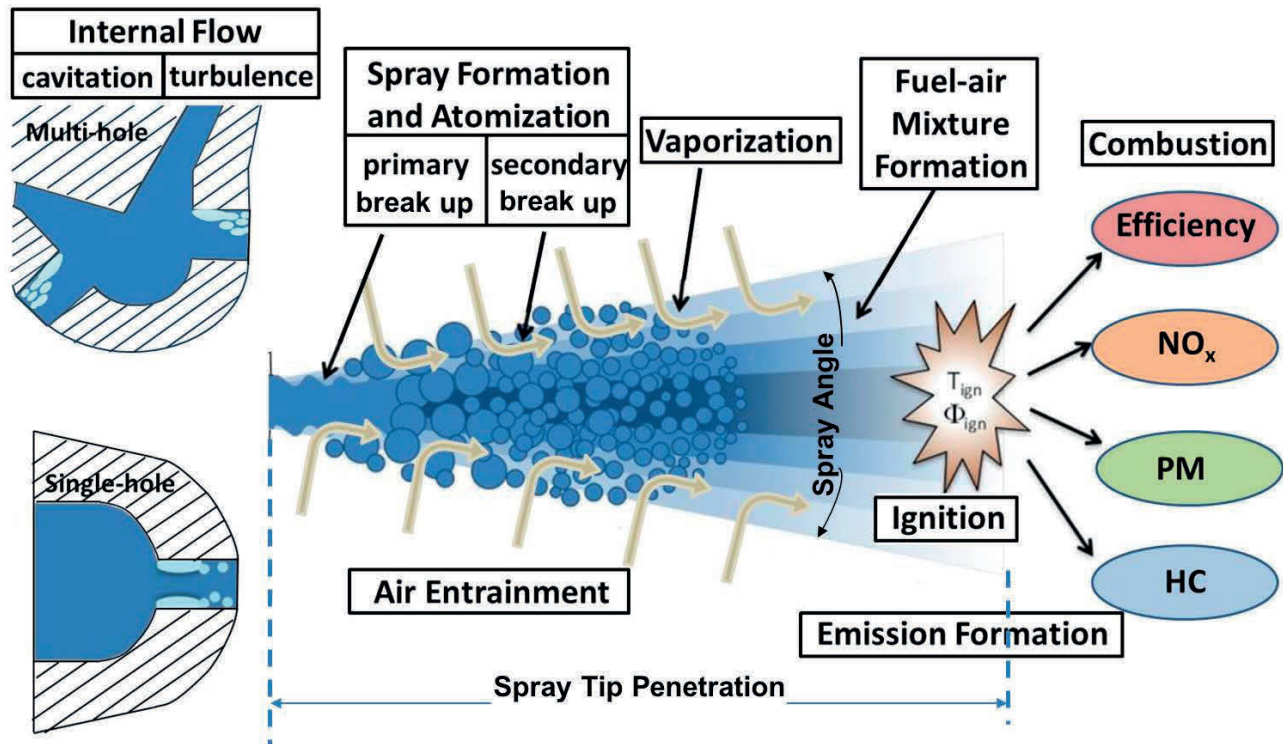


Figure 1.19 Schematic of Diesel spray propagation process

Compared with the investigation of microscopic spray characteristics in last section, the macroscopic spray characteristics is easier to observe. The most popular parameter about macroscopic spray characteristics are spray tip penetration and spray cone angle. Figure 1.19 shows a schematic of Diesel spray propagation process in the chamber and the definition of spray tip penetration and spray cone angel of Single-hole and multi-hole nozzles.

Spray tip penetration and spray angle can affect the ambient gas entrainment and the mixture formation quality. Concerning the wall wetting effect of diesel spray, overlong spray tip penetration can result in higher hydrocarbon (HC) and carbon monoxide (CO) emissions, and also higher consumption of fuel and lubricant. However, too short spray tip penetration can deteriorate the utilization of ambient gas. During the past several decades, study about semi-empirical relations between spray cone angle and spray tip penetration and the boundary conditions have been carried out by different researchers. Based on an overall momentum conservation and the fuel mass balance under the supposition that relative velocity between droplets and air in the spray is negligible, Wakuri et al. [1960] proposed a spray penetration empirical equation as follow,

$$S = \left(\frac{2C_a \Delta P}{\rho_a}\right)^{0.25} \cdot \left(\frac{t \cdot D}{\tan(\alpha/2)}\right)^{0.5} \quad (1.4)$$

C_a is the area contraction coefficient, α means the spray cone angle, ΔP is the pressure drop at the nozzle exit, and t stands for evolution timing.

Dent [1971] took into account of the effect of ambient temperature T_a on spray tip penetration prediction in a experimental rig of constant volume chamber, and he concluded that the spray penetration length is inversely proportional to the fourth root of ambient temperature as shown in Equation (1.5).

$$S = 3.07 \cdot \left(\frac{\Delta P}{\rho_a}\right)^{0.25} \cdot (t \cdot D)^{0.5} \cdot \left(\frac{294}{T_a}\right)^{0.25} \quad (1.5)$$

Hiroyasu and Arai [1990] separated the time-resulted spray tip penetration length into two stages. The first stage is the liquid core without integration because the low needle lift and the low flow rate. The spray tip penetration is proportional to the time after start of injection. However, during the second stage, the spray consists of large number of droplets. Although the spray still continually penetrates to further destination, which is attributed to the impetus of the latter injected high momentum fuel, the rate of the penetration increasing is decreased, and the penetration length agrees with a square root function over the time after start of injection.

$$t < t_{break} : S = 0.39 \cdot \left(\frac{2\Delta P}{\rho_l}\right)^{0.5} \cdot t \quad (1.6)$$

$$t > t_{break} : S = 2.95 \cdot \left(\frac{\Delta P}{\rho_a}\right)^{0.25} \cdot (t \cdot D)^{0.5} \quad (1.7)$$

$$\text{where } t_{break} = \frac{28.65 \cdot \rho_l \cdot D}{(\rho_a \cdot \Delta P)^{0.5}} \quad (1.8)$$

Recently, Naber and Siebers [1996] proposed a new spray penetration prediction method for non-evaporating condition based on the idealized model of Wakuri et al. [1959], as shown in Figure 1.20. Based on the fuel mass and overall momentum conservation in the axial direction of the spray, they modified the estimation for the arbitrary constant in a control surface of the spray tip penetration. they summarized the experience equations as follows:

$$S < S_r : S = C_v \cdot \left(\frac{2\Delta P}{\rho_l}\right)^{0.5} \cdot t \quad (1.9)$$

$$S > S_r : S = \sqrt{\frac{C_v \cdot \sqrt{2C_a}}{\tan(\alpha/2)}} \cdot \left(\frac{\Delta P}{\rho_a}\right)^{0.25} \cdot (t \cdot D)^{0.5} \quad (1.10)$$

$$\text{where } S_r = \frac{\sqrt{C_a} \cdot D}{\tan(\alpha/2)} \cdot \sqrt{\frac{\rho_l}{\rho_a}} \quad (1.11)$$

where C_v is the velocity coefficient, and the equations are a little similar with the equations of 1.6-1.8, which were proposed by Hiroyasu and Aria. However, Naber and Siebers replaced the original time- standard with the physical length to define the transition of the spray, and the nozzle hole flow coefficient was taken into account as well.

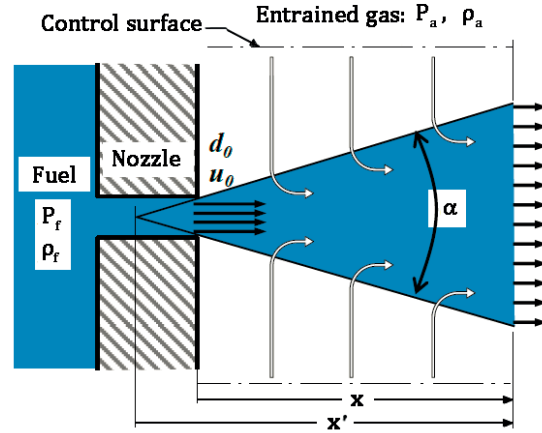


Figure 1.20 Schematic of the idealized model fuel jet [Naber and Siebers, 1996].

As introduced before, the break-up process is mainly dominated by the aerodynamic force, which mainly performs as the ambient gas entrainment, especially for the secondary break up processes. Therefore, the air entrainment attracts widely attention of the researchers. Ricou and Spalding [1969] proposed an air entrainment coefficient for a turbulent gaseous jet in 1961, which

was injected into the stagnant air with uniform pressure environment by applying the “porous-wall technique”. The ambient gas time-resolved velocity distribution around the spray was investigated by Ha et al. [1984] using a hot wire anemometer, and they concluded that the ambient gas mainly entrained into the spray volume from the upstream, while the gas was pushed away in the spray tip region. Cossali et al. [1991, 1996] introduced the Laser Doppler Velocimetry (LDV) into the study for the air entrainment in transient Diesel spray, they found that the ambient gas entrainment rate during the quasi-stable injection period is constant. The surrounding gas flow behaviors and the relationships between the gas entrained rate and ambient gas density and temperature were also investigated by them. Recently, the development of Particle Image Velocimetry (PIV) technique promotes more possibility to observe the ambient gas flow and mixture formation processes. There is a common acceptance agreement that the surrounding airflow could be divided into three regions based on the flow properties [Araneo et al., 1999; Rajalingam and Farrell, 1999; Rhim and Farrell, 2002; Sepret et al., 2010]. When the injection happens, the ambient gas is pushed away firstly by the spray head (region 1: head vortex zone), and then the ambient gas recirculates along two sides of the spray head (region 2: gas recirculation zone), finally the gas entrains into the following spray zone from the spray tail region (near quasi static zone).

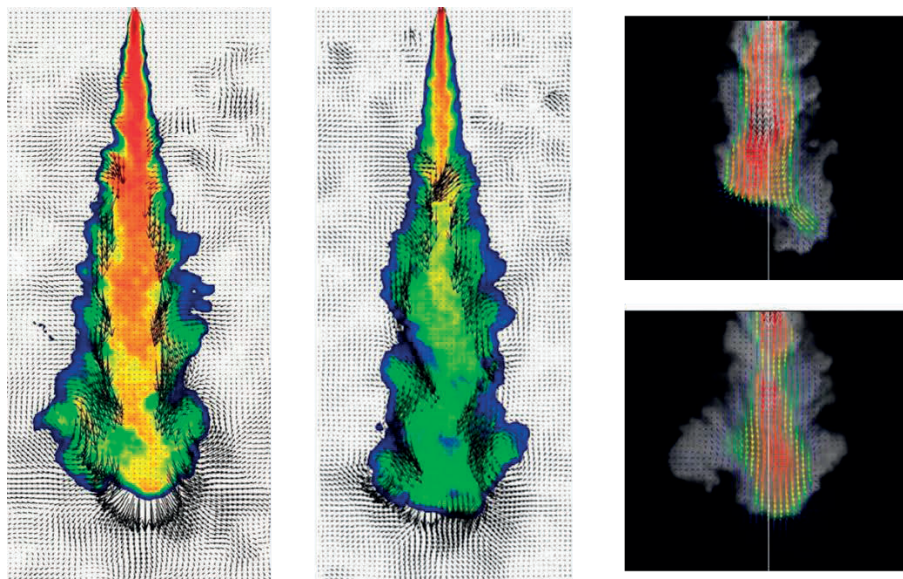


Figure 1.21 Air entrainment and fuel concentration image of Diesel-liked gas spray. Fuel concentration in color scale and flow velocity in black vectors [Bruneaux et al., 2011].

Bruneaux et al. [2011] applied Laser Induced Fluorescence (LIF) and PIV techniques, simultaneously. The air entrainment and fuel concentration characteristics were discussed, and different from the traditional conclusions, they found that there was also evident air entrainment in the recirculation zone, as shown in Figure 1.21.

In the recent decades, observing the distributions of vapor and liquid phases of the fuel spray, simultaneously, is widely studied by many scholars. Yeh et al. [1994] found that the Laser Induced Exciplex Fluorescence (LIEF) technique is suitable for this observation based on the function of vapor concentration and fluorescence intensity. Espey et al., [1997] tried to use Rayleigh Scattering (LRS) technique to get Images of quantitative fuel vapor concentrations in an evaporating Diesel spray. Moreover, the Spontaneous Raman Scattering (SRS) technique was also used to obtain air-fuel ratio distribution of Diesel spray, and Heinze [1989] and Rabenstein [1998] used this technic and found that the mixture formation process highly depends on the propagation velocity of inner and front spray. Schmalzing et al. [1999] applied Shadowgraph and Schlieren Photography technique to observe the liquid and vapor phase penetration, and they found that the vapor phase penetrated longer than the liquid phase under the engine operation condition. Bruneaux [1999] made an investigation on the vapor phase mixing using LIEF and announced that the mixing formation could be improved by increasing injection pressure or reducing hole diameter. Zhang [2001] achieved the equivalence ratio distributions of vapor phase and liquid phase of Diesel-liked spray simultaneously by applying the Laser Absorption-Scattering technique (LAS). He revealed that the upstream region of the spray is mainly occupied by high equivalence ratio of liquid phase, while the high equivalence ratio vapor region, where the auto-ignition is possible occurs, locates near the spray tip. The specific introduction about this method will be presented in Chapter 2, and the evaporating spray characteristics of multi-hole nozzles will also be investigated by applying this method, which will be discussed in Chapter 7.

1.4.3.2 Spray Combustion and Emissions

The combustion process in Diesel engines is initiated by the auto-ignition, which is resulted from the increasing temperature and pressure inside the cylinder during the compression process. Due to the high calorific value of diesel and high compression ratio of diesel engine, the pressure and temperature around the top dead center (TDC) range in 4~12 MPa and 1000~2000 K, respectively [Kaminoto and Kobayashi, 1991]. The typical variation trend between fuel injection rate, cylinder pressure, and heat release rate for Diesel engine is shown in Figure 1.22

The combustion process can be divided into three stages. The first one is premixed combustion stage, when the premixed mixture, which is formed during the ignition delay, undergoes reaction. The flame temperature and heat release rate increase quickly and the flame luminosity mainly comes from the weak chemical radicals during this stage. The second one is diffusion combustion stage. The combustion during this stage mainly locates in the periphery

region of the spray, and the flame luminosity is much higher because of soot incandescence. The last combustion stage usually happens after the end of injection (EOI), when the soot oxidation rate is higher than the production rate.

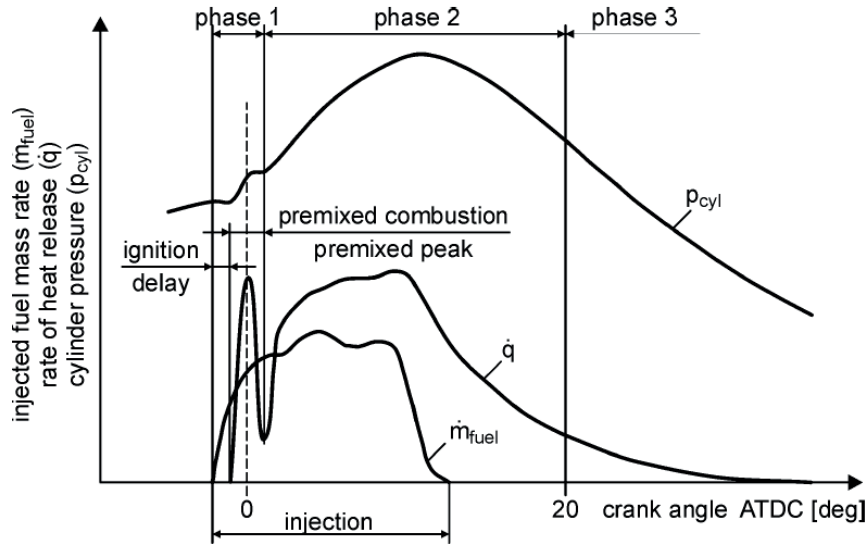


Figure 1.22 Phases of the conventional diesel combustion process [Baumgarten, 2006].

Dec (1997) and Flynn et al. (1999) firstly described the Diesel engine combustion concept systematically. They carried out the investigation in an optical engine to observe the auto-ignition by adopting chemiluminescence imaging system, to measure soot concentration by using Laser Induced Incandescence (LII) method, and to determine polycyclic aromatic hydrocarbons (PAH) by applying Planar Laser-Induced Fluorescence (PLIF) technique. Several interesting results were observed by their experiments. a sheath of fuel vapor and hot air is formed around the spray and also at the leading edge of the spray after the fuel is injected into the chamber; The auto-ignition occurs at multi points nearly simultaneously at the spray downstream region, and the premixed combustion mainly occurs volumetrically throughout the cross section of the leading portion of the jet; As shown in Fig 1.23, the injected fuel is heated to 825 K by mixing with the entrained hot gas, and the reactions consumes 15% of the total combustion heat. Moreover, a thin diffusion flame is formed surrounding the burning plume, and the rich combustion products (CO, UHC and particles) are completely burnt in this region. At the same time, the high temperature and high oxygen concentrations at the diffusion flame interface can provide ideal environment for NO_x formation reactions [Zeldovich, 1946]. It is well known that it is impossible to both reduce soot and NO_x emissions simultaneously in traditional D.I. Diesel engines, and this phenomenon is called as soot - NO_x trade off [Baumgarten, 2006].

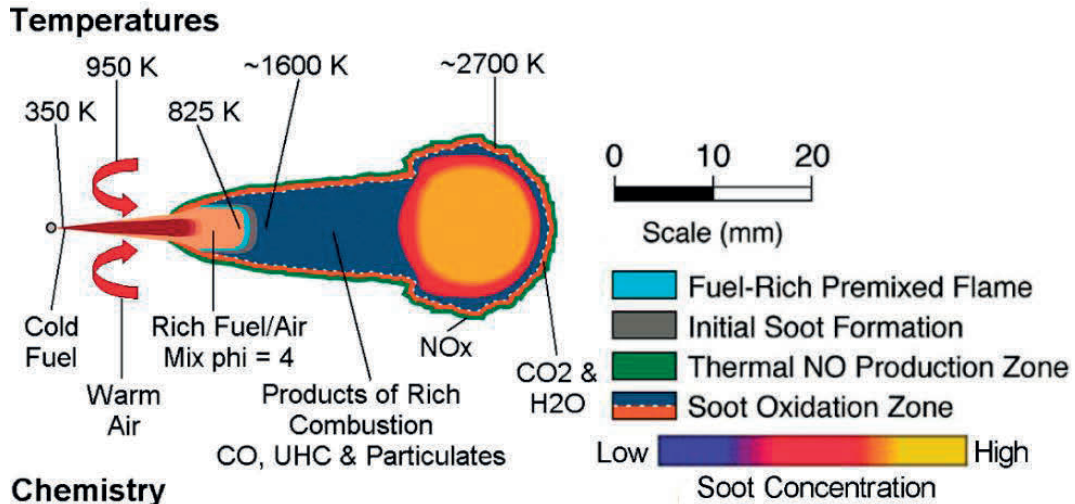


Figure 1.23 Schematic of conceptual model of Diesel spray combustion [Dec, 1997 and Flynn et al., 1999].

In the conceptual combustion model introduced above, the ignition process was detected by applying a line-of-sight technique of chemiluminescence recording system, which was not able to provide the spatially resolved information. Moreover, the soot formation processes caused by the soot particles from their precursors have not been investigated deeply. Kosaka et al. [2005] presented a detail combustion model as shown in Figure 1.24, which makes the ignition processes spatially clearly and also makes an extensive research on soot formation and oxidation processes.

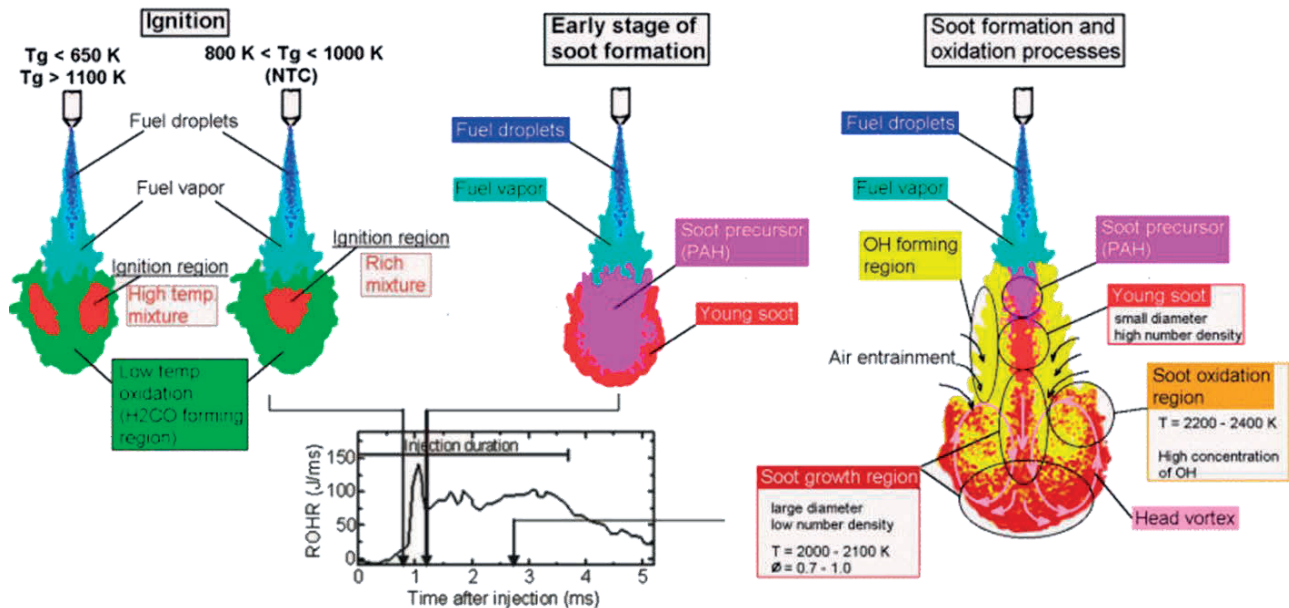


Figure 1.24 Conceptual models of ignition, soot formation, and oxidation process in a diesel spray flame [Kosaka et al., 2005].

They applied formaldehyde (HCHO) LIF method to detect the ignition position because the formaldehyde is one of the intermediate species marking the start of oxidation reactions [Kosaka et al., 2000]. It was found that the auto-ignition region has highly dependence on the ambient gas temperature. As the soot precursor, PAH [Tree and Svensson, 2007] was observed in the spray downstream at the start of mixing controlled combustion timing. When it comes to the diffusion combustion stage, PAH and young soot are formed in sequence in the central fuel rich region, and grows to the spray tip with the convection flow. Finally, the soot particles are delivered to the upstream side by the head vortex, and then they are oxidized quickly by the lean combustion.

The latest Diesel engine combustion model was proposed by Bruneaux [2008], which is shown in Figure 1.25. This model pays more attention to the low temperature fuel decomposition and high temperature burnt gases by applying LIF 355 and hydroxide (OH) LIF techniques compared with the previous combustion models. It is found that the hot ignition occurs inside the HCHO cloud. At the initial stage of diffusion combustion, the low temperature reaction still occurs in the peripheral region. During the whole mixing controlled combustion process, there is a shell-shaped region of OH between reaction zone of diffusion flame and soot cloud [Li K.C., 2014].

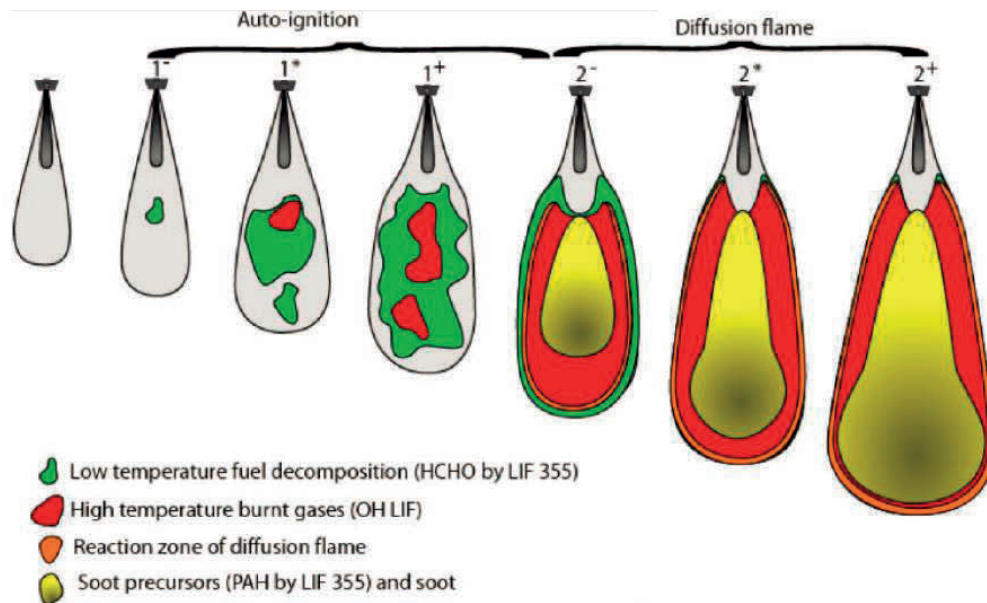


Figure 1.25 Conceptual Diesel spray combustion model [Bruneaux, 2008].

In these three diesel combustion models, it is evident that there is distance between nozzle tip and the most upstream of stable combustion region during the quasi-steady combustion process, which was defined as flame lift-off length [Higgins and Siebers, 2001; and Siebers and Higgins, 2001;]. It is believed that the flame lift-off length plays a significant role in combustion and

emission processes [Chraplyvy and Karlsson, 1996], because the premixing of injected fuel and gas entrainment, which have important effects on the subsequent combustion, just occurs in the downstream of the lift-off length.

1.4.4 Optical Diagnostic Technique for Diesel Spray

In order to get thorough understand of the nature of Diesel sprays, the optical diagnostic techniques are been widely applied in the studys. Most of the techniques have already been summarized excellently by Zhao and Ladommatos [2001]. In this section, some typical spray visualization diagnostic techniques will be reviewed briefly based on their work, and Table 1.1 shows the list of these techniques [Li, 2014].

Table 1.1 Summary of optical techniques for spray evolution measurement

Technique	Applications	Advantages	Limitations
Mie Scattering	Liquid fuel distribution	Simple setup	Sensitive to large droplets
Schlieren and Shadowgraph	Observation of overall spray	Simple setup	Sensitive to both liquid and vapor phases
LRS	Density measurement Vapor concentration	Strong signal Simple setup 2-D imaging	Interference from Mie and spurious scattering Limited to gaseous fuel
SRS	A/F ratio Residual gas fraction	Multi-species detection Multi-point detection Most accurate A/F readings Unaffected by windows fouling	Weak signal
LIF	Fuel concentration	Strong red shifted signal 2-D image of fuel	Quenching at high pressures Difficult to calibrate
FARLIF	A/F ratio	Direct A/F measurements 2-D imaging	Careful calibration required High pressure operation
LIEF	Fuel vaporization & atomization	2-D imaging Simultaneous detection of vapor and liquid	Quenching by oxygen
LEA (LAS)	Fuel vaporization & atomization	Quantitative concentration measurements Droplet size information	Poor spatial resolution

Because of the simplicity and explicitness of Mie scattering method, it is mainly applied to detect the spray liquid phase. According to the Lorenz-Mie theory, when the droplets are spherical

and their diameter is larger than 1 μm , the scattering intensity is mainly determined by the droplets concentration and the square of droplet diameter [Kim et al., 2002]. Hodges et al., [1991] applied ensemble-scattering polarization ratio method, based on the Mie scattering, to measure the droplet size and concentration. One year after that, the spray fuel concentration was measured by Kosaka et al., [1992] quantitatively by applying a 2-D Mie scattering technique. However, compared with recently developed techniques, the accuracy of the droplet diameter concentration measured from the Mie scattering experiment is not high enough. As a result, this technic is usually applied to detect the spray structure [Gulder et al., 1992] and the liquid phase penetration [Siebers, 1998].

As two of the earliest optical diagnostics Schlieren and shadowgraphy can be used to observe the spray liquid and vapor phase, simultaneously. Normally, they are also usually adopted to measure the spray structure, because of the limitation of quantitative analysis. However, compared with Mie scattering method, their superiority is that they can not only detect the spray liquid phase but also distinguish the vapor phase. Furthermore, the interface between liquid and vapor phase can be evaluated through the gradient of intensity roughly. As a result, it also has been used to identify the evaporating spray boundary [siebers, 1998; Pickett et al., 2009].

Arcoumanis et al., [1985] demonstrated the availability of LRS for fuel concentration measurement firstly. After that, he applied it in a port injected SI engine to measure the fuel vapor concentration [Arcoumanis and Enotiadis, 1991]. Moreover, as shown in Figure 1.26, Espey et al., [1997] used planar LRS technique, and got the quantitative fuel vapor concentration images successfully.

It is known that a small amount of light energy is scattered, when a light beam passes through the vapor phase. When the incident wavelength is not changed much by the scattering effect, it is called Rayleigh scattering. However, when the scattered light wavelength is far away from the incident wavelength, it is defined as Raman scattering. The scattered light intensity is proportional to the number density of gas molecules, and the Laser Rayleigh Scattering (LRS) is possible to analyze vapor phase concentration because of the lager cross section of scattering. Thanks to the monochromatic illuminant laser technique, the elastic scattering method could be adopted in spray vapor phase measurement effectively.

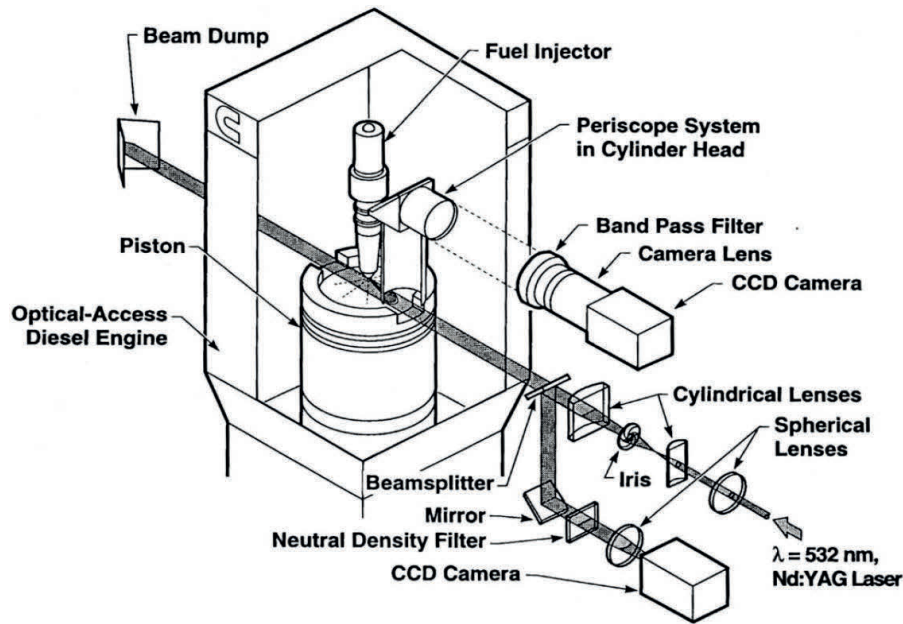


Figure 1.26 Schematic of the optical setup for LRS measurements [Espey et al., 1997].

The Spontaneous Raman Scattering (SRS) can be used to identify the molecular species and measure the gaseous species concentrations, and also calculate the air/fuel ratio. Johnston [1979] observed the air/fuel ratio by applying SRS technique in 1979. Ten years later, this technique was also applied by Heinze and Schmidt [1989] to take the ensemble-averaged 2-D images of air/fuel ratio quantitatively, and it was claimed that the precision of result was within $\pm 8\%$. As for the species detection, spatial distributions of different species and molar fraction of gaseous species were investigated by Sawersyn et al., [1986] and Miles and Hinze [1998] successfully, respectively. However, because the signal energy of SRS is dependent on the small scattering cross section, it always suffers the noises of image background and Mie scattering.

Laser Induced Fluorescence (LIF) is an electronic absorption and emission process which can produce relatively strong signal with high spatial resolution [Andresen et al., 1990]. When the atom or molecule absorbs the specified laser energy, the electronic state energy is excited to an upper level. Because of the instability, the electronic goes back to state ground immediately accompanied with the emission light, which is usually called as fluorescence. Therefore, the fluorescence intensity can be used to estimate the fuel concentration because it is proportional to the molecular density. As a result, LIF is widely used to measure mass distribution [Yeh et al., 1994; Bruneaux, 2002]. However, fluorescence intensity is very sensitive to the quenching effect, the quantitative measurements for the fuel spray are difficult under the engine-like conditions.

Melton and Verdieck [1985] developed the Laser Induced Exciplex Fluorescence (LIEF), and it is believed as an available method to measure spray vapor and liquid phase quantitatively simultaneously. In their theory, when one excited state fluorescence molecule, which is called monomer, have reaction with another molecule, a kind of second fluorescent species, which is called exciplex can be formed. Moreover, the monomer is the dominant emitter of the vapor phase, and the exciplex is the dominant emitter of the liquid phase. Meanwhile, it is possible to record the monomer and exciplex fluorescence individually based on the deviation between them. The fluorescence intensity is directly proportional to the fuel concentration. Therefore, the information of liquid and vapor concentrations can achieved using this technique. Senda et al. [1992;1997;] implemented this method to conduct a series of investigations on spray vapor concentration. This technic was also selected by Bruneaux [2001] to investigate the structures and concentrations of liquid phase and vapor phase, and the effect of injection pressure on nozzle tip near-field atomization and the vapor distribution were analyzed in detail. However, it should be emphasized that careful considerations about the test fuel type and ambient conditions is the key when applying the LIEF technique, because there is oxygen quenching limitation, which affects the signal a lot.

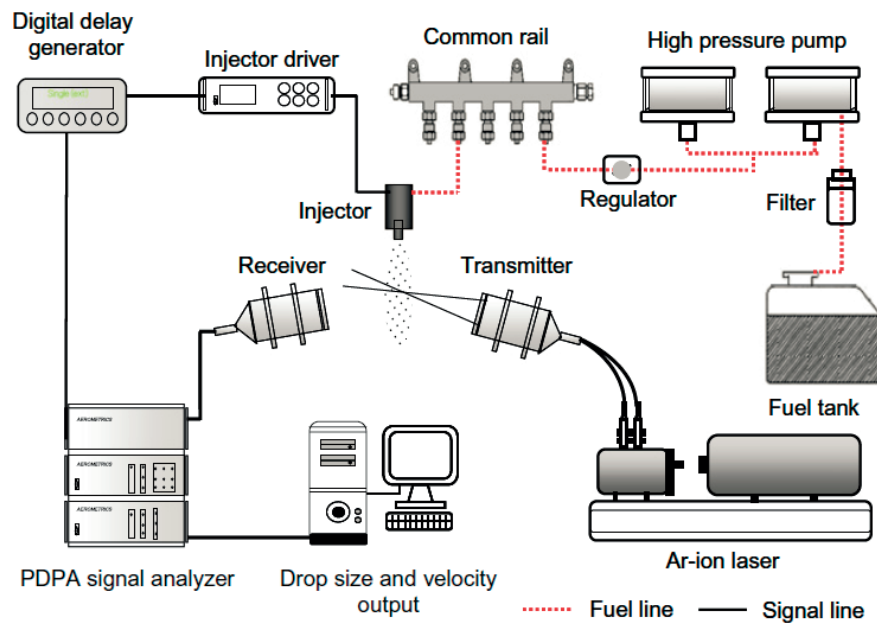


Figure 1.27 Typical PDPA system for analyzing droplets size and velocity [Suh et al., 2007].

Except for the technic introduced above, there are also several other techniques, which are available for the spray flow velocity, ambient gas flowing velocity, and spray droplet size measurements. For example, the Laser doppler velocimetry has been widely applied and well developed, including the Laser Doppler Anemometer (LDA) and Phase Doppler Anemometry (PDA),

which is also known as the name of Phase Doppler Particle Analysis (PDPA) techniques. Based on the Doppler shift of the laser light, which is scattered from the small particles within the moving fluid, LDA is usually applied to measure the flow velocity or turbulent scale. Although some researchers introduced the LDA to the flow measurement inside the engine [Corcione and Valentino, 1990; Baby and Floch, 1997], the drawback, that only one velocity component at the single point can be recorded one time, obstructed the wider applications range of this technique.

As maintained above, based on the principle that when the spray pass through the detected volume, the dispersed beam signal can be recorded with the adjusting of the measurement time and position, where the droplet velocity and droplet size can be obtained, respectively. Therefore, the PDA and PDPA technic have received wide acceptance as one of the reliable means to characterize the sprays, such as droplet size, velocity, density, and volume flux and so on. The accuracy of this method is very sensitive to the droplet density. Hence when applied to the diesel spray, it still needs to be improved. For example, Suh et al., [2007] applied PDPA technique to investigate the effects of fuel injection rate and injection delay on droplet size, and the experimental setup is shown in Figure 1.27. They concluded that the piezo-driven can obtain smaller droplet size compared with solenoid-driven system. Payri et al. [2008].also conducted PDPA the experiment to characterize the diesel spray emerging from the convergent nozzles

Another measurement technique, which is called as Particle Image Velocimetry (PIV), is usually applied to obtain the whole field velocities instantaneously. The double-pulsed laser light sheet is used to illuminate the specified flow field, and the scattered light can be recorded by the camera, and then the flow field velocity can be calculated out simply by dividing the time interval from the difference in two images. The detailed introduction about the PIV mechanism was published by Kompenhans and Kähler [2002]. Now this technic is widely applied to the measure the ambient gas flow and spray evolution processes. Moreover, a series of advanced PIV techniques are developed out with several decades improvement, such as the UV-PIV [Fajardo et al., 2009], FPIV (Fluorescent-PIV) [Sepret et al., 2010], and LIF-PIV [Lee et al., 2002] and so on.

1.5 SUMMARY

In this chapter, the background and motivation of this study is introduced firstly. After that, the outline is shown before a series of study review. From the nozzle internal to spray atomization and combustion, a lot of classic theories developed form experimental and numerical researches were described in detail. After that, the corresponding technical approaches were also introduced one by one.

Based on the review of previous study about the diesel combustion system, multi-hole nozzles are used for actual Diesel engines to deliver the well atomized and adequate fuel under high injection pressure conditions. However, single-hole nozzles are originally applied in the fundamental research to provide insights into the spray characteristics. Meanwhile, previous research has also shown that the optimized nozzle design is effective for improving the fuel atomization, evaporation, and mixture homogeneity. Therefore, unveiling the in- and near- field dynamics of the multi-hole nozzle is crucial to interpret the intrinsic nature of the fuel spray under more practical situations.

In the following chapters, the experimental and computational investigations method applied in this study and the results about the effects of nozzle configurations and operation conditions on the internal flow and spray properties will be presented.

CHAPTER 2 EXPERIMENTAL APPARATUS AND MEASUREMENT METHOD

2.1 HIGH PRESSURE AND HIGH TEMPERATURE AMBIENT CONDITION ACQUIRING SYSTEM

In order to acquire the engine-like ambient condition and high quality of visualization of spray evolution, a special high pressure and high temperature chamber was applied, and the specific introduction will be shown in this section.

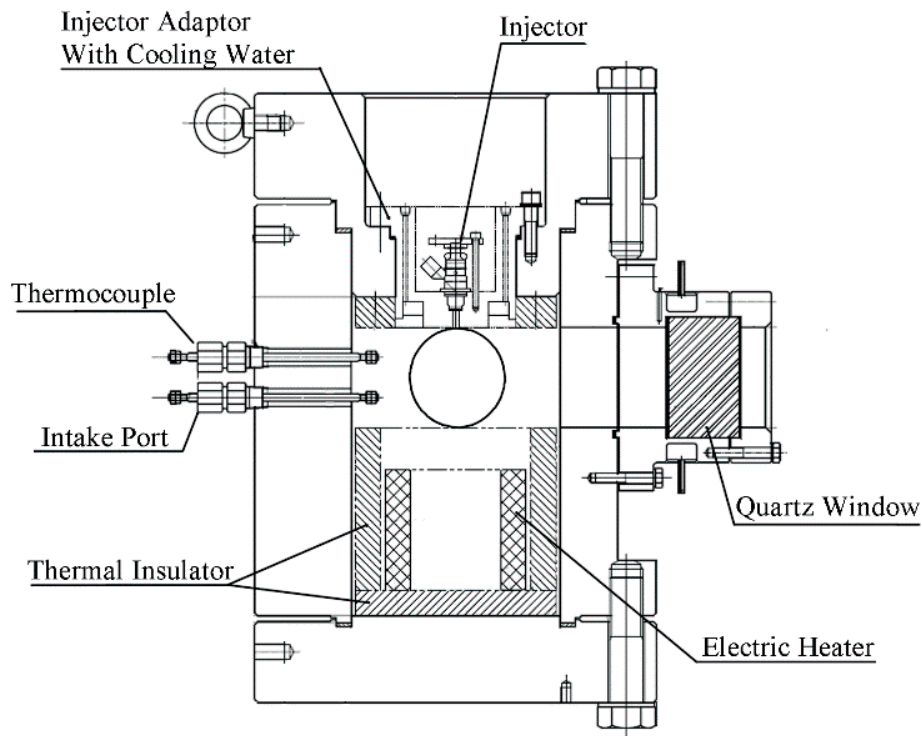


Figure 2.1 Schematic of the constant volume vessel.

The schematic of the constant vessel structure is shown in Figure 2.1. The vessel is the same with that applied in the previous study in the laboratory [Zhang, 2008], and it has four available windows, and according to the specific experiment the utilized window was variable. The quartz glass with diameter of 100 mm was mounted in the utilized window adaptor. At most six thermocouples could be fixed by the thermocouple adaptor. By dispersed distribution, the thermocouples can detect temperatures at different positions of the chamber. A kanthal alloy heating unit was placed inside the chamber to produce the engine like high temperature and high temperature condition as high as 1000 K. The internal and external surfaces of the chamber are

covered by the thermal insulator to avoid the heat conduction and maintain the stable environment. There were cooling water circulations inside the injector adaptor and the quartz glass adaptor to avoid overheating. There are different kinds of chamber head to install single-hole and multi-hole nozzles, and the structure will be shown in next sections.

The high pressure condition inside the combustion chamber was produced by applying a gas cylinder, which can increase the chamber pressure to above 5 MPa. A preheater was employed, as shown in Figure 2.2, to avoid the overload of the electric heater due to the low temperature and high pressure gas, and also to receive the stable ambient condition during the fuel injection processes. The preheat equipment had a “room” which was produced by surrounding heaters, the temperature in the “room” can reach to 700 °C. When the high pressure gas passes through the helical pipe which is mounted in the high temperature “room”, it can be heated to about 480-500 °C before the high temperature gas enters into the constant volume vessel.

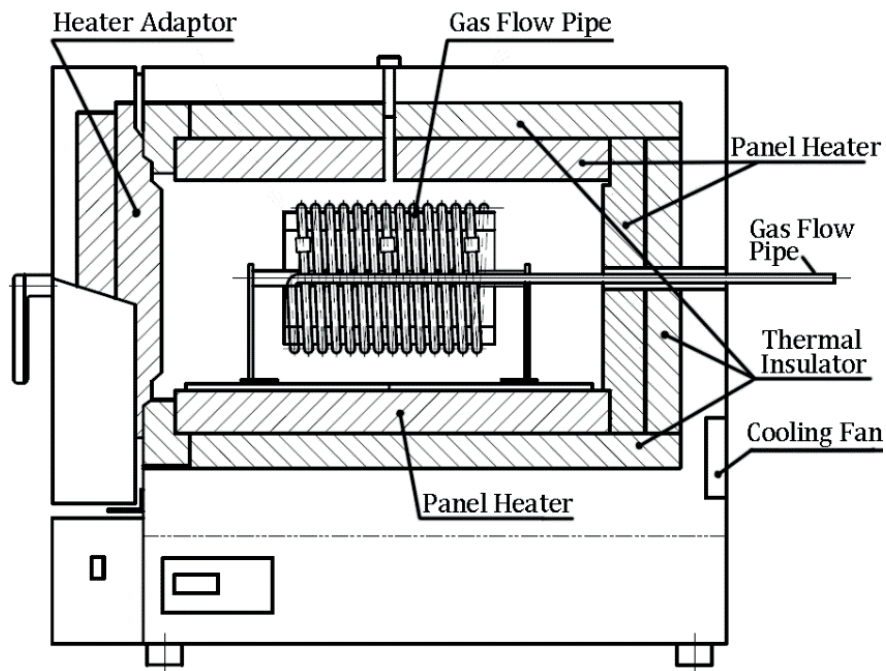


Figure 2.2 Schematic of ambient gas preheater.

2.2 HIGH PRESSURE INJECTION SYSTEM AND INJECTION RATE MEASUREMENT SYSTEM

As it is known that the fuel injection pressure in Diesel engine is very high, and in the current study, in order to get the high enough injection pressure, two kinds of high pressure injection systems were applied under the non-evaporating and evaporating conditions, respectively.

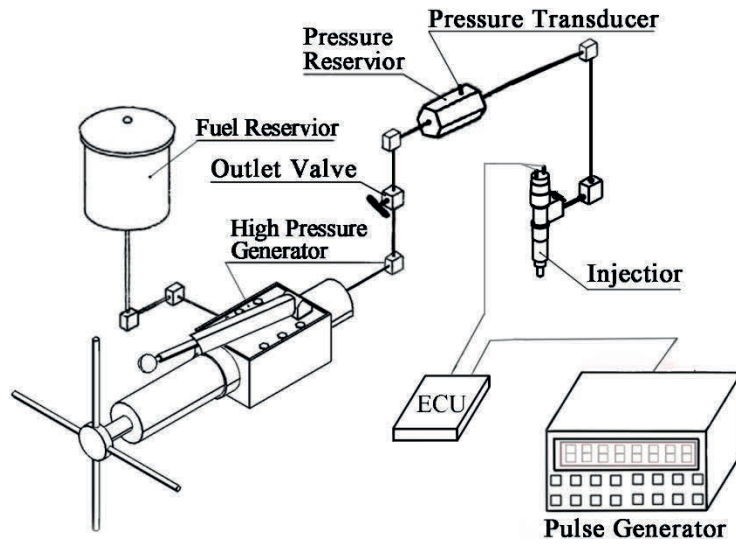


Figure 2.4 Schematic of hand-pump high pressure injection system.

There are two kinds of injectors applied in this study. One is the single-hole type, and the other one is the multi-hole type. They are all solenoid type injectors with min-sac nozzles. The typical schematic is Figure 2.5, and the specific nozzle structure will be shown in the corresponding sections when investigating the effect of different kind of factors on the nozzle internal flow and spray characteristics.

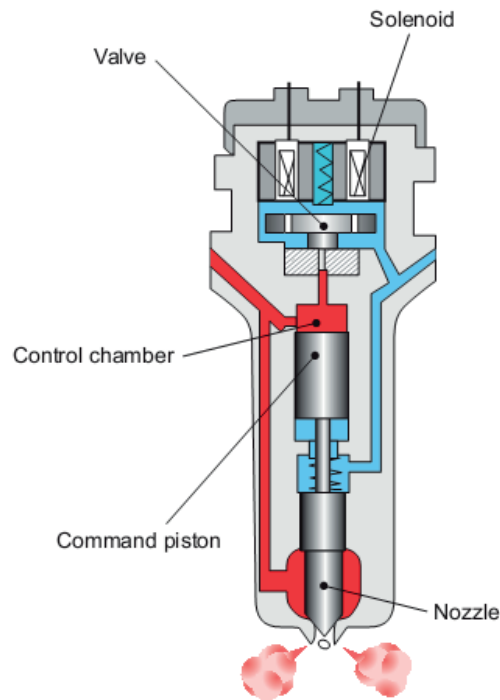
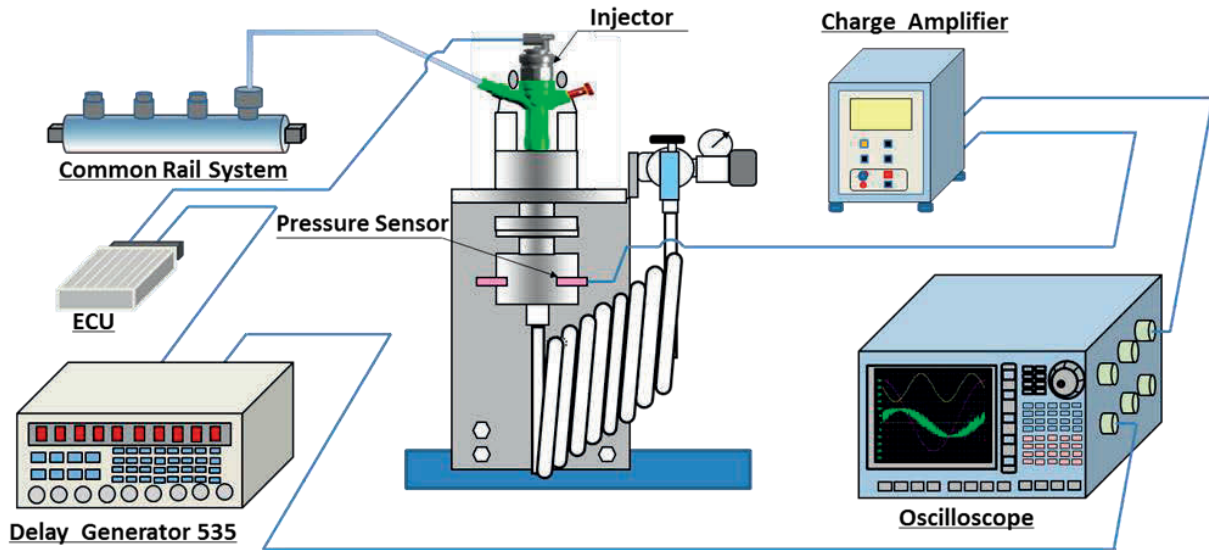
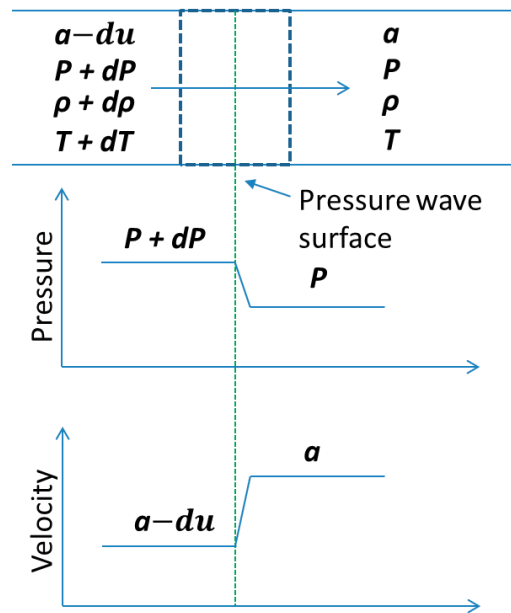


Figure 2.5 Solenoid type injectors

Before the experiments the injection rate of each condition is very important for the analyzing the phenomena. As a result, the injection rate measurement apparatus will also be introduced in this section. The specific Schematic of injection rate measurement experiment apparatus is shown in Figure 2.6.



(a) Schematic of injection rate measurement experiment apparatus



(b) Definition of Measurement Volume

Figure 2.6 Injection rate measurement experiment

In this study, the BOSCH rate of injection meter [Bower, G. and Foster, D., 1991] was applied. The experimental conditions corresponded to the spray observation experiments, which will be introduced in upcoming sections.

The principle of BOSCH rate of injection meter is that when the fuel is injected into the long tube, the pressure inside the tube is recorded, and the injection rate can be calculated based on the pressure fluctuation waves. Paying attention to the pressure wave inside the tube, as shown in Figure 2.6-(b), according to the momentum equations before and after the wave, the equation 2.1 can be obtained,

$$(P + dP)A - PA = (A\rho \cdot a \cdot a) - A\rho \cdot a(a - du) \quad (2.1)$$

where a is sound velocity, P is the pressure, ρ is density, T is temperature. According to equation 2.1, the equation 2.2 is shown as below.

$$\begin{aligned} dP &= \rho \cdot a \cdot du \\ P &= \rho \cdot a \cdot u \end{aligned} \quad (2.2)$$

As a result, the injection rate can be calculated by equation 2.3,

$$\frac{dQ}{dt} = \frac{A}{a \cdot \rho} P \quad (2.3)$$

where Q is just the injection volume.

2.3 ELECTRICAL CONTROLLING SYSTEM

In the experiments, the injection timing, imaging timing, and laser induced timing are all controlled by the electrical controlling system. Specifically, the injector was controlled by the injector electronic control unit (ECU). Injection timing, injected mass and image taken timing were controlled by a delay pulse generator (Stanford Inc., DG 535 or DG645). The basic information of the signal for injector, camera is shown in Figure 2.7.

However, it can be seen that there is a delay between the injection signal and the fuel injection, which can cause the difficulties in deciding the start of injection and time after start of injection by the high speed images. In order to find the start of injection timing as accurately as possible, the injection delay measurement was conducted by comparing the pulse signal and the injection rate signal during the injection rate measurement experiments. The imaging time of the camera and laser induced setting are changing according to the injection delay variation.

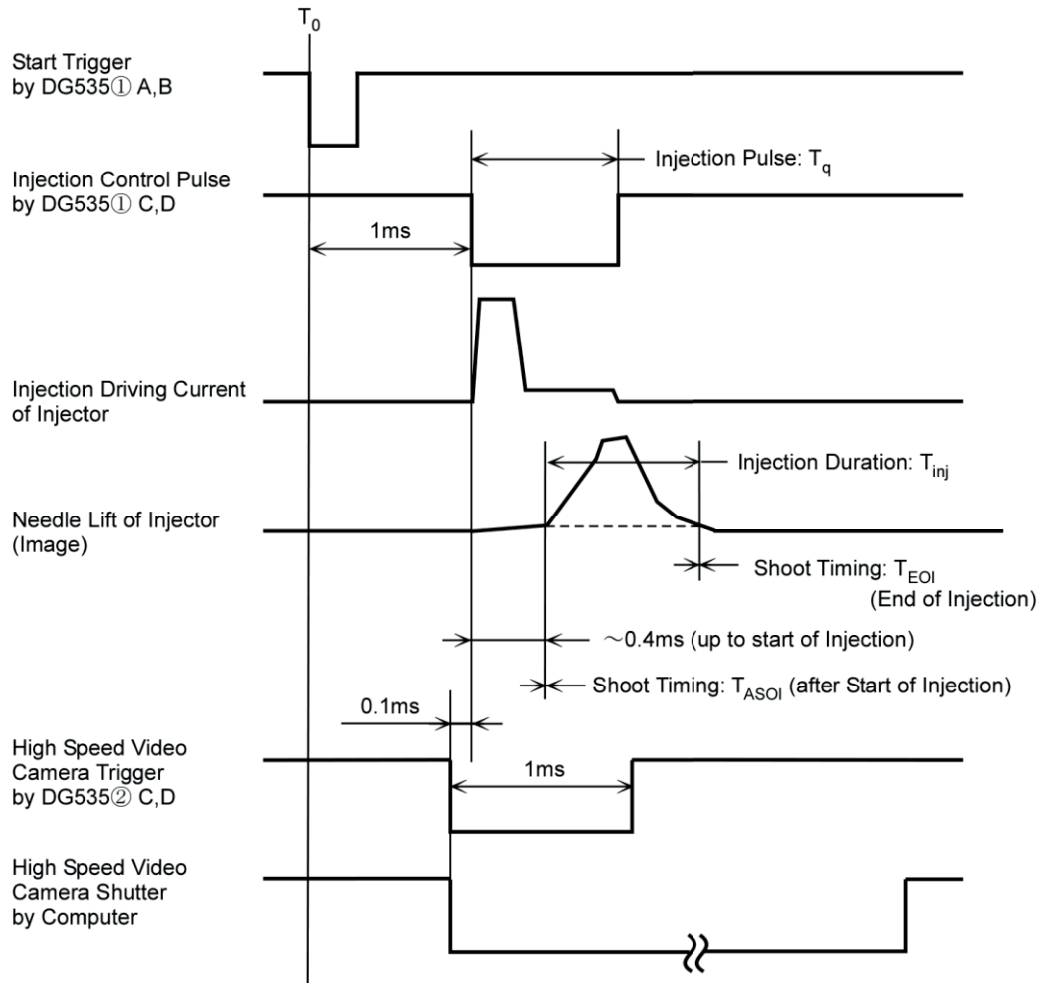
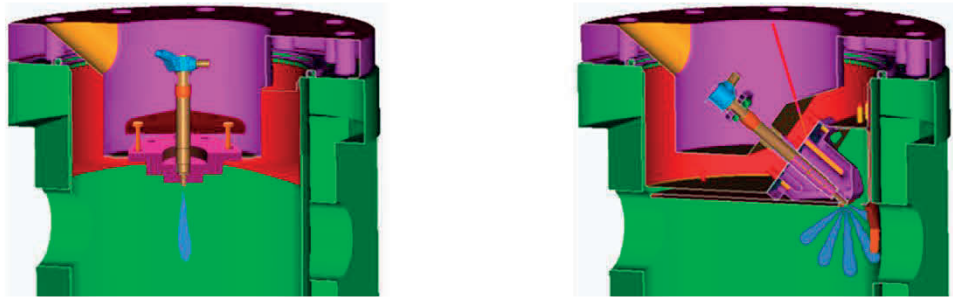
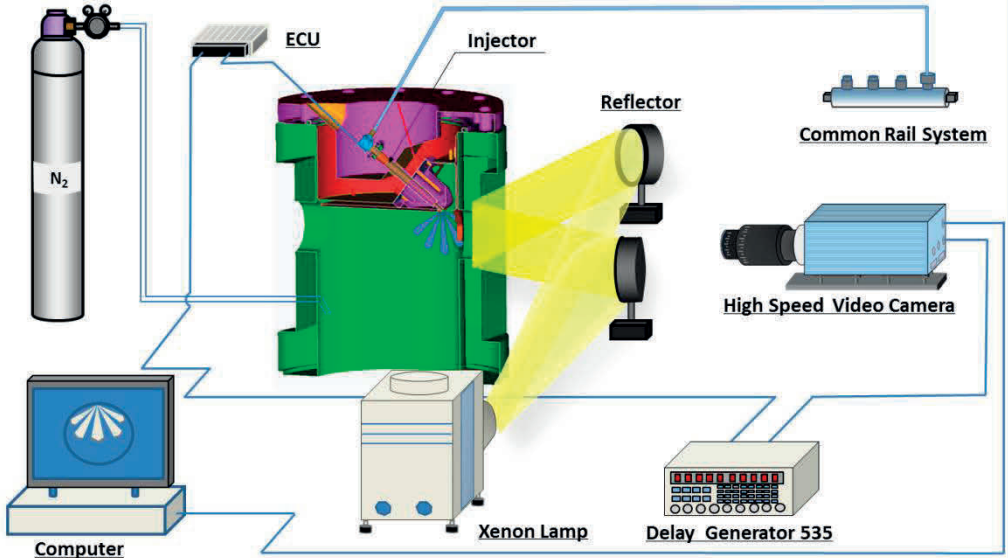


Figure 2.7 Timing chart of signal

2.4 OPTICAL MEASUREMENT SYSTEMS

2.4.1 Mie Scattering Method

In order to observe the spray development process under the non-evaporation condition, a Mie scattering experiment was performed using single-hole and multi-hole injectors, and the specific experimental apparatus are shown in Figure 2.8. Figure 2.8-(a) presents the global experimental arrangement, including the high-pressure chamber, injection system, and optical system. The internal volume of the high-pressure chamber has a height of 300mm and a radius of 100 mm, which can provide a sufficient space ($9.4 \times 10^6 \text{ mm}^3$) to ensure that the free spray develops under the nearly quiescent condition. The compressed ambient gas can be introduced from the intake port to produce the in-cylinder pressure as high as 6 MPa, and the optical access is available from four sides of the chamber.



(b) Chamber covers for single-hole and multi-hole nozzles

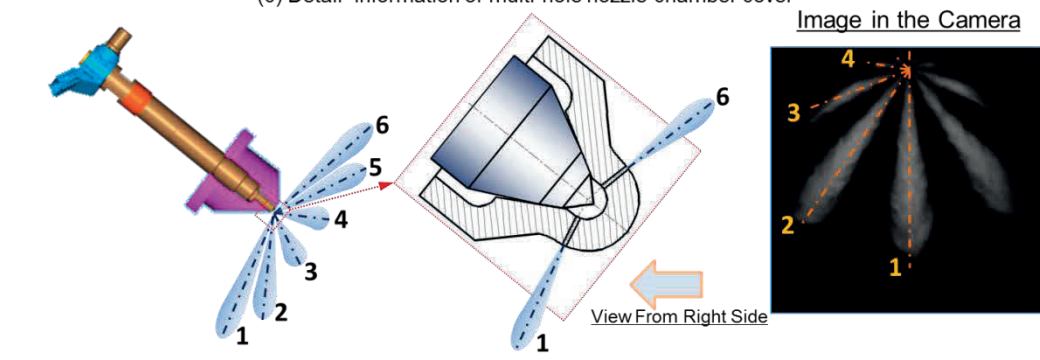
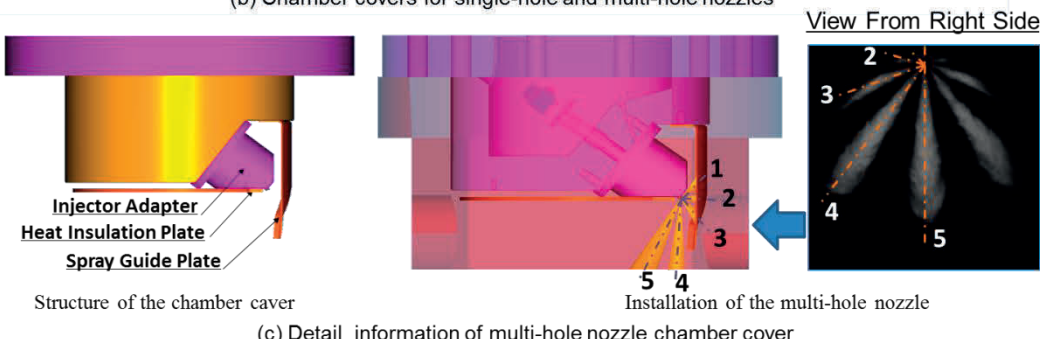


Figure 2.8 Experimental apparatus and arrangement for Mie scattering experiment.

Diesel fuel was injected into a high-pressure constant volume vessel by a high-pressure common rail injection system assembling different types of injectors, which could generate an injection pressure up to 200 MPa. Transparent quartz windows were employed to make the inside observable and optically accessible. The injection time, fuel quantity, and image timing were controlled by an electronic control unit (ECU) and a delay pulse generator (Stanford Inc., DG535). A sampling method was selected to determine the injection pulse. An air cylinder was applied to produce the ambient environment. The optical system consists of a xenon lamp (USHIO Corp., SX-UID501XAMQ), two reflected mirrors, and two high-speed video (HSV) cameras (Photron FASTCAM-APX RS and Nac MEMRECAM HX-3) coupled with different lens. The xenon lamp could emit continuous and high intensity light. The incident light was reflected by the two mirrors, which were fixed with an appropriate angle between the high-pressure chamber and the HSV camera. In that way, the two beams could concentrate on the spray area through the quartz window, where a strong and uniform light intensity for scattering could be achieved.

When it comes to the installation of different injectors, in the case of single-hole injector, the method of nozzle installation is shown in Figure 2.8-(b). It is well known that the observation of multi-hole spray is difficult due to the conical structure formed by sprays. To prevent spray interference, in this study, the multi-hole injector was installed into a specialized chamber head obliquely, as shown in Figure 2.8- (b) and (c). An appropriate angle between the axis of the multi-hole nozzle and the horizontal plane was designed to maintain one of the spray plumes to be observed as vertically as possible. A special correction method was applied in the experiment to eliminate the error in measurement caused by the spray direction deflection.

2.4.2 Laser Absorption-Scattering (LAS) Technique

2.4.2.1 Experiment apparatus

The spray development and mixture formation processes under the evaporating conditions were investigated by applying the LAS technique. The LAS experiment was performed in a high-pressure, high-temperature constant volume combustion vessel. The optical arrangement of LAS equipment and injection system is shown in Figure 2.9. The experimental apparatus had been systematically describes in detail in our previous papers [Li and Dong, 2014]. Inside the chamber, transparent quartz windows were employed to make the inside observable and optically accessible. A pulsed YAG laser (Continuum NY61-10) was used to form the Vis (second harmonic, 512 nm) and UV (fourth harmonic, 266 nm) lights.

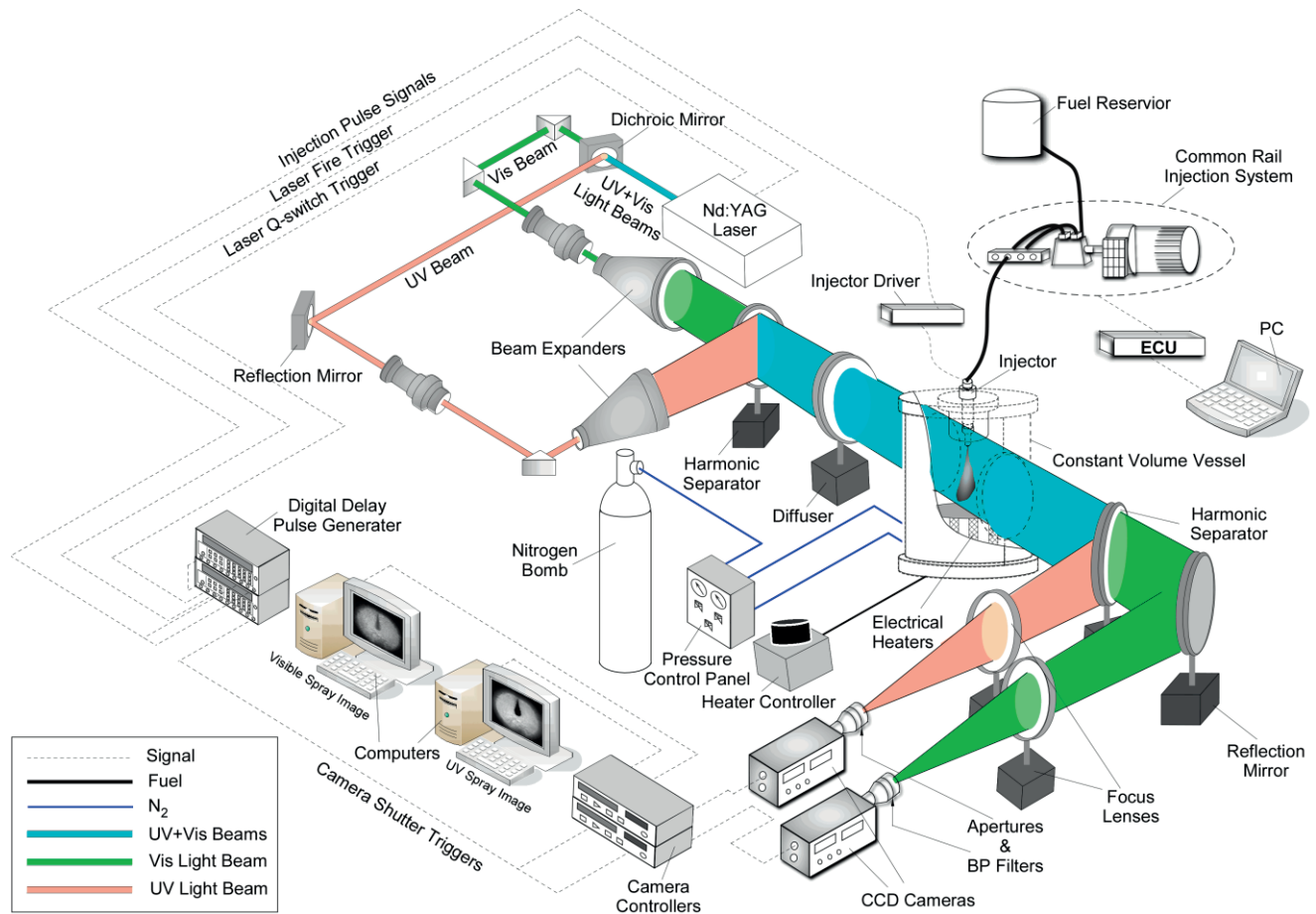


Figure 2.9 Experimental setup of LAS system.

The two beams were separated by a dichroic mirror, and then the UV and Vis beam were expanded respectively. Before pass through the chamber, the two beams were made coaxial again. After being attenuated by the spray, the beams were separated again and were recorded by two CCD cameras (C4880, Hamamatsu Photonics). The light extinction at the two wavelengths was recorded as 14 bit images by CCD camera chips, and the mathematical algorithm processing of the image was carried out by an IPLab (Spectrum Signal Analytic) system.

2.4.2.2 Principles of LAS Technique

The principle of the technique had also been systematically describes in detail in our previous papers [Li and Dong, 2014]. Two kinds of laser beams, 512 nm (visible, λ_T) and 266 nm (ultraviolet, λ_A), are applied in this method. As shown in Figure 2.10, when these two incident laser beams pass through the spray, the intensities are decreased due to the attenuation effect. In the ultraviolet (UV) image, the intensity attenuation is because of liquid scattering, liquid absorption, and vapor absorption, while the effect of liquid absorption is negligible [Zhang, 2001]; In the visible (Vis) image, the extinction is only resulted from the droplets scattering. Therefore, the line-of-sight vapor

phase optical thickness could be achieved by subtracting the visible side optical thickness from the UV side optical thickness. The concentration of vapor will be calculated by applying Bouguere-Lambert-Beer theory, and the droplet concentration will be calculated by adopting the relationship between the Sauter Mean Diameter (SMD) D32 and the optical thickness of visible side.

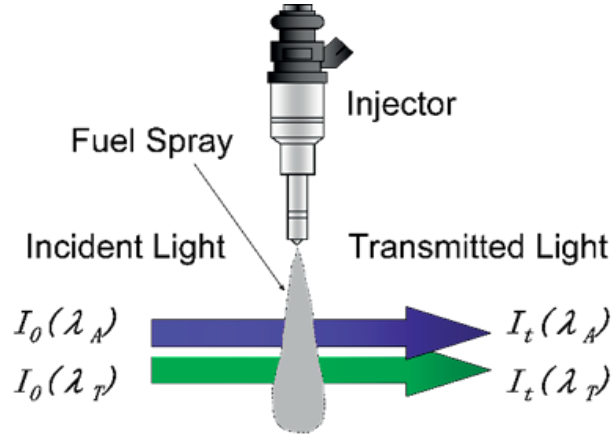


Figure 2.10 Principle of LAS technique.

Specifically, the light extinction of UV can be expressed in Equation (2.4),

$$\ln \left(\frac{I_0}{I_t} \right)_{\lambda_A} = \ln \left(\frac{I_0}{I_t} \right)_{L_{sca}+L_{abs}} + \ln \left(\frac{I_0}{I_t} \right)_{V_{abs}} \quad (2.4)$$

where subscript of L_{sca} , L_{abs} , and V_{abs} are the light attenuation caused by liquid scattering, liquid absorption, and vapor absorption, respectively.

The light extinction of Vis can be expressed as Equation (2.5),

$$\ln \left(\frac{I_0}{I_t} \right)_{\lambda_T} = \ln \left(\frac{I_0}{I_t} \right)_{L_{sca}} \quad (2.5)$$

It has been proved that the droplet plays the same role in the attenuations of scattering for UV and Visible beams [Zhang, 2001], which implies that the first items of the right sides of Equation (2.4) and (2.5) are equal to each other. In this way, by subtracting Equation (2.5) from Equation (2.4), the attenuation of UV beam caused by the vapor absorption can be calculated out:

$$\ln \left(\frac{I_0}{I_t} \right)_{V_{abs}} = \ln \left(\frac{I_0}{I_t} \right)_{\lambda_A} - \ln \left(\frac{I_0}{I_t} \right)_{\lambda_T} \quad (2.6)$$

After that, the Lambert-Beer theory can be introduced to get the vapor phase concentration. The specific process is shown as follows:

The attenuation of UV beam absorbed by vapor phase can be expressed based on the Lambert-Beer theory like this,

$$\ln\left(\frac{I_0}{I_t}\right)_{V_{abs}} = \int_0^L \alpha dx = \int_0^L \frac{\varepsilon \times 10^2}{MW} \cdot C_v dx \quad (2.7)$$

where α : the absorption coefficient

ε : molar absorption coefficient

MV: mole weight

L : optical path length

C_v : vapor mass concentration

Assuming the vapor in the concerned field is homogeneous, the vapor phase concentration can be expressed as

$$C_v = \frac{MW \cdot \ln(I_0/I_t)_{V_{abs}}}{\varepsilon \cdot L \times 10^2} \quad (2.8)$$

After that, the vapor phase equivalence ratio can be calculated by

$$\Phi_v = \frac{AF_{stoich}}{AF_v} = \frac{AF_{stoich}}{\left(\frac{C_a}{C_v}\right)} \quad (2.9)$$

where the AF_v is the vapor actual air-fuel ratio, the AF_{stoich} is the stoichiometric air-fuel ratio, and the C_a is the entrained gas concentration.

Based on Bouguer's law, neglecting the multiple scattering and assuming the droplet is approximately spherical, the attenuation of Vis can be expressed as

$$\ln\left(\frac{I_0}{I_t}\right)_{\lambda_T} = \int_0^L \int_0^\infty \frac{\pi}{4} R_k Q_{ext} C_n N(D) D^2 dD dx \quad (2.10)$$

Where the R_k represents the correction factor for extinction efficiency Q_{ext} , $N(D)$ is the droplet size distribution function, and C_n is the droplet number density. These parameters can be obtained from the Mie scattering theory.

As a result, the concentration of the droplets of the liquid phase fuel C_d is

$$C_d = \frac{1}{L} \int_0^L \int_0^\infty \frac{\pi}{6} \rho_f D^3 C_n N(D) dD dx \quad (2.11)$$

where ρ_f is the liquid fuel density.

Assuming that the diameter of droplets in the entire spray plume can be replaced by Sauter mean diameter D_{32} , combining with Equation (2.10), the definition of D_{32} is shown as below

$$D_{32} = \frac{\int_0^{\infty} D^3 C_n N(D) dD}{\int_0^{\infty} D^2 C_n N(D) dD} \quad (2.12)$$

Then the liquid phase concentration can be rewritten as

$$C_d = \frac{2}{3} \rho_f D_{32} \frac{1}{L} \int_0^L \int_0^{\infty} \frac{\pi}{4} D^2 C_n N(D) dD dx = \frac{2}{3} \rho_f D_{32} \frac{\text{Ln}\left(\frac{I_0}{I_t}\right)_{\lambda_T}}{R_k Q_{ext} L} \quad (2.13)$$

In Equation (2.13), the D_{32} can be calculated out by applying light extinction method proposed by Kamimoto et al [1989] concerning the total fuel mass and spray optical thickness.

$$D_{32} = \frac{0.63 R_k Q_{ext} M_d}{\rho_f \sum_S \text{Ln}[I_0(\lambda_T)/I_t(\lambda_T)] \cdot \Delta S} \quad (2.14)$$

where, ΔS is the unit project area, S is the project area over the entire area spray, and M_d means the fuel mass of liquid phase.

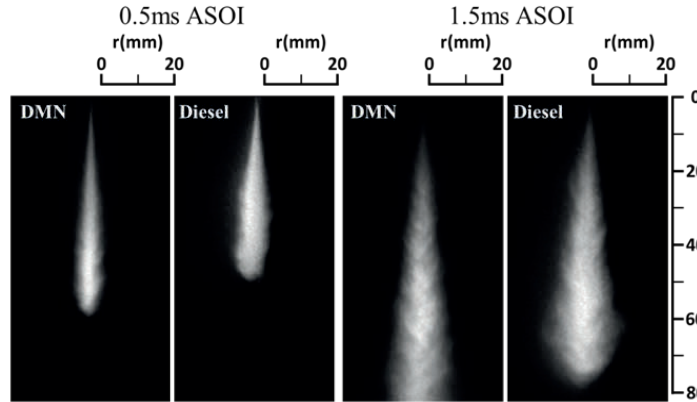
Therefore, the equivalence ratio (ϕ_d) of the line-of-sight liquid phase fuel is that

$$\phi_d = \frac{AF_{stoich}}{AF_d} = \frac{AF_{stoich}}{\left(\frac{C_a}{C_d}\right) - \left(\frac{C_a}{\rho_f}\right)} \quad (2.15)$$

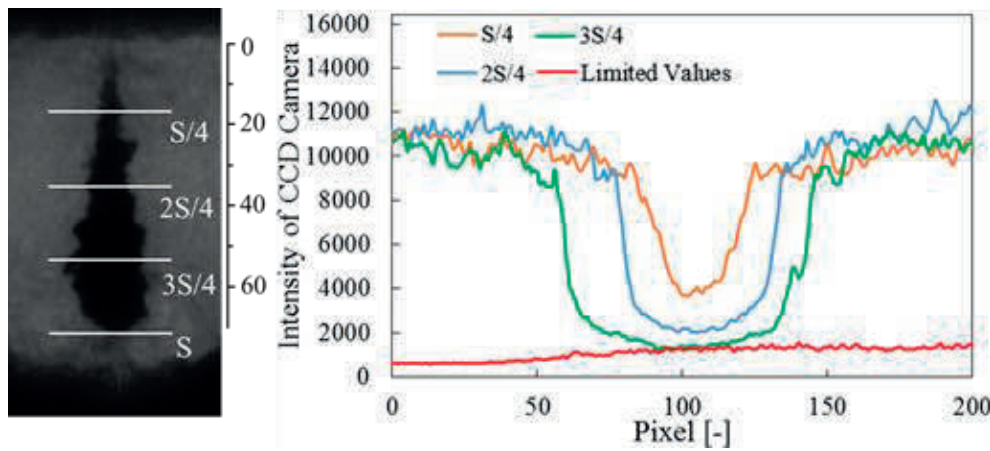
where AF_d is the real air-droplet mass ratio of line-of-sight.

2.4.2.3 Test Fuel for the LAS Technique

The discussion about the test fuel was conducted in the paper published before [Li and Dong, 2014]. Taking the LAS principle into account, the test fuel type is very important for the precision of LAS technique, and the fuel must have the characteristics of: (1) the similar chemical and physical properties with Diesel fuel; (2) absorbs UV light but does not absorb visible light. Previously, 1, 3-dimethylnaphthalene (1, 3-DMN) was thought as a substitute fuel of Diesel for LAS technique [Zhang, 2001]. However, it was found that the UV absorption ability of 1, 3-DMN is very strong which results in absorbance saturation as shown in Figure 2.11. In Figure 2.11-(b), left is the absorbance image of UV beam at 1.0 ms ASOI under 760 K, 3.6 MPa ambient conditions, right is the absorbance distribution along the horizontal lines defined in the left figure. It was found that the variations of the absorbance along the lines are unobvious, and the distribution presents a flat shape. In fact, the absorbance along the horizontal line such as shown in Figure 2.11 should follow Gaussian distribution in an unsaturated image. This kind of saturation image can introduce some measurement error of LAS technique. As a result, it is necessary to find out another substitute fuel which has appropriate absorptive ability of UV beam for this technique.



(a) Comparison of Spray Behavior between DMN and Diesel Fuel $P_{inj}=100MPa$ $P_a=1.4MPa$ $T_a=300K$



(b) Intensity in Spray by UV light (image of 1, 3- DMN spray)

Figure 2.11. Disadvantage of DMN fuel

The absorption spectra of liquid fuels, which have similar physical properties with those of the Diesel fuel is shown in Figure 2.12, and the property of different candidate fuel is listed in Table 2.1. Almost all of the candidates have been applied in the measurement when developing the LAS technique. However, because of the strong absorption ability for the UV beam, the fuel of 1, 3-DMN and α -MN have strongly saturation images as analyzed before. When it comes to the other fuels, such as the, n-tetradecane, n-pentadecane, n-cetane, and n-tridecane, on the contrary, they do not have the strong absorption properties for the UV beam. As a result, the image is not clear enough to analyze the spray evaporation. Until now, the pure fuel which can be perfectly adopted for LAS technique has not been discovered. Therefore, the attentions were paid to blend fuel, which will be introduced in the following page.

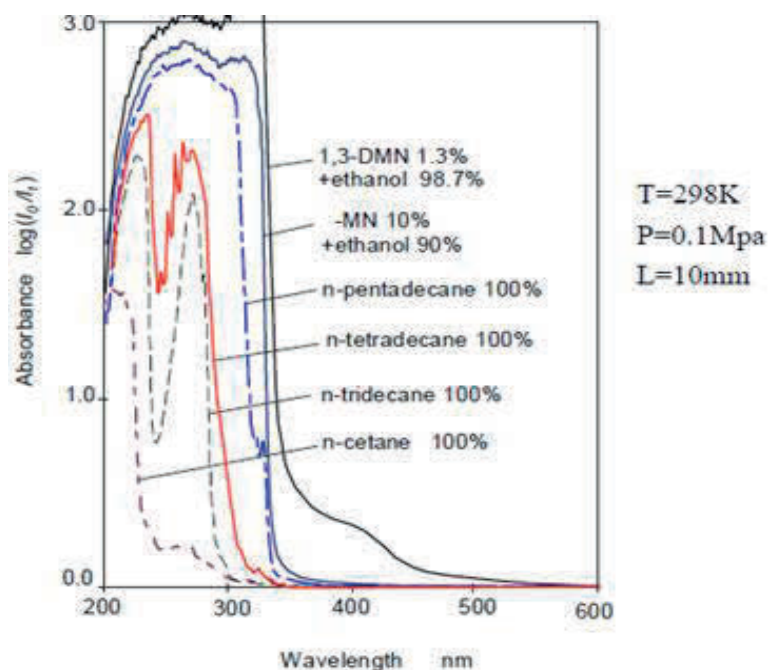


Figure 2.12 Absorption spectra of liquid fuels with physical properties similar to those of Diesel fuel

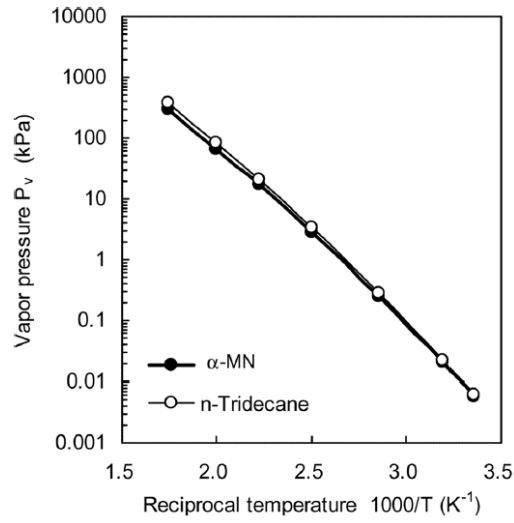
Table 2.1 Properties of candidate fuel

Substance	Diesel JIS#2	1,3-Dimethyl- naphthalene	α -Methyl- naphthalene	n-Tridecane	n-Pentadecane	n-heptane	n-hexadecane [cetane]
Formula	-	C ₁₂ H ₁₂	C ₁₁ H ₁₀	C ₁₄ H ₃₀	C ₁₅ H ₃₂	C ₇ H ₁₆	C ₁₆ H ₃₂
Boiling point [°C] (1atm)	280±10(T50)	262.5	244.7	235	270.6	98	287
Density [kg/m ³]	820~845	1018	1016	756	770	684	780
Kinetic viscosity [mm ² /s]	3.5±0.5	3.95	2.58	2.47	3.73	0.606	4.52
Molecular structure	-						

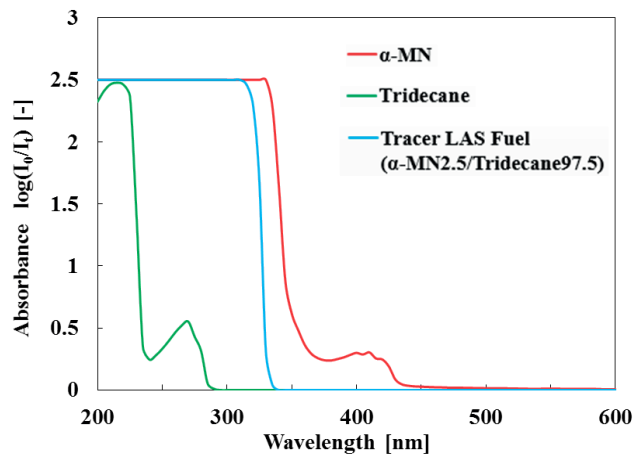
As published before, the blend fuel for LAS technique must meet that: first, the applied fuels have intersolubility; second, the selected fuels should have the similar vaporizing velocity and the similar properties with Diesel; third, the appropriate ability of absorbance for UV beam. According to the above requirements, a blend fuel with 2.5 volumetric percentage of α -MN and 97.5 volumetric percentage of n-tridecane was proposed. This is because that the evaporation characteristics of α -MN and n-tridecane are nearly the same, and the properties of them are similar with Diesel fuel. The properties of blend fuel are shown in Table 2.2.

Table 2.2 Properties of Tracer LAS Test Fuel

Substance	Formula	Boiling point [°C]	Density [kg/m ³]	Kinetic viscosity [mm ² /s]
α -Methyl-naphthalene	C ₁₁ H ₁₀	244.7	1016	2.58
n-Tridecane	C ₁₃ H ₂₈	235.0	756	2.47
Tracer fuel [α -MN 2.5% + n-Tridecane 97.5%]	-	235.8	767	2.48
Diesel JIS#2	-	~273	~830	~3.86



(a) Vapor pressure of α -MN and n-tridecane [Reid et al., 1985].



(b) Absorption spectrum of tracer fuels

Figure 2.13 Vapor pressure and absorption spectra of different liquid fuels.

Moreover, Figure 2.13 gives the vapor pressures and absorption spectra of α -MN and n-tridecane which was published by Reid et al., [1985], and it is found that the vapor pressures are correspond with each other perfectly. The blend fuel absorbance image under the same condition with that in Figure 2.1, and the distribution along the typical line is shown in the Figure 2.14. It is obvious that the red curve is close to Gaussian distribution without losing the sharpness of spray. Therefore, it can be proved that the blend fuel of α -MN and n-tridecane in the volumetric percentages of 2.5 and 97.5, respectively, is one of the ideal test fuels for this technique.

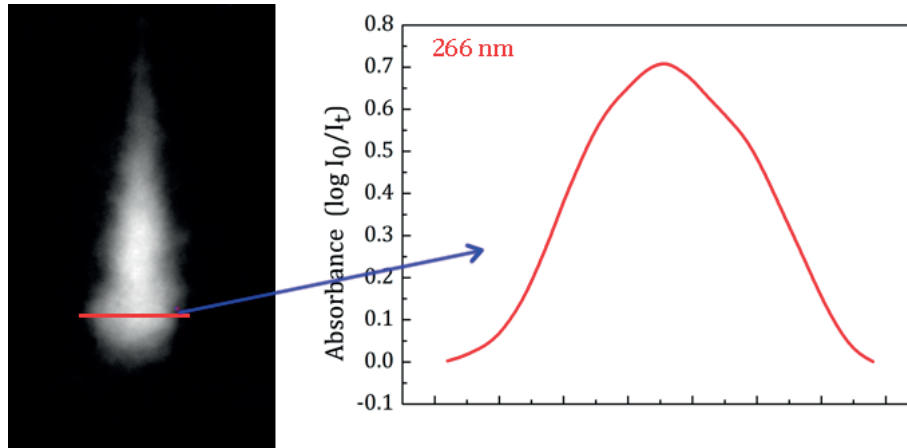


Figure 2.14 Typical absorbance distribution of blend fuel spray image.

2.5 SUMMARY

In this chapter, the experimental apparatus applied in this dissertation are introduced in detail, for example, high pressure and high temperature ambient condition acquiring system, high pressure injection systems, and injection rate measurement system and so on. Moreover, the measurement technology, including the Mie scattering and LAS technic, which are corresponding to the non-evaporation and evaporation condition measurements, respectively, are also introduced in this chapter. All of the apparatus and technic introduced here will be applied to investigate the spray evolution and mixture formation processes inside the chamber. In next chapter, the numerical methods applied in this study will be introduced.

CHAPTER 3 MODELS AND THEORETICAL BASIS APPLIED IN NUMERICAL STUDY

The basic principles of CFD: all processes of flow, heat and mass transfer are governed and controlled by the conservation of mass, momentum, and energy, which are the three basic laws of physics. The mathematical expressions (partial differential equations) of these basic laws are called control equations. The initial condition and boundary condition can maintain a process different from another one, which are called the single-value conditions. The control equations and the corresponding initial, and boundary conditions constitute a complete mathematical description of a physical process (or physical model). For the mathematical simulation of flow problems, it can be simplified to determine the proper initial, boundary conditions, depending on the flow characteristics to finish the selection and solving of the suitable mathematical conservation equations. For combustion problems, involving chemical component mass transfer, chemical reactions, and other processes, while it also should have appropriate control procedures and boundary conditions.

The basic steps of numerical solution are as follows: instead of the original spatial coordinates continuous physical fields (such as concentration, temperature, velocity, etc.), it is replaced by the set of values of a finite number of discrete points, and then based on certain criteria, variable values of these discrete points can be used to establish a relationship between the algebraic equations (or discrete equations). Finally, try to solve the algebraic equation is to obtain the solution or the approximation of the variables.

3.1 MULTI-PHASE FLOW COMPUTATION METHOD APPLIED IN NOZZLE INTERNAL FLOW STUDY

So far, several cavitated flow models have been reported, and the most representative cavitation nozzle flow model are three, namely, the single-fluid model developed by Schmidt et al. [1997;1999;] based on the positive pressure relations, another single-fluid model developed by Yuan et al. [2001] based on the phase volume fraction transport equation and cavitation fluid dynamic equations, and a two-fluid model developed by Alajbegovic et al. [1999]. In this study, this three models will be evaluated from the view of modeling ideas, calculation realization, and ability of reflecting the details of cavitation flow, and then a relatively reasonable cavitation flow model will be chosen.

3.1.1 Basic Description for Multi-Phase Flow Models

Positive pressure single-fluid model of Schmidt et al. [1997;1999;]

The model is developed in the framework of the continuous medium method. The main idea of modeling is: the gas-liquid two-phase nozzle cavitation flow is considered to be a completely homogeneous compressible flow medium, while assuming that both phases are flowing at the same velocity. Hence, it can also be interpreted as a single phase fluid, whose density, viscosity, and can be replaced by the mixed density and a mixed viscosity. Thus, control equations of the cavitation flow model are similar to the single-phase flow. Among them, the continuity and momentum equations are:

$$\frac{\partial \rho}{\partial t} + \vec{\nabla} \cdot \rho \vec{V} + \omega H_\rho = 0 \quad (3-1)$$

$$\frac{\partial \rho u}{\partial t} + \vec{\nabla} \cdot \rho u \vec{V} + \omega H_x = -\frac{\partial p}{\partial x} + \nabla \mu \nabla u + \omega H_{xv} \quad (3-2)$$

$$\frac{\partial \rho v}{\partial t} + \vec{\nabla} \cdot \rho v \vec{V} + \omega H_y = -\frac{\partial p}{\partial y} + \nabla \mu \nabla v + \omega H_{yv} \quad (3-3)$$

where ρ is mixture density, and μ s mixture viscosity.

To close the equations above, Schmidt et al. added a simple positive pressure relationship between the gas-liquid mixture, which is one of the points of the model. Positive pressure relationship is as follows:

$$\alpha^2 \frac{D\rho}{Dt} = \frac{Dp}{Dt} \quad (3-4)$$

where α is the velocity of sound inside the mixture fluid. Combing the sound velocity equation of Wallis [1997], the equation group can be solved. The gas phase volume fraction and distribution can be obtained to predict the cavitation structure and location.

Single-fluid model of Yuan et al. [2001]

Modeling method of single-fluid model of Yuan et al. [2001] is in accordance with the positive pressure modeling method developed by Schmidt et al. [1997]. Assuming the two-phase cavitation flow is a completely homogeneous compressible flowing medium, and its density and molecular viscosity coefficient were the mixed density and mixed-viscosity coefficient, and there is no slip between the two phases. However, Yuan et al. [74] did not apply the positive pressure relationship to close the equations. They applied the additional phase volume fraction transport equation approach to close the equations. These single-fluid model equations are as follows:

$$\frac{\partial \rho}{\partial t} + \frac{\partial(\rho u_j)}{\partial x_j} = 0$$

$$\frac{\partial(\rho u_i)}{\partial t} + \frac{\partial(\rho u_i u_j)}{\partial x_j} = -\frac{\partial p}{\partial x_i} + \frac{\partial(\bar{\tau}_{ij} + \tau_{ij})}{\partial x_j}$$

$$\frac{\partial \alpha}{\partial t} + \frac{\partial \alpha u_j}{\partial x_j} = \frac{(1-\alpha)\rho_j}{\rho} \cdot \frac{n_0}{1+n_0 \cdot \frac{4}{3}\pi R^3} \cdot \frac{d}{dt} \left(\frac{4}{3}\pi R^3 \right) \quad (3-5, 6, 7)$$

where u_i is the velocity component on the x_i axis; i, j , and k represent the direction of the coordinates; p is the pressure, and ρ and μ is mixture density and mixture viscosity coefficient.

$$\rho = \alpha \rho_v + (1 - \alpha) \rho_l$$

$$\mu = \alpha \mu_v + (1 - \alpha) \mu_l \quad (3-8, 9)$$

where α is the gas phase volume fraction. $\rho_l, \rho_v, \mu_l, \mu_v$ is the liquid and vapor density and viscosity coefficient, which is set as constant in the model.

The viscous stress component of the molecule is calculated by the following equation.

$$\bar{\tau}_{ij} = \mu \left(\frac{\partial u_i}{\partial x_j} + \frac{\partial u_j}{\partial x_i} + \frac{2}{3} \frac{\partial u_k}{\partial x_k} \delta_{ij} \right) \quad (3-10)$$

The n_0 in equation 3-7 is the cavitation bubble density inside the liquid phase. R is the radius of one bubble, and it is adjustment. The definition of the vapor volume fraction α is:

$$\alpha = \frac{n_0 \cdot \frac{4}{3}\pi R^3}{1+n_0 \cdot \frac{4}{3}\pi R^3} \quad (3-11)$$

The equations described above can be used to consist of the equation group. The bubble radius variation rate can be calculated by solving these equations and predict the cavitation phenomenon.

Double-fluid model of Alajbegovic et al. [1999]

This model is a simplified continuum multiphase flow model, and the model were established by gas-liquid two-phase conservation equations. An additional source is also applied to consider alternate interaction, and the model can reflect more useful flow field detail. The amount of calculation required is also relatively small.

The flow and combustion process inside the internal combustion engine is the turbulent process and therefore in the establishment of the mathematical model used in engineering calculations, Renault Decomposition Method is commonly used. The dependent variable in equations of motion is processed by Renault decomposition firstly to obtain turbulent mean flow control equations. It is a set of partial differential equations, including the mass conservation

equation (continuity equation), momentum conservation equation, energy conservation equation, and the equation of state of gas. In the Cartesian coordinate system, for each basic equation, they can be expressed as the following fore equations.

(1) Continuity equation

$$\frac{\partial \rho}{\partial t} + \frac{\partial}{\partial x_j} (\rho u_j) = s_m \quad (3-12)$$

where t is the time, $x_j (j = 1, 2, 3)$ is the coordinate, ρ is density, u_j is the component on three

different axis, s_m is the mass source, $\frac{\partial}{\partial x_j} (\rho u_j)$ is the tensor glyph, it can be expressed as:

$$\frac{\partial}{\partial x_j} (\rho u_j) = \frac{\partial}{\partial x_1} (\rho u_1) + \frac{\partial}{\partial x_2} (\rho u_2) + \frac{\partial}{\partial x_3} (\rho u_3) \quad (3-13)$$

(2) Momentum conservation equation (such as on i direction)

$$\frac{\partial (\rho u_i)}{\partial t} + \frac{\partial}{\partial x_j} (\rho u_j u_i - \tau_{ij}) = -\frac{\partial p}{\partial x_i} + g_i - f_i \quad (3-14)$$

where ρ is the density, u_i is the velocity on i direction, p is the vapor pressure, g_i and f_i is the gravity and resistance component on i direction, τ_{ij} is viscous stress tensor, it is connected with strain tensor s_{ij} by applying The generalized Newton's law:

$$\tau_{ij} = 2\mu s_{ij} - \frac{2}{3}\mu \frac{\partial u_k}{\partial x_k} \delta_{ij} - \overline{\rho u_j' u_i'} \quad (i, j, k = 1, 2, 3) \quad (3-15)$$

$$s_{ij} = \frac{1}{2} \left(\frac{\partial u_i}{\partial x_j} + \frac{\partial u_j}{\partial x_i} \right) \quad (3-16)$$

μ is dynamic coefficient of viscosity, u' is Turbulent fluctuation velocity, “—” means average, δ_{ij} is Crowe, Neil symbols, when $i = j$, it is equal to 1, when $i \neq j$, it is 0.

(3) Energy conservation equation

$$\frac{\partial (\rho h)}{\partial t} + \frac{\partial}{\partial x_j} (\rho u_j h + \overline{\rho u_j' h'}) = \frac{\partial p}{\partial t} + u_j \frac{\partial p}{\partial x_j} + \tau_{ij} \frac{\partial u_i}{\partial x_j} + s_h \quad (3-17)$$

where h is the vapor specific enthalpy, s_h is the source term of energy equation.

h can be calculated by the temperature T :

$$h = \int_{T_o}^T c_p dT \quad (3-18)$$

where c_p is vapor specific heat at constant pressure, T is temperature, and T_0 is the reference temperature.

(4) Gas state equation

$$p = \rho RT \quad (3-19)$$

where R is the gas constant.

Equation (3-12), (3-14), (3-17) and (3-19) constitute the basic computational fluid dynamics equations for internal combustion engine. Due to turbulence flow characteristics of the internal combustion engine, Reynolds stress term appears in the momentum equations, turbulent diffusion appears in energy equation, so that the basic governing equations cannot be closed. In order to solve the control average flow basic equations mathematically, the turbulence model is needed, which will be introduced latter.

3.1.2 Analysis about Multi-Phase Flow Models

Positive pressure single-fluid model of Schmidt et al. [1997;1999;]

The parameters inside this model are all set as the normal condition. This model is suitable for the stable normal flow, while it cannot reflect the microscopic mechanism of bubbles and cavitation flow, such as distribution of vacuoles, cavitation dynamics, etc. Thus they are not the detailed model of cavitation flow, and the property of the flow field reflected by this model is very limited. Despite the positive pressure model has been more widely used in the simulation of diesel nozzle internal flow, considering the above reasons, the unstable cavitation process in this study may not be reproduced by this model.

Single-fluid model of Yuan et al. [2001]

Although this model is also built based on the single-fluid model concept of quasi fluid and equilibrium flow, it is more advanced than the last one. This is mainly because this single-fluid model takes into account the microscopic mechanism of cavitation process, such as the distribution of cavitation bubbles, air bubble dynamics, and so on. Of course, it also has obvious shortcomings, such as on the process about cavitation bubble number density and cavitation pressure threshold. Yuan et al. proposed a simple but practical solution at this stage to deal with the microscopic characteristics of cavitation bubbles. The cavitation bubble number density N_0 and initial radius R_0 are adjustable in the model, and those can be decided by comparing the numerical results with experimental data. The disadvantage of this model is that it ignores the gas-liquid cavitation flow momentum transfer and energy transfer between the two phases, and it is only suitable when the two-phase gas-liquid cavitation flow is in the case of strong coupling. In addition, although the

model takes into account the microscopic mechanism of cavitation process, but cavitation bubbles distribution and the critical condition of the occurrence of cavitation is dealt with too simple ways, and there is a theoretical flaw, which has to be improved.

Double-fluid model of Alajbegovic et al. [1999]

By the introduction about this model, it shows that two-fluid model and single-fluid models are all based on the continuum method, and are considering some of the main microscopic characteristics of cavitation flow. However, compared with the single-fluid model, the two-fluid model in the framework of its construction can reflect more details of the flow field. For example, white slip in a two-fluid cavitation flow and the force of the two-phase interface are all considered. At the same time, bubbles movement-induced eddy viscosity has also been included in the calculation of turbulent viscosity. In theory, these details generated in the gas-liquid two phases flow is mainly because of the relative speed existing between the two phase, which cannot be ignored. relative velocity between the liquid and the bubble is usually around 10% of the average speed of [singhal A.K. et al., 2002] in the cavitation flow, the diesel nozzle internal flow at high velocity is even more than this ratio. However, one important assumption of single-fluid model is slip-free between vapor and liquid phases, so it is not able to reflect the details of the flow field. From view of the development potential of the model framework, the two-fluid cavitation flow model is clearly more advanced than the single-fluid model of cavitation flow.

According to the comparison, the study will select the two-fluid model to calculate the diesel nozzle internal instability cavitation flow. The main reasons are: First, in the modeling framework of this two-fluid model, a number of important details or features of cavitation nozzle flow can be addressed after passing through a certain method of modeling, which is very conducive to the model development. Second, the value of the model parameters of the vapor-liquid will not seriously deviate from the physical substance values under the calculate stability requirements. Third, with the improvement of computer capacities, the increase amount of two-fluid model calculation has not been a problem.

3.1.3 Numerical Solution Method for Multi-Phase Flow Model

According to the basic modeling idea of two-fluid model described previously, after processing the control equations the corresponding discrete equations may be established, namely the establishment of algebraic equations, which can be solved step by step. The greatest difficulty for the above equation to solve is how to calculate the pressure in the momentum equation, or how to solve the coupled pressure field and velocity field separately. In this study, SIMPLEC algorithm,

which is proposed by Van Doormaal and Raithby [1984] is applied to solve this problem. SIMPLEC is SIMPLE Consistent shorthand, meaning coordinated SIMPLE (Semi-Implicit Method for Pressure-Linked Equations) algorithm. SIMPLEC is one of the improvements of SIMPLE algorithm, and the system belongs to the pressure correction algorithm of the discrete equations separation solving method.

The above describes a complete set of numerical methods corresponding to the two-fluid model. Finally, it should be noted that the two-fluid cavitation flow model and numerical methods described above have been implanted in CFD (Computatioal Fluid Dynamics) program ---AVL FIRE, and thus the subsequent numerical analysis will be conducted by means of AVL FIRE v2013.

3.2 MATHEMATICAL MODELS APPLIED IN NOZZLE INTERNAL FLOW STUDY

3.2.1 Turbulence Model

The $k-\varepsilon$ model and *RNG* $k-\varepsilon$ model are usually used in the traditional simulation study for internal combustion engine. However, with the increase of the power density, rotation speed and the injection pressure, it is necessary to improve the original linear eddy viscosity model to match up the development of modern internal combustion engine. $k-\varepsilon$ two-equation model is based on the Boussinesq assumption that the viscosity coefficient of each Reynolds stress component has the same value, i.e. the turbulence is the isotropic scalar. However, under the condition of intense turbulence and bending streamlines, the turbulence is anisotropic, and the viscosity coefficient should be the anisotropic tensor. This assumption can cause inevitable deviation between the practical condition and the simulation result.

On the contrary, $k-\zeta-f$ model introduces new transportation equations to describe the variable ζ which has relationship with turbulence viscosity. As a result, the property of anisotropic turbulence can be taken into consideration. The precision of simulation for separated flow and rotational flow is increased. At the same time the calculation timing is not increased obviously. In fact, the $k-\zeta-f$ model is the v^2-f model proposed by Durbin [1995]. In order to improve its calculation convergence characteristic, Popovac and Hanjalic introduced ζ that presents the turbulent velocity scale into this model [2004].

The eddy-viscosity is obtained from

$$\mu_t = \rho C_\mu \zeta k^2 / \varepsilon \quad (3-20)$$

where C_μ is empirical constant, k is the turbulent kinetic energy and ε is the turbulent dissipation rate. The basic two equations and the corresponding transport equations are shown as follows.

$$\rho \frac{Dk}{Dt} = \rho(P_k - \varepsilon) + \frac{\partial}{\partial x_j} \left[\left(\mu + \frac{\mu_t}{\sigma_k} \right) \frac{\partial k}{\partial x_j} \right] \quad (3-21)$$

$$\rho \frac{D\varepsilon^*}{Dt} = \rho \frac{C_{\varepsilon 1} P_k - C_{\varepsilon 2} \varepsilon}{\tau} + \frac{\partial}{\partial x_j} \left[\left(\mu + \frac{\mu_t}{\sigma_\varepsilon} \right) \frac{\partial \varepsilon}{\partial x_j} \right] \quad (3-22)$$

$$\rho \frac{D\zeta}{Dt} = \rho f - \rho \frac{\zeta}{k} P_k + \frac{\partial}{\partial x_j} \left[\left(\mu + \frac{\mu_t}{\sigma_\zeta} \right) \frac{\partial \zeta}{\partial x_j} \right] \quad (3-23)$$

$$f - L^2 \frac{\partial^2 f}{\partial x_j \partial x_j} = (C_1 + C_2 \frac{P_k}{\zeta}) \frac{(2/3 - \zeta)}{\tau} \quad (3-24)$$

where P_k is the production item of turbulent kinetic energy, L is the spatial scale, T is the time scale, and C_1, C_2 are the empirical constants. Additional modification to the ε equation is that the constant $C_{\varepsilon 1}$ is dampened close to the wall. This is computationally more robust than the original v^2 - f model.

$$C_{\varepsilon 1}^* = C_{\varepsilon 1} [1 + 0.045(1/\zeta)^{0.5}] \quad (3-25)$$

The turbulence of both phases is modeled in the framework of RANS (Reynolds-Averaged Navier–Stokes) method. This model is numerically robust and has been extensively used in the modeling of multiphase flow in diesel nozzles [Wang et al., 2012; He et al., 2013;]. A detailed description of the turbulence kinetic equation, the turbulence energy dissipation equation, and the assumptions for modeling closure terms can be found in the work of Berg et al. [2005]. It has to be mentioned that the turbulent viscosity of liquid phase in the nozzle includes not only the typically encountered shear-induced turbulent viscosity, but also the bubble-induced turbulent viscosity, which is calculated with the formula suggested by Sato and Sekoguchi [1975].

3.2.2 Cavitation Model

In the two-fluid model, both liquid and vapor phases are treated as continuous medium, and conservation equations are solved separately for each phase. The mass and momentum exchange between phases are calculated by additional source item in the conservation equations. Moreover, the simplified bubble dynamic equation is employed to describe the evolution of a single bubble. The outline of this model is as follows.

Mass conservation equation:

$$\frac{\partial(\alpha_k \rho_k)}{\partial t} + \nabla \cdot (\alpha_k \rho_k V_k) = \sum_{l=1, l \neq k}^2 \Gamma_{kl} \quad (3-26)$$

where α_k and ρ_k are separately the volume fraction and density of the phase k .

Volume fractions have to obey the compatibility equation:

$$\sum_{k=1}^2 \alpha_k = 1 \quad (3-27)$$

Γ_{kl} is the mass exchange term between liquid and vapor phases, given by the following formula:

$$\Gamma_{12} = \rho_1 \frac{N}{C_R} 4\pi R^2 \frac{\partial R}{\partial t} = -\Gamma_{21} \quad (3-28)$$

where N is bubble number density, calculated by the following equation [Alajbegovic A et al., 2002]:

$$N = \begin{cases} n_0 & \alpha_1 \leq 0.5 \\ 2(n_0 - 1)(1 - \alpha_1) & \alpha_1 > 0.5 \end{cases} \quad (3-29)$$

where n_0 is the initial bubble number density. This is a heuristic formula used to model the coalescence effects at conditions of higher volume fraction.

In equation (3-28), C_R is an empirical coefficient adjusting the onset of bubble collapse. R is the mean bubble radius, determined by bubble number density N and volume fraction of vapor phase α_1 :

$$R = \sqrt[3]{\frac{3\alpha_1}{4\pi N}} \quad (3-30)$$

The time derivative of the mean bubble radius R is estimated from the Rayleigh equation:

$$R\ddot{R} + \frac{3}{2}\dot{R}^2 = \frac{\Delta p}{\rho_2} \quad (3-31)$$

where Δp presents the effective pressure difference causing bubble growth and collapse, and it is calculated by the following expression [Von Berg E et al, 2005]:

$$\Delta p = p_v - (p - C_E \frac{2}{3} \rho_2 k_2) \quad (3-32)$$

where p is the local pressure, C_E is Egler coefficient depending on local turbulence level.

Momentum conservation equation:

$$\begin{aligned} \frac{\partial(\alpha_k \rho_k V_k)}{\partial t} + \nabla \cdot (\alpha_k \rho_k V_k V_k) &= -\alpha_k \nabla p + \nabla \cdot \alpha_k (\tau_k + T_k^t) \\ &+ \alpha_k \rho_k g + \sum_{l=1, l \neq k}^2 M_{kl} + V_k \sum_{l=1, l \neq k}^2 \Gamma_{kl} \end{aligned} \quad (3-33)$$

where g is the acceleration of gravity, M_{kl} presents the interfacial momentum exchange between liquid and vapor phases. The interfacial forces at bubble surface mainly consist of drag force and turbulent dispersion force. Consequently, M_{kl} takes the following form:

$$M_{12} = F_{12}^D + F_{12}^{TD} = -M_{21} \quad (3-34)$$

The drag force F_{12}^D and the turbulent dispersion force F_{12}^{TD} read as follows:

$$F_{12}^D = -F_{21}^D = C_D \frac{3\alpha_1 \rho_2}{8R} |V_1 - V_2| \cdot (V_2 - V_1) \quad (3-35)$$

$$F_{21}^{TD} = -F_{12}^{TD} = C_{TD} \rho_2 k_2 \cdot \nabla \alpha_1 \quad (3-36)$$

where C_D is the drag coefficient, calculated with the correlation as suggested by Ishii and Mishima et al. [1984], and C_{TD} is the turbulent dispersion coefficient, with a value of approximately 0.1, according to Bertodana [1992].

In the current paper, the fuel injection processes are assumed to be isothermal, ignoring the effects of heat transfer. Therefore, energy conservation equation is not needed.

3.3 NUMERICAL METHOD APPLIED IN SPRAY SIMULATION STUDY

Some previous studies have analyzed the effect of cavitation and turbulence inside the nozzle hole on the jet atomization, and a very important consensus is reached that the ultra cavitation flow and correspondingly high turbulence intensity inside the spray holes increases disturbance of jet surface, and the two factors are a major cause of the first atomization process. However, most of these studies are conducted under the single-hole nozzle and quasi-steady state conditions ignoring some important factors of instability role caused by the nozzle configurations. In this study, a discrete droplet model (DDM) is applied to describe the process of mixture formation in the cylinder of diesel engine, and the flow field is dealt with the Euler way, and droplet phase is regarded as a discrete system, and the Lagrange motion coordinate is used to study the kinetic and thermodynamic characteristics of droplets in the flow field, focusing on the interaction between gas-liquid boundary surface, namely, mass, momentum and energy exchange process between the two phase. The drag force effect of the vapor phase on the liquid droplet was taken into the consideration when describing the droplet moving.

3.3.1 Spray Sub-models

As it is known that the spray evolution inside the chamber is very complex, and the atomization is the first step for the mixture formation, just as shown in Figure 3.1. Before introducing the atomization models, it is better to introduce the important concepts of primary breakup (first break up) and the secondary breakup models. The primary breakup refers to the process that after the high pressure liquid spray leaving the nozzle, surface of continuous jet liquid begins to form liquid ligament and droplets, which is closely related to the flow within the nozzle. It is caused by the aerodynamic instability, turbulence, cavitation, and other instability. The secondary atomization is process that the further break up of the dispersed liquid droplets or the liquid ligament, which is mainly due to aerodynamic instability. Obviously, primary breakup is much more complex than the secondary one. In this study, two atomization processes will be considered separately, following the relevant mathematical models, which will be introduce from next page.

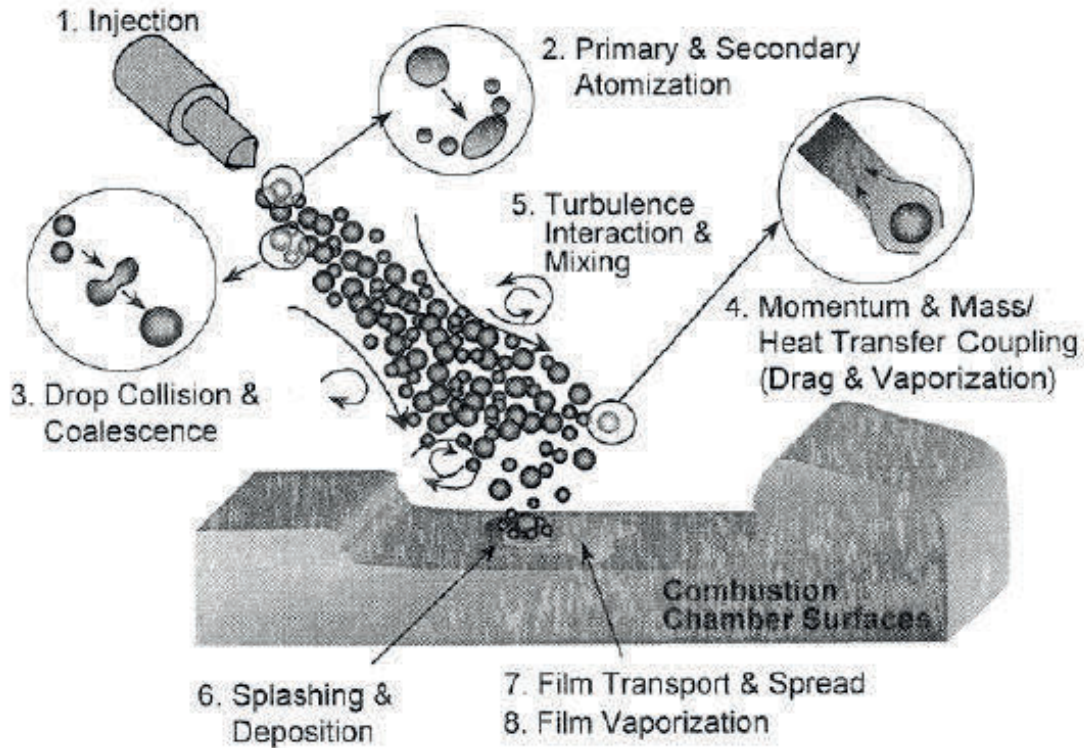


Figure 3.1 Spray evolution inside the chamber

The primary breakup model

The first break model, which is applied in this study, is proposed by Tatschl [2000]. It takes the effect of aerodynamic, internal flow cavitation, and turbulent together. The break up is dominant by the competition of the two factors. The schematic of the model is shown in Figure 3.2. The left figure is the real phenomenon observed in the experiments, and the right figure is the assumption of this model. It assumes that there are large discrete liquid blobs near the nozzle hole, and the first break up and the second break up happen continually [Reitz & Diwakar, 1987]. As a result, it is also called “Blob model”. The cavitation and turbulent information inside the nozzle is necessary when applying this model. It should also be noted that there is no initial droplet size distribution assumption for the initial liquid jet because of the introducing of internal flow result.

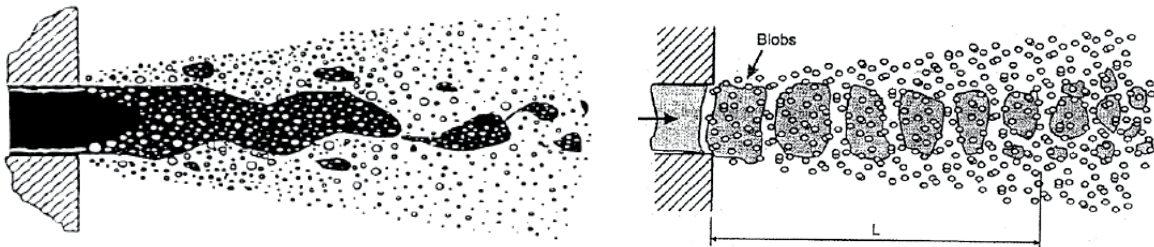


Figure 3.2 Introduction about the first break up model applied in this study [Reitz & Diwakar, 1987]

The first liquid jet break up process, which is caused by the aerodynamics, is considered by using the famous wave model concept, which is shown in Figure 3.3 [Reitz, 1987].

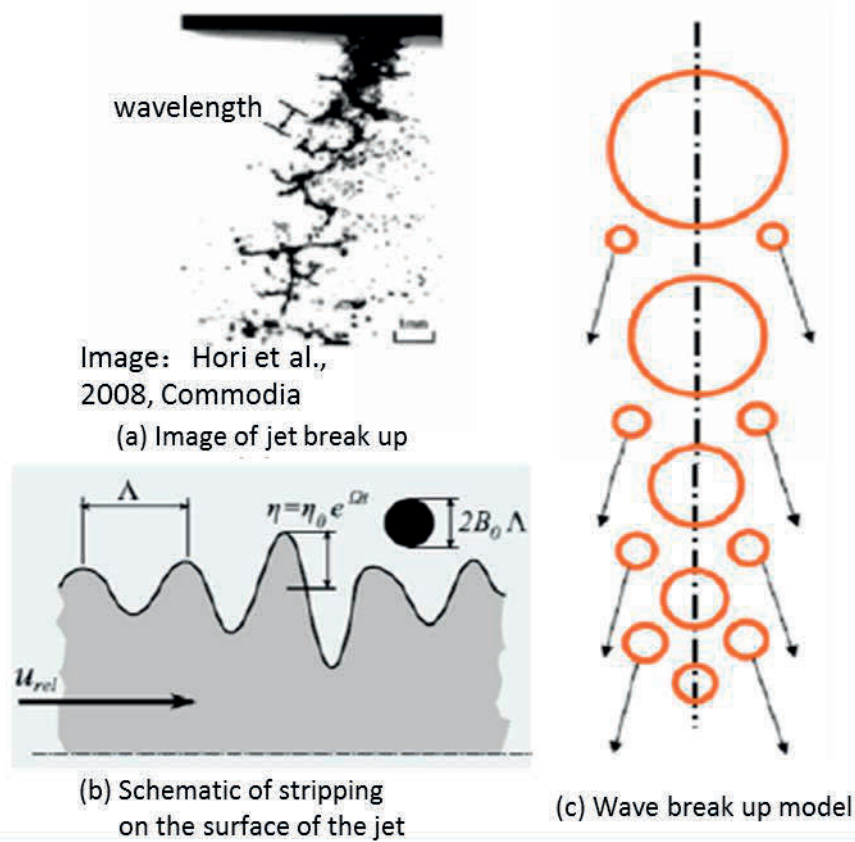


Figure 3.3 Introduction about the wave break up model concept [Reitz, 1987]

As introduced before, the break up processes caused by the internal flow patterns is considered by the internal flow computation result in this study. As a result, the “two steps method” needs the nozzle internal flow calculation information, which is the boundary condition of the Blob first break up model. The droplet surface tension effect was included inside the calculation with the ignoring of liquid-viscosity. The same way was also adopted in the secondary break up model.

The secondary breakup model

After the first break up process, the droplets entry into the ambient gas with very high velocity, which can induce the further break up and atomization caused by aerodynamics factors. In the high-pressure spray of diesel fuel, the type of secondary break up state of the droplets are primarily mutation break up, and followed by shear and crushing bag break up. Taking into account the above-mentioned crushing characteristics, the two kinds of KH (Kelvin-Helmholtz) and RT

(Rayleigh-Taylor) models are applied in this study, which are the surface wave instability theory, to describe the secondary atomization process, and the model is often called as the KH- RT model [Su T.F., et al., 1996]. The corresponding model assumption is shown in Figure 3.3. During the movement of the droplets, the KH and RT processes have competition, until the break up happens.

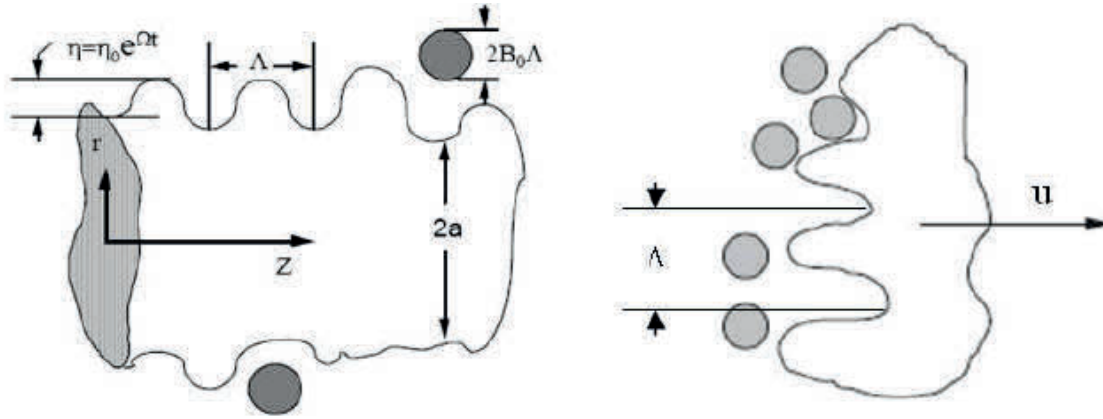


Figure 3.3 Break up processes of KH (left) and RT (right) concepts [Su T.F., et al., 1996]

Droplet collision and coalescence model

In a dense area of the liquid spray, the distance between droplets is much smaller than the mean free path, even up to the same order of magnitude of diameter. Therefore, there is a strong interaction between the droplets, which is mainly manifested as droplets collide and aggregate. O'Rourke statistical model [O'Rourke, P.J., 1981] is applied in this study to simulate the droplets interaction. In order to determine whether a collision occurs between the droplets, concept of collision frequency is introduced, and then it is used to calculate the probability of collision between droplets.

3.4 SUMMARY

The models and theoretical basis applied in numerical study are introduced in detail in this chapter, and the summary is shown as below:

1. Three typical models, which are famous to simulate the cavitated flow, are introduced and compared in this chapter, and the two-phase model is proved to have more advantage for this study.
2. The turbulent and cavitation models applied in the study are also described deeply in this section.
3. The theory and sub models, which are coupled with the internal flow information and implemented in the spray simulation study, are also introduced specifically in this chapter.

CHAPTER 4 SPRAY EVOLUTION OF MULTI-HOLE NOZZLES UNDER NON-EVAPORATION CONDITIONS

4.1 VISUALIZATION OF SPRAY BY MIE-SCATTERING

4.1.1 Experimental Condition

In this chapter, the injection process and spray characteristics of multi-hole nozzles will be investigated, and a comparison between the conventional single-hole nozzle and the practical multi-hole nozzle will also be conducted under the non-evaporation conditions. The experimental conditions, which are shown in detail in Table 4.1, were determined in consideration of real operating conditions of small diesel engines. JIS #2 diesel was selected as the test fuel. The injection pressure range varied from 80 MPa to 180 MPa, and 120MPa was set as the baseline condition. The injection quantity was held at 0.3 mm³/hole and 2 mm³/hole to simulate the pilot, main and post injection duration in real diesel engines, while the ambient pressure and temperature for fundamental spray research were selected as 1.5 MPa and 300 K, respectively, which also could keep the ambient gas density similar to that of combustion conditions. In addition, each experimental condition was conducted at least 10 times in consideration of the cycle-to-cycle variations.

Table 4.1 Experimental conditions

Injection Conditions		
Fuel (Diesel JIS#2)	Density (20 °C, 1 atm) : ~830 kg/m ³	
	Boiling Point (1 atm) : ~273 °C	
	Kinetic Viscosity (20 °C, 1 atm) : ~3.86 (10 ⁻⁶) m ² /s	
	Cetane Index : >=45	
	Sulfur : 10 ppm	
Injector	Single-Hole	Multi-Hole
Injection Quantity: Q _{inj} (mm ³ /hole)	0.3 2.0*	0.3 2.0*
Rail Pressure: P _{inj} (MPa)	80 120* 180	80 120* 180
Ambient Condition		
Ambient Gas	Air	
Ambient Pressure : P _a (MPa)	1.5	
Ambient Temperature : T _a (K)	300	
Ambient Density : ρ _a (kg/m ³)	17.4	

*Baseline Condition

When it comes to the injectors applied in the study, there several single-hole and multi-hole nozzles (10 holes). The parameters of the nozzle changes from the hole diameter to nozzle hole length, the properties of nozzle spray to these parameter variation will be discussed one by one.

4.1.2 Image Processing and Analysis Method

The spray in non-reaction environments can be characterized by many features and parameters. A review of various spray imaging techniques and definitions for both macroscopic and microscopic spray parameters was published by Soid et al. [2011]. The typical image processing method and spray property definitions used in the current study are shown in Figure 4.1. The same processing method was applied to spray images of single-hole and multi-hole nozzles.

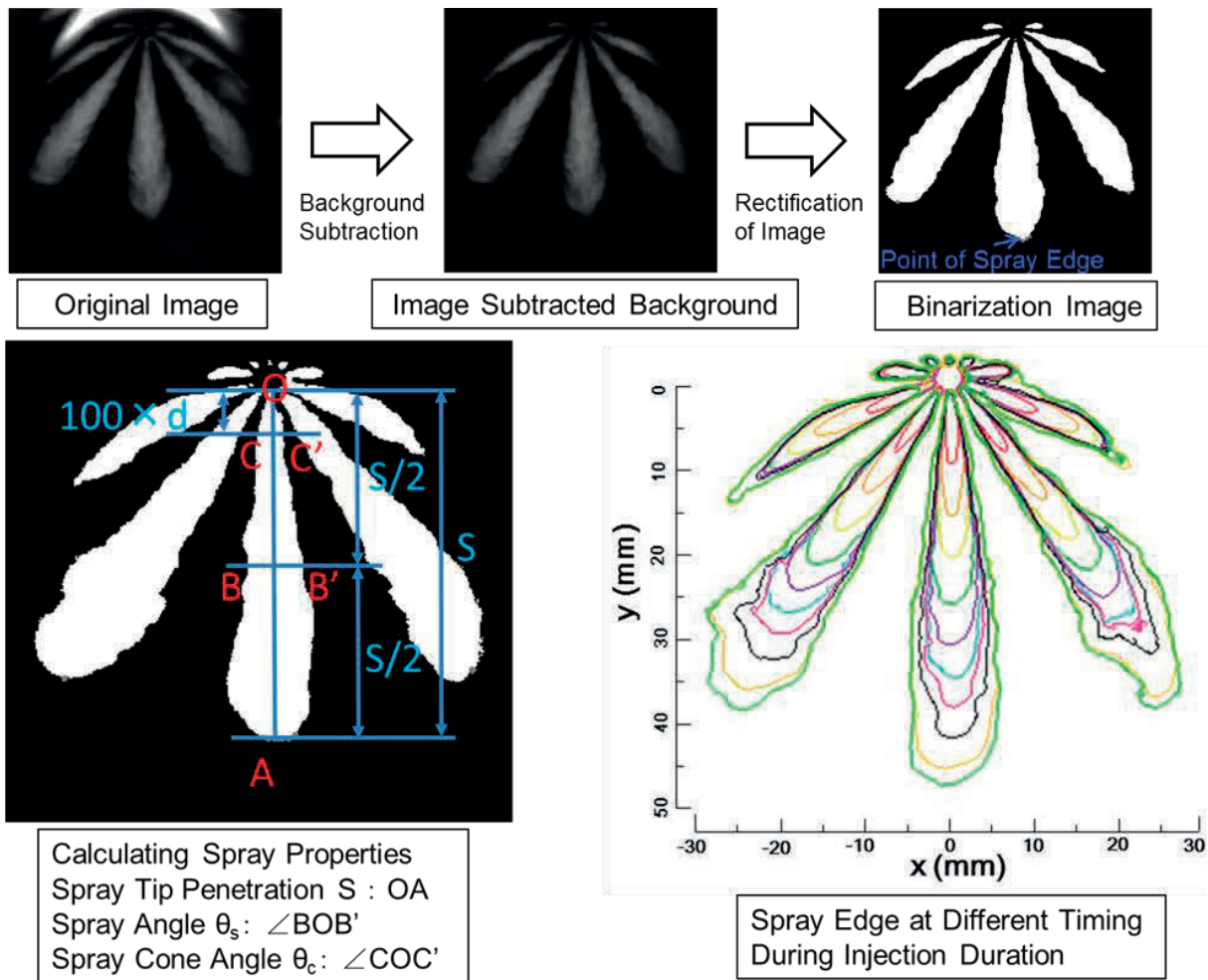


Figure 4.1 Image processing for spray properties measurement

In Figure 4.1, multi-hole spray under the baseline condition is taken as an example. For each frame, the central spray was characterized in terms of the spray tip penetration (i.e., the maximum penetration distance of the spray S), the corresponding angle of the half spray tip penetration (i.e., spray angle θ_s), and the corresponding angle of 100 times hole diameter distance from the orifice tip (i.e., spray cone angle θ_c) as a function of different types of nozzles and fuel injection pressures. Spray images were processed to calculate their properties by the following steps. First, each frame was converted to the effective image by subtracting the background, and then rectification for the effective image was conducted using the different scale images taken at different positions. In this way, the error introduced by the spray direction deflection could be eliminated. After that, a threshold algorithm was applied to the processed image. Finally, the spray edge could be detected using the binarization image. The temporal variations of the spray edges are shown in the lower right corner of Figure 4. It can be seen that the spray contour at each recording time is well captured spatially. These contours of the central spray were sampled along different vectors, which all started from the corresponding orifice point, to determine the spray tip penetration. Moreover, the spray angle and spray cone angle could also be calculated based on this algorithm.

One of the most important features that can introduce uncertainty into the measurement results is the selection of the threshold. Hence, the assessment of the threshold value is necessary for this algorithm, especially for multi-hole nozzle spray, which includes not only cycle-to-cycle variation but also hole-to-hole variation. After a series of statistics, the intensity threshold of 5 (maximum intensity is 255) was selected to be applied in this study, with the consideration that the deviation of the measurements caused by the intensity cut-off value selection was within the deviation of cycle-to-cycle and hole-to-hole spray fluctuations.

4.2 CHARACTERISTICS OF INJECTION PROCESSES AND SPRAY BEHAVIORS OF SINGLE-HOLE AND MULTI-HOLE NOZZLES

The comparison of single-hole and multi-hole nozzles will be introduced in this section, and the discussion is mainly around the injection rate, spray images, and spray parameters. Figure 4.2 shows the scheme of single-hole and multi-hole nozzles used in this study. Both of the injectors were the solenoid-operated type. The multi-hole nozzle has 10 holes, 0.1 and 0.07 mm in diameter. To make the comparison, the reference single-hole nozzle also had the same sac configuration, hole length, and diameter as the multi-hole nozzles.

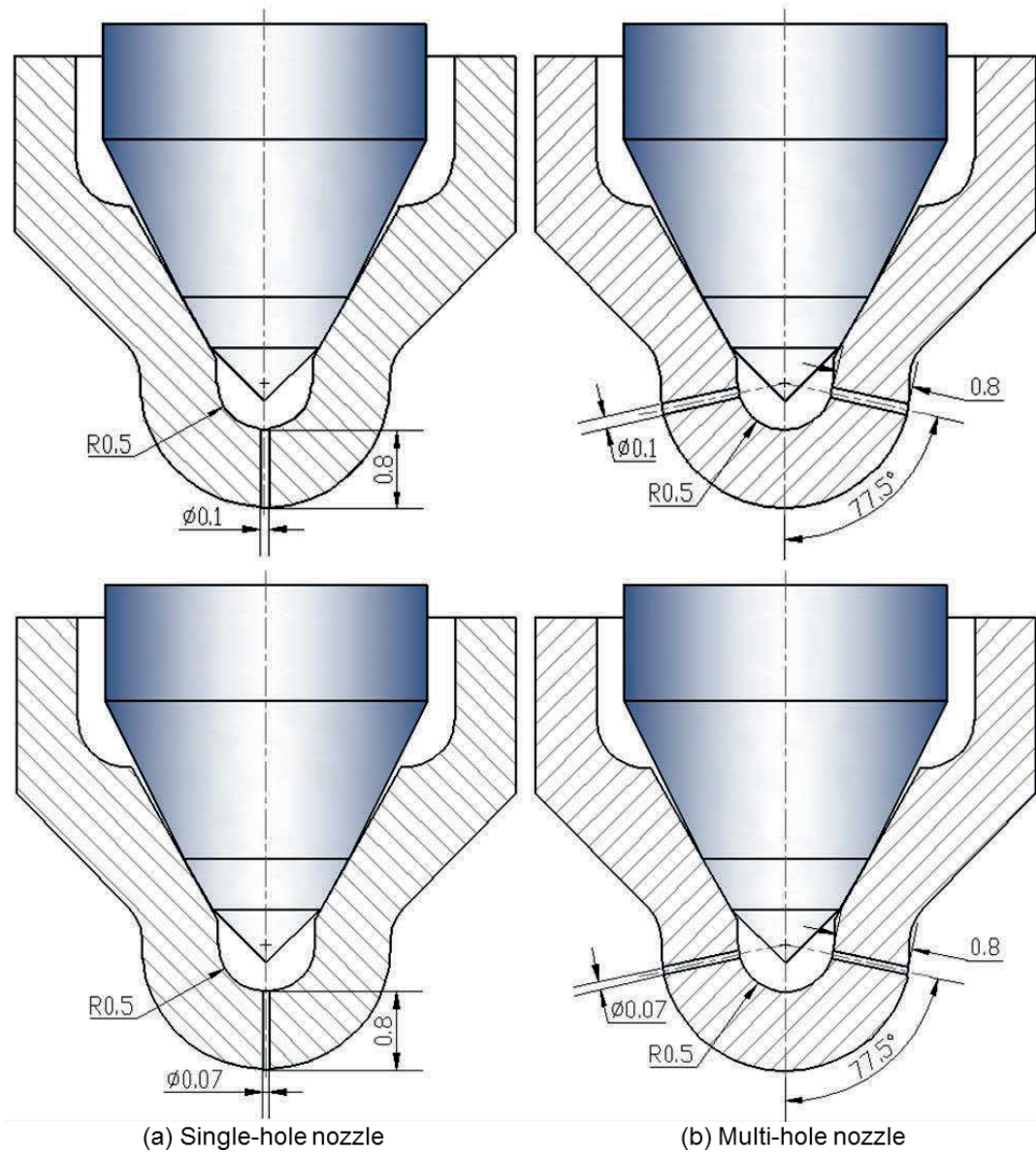


Figure 4.2 Scheme of single-hole and multi-hole nozzles

4.2.1 Injection Rate of Single-hole and Multi-hole Nozzles

Comparison between single-hole and multi-hole nozzle

The measured injection rate curves are shown in Figure 4.3-(a), and the Bernoulli Equation is used to calculate the corresponding averaged sac pressure variations, which are shown in Figure 4.3-(b).

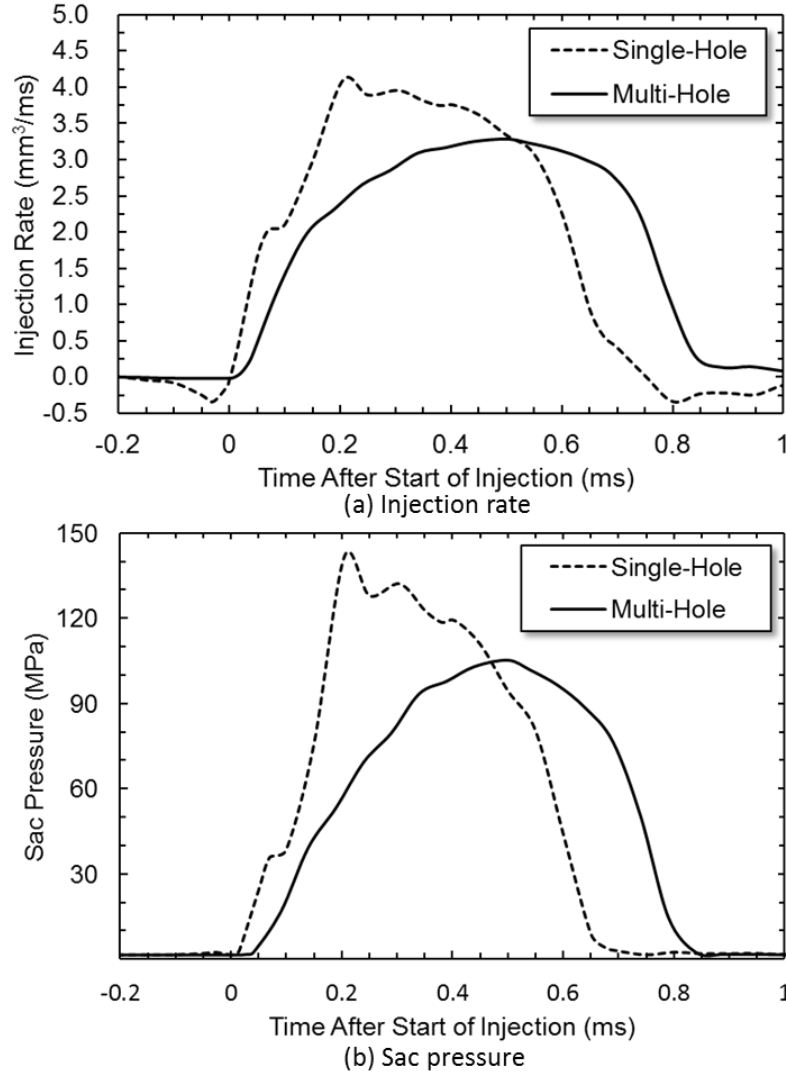


Figure 4.3 Injection rate per orifice and the calculated sac pressure of single-hole and multi-hole injectors. $P_{inj}=120$ MPa, $P_a=1.5$ MPa, and $Q_{inj}=2$ mm³/hole.

The equation is written as below, where Q_f is the injection rate, α is the average flow coefficient, A represents the theoretical flow area, and P_s is the sac pressure.

$$Q_f = \alpha A \sqrt{\frac{2(P_s - P_a)}{\rho_f}} \quad (4.1)$$

As for α , it is related to the flow discharge coefficient of the nozzle hole, which is a direct reflection of the cavitation intensity inside the hole. Payri et al. [2004] concluded that, under cavitation conditions, the flow discharge coefficient depended on the cavitation number.

$$C_N = \frac{(P_{inj} - P_v)}{(P_{inj} - P_a)} \quad (4.2)$$

However, all of these experiments were conducted under quasi-steady conditions. Until now, it remains difficult to acquire accurate quantitative data from the realistic diesel injector internal flow (high pressure, high velocity, and micro size). In the current study, the theory developed from the quasi-steady condition was expanded to the transient condition, and a qualitative comparative analysis was made between the single-hole and multi-hole nozzles to provide a reference for explaining the different spray behaviours emerging from different nozzles.

From Figure 4.3-(a), it is obvious that the injection rate of the single-hole nozzle is higher than that of the multi-hole nozzle, especially in the initial stage of injection. However, the injection duration of the single-hole nozzle is shorter than that of the multi-hole nozzle when maintaining the same injection quantity per hole. This phenomenon can be explained by the fact that the effective flow area of the multi-hole nozzle, which has ten injection holes, is ten times of that of the single-hole nozzle. In other words, the theoretical flow coefficient of single-hole nozzle is one tenth that of the multi-hole nozzle. As a result, its sac pressure discharge rate is also much lower than that of the multi-hole nozzle, which coincides with the calculated sac pressure in Figure 4.3-(b). The sac pressure of the single-hole nozzle increases dramatically as soon as the injection starts. Its maximum sac pressure is notable, in that it is even a little higher than the rail pressure. There are two main reasons for this occurrence. The average flow coefficient used in Equation (1) is one factor, and the “water-hammer” effect accompanying the needle lifting and the restricted out flow from the single-hole nozzle is another significant factor that can generate this super high sac pressure [Moon et al., 2015]. On the contrary, the sac pressure of the multi-hole nozzle increases slowly from the start of injection. It takes a relatively longer time for the multi-hole nozzle to reach its peak value, but this value is much lower than the rail pressure. This again verifies previous analysis concerning the discharge rate of the sac pressure.

Under different injection pressure conditions

In this section, three injection pressures were selected to investigate the influence of rail pressure on the injection processes and spray behaviours of single-hole and multi-hole nozzles. The injection pressures were 80 MPa, 120 MPa, and 180 MPa. Under these injection pressure conditions, the injection quantity and ambient conditions were held constant.

The measured injection rate curves under different rail pressure conditions are shown in Figure 4.4. According to the injection rate curves for both of the injectors, the injection duration decreases with increasing rail pressure.

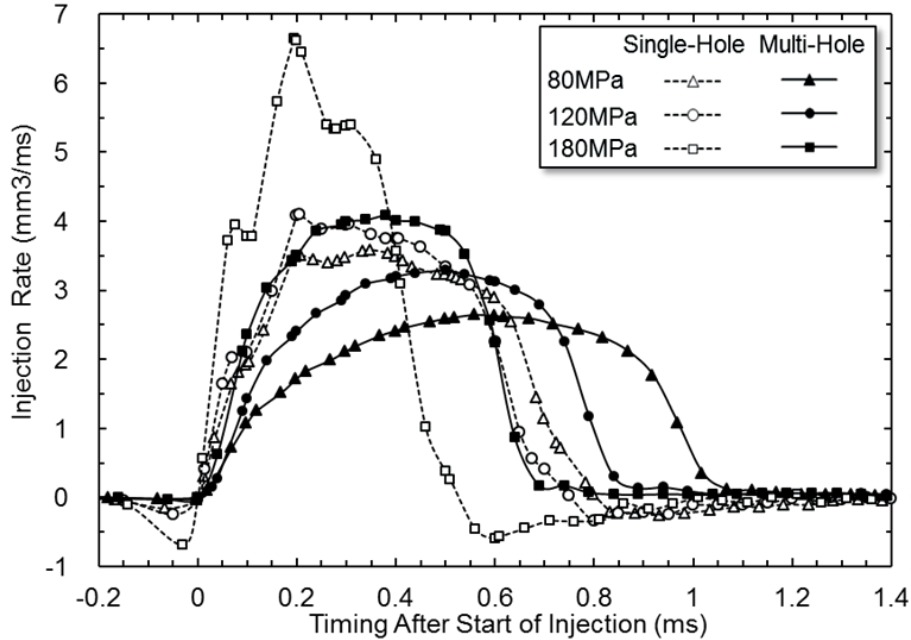


Figure 4.4 Injection rate results of single-hole and multi-hole injectors under different rail pressure conditions. $P_{inj}=80,120,180$ MPa, $P_a=1.5$ MPa, and $Q_{inj}=2$ mm³/hole.

Under different rail pressure conditions, the injection durations of the single-hole nozzle are all shorter than those of the multi-hole nozzle, namely the maximum single-hole nozzle injection rate values are higher than those of the multi-hole one. Comparing the difference of injection rate values between the two injectors under different rail pressure conditions, this difference is more sensitive to the higher (180MPa) and lower (80 MPa) rail pressure conditions.

Under different injection quantity conditions

The injection rate results measured by the BOCSH long tube method is shown in Figure 4.5. The calculated sac pressure under different conditions is shown in Figure 4.6. For the single-hole nozzle, there are fluctuations under both tiny and normal injection quantity conditions, especially under the tiny one. It seems that there is pressure oscillation inside the sac of the single-hole nozzle, and the needle movement is a little nonlinear [Benajes et al, 2004]. The water hammer effect caused by the limited effective flow area (single-hole) and the super short energizing duration may contribute to this issue. On the contrary, for the multi-hole nozzle, the injection rate curves are all smooth under different injection quantity conditions, and the trend of the two curves changes placidly with the time after start of injection. This is attributed to the lower increasing rate of the sac pressure caused by the large fuel flow area (10 holes) and the relatively longer energizing period of the injection signal.

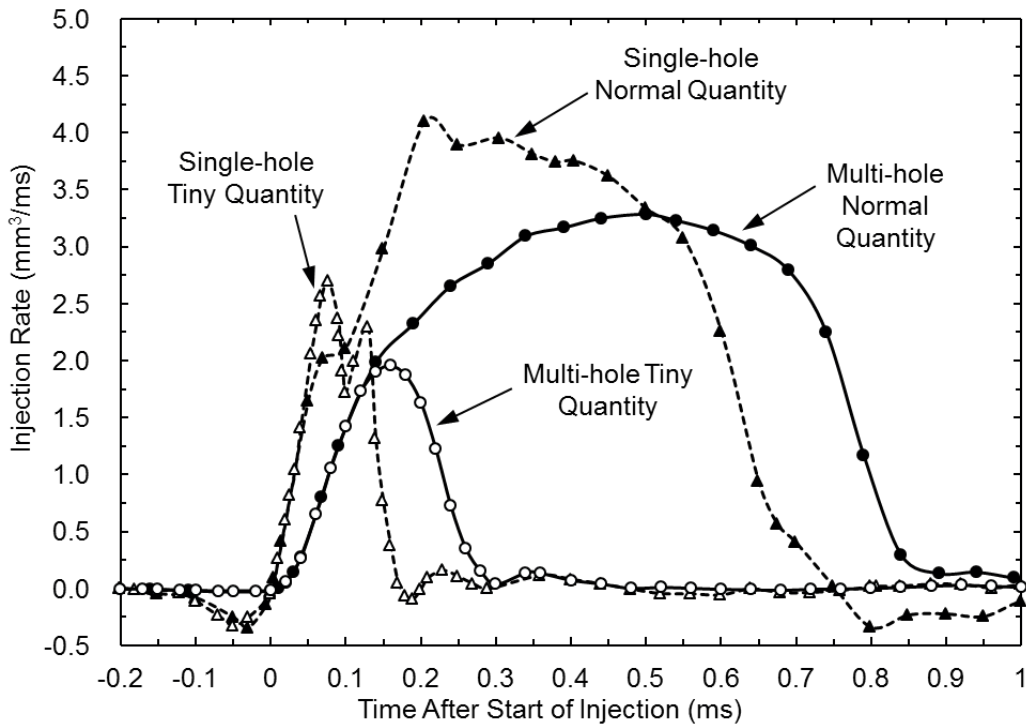


Figure 4.5 Injection rate per orifice of single-hole and multi-hole injectors. $P_{inj}=120$ MPa, $P_a=1.5$ MPa, and $Q_{inj}=0.3$ and 2 mm³/hole.

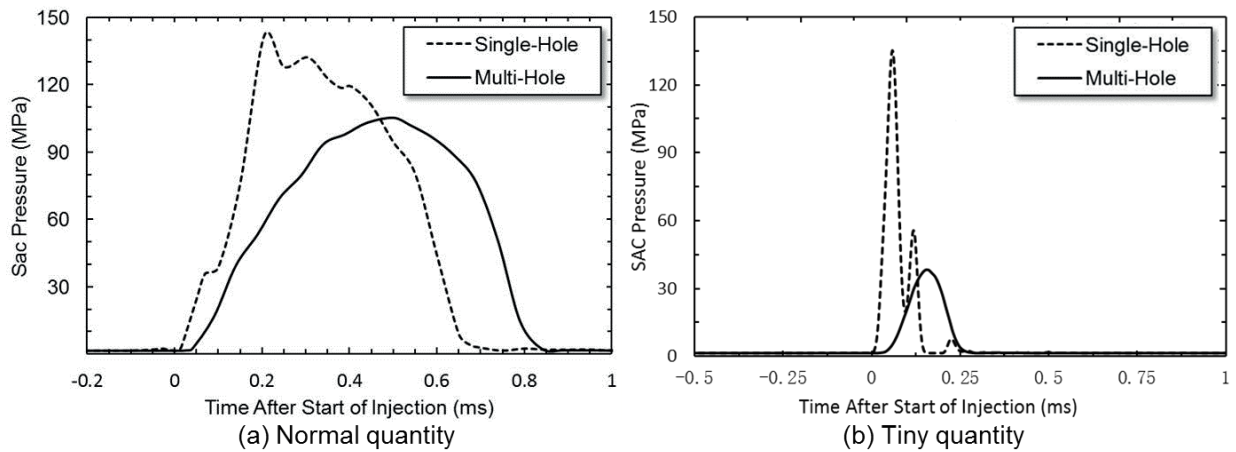


Figure 4.6 Sac pressure of single-hole and multi-hole injectors. $P_{inj}=120$ MPa, $P_a=1.5$ MPa, and $Q_{inj}=0.3$ and 2 mm³/hole.

From another view, no matter under tiny or normal injection quantity condition, it is obvious that the injection rate of the single-hole nozzle is higher than that of the multi-hole nozzle, especially at the initial stage of injection. However, the injection duration of the single-hole nozzle is shorter than that of the multi-hole nozzle when maintaining the same injection quantity per hole.

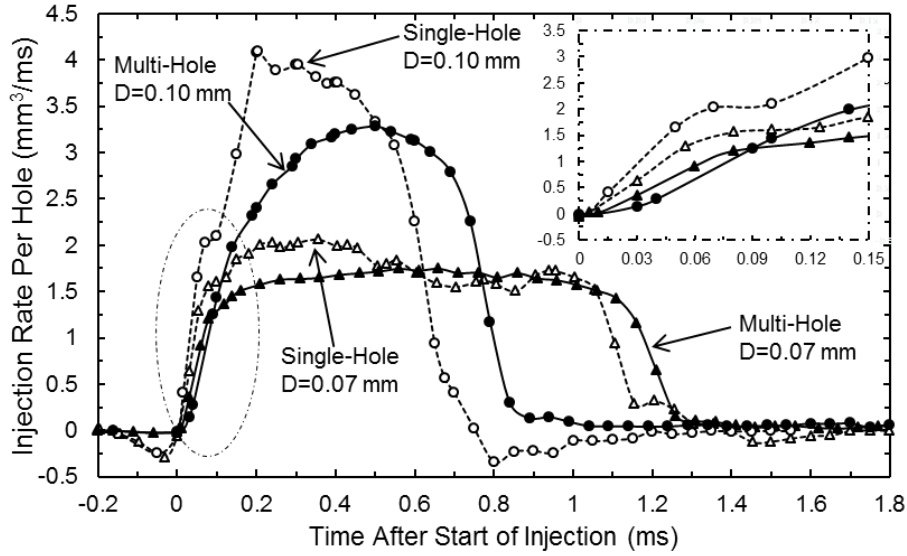
Compared with the tiny injection quantity condition, the difference in the injection rate and injection duration between the single-hole and multi-hole nozzles is larger under the normal injection quantity condition. The following discussion will give deeper analysis about the phenomenon described above.

Effect of micro nozzle hole diameter

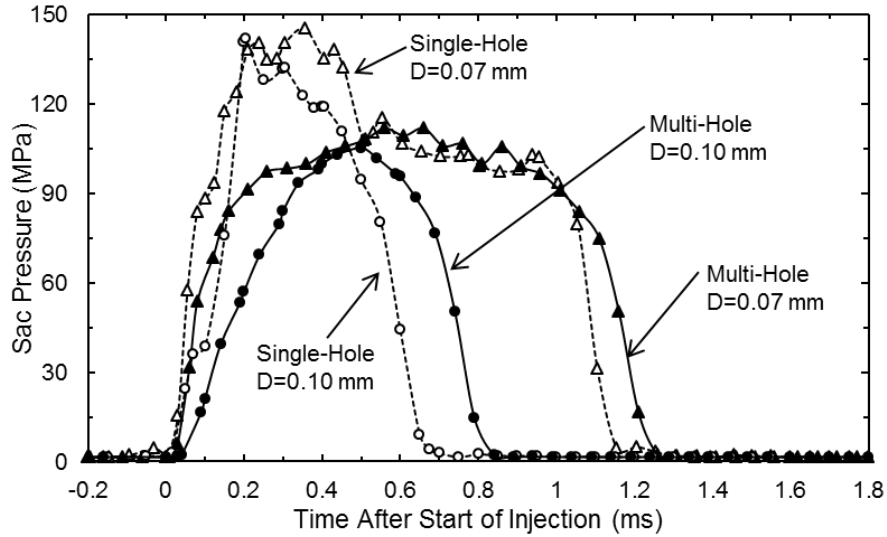
The measured injection rate curves of four different nozzles under the same conditions ($P_{\text{rail}}=120$ MPa, $P_a=1.5$ MPa, $Q_{\text{inj}}=2.0$ mm³/hole) are shown in Figure 4.7-(a), and the Bernoulli equation is used to calculate the corresponding averaged sac pressure variations which are shown in Figure 4.7-(b).

In the case of larger hole diameter ($D=0.10$ mm), it is obvious that the injection rate of the single-hole nozzle is higher than that of the multi-hole nozzle, especially in the initial stage of injection. Consequently, the injection duration of the single-hole nozzle is shorter when maintaining the same injection quantity per hole. There are two factors that can affect the injection rate. One is the fuel velocity and the other one is the effective flow area. Further, the fuel velocity depends on the sac pressure, and the effective flow area depends on the hole diameter, hole numbers, and the discharge coefficient. Hence, this phenomenon can be explained as that the theoretical flow area of the multi-hole nozzle, which has ten injection holes, is ten times of that of the single-hole nozzle. As a result, its sac pressure discharge rate is also much higher than that of the single-hole nozzle, which coincides with the calculated sac pressure in Figure 4.7-(b). The sac pressure of the single-hole nozzle increases dramatically as soon as the injection starts. Because of the water-hammer effect in the sac of the single-hole nozzle [Moon et al., 2015] and the applying of average discharge coefficient in Equation (4.1), the maximum sac pressure is a little higher than the rail pressure. On the contrary, the sac pressure of the multi-hole nozzle with larger orifices increases slowly after start of injection (ASOI). It takes relatively longer time to reach its peak value, but it is much lower than the rail pressure. This verifies previous analysis about the discharge rate of the sac pressure.

When it comes to the micro hole ($D=0.07$ mm) condition, the regularity of their injection processes has changed conspicuously. Compared with the larger hole diameter condition, both single-hole and multi-hole nozzles with micro orifices have longer injection duration and lower injection rate.



(a) Injection Rate



(b) Sac Pressure

Figure 4.7 Injection rate and calculated sac pressure of single-hole and multi-hole injectors.

$$P_{\text{rail}}=120 \text{ MPa}, P_a=1.5 \text{ MPa and } Q_{\text{inj}}=2 \text{ mm}^3/\text{hole}.$$

Although the injection duration of the single-hole nozzle is also shorter than that of the multi-hole one under micro hole condition, the deviation becomes much smaller. As for the injection rate, the difference between the single-hole and multi-hole nozzles is also reduced obviously, especially during the second half of their injection periods, they even have the same trend and values. The corresponding calculated sac pressure also presents the interesting phenomenon. The sac pressure of both single-hole and multi-hole nozzles with micro orifices is all higher than that of the larger hole diameter ones.

With the decrease in the hole diameter, the effective flow area is reduced. In that way, the sac pressure discharge rate is reduced, especially for the multi-hole nozzle. It should be noted that in the initial stage of injection the effect of micro holes on multi-hole nozzles is different from that on the single-hole ones. The injection rate of the multi-hole nozzle with micro orifices is higher than that of the multi-hole one with larger orifices in the initial stage of injection. It reveals that the higher sac pressure and higher flow velocity inside the hole volume dominate the injection rate of multi-hole nozzles on this stage. However, the injection rate of the single-hole nozzle with a micro orifice is lower than that of the single-hole one with larger orifice. It means that the larger effective flow area dominates the injection rate of the single-hole nozzles in the initial stage of injection.

4.2.2 Far-field and Near-field Spray Images

Comparison between single-hole and multi-hole nozzle

Typical false-coloured and temporal spray images of single-hole and multi-hole injectors are shown in Figure 4.8. The illumination light intensity is a symbolic characteristic of the fuel droplet size and concentration. Spray contours can help elucidate the effects of ambient gas entrainment and interactions between spray plumes [Eagle et al., 2014].

Comparing the spray of the single-hole nozzle and the central spray of the multi-hole nozzle, which are shown in Figure 4.8-(a) and Figure 4.8-(b), respectively, there are many interesting distinctions. First, the global intensity of the single-hole spray is much higher than that of the multi-hole spray, particularly in the beginning stage of the injection, although this regularity occurs whether within the injection duration or after the end of injection. Furthermore, the high intensity even can extend to the downstream region of the single-hole nozzle spray, which means that the fuel distribution of the multi-hole nozzle is more homogeneous. This also indicates that the fuel quantity injected from the single-hole injector is larger than that from one of the ten holes of the multi-hole injector at the same time after start of injection within the injection duration, even the total injection mass per hole remains constant. This issue coincides with the previous discussion for Figure 4.3. It is because of the limited effective flow area and high sac pressure that the single-hole nozzle injection duration is shorter than that of the multi-hole nozzle and the injection rate is higher than that of the multi-hole one. Second, as for the spray geometry and shape, neat edges are observed in the spray images of the single-hole nozzle at 0.2, 0.4 and 0.6 ms after start of injection (ASOI), and the sprays have round and smooth heads in the downstream region. At 0.8 ms ASOI, near the end of injection, the spray shape does not change much. At 1.0 ms ASOI the spray distributes freely with the remaining injection momentum.

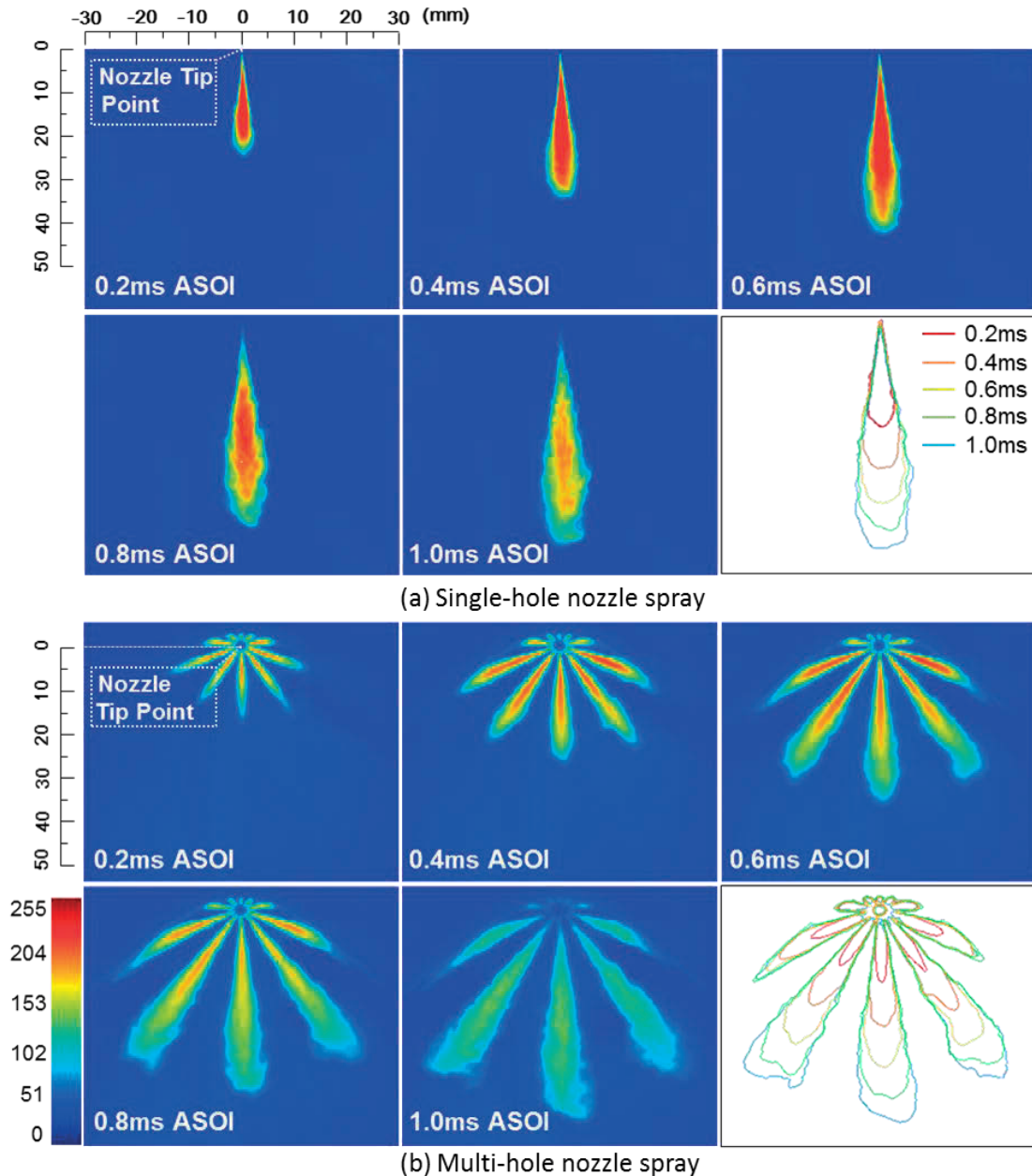


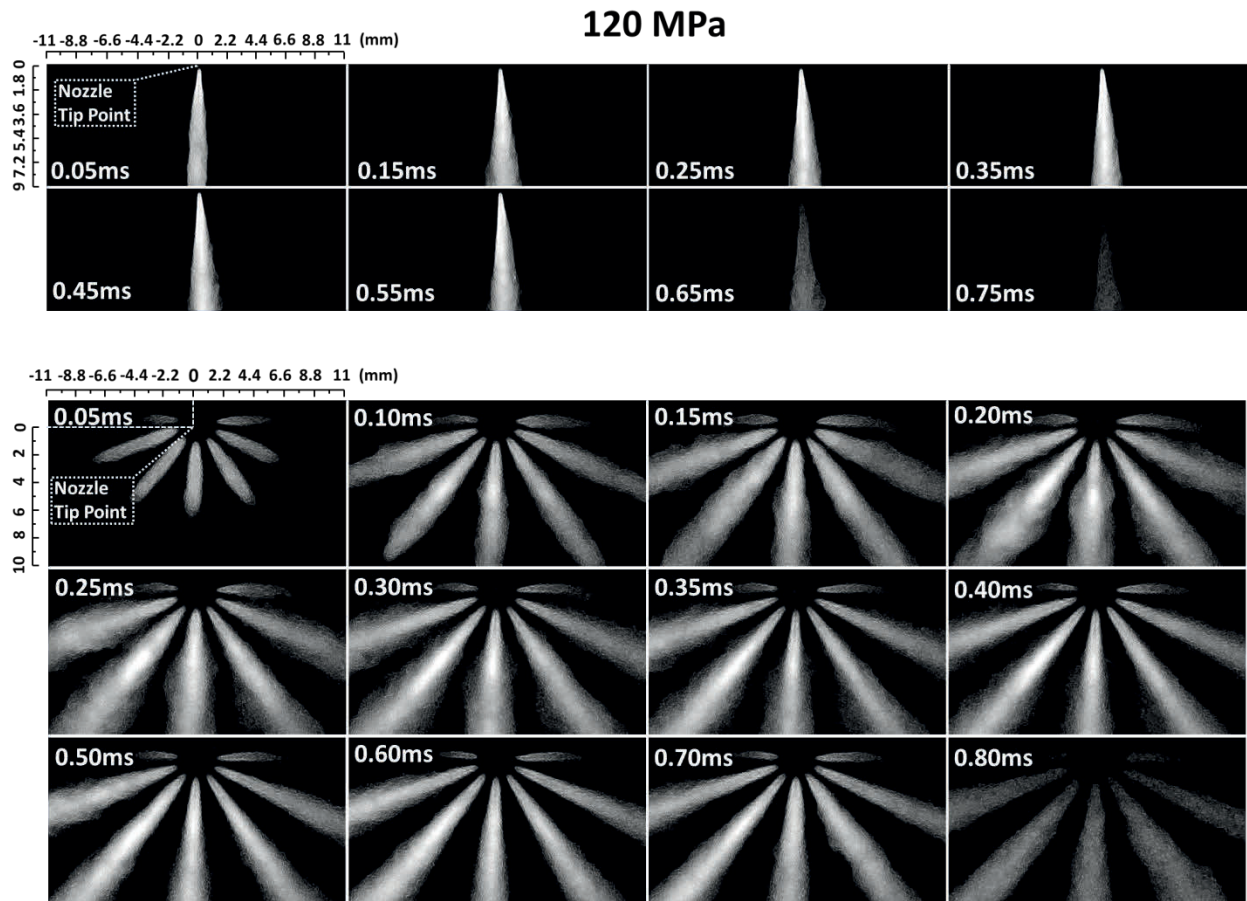
Figure 4.8 False-colored far-field spray images of single-hole and multi-hole injectors.

$$P_{inj}=120 \text{ MPa}, P_a=1.5 \text{ MPa}, \text{ and } Q_{inj}=2 \text{ mm}^3/\text{hole}.$$

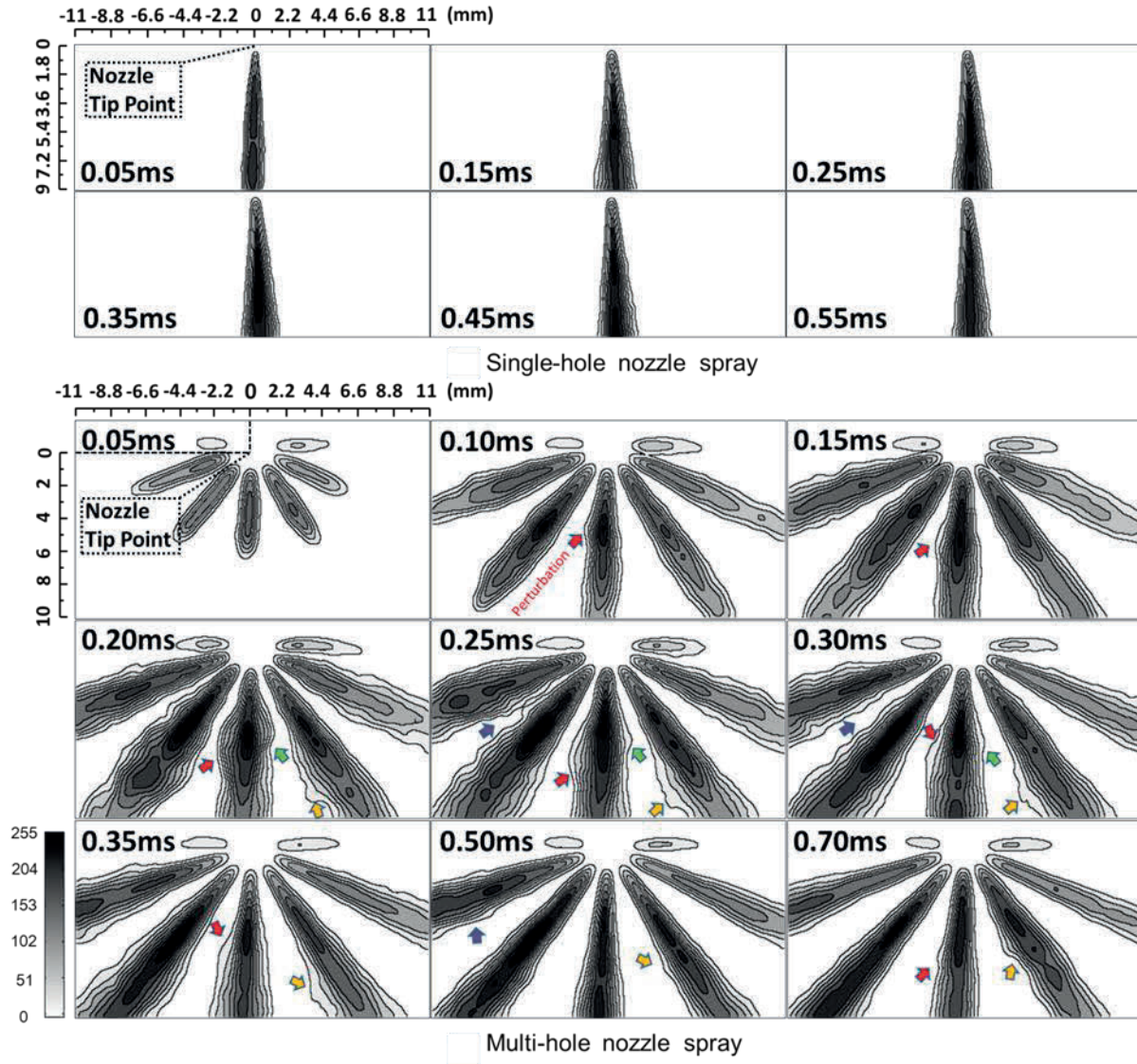
As a result, the intensity declines significantly. When it comes to the multi-hole nozzle sprays, the edges are irregular and the spray plumes are flanked by evident wavelike contours. Of particular interest is the early transient flow regime (0.2ms ASOI) when the spray shape is very different from that of the single-hole nozzle spray. This phenomenon has a strong relationship with the injection rate results, shown in Figure 7. Third, for the multi-hole nozzle sprays around the end of injection (0.8 and 1.0 ms ASOI), the figure shows a large movement in the spray-tip compared to

its centroid, and the other two plumes next to the central spray are also asymmetrical. The Coanda effect plays a significant role in these issues [Skogsberg et al, 2005]. Different spray plumes originally propagate along their spray axis with high velocity, and the air entrainment increases with the development of the spray plumes. Since enough ambient gas cannot enter into the regions between two plumes in time, the local pressure of these regions may decrease. As a result, the low-pressure regimes between sprays can enhance the sprawling diffusion of the multi-hole nozzle sprays and the consequent asymmetric spray morphology.

In order to investigate the spray behaviors near the nozzle tip region in detail, high speed imaging of 100000 fps was applied to take a close-up view for this regime (see Figure 4.9).



(a) Original spray images



(b) Processed intensity gradient spray images

Figure 4.9 Far-field spray images of single-hole and multi-hole injectors. $P_{inj}=120$ MPa, $P_a=1.5$ MPa, and $Q_{inj}=2$ mm³/hole.

Firstly, paying attention to the baseline condition (120 MPa), according to the images of typical timings, the multi-hole nozzle sprays pulsate out from the nozzle tip to the radial direction, and the edges of them fluctuate seriously compared with those of the single-hole nozzle spray, especially in the initial stage of injection (0.1-0.25 ms ASOI). The perturbations maintained above can be observed clearly by processing the original images to the gradient images of Figure 4.9-(b).

The integrated speculations and reasonable explanations for this phenomenon can be excavated out by linking the previous results [Inaba et al., 2014] and the current study. It is well

known that there is vortex flow inside the sac of multi-hole nozzles due to the off-axis arrangement of the orifices, especially under the low needle lift condition. The location of the unstable vortex core varies with the needle moving, which results in the unstable spiraling fuel flow pattern with vortex emerging through the orifice. Furthermore, the string-type cavitation generated in the sac and hole volume also play a significant role in this phenomenon [Kim et al., 1997; Hayashi et al., 2014].

Under different rail-pressure conditions

The far-field spray images of single-hole and multi-hole nozzles under different rail-pressure and constant injection quantity conditions are shown in Figure 4.10, respectively.

It can be seen that with the increasing of injection pressure, the spray scattering light intensity is increased a lot, especially for the multi-hole nozzles. Moreover, under different injection pressure condition, the difference in spray properties is all very prominent, which has already been explained in detail in last section. However, it seems that the difference is more sensitive under the lower rail pressure conditions, because of the difference in sac pressure between the single-hole and multi-hole nozzle is larger, which has already been analyzed before.

Figure 4.11 and Figure 4.12 show the close-up spray images of single-hole and multi-hole nozzles with the orifice diameter of 0.1 mm under 80 MPa and 180 MPa rail pressure conditions, respectively. The comparison under 120 MPa rail pressure condition is already shown in Figure 4.9.

When it comes to the effect of rail pressure on the near-field nozzle spray behaviors, because the injection duration is very different, the time of image selection is also a little different. It can be seen that the single-hole nozzle near-field spray presents tiny variation with the variation of injection pressure. However, the multi-hole nozzle near field spray presents interesting phenomenon, which will be described latter on.

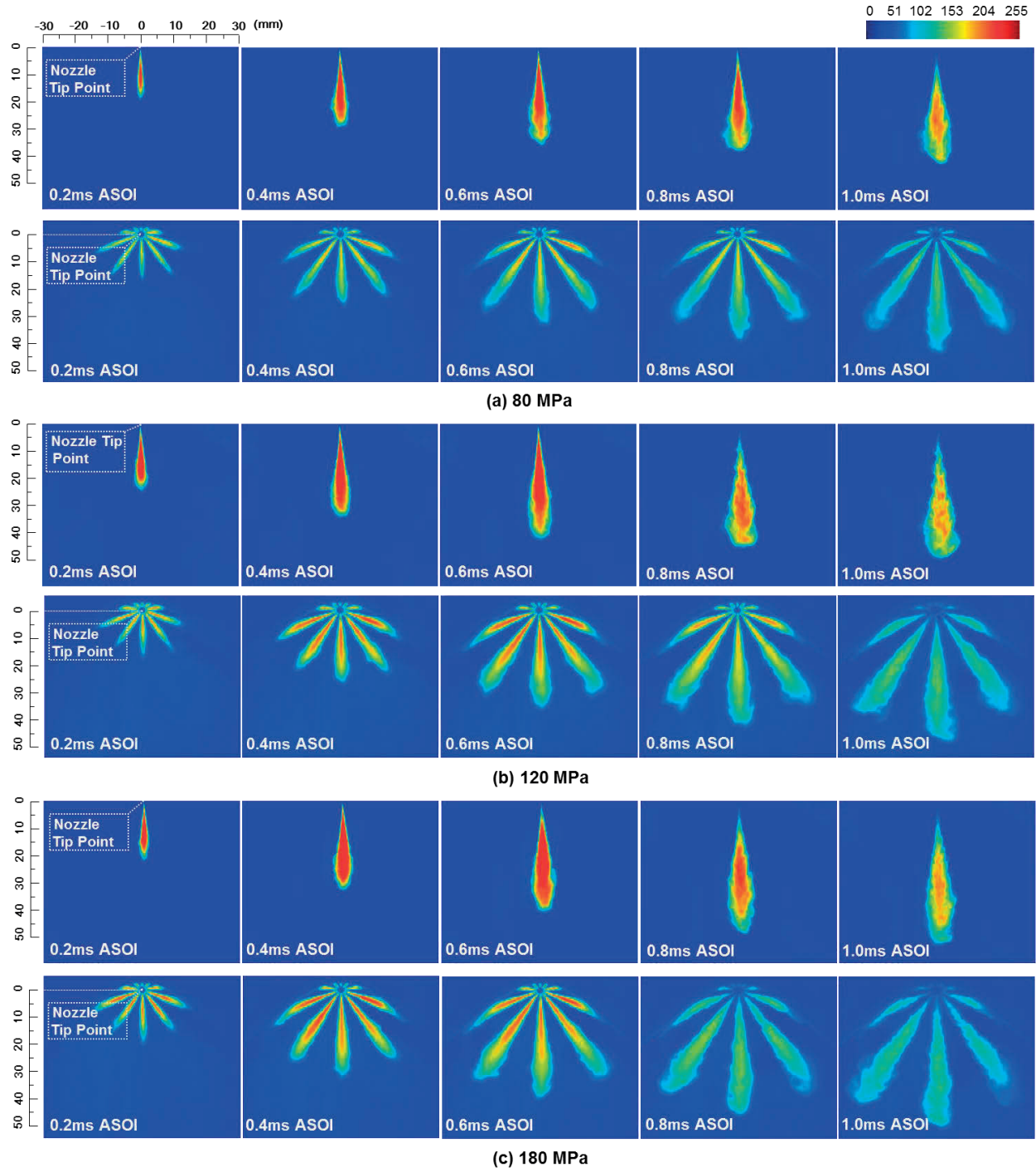


Figure 4.10 Far-field spray images of single-hole and multi-hole injectors under different rail pressure conditions. $P_{inj}=80,120,180$ MPa, $P_a=1.5$ MPa, and $Q_{inj}=2$ mm³/hole.

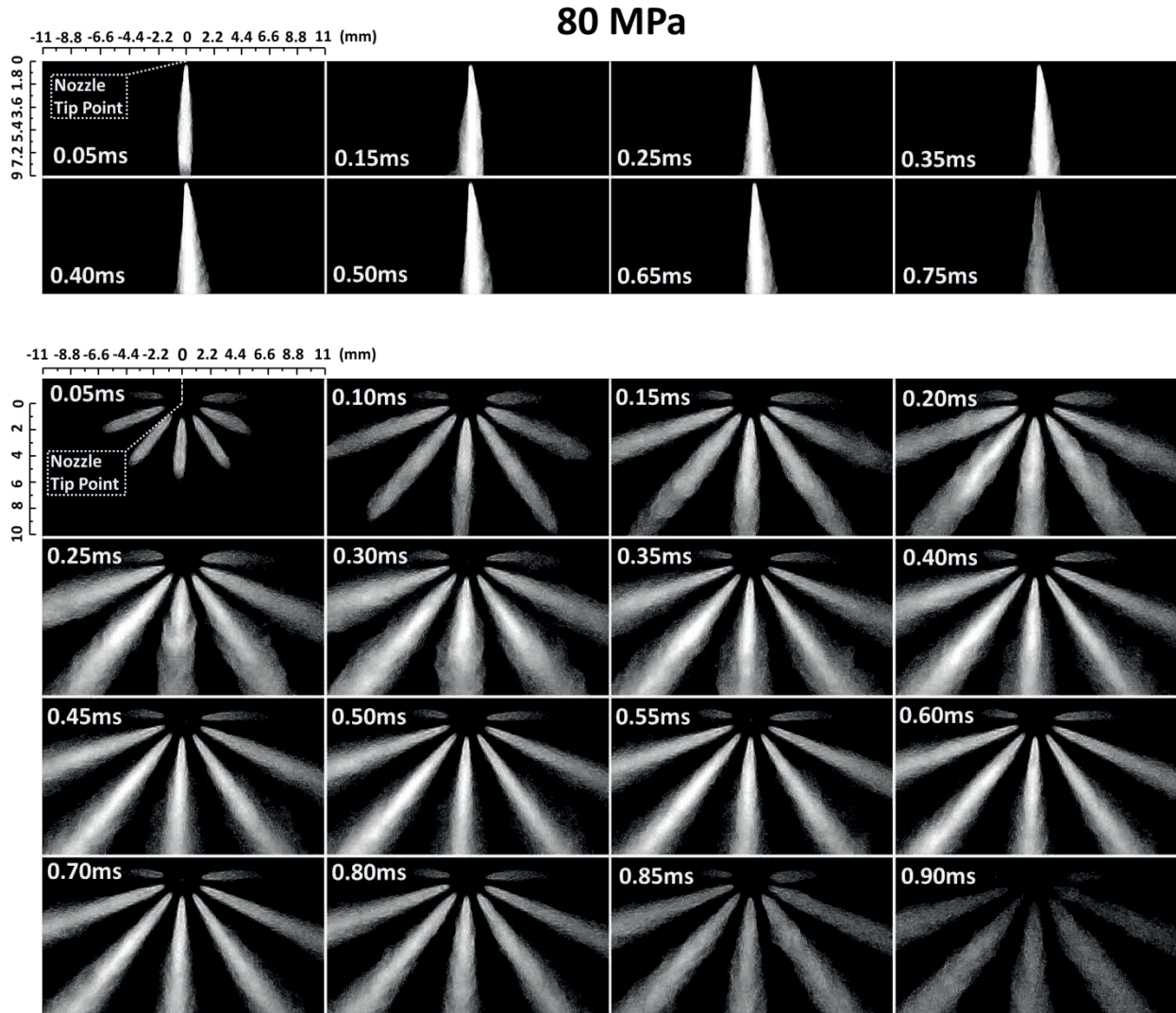


Figure 4.11 Far-field spray images of single-hole and multi-hole injectors. $P_{inj}=80\text{MPa}$, $P_a=1.5\text{MPa}$, and $Q_{inj}=2\text{mm}^3/\text{hole}$.

Under the lower rail pressure conditions, such as 80 and 120 MPa, the differences in nozzle near-field spray is more obvious, which is also caused by the different sac pressure increasing rate. As analyzed before, under the lower rail pressure conditions, the sac pressure inside multi-hole nozzle increases very slowly, the momentum of the spray is lower relatively. As a result, the sac pressure deviation between single-hole and multi-hole nozzles is larger under the lower rail pressure conditions. And then the turbulent and cavitated initial fuel jet is easier to distribute to the radical direction, and the pulsated spray is easier to be generated and observed.

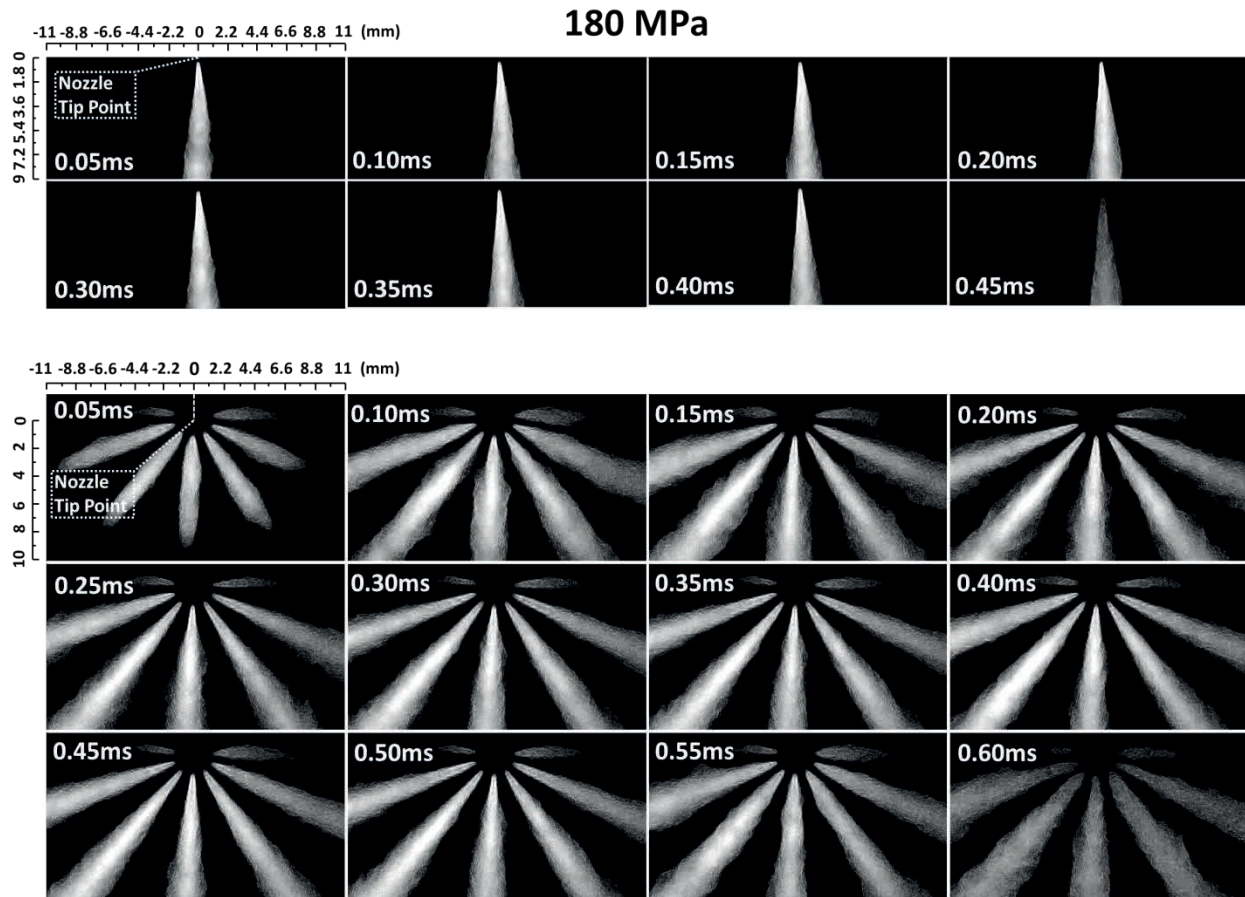


Figure 4.12 Far-field spray images of single-hole and multi-hole injectors. $P_{inj}=180$ MPa, $P_a=1.5$ MPa, and $Q_{inj}=2$ mm³/hole.

Under different injection quantity conditions

The typical false-coloured and temporal spray images under different injection quantity conditions, which are converted from the black-white images, are shown in Figure 4.13. It is known that the illumination light intensity and the spray contours are symbolic characteristics of the fuel droplet size, concentration, the effects of ambient gas entrainment, and interactions between spray plumes.

Affected by the different injection duration, the selection of the typical timings for different injection quantity conditions is a little different. Comparing the spray developing from different nozzles under tiny and normal injection quantity conditions, there are many interesting distinctions. For the single-hole nozzle, under both tiny and normal injection quantity conditions, the sprays all have high scattering light intensity. Except for the obvious difference in the spray length and spray area, it seems that the spray profiles under the tiny injection quantity condition are more irregular relatively, while the difference in the overall appearance of the single-hole

nozzle spray between tiny and normal injection quantity conditions is not so much apparent. However, for the multi-hole nozzle, the difference in the spray properties between tiny and normal injection quantity conditions is very large. The scattering light intensity of the tiny quantity spray is much weaker, which is coincided with the lowest injection rate result discussed before.

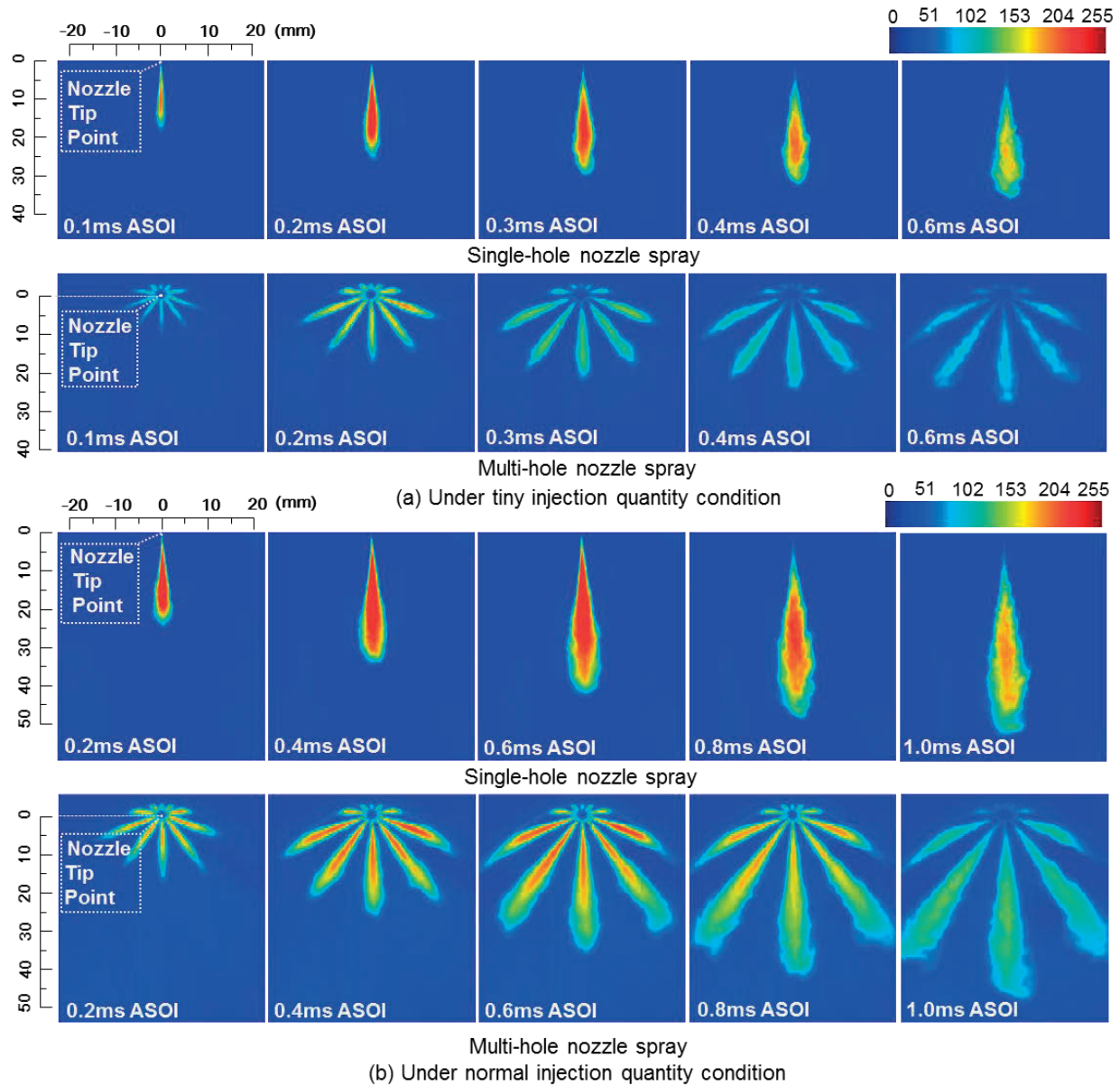


Figure 4.13 Spray evolution of different nozzles under tiny and normal injection quantity conditions. $P_{inj}=120$ MPa, $P_a=1.5$ MPa, and $Q_{inj}=0.3$ and 2 mm³/hole.

When the attention is paid on to the different spray properties between the single-hole and multi-hole nozzle, in Figure 4.13 it can be seen that compared with the normal injection quantity condition, the difference in the spray morphology between the single-hole and multi-hole

nozzles is more apparent under the tiny injection quantity condition, especially for the spray luminance and volume. This regularity is opposite to that of the injection rate results, which indicates that the effect of injection quantity plays different roles in the injection processes and the spray evolution of different nozzles.

Figure 4.14 shows the close-up spray images of the single-hole and multi-hole nozzles, respectively. The original pictures were processed using the simple Sobel operator method [Qu et al., 2005] to make the spray profiles more prominent.

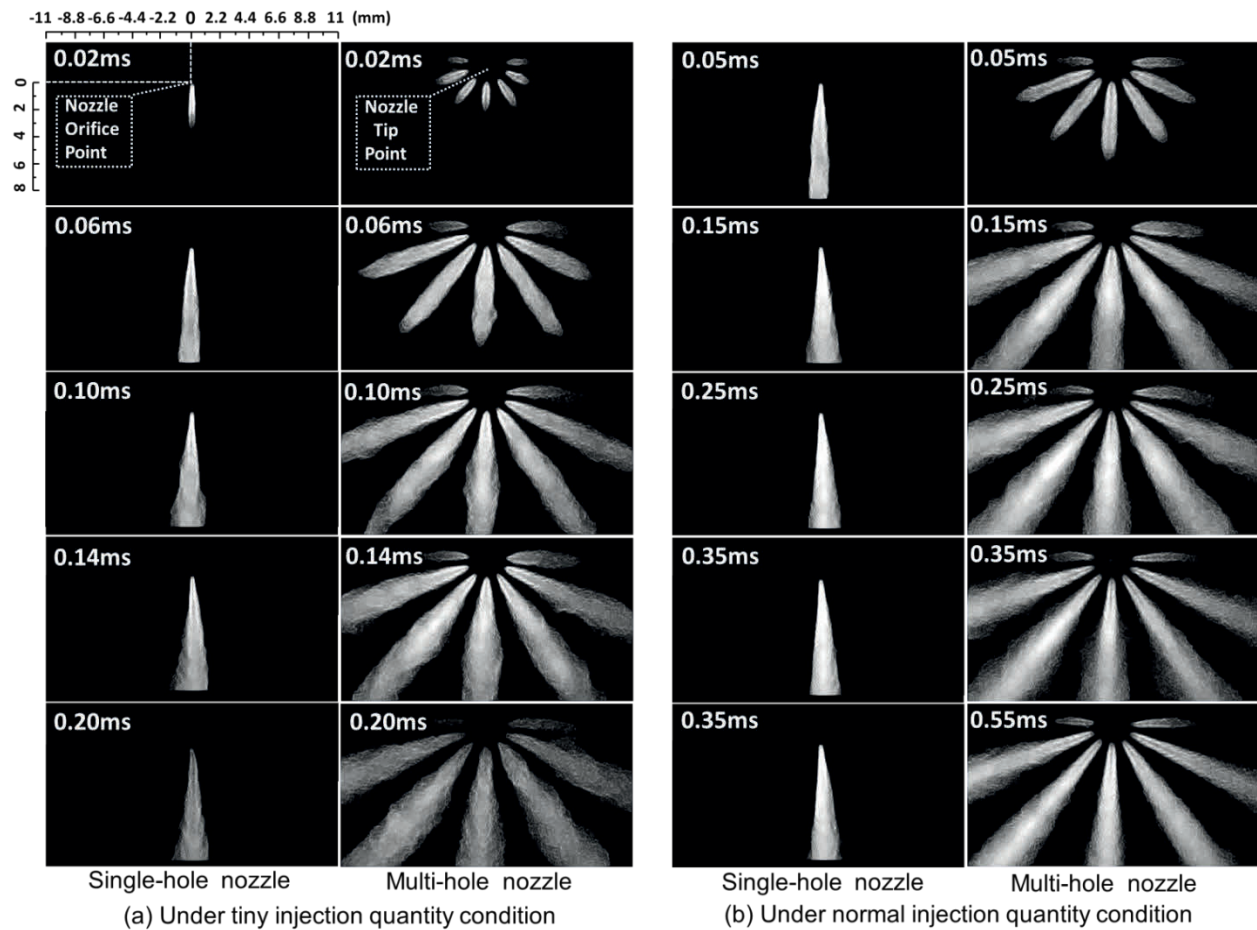


Figure 4.14 Spray behaviour near the nozzle orifices under different injection quantity conditions

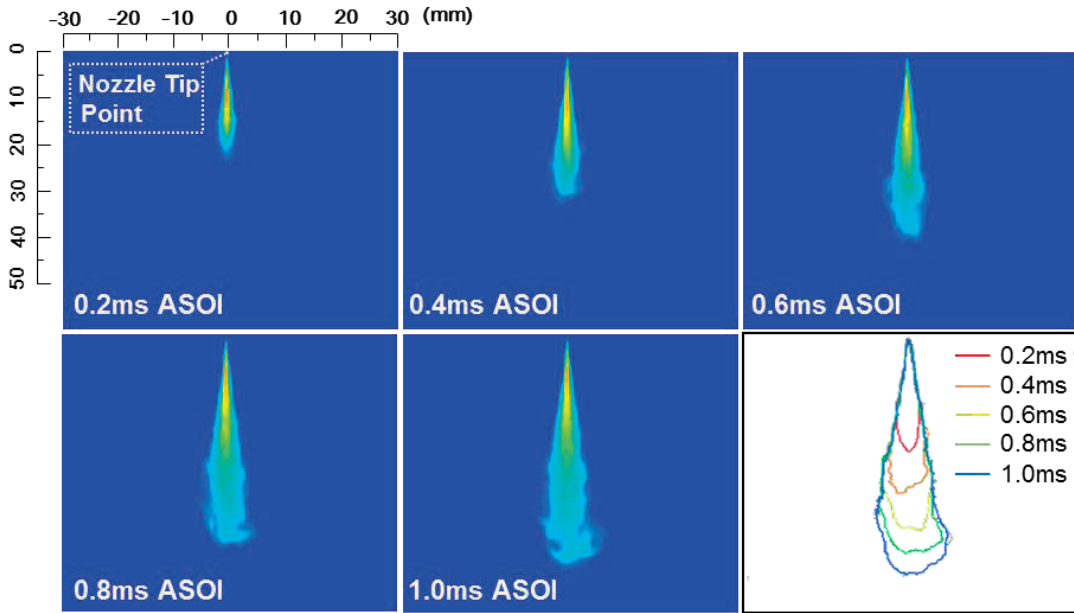
Focusing on the spray properties of the single-hole nozzle, different from the normal quantity condition, the spray under the tiny injection quantity condition has lower scattering light intensity and relatively rough edges. However, under the multi-hole nozzle condition, the spray has obvious irregular contours under both tiny and normal injection quantity conditions.

Considering the effect of different nozzle structure, according to the images of typical timings, the multi-hole nozzle sprays all pulsate out from the nozzle tip to the radial direction, and the layering of the spray intensity is more prominent, compared with the single-hole condition. Furthermore, the edges of the multi-hole nozzle sprays fluctuate seriously compared with those of the single-hole nozzle spray under both tiny and normal injection quantity conditions.

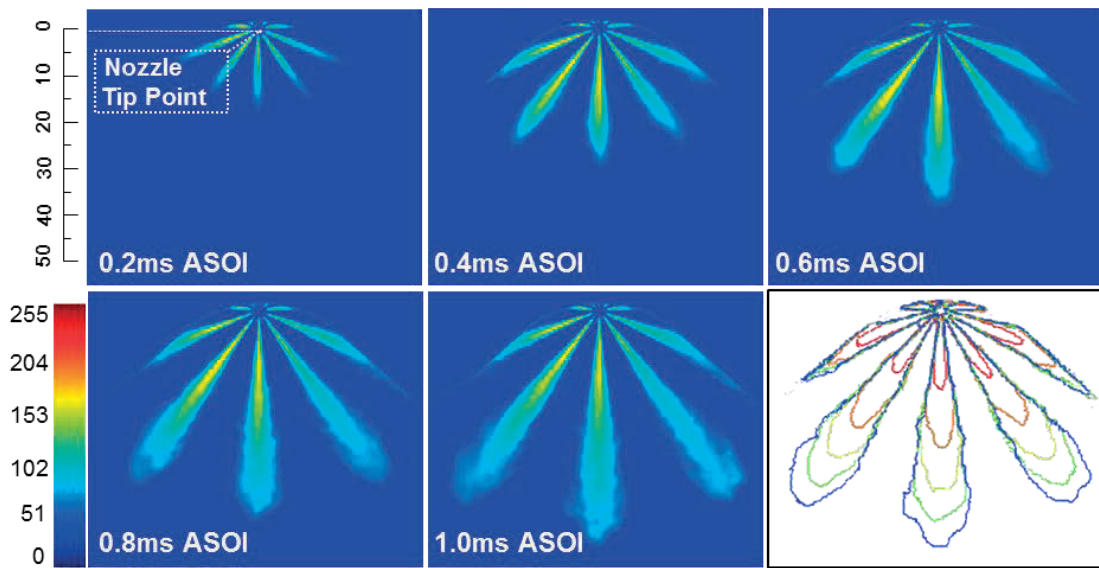
Effect of micro nozzle hole diameter

Figure 4.15 shows the typical false-colored and temporal spray images of single-hole and multi-hole injectors with micro orifices ($D=0.07$ mm). Globally, the spray intensity is much lower than that of nozzles with larger orifices, shown in Figure 4.8. Based on the theoretical foundation of Mie scattering, this verifies that the fuel concentration is lower, the droplet size is smaller, and the atomization effect is better under the micro hole condition [Matsumoto et al. 2007]. Furthermore, the edges of spray upstream regions are more orderly than those of nozzles with larger hole diameter, which indicates that the spray diffusion is more stable. In the case of micro orifice nozzles, the difference of the spray intensity and spray shape between single-hole and multi-hole nozzles is not so great as that under the larger hole diameter condition. It is safe to say that decreasing the hole diameter can supposedly reduce the effect of different nozzle configurations on the spray properties. The more specific investigation and discussion about this phenomenon will be introduced in upcoming sections.

The close-up spray images of the single-hole and multi-hole nozzles with micro orifices ($D=0.07$ mm) are shown in Figure 4.16 shows, respectively. Since the injection duration is longer under the smaller orifices condition when maintaining the same injection quantity, the selection for the typical timing of the images is a little different from that in Figure 4.9. With the same results under the imaging rate of 10000 fps, the spray illumination intensity is weaker than those in Figure 4.9. The profiles are more similar between the sprays emerging from the single-hole and multi-hole nozzles. It is impeded for the flow to entry into the narrower orifices from the sac, and the reduced flow transverse suppresses the vortex and cavitation level, which causes relatively steady spray morphology and the narrower spray width of the multi-hole nozzle.



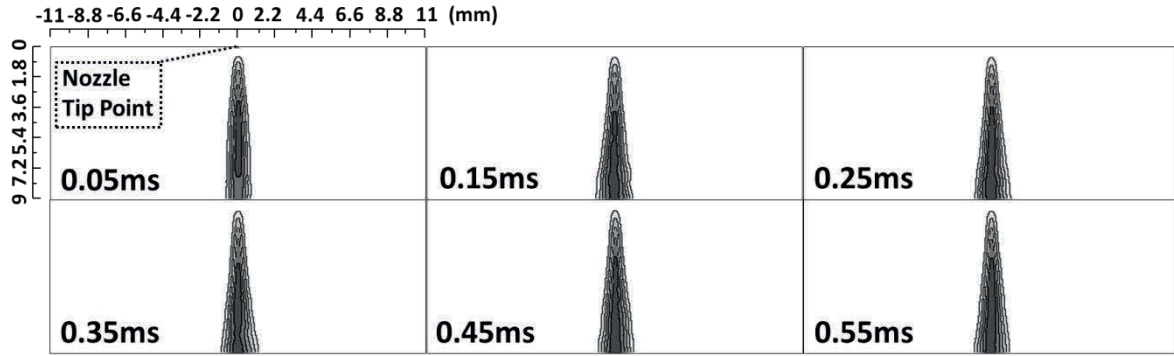
(a) Single-hole nozzle spray



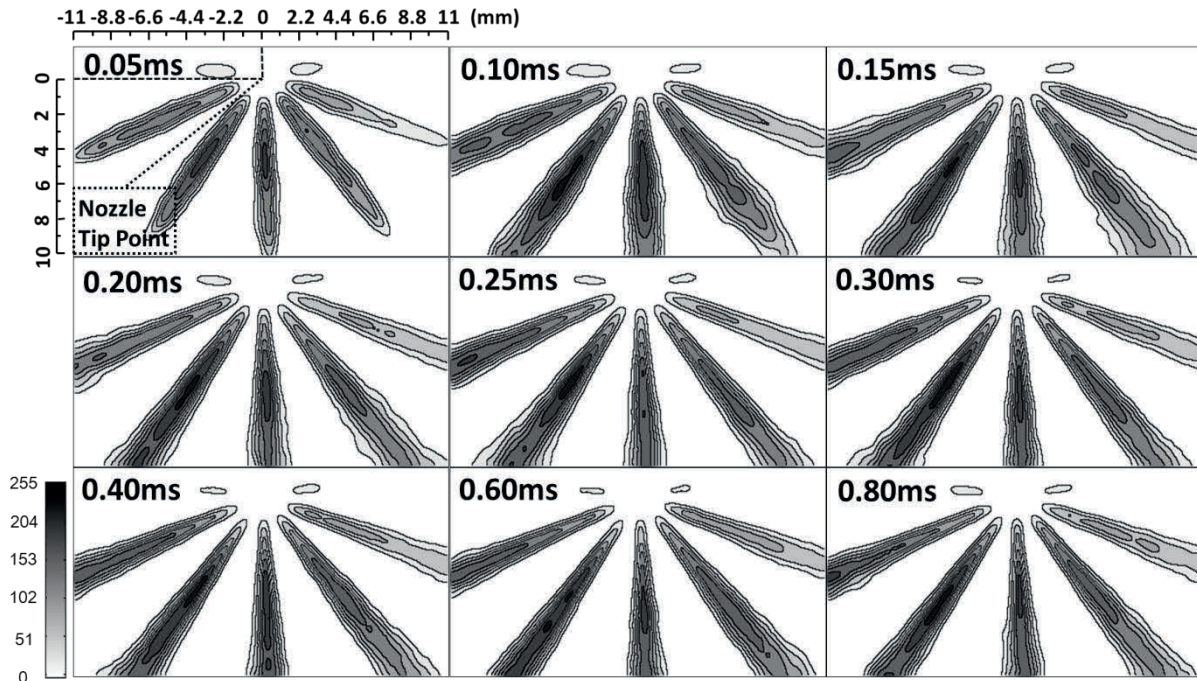
(b) Multi-hole nozzle spray

Figure 4.15 False-colored spray images of single-hole and multi-hole injectors.

$D=0.07$ mm, $P_{rail}=120$ MPa, $P_a=1.5$ MPa and $Q_{inj}=2\text{mm}^3/\text{hole}$.



(a) Single-hole nozzle spray



(b) Multi-hole nozzle spray

Figure 4.16 Close-up view of sprays injected from single-hole and multi-hole injectors.

$D=0.07$ mm, $P_{rail}=120$ MPa, $P_a=1.5$ MPa and $Q_{inj}=2$ mm³/hole.

4.2.3 Comparison of Time-resolved Spray Characteristics

Under the baseline condition ($P_{rail}=120$ MPa, $P_a=1.5$ MPa and $Q_{inj}=2$ mm³/hole)

Temporal variation in the spray behaviours (spray tip penetration, spray angle, and spray cone angle) are shown in Figure 4.17. There is an evident distinction between the spray tip penetrations of these two kinds of injectors. The single-hole nozzle spray penetrates further than that of the multi-hole nozzle, especially at the beginning of injection (0.1 ms ASOI). The deviation is as long as 13 mm.

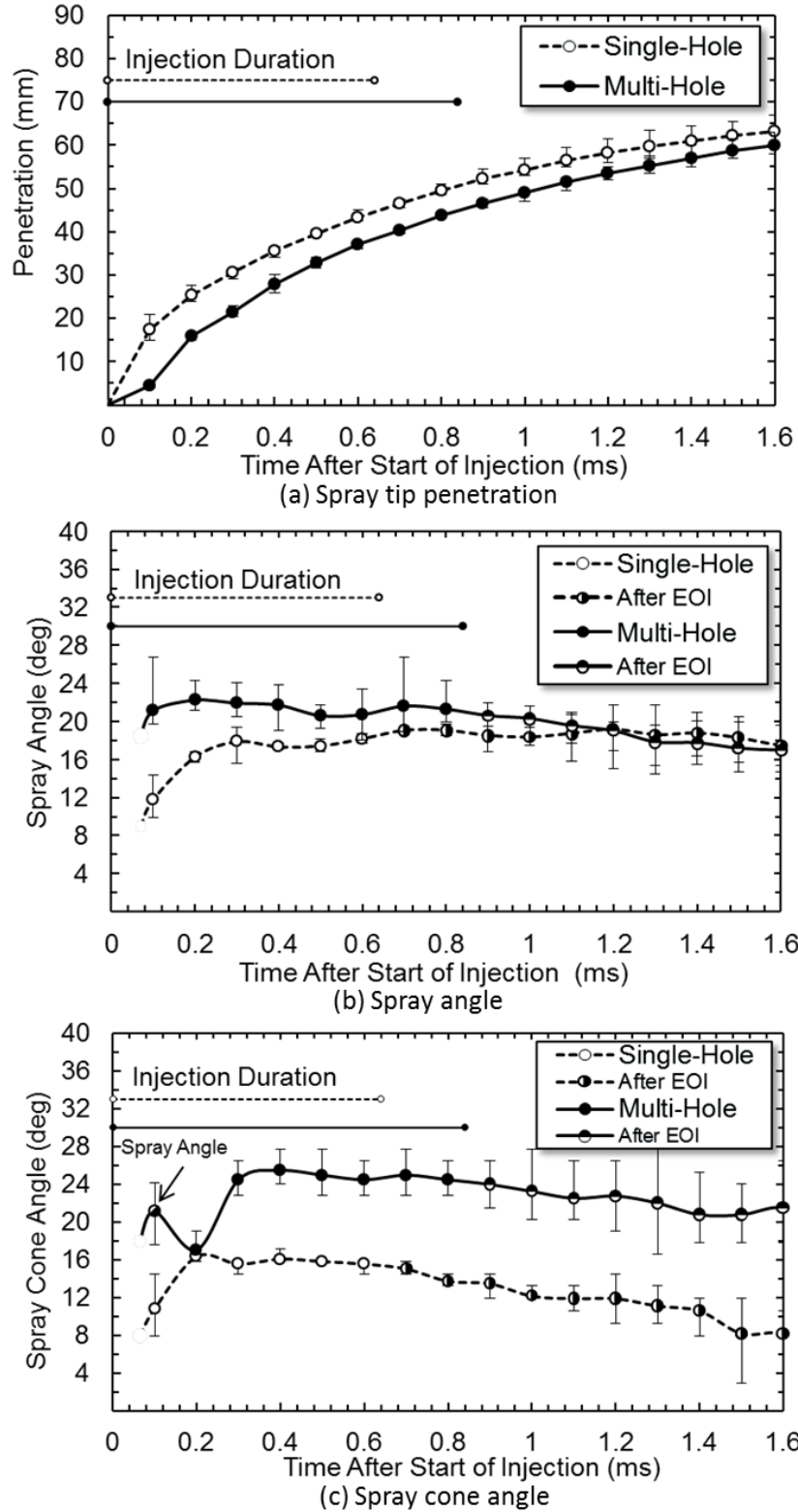


Figure 9. Spray behaviors of single-hole and multi-hole injectors. $P_{inj}=120$ MPa, $P_a=1.5$ MPa, and $Q_{inj}=2$ mm³/hole.

Figure 4.17 Spray parameters of single-hole and multi-hole injectors.

This can be explained by different injection rates and different sac pressures of the two nozzles. As time elapsed, the difference is reduced because the injection duration of the multi-hole nozzle is longer. The spray angle of the multi-hole nozzle is wider than that of the single-hole nozzle. The maximum deviation appears at 0.1 ms ASOI as well, up to 10°. For the spray angle of the multi-hole nozzle, there are fluctuations with a declining trend, the error range of which is larger too. This is mainly caused by the spray interaction and the Coanda effect as previously mentioned. The difference between the spray cone angles is more obvious. It should be noted that the penetration of the multi-hole nozzle is shorter than 100 times the hole diameter at 0.1 ms ASOI; hence, only the spray angle can be measured, as shown in Figure 4.17-(c). At 0.2 ms ASOI, the spray cone angle difference is negligible. However, after that, the multi-hole spray cone angle increases a great deal, which is mainly attributed to the different internal flow in different nozzles. This will be further discussed in the following sections using simulation results. From the error bar, it can be concluded that, (1) the error bar range of the multi-hole spray cone angle is larger than that of the single-hole one, and (2) for both of the nozzles, on the initial stage of injection and after the end of injection, the spray behaviours are unstable.

The comparison of the spray dispersion angle results from the close-up images are shown in Figure 4.18.

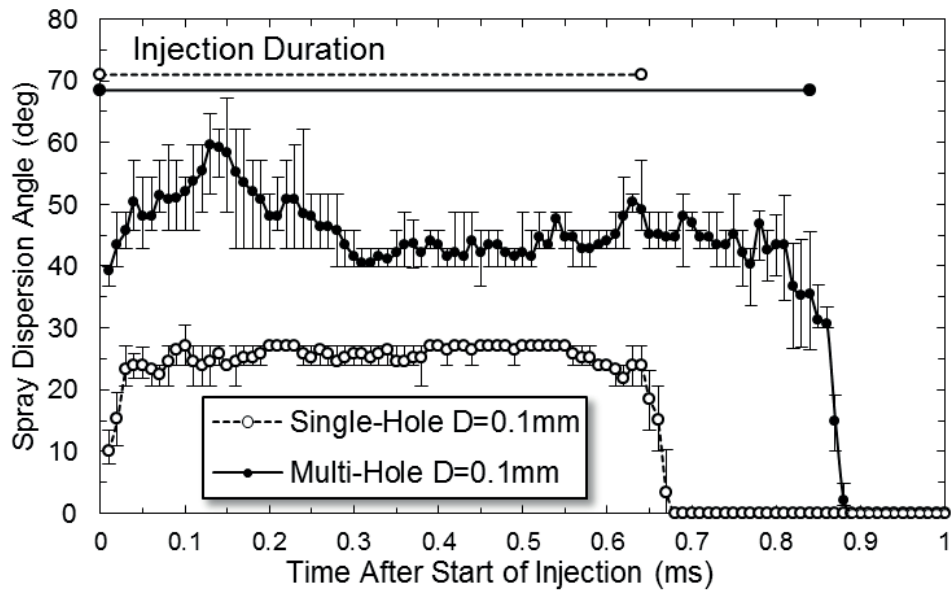


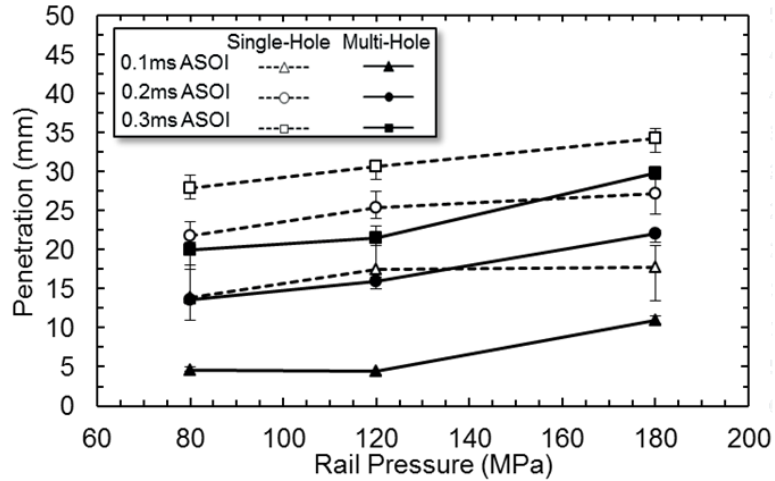
Figure 4.18 Close-up spray behaviors injected from single-hole and multi-hole injectors.

Here, this angle is determined by 10 times of the hole diameter away from the nozzle tip. Under the hole diameter of 0.10 mm, the spray dispersion angle of the multi-hole nozzle is much wider than that of the single-hole one. Caused by the pulsating phenomenon, the curve of the spray dispersion angle of the multi-hole nozzle has waves and fluctuations, especially in the initial stage of injection, when the needle lift is relatively low.

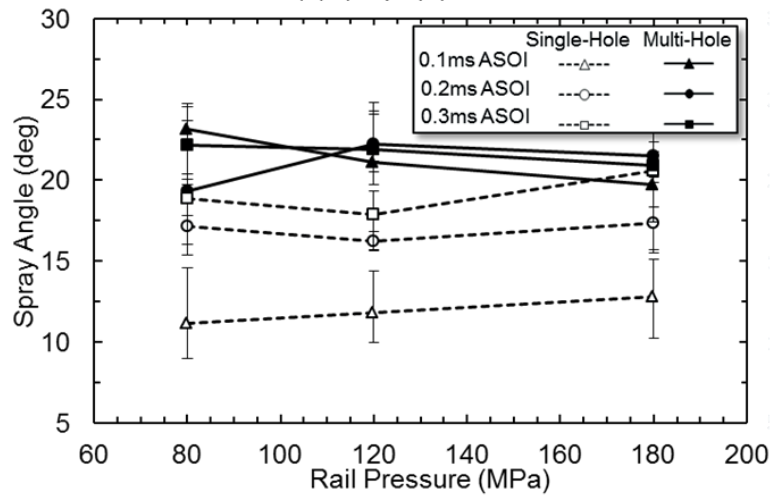
Under different rail-pressure conditions

Far-field spray behaviours in the initial stages (0.1, 0.2, and 0.3 ms ASOI) of injection under different rail pressure conditions are plotted in Figure 4.19. According to the legend, the special spray behaviors of the two nozzles at different injection timing under the three rail pressure conditions are clear at a glance. Globally, the sprays of the two injectors all penetrate further with increasing rail pressure, whereas the penetration of the single-hole nozzle is always longer than that of the multi-hole nozzle. At 0.1 ms ASOI, for these two nozzles, their susceptibility to the pressure variation is quite different. The single-hole penetration under the 80 MPa condition is much shorter than that under the 120 and 180 MPa rail pressure conditions. However, the multi-hole nozzle penetration under the 80 MPa condition is almost equal to that at the 120 MPa condition, and both are much shorter than that at the 180 MPa rail pressure condition. Additionally, the different sensitivity of the spray properties of different nozzles to the rail pressure variation is also prominent at 0.2 ms and 0.3 ms ASOI. All of the instances discussed above are contributed by the different effective flow area and the corresponding different sac pressures between the single-hole and multi-hole nozzles. Compared with the single-hole nozzle, higher pressure can exert more influence on the multi-hole nozzle sprays.

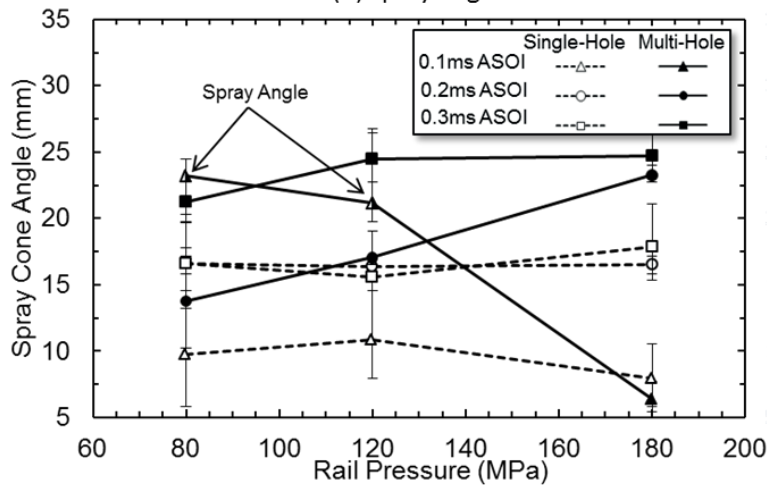
In the case of the spray angle under the three rail pressure conditions, the multi-hole nozzle spray angle is larger than that of the single-hole one, although the difference decreases as time elapses. The maximum difference value, reaching 12° , appears at 0.1 ms ASOI under the 80 MPa rail pressure condition. At this time, as the rail pressure increases, the spray angle of single-hole nozzle increases, but the multi-hole one decreases. At 0.2 ms ASOI, the single-hole spray angle does not change much with the pressure variation, while the multi-hole one increases a great deal under the higher-pressure condition. At 0.3 ms ASOI, a smaller value for the single-hole nozzle spray angle is attained under the 120 MPa condition.



(a) Spray tip penetration



(b) Spray angle



(c) Spray cone angle

Figure 4.19 Spray behaviors of single-hole and multi-hole injectors in the initial stage of injection duration. $P_{inj}=80,120,180\text{MPa}$, $P_a=1.5\text{MPa}$, and $Q_{inj}=2\text{mm}^3/\text{hole}$.

However, the multi-hole spray angle has a slight decreasing trend as pressure increases, because its sac pressure is more sensitive to the rail pressure variation and the increasing rate of its penetration is higher, which can affect the spray angle. If attention is paid to the temporal spray angle variation of one nozzle under one rail pressure condition (i.e., connecting the triangle, circle, and quadrilateral, which have the same feature marked, and referring to Figure 4.17), it is found that, as time elapses, the single-hole nozzle spray angle increases monotonously. However, the multi-hole one reaches a high level as soon as the injection starts, and then has small fluctuations during the entire initial injection duration. These findings verified that the spray angle of the multi-hole nozzle is affected by the injection pressure, internal flow, and the Coanda effect simultaneously [Gao et al, 2009; Nishida et al, 2009].

Before discussing the spray cone angle, it should be noted that the spray tip penetration of the multi-hole nozzle at 0.1 ms ASOI under conditions of 80 and 120 MPa rail pressures are less than 100 times the orifice diameter; hence, the corresponding spray angles are plotted in Figure 4.19-(c). Of particular interest is that with this timing the spray cone angle of the multi-hole nozzle under the 180 MPa condition is smaller than that of the single-hole nozzle. At 0.2 ms ASOI, the spray cone angle of the single-hole nozzle increases dramatically, but it does not change as much with pressure variation. For the multi-hole nozzle, this angle increases a great deal with increasing pressure, but it is smaller than that of the single-hole nozzle under the 80 MPa rail pressure condition. All of these interesting phenomena are supposedly attributed to the lower sac pressure of the multi-hole nozzle at the beginning of injection, when the complete internal flow has not been established. At 0.3 ms ASOI, the cone angle for the single-hole nozzle is nearly constant, but for the multi-hole one it increases farther. This illustrates that the degree of cavitation and turbulence that can affect the spray cone angle increases greatly inside the multi-hole nozzle with the needle lifting up [29].

Figure 4.20 shows the spray behaviours in the middle and post stages (0.4, 0.5, and 0.6 ms ASOI) of the injection under three rail pressure conditions. The spray tip penetration follows the same rules as that of the initial injection stage. The multi-hole nozzle spray penetration is more sensitive to the higher rail pressures.

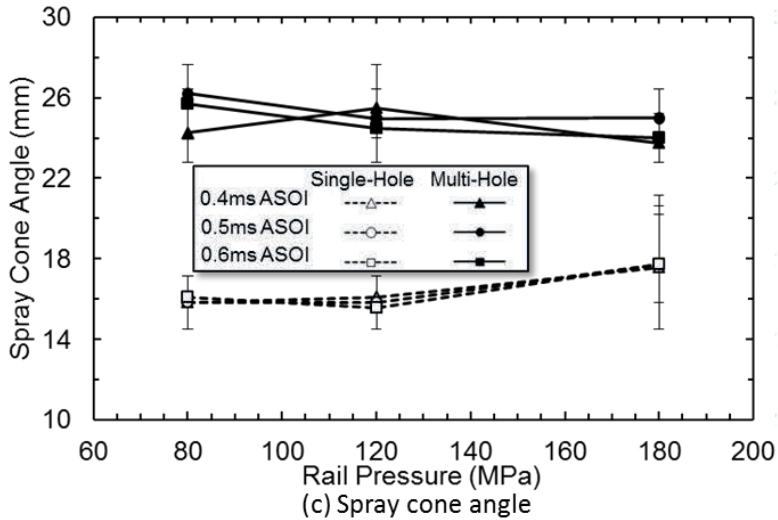
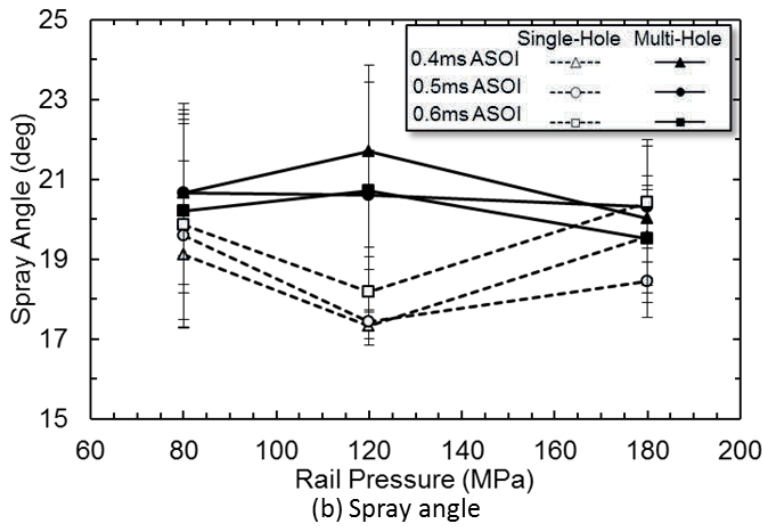
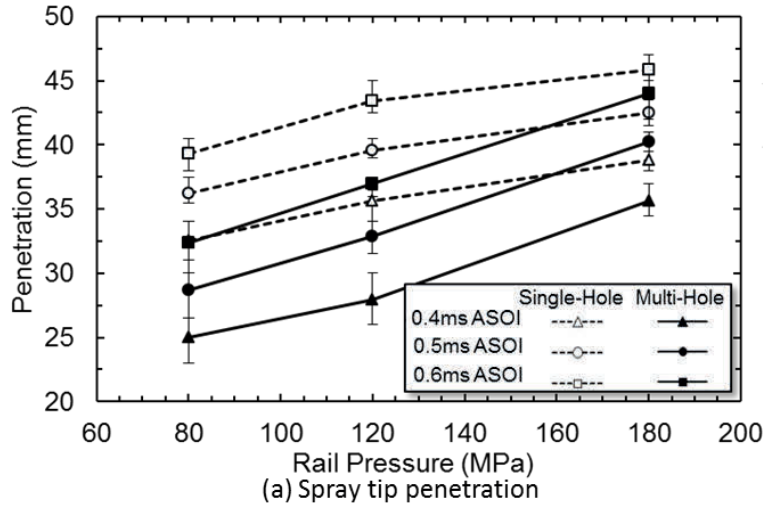


Figure 4.20 Spray behaviors of single-hole and multi-hole injectors in the middle and post stages of injection duration. $P_{inj}=80,120,180$ MPa, $P_a=1.5$ MPa, and $Q_{inj}=2$ mm³/hole.

As for the spray angle, overall, the multi-hole nozzle spray angle is wider. Nevertheless, the opposite effects of pressure variation are presented for these two nozzles at the three typical timings. The multi-hole spray angle reaches its peak under 120 MPa rail pressure condition. On the contrary, the single-hole spray angle reaches minimum. A reasonable explanation is that, in order to maintain the same injection quantity, along the same timeline, the corresponding injection stages of these two nozzles are entirely different under different rail pressure conditions. For example, the injection of multi-hole nozzle under 120 MPa condition at 0.5 ms ASOI experiences its middle stage, but this timing is the post injection stage for the single-hole nozzle. Awareness of this kind of discrepancy, caused by different injectors and rail pressures, is meaningful for setting the engine control strategies reasonably [Li et al, 2014].

The spray cone angle is dominated by the rail pressures and internal flow, synthetically [Lai et al, 2011]. As shown in Figure 4.20-(c), the spray cone angle of the multi-hole nozzle is much larger than that of the single-hole nozzle under the three rail pressure conditions. It is conceivable that the internal flow in the nozzle can develop sufficiently in the middle and post injection stages, and different internal flow patterns play significant roles in the variation of the spray cone angle. This will be discussed in depth in the next section.

The near field spray width variation, which is defined as spray dispersion angle, is shown in Figure 2.21 under single-hole and multi-hole conditions.

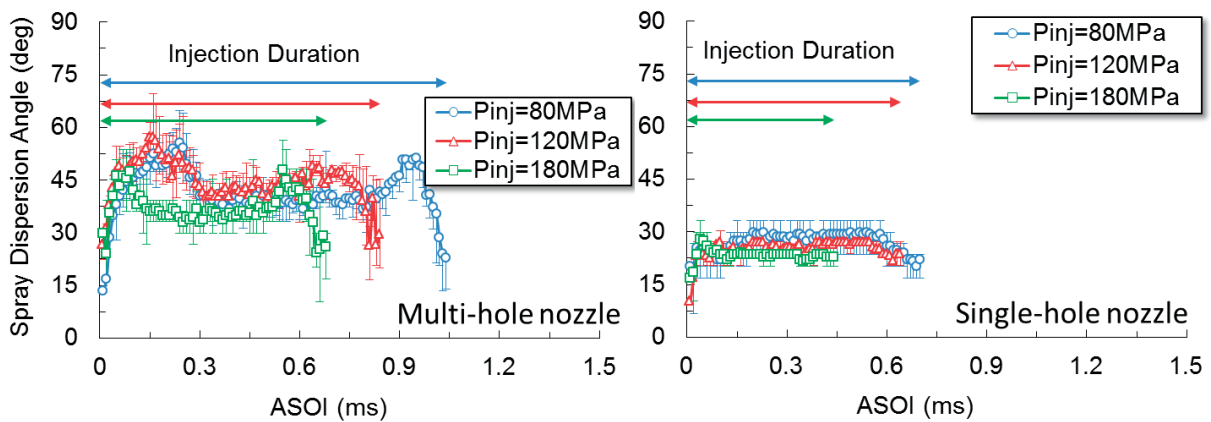


Figure 4.21 Near field spray width variation of different nozzles under different pressure conditions

Just as discussed in the spray images results, the multi-hole nozzle near-field spray width is more sensitive to the rail pressure variation. No matter the single-hole or the multi-hole, the near-field spray width can be decreased under the higher rail pressure conditions.

Under different injection quantity conditions

The sac pressure variation results of different nozzles, calculated from the injection rate curves qualitatively based on the Bernoulli's equation, are shown in Figure 4.22, and the corresponding spray tip penetration results measured from the high speed video images are also shown in this figure. The comparison of sac pressure and the effect of injection pressure have already been discussed. Because the spray tip penetration is affected directly by the sac pressure, the results shown here is for analyzing the spray tip penetration easily.

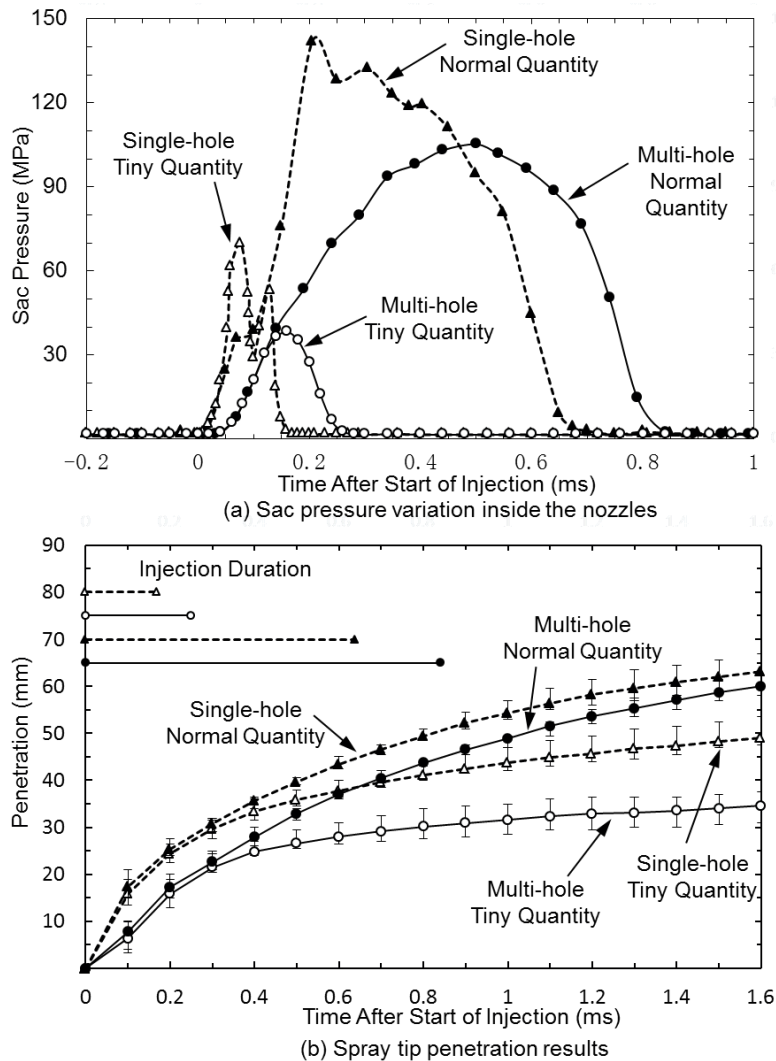


Figure 4.22 Sac pressure and spray tip penetration variation results under different injection quantity conditions

When it comes to the difference in the penetration results between different nozzles, the single-hole nozzle spray tip penetration is all longer than that of the multi-hole nozzle one under the two kinds of injection quantity conditions. Furthermore, the gap between the two nozzles is

larger under the tiny quantity condition, which is also in accordance with the analysis for the high speed video observation images. The tiny injection quantity condition can exert more effect on the deviation of the spray properties between the single-hole and multi-hole nozzles.

The temporal variation of the spray width was characterized as spray cone angle. It should be noted that the penetration of the multi-hole nozzle is still shorter than 100 times of hole diameter at 0.1 ms ASOI, hence only spray angle can be measured as shown in Figure 4.23.

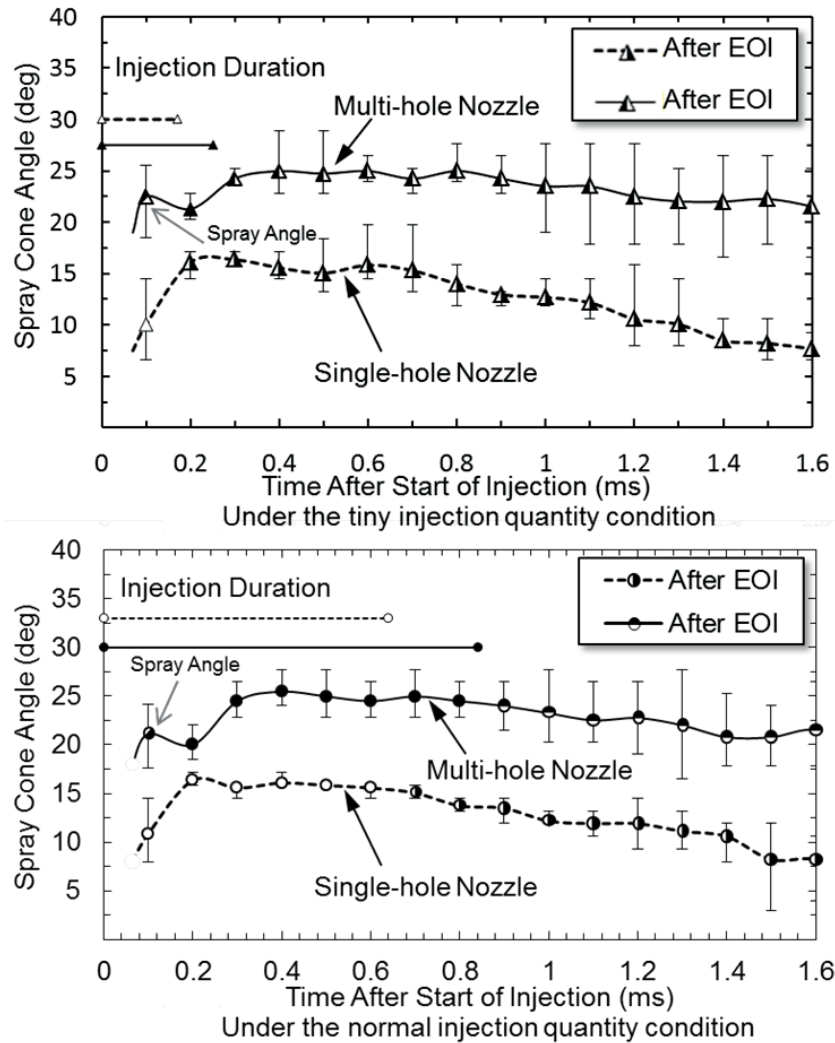


Figure 4.23 Spray width variation under different injection quantity conditions

Comparing the results in these two figures, for either single-hole or multi-hole nozzle, its spray width is not affected greatly by the injection quantity variation. However, it can be seen that there are all evident distinction in the spray cone angle results between single-hole and multi-hole nozzles under both tiny and normal injection quantity conditions. Except for the spray interaction

and the Coanda effect, it is the different internal flow characteristics inside the two nozzles that attributes to the deviation between the two kinds of spray properties [Desantes, J.M., 2010]. Moreover, under tiny and normal injection quantity conditions, the difference in the spray width between the single-hole and multi-hole nozzles does not change so much. The close-up view for the orifice near-field spray in the following paragraph can illustrate these phenomena deeply.

The spray dispersion angle measured from the close-up images of single-hole and multi-hole nozzles under large and tiny injection quantity conditions is shown in Figure 4.24, the same with spray cone angle results, for either single-hole or multi-hole nozzle, its spray width is not affected greatly by the injection quantity variation, even the deviation between the single-hole and multi-hole is still prominent.

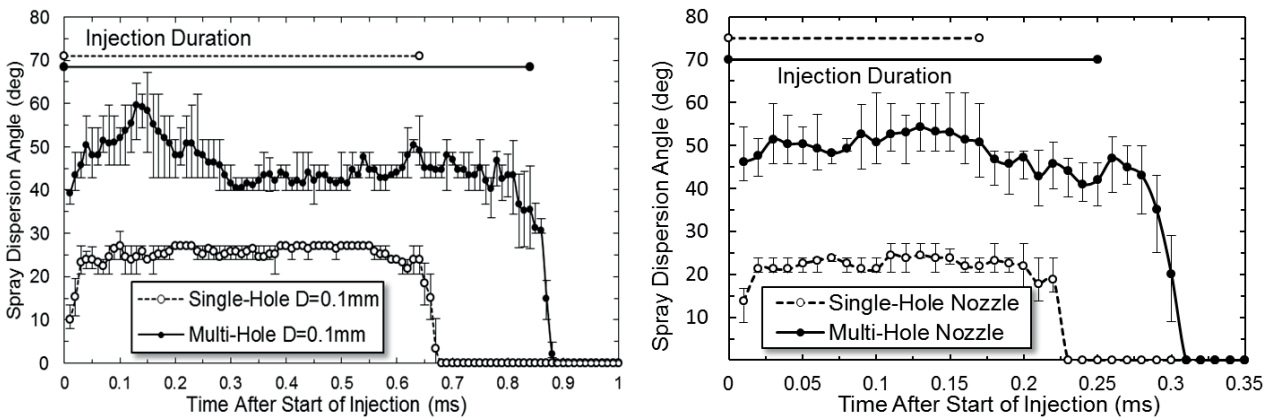


Figure 4.24 Spray dispersion angle measured from the close-up images

Effect of micro nozzle hole diameter

It is known that the spray deceleration and diffusion are associated with the transfer of the spray momentum to the turbulence energy [Moon et al., 2014]. Temporal variation of the spray behaviours (spray tip penetration, spray angle, and cone angle) are shown in Figure 4.25.

Under the condition of larger hole diameter ($D=0.10$ mm), there is an evident distinction between the spray tip penetrations of the single-hole and multi-hole nozzles. The single-hole nozzle spray penetrates further than that of the multi-hole nozzle, especially at the beginning of injection (0.1 ms ASOI). The deviation is as long as 13 mm. This can be explained by different injection rates and different sac pressures of the two nozzles. However, the deviation between the spray tip penetrations of the single-hole and multi-hole nozzles is quite small under the condition of the micro hole diameter ($D=0.07$ mm), although the single-hole nozzle still penetrates a little longer than the multi-hole one.

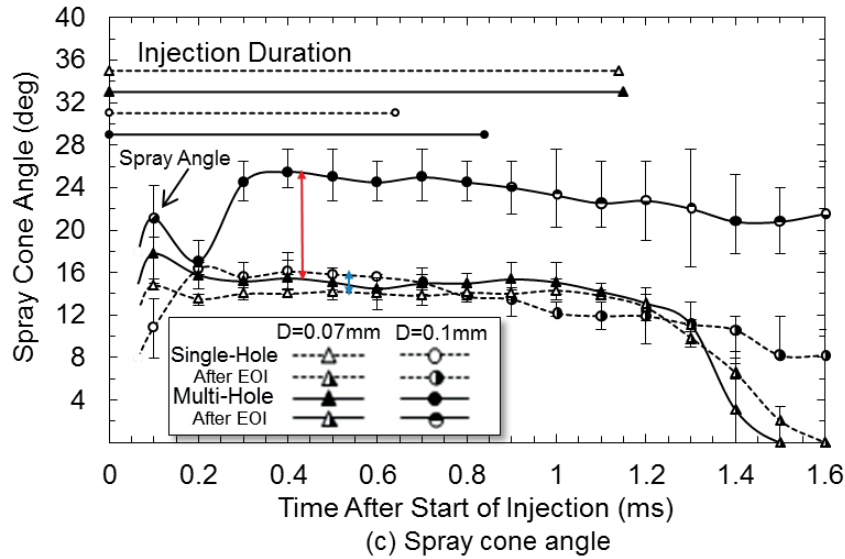
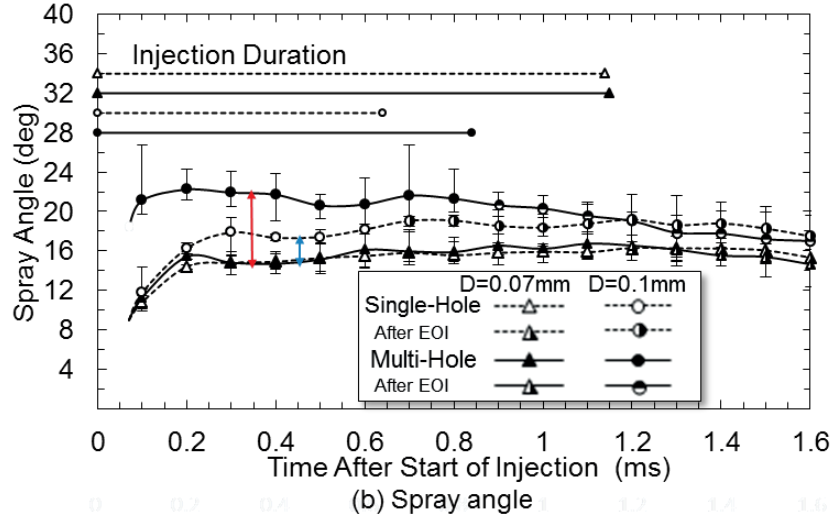
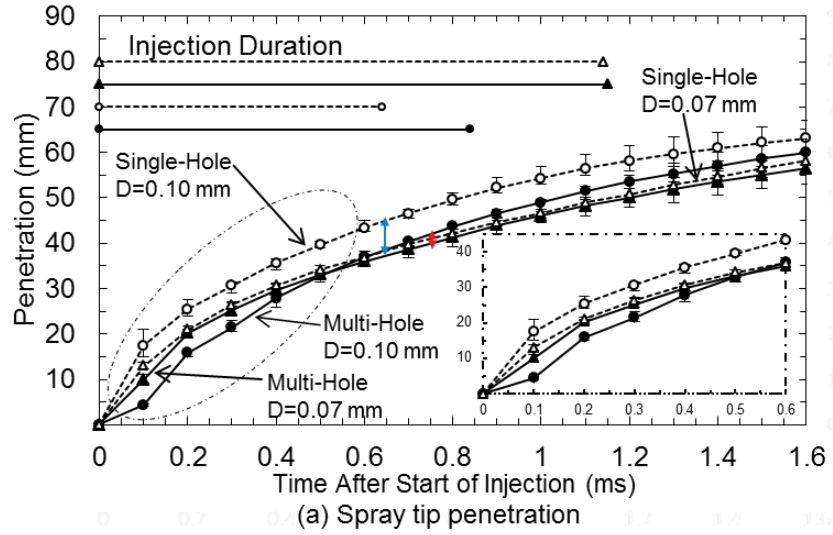


Figure 4.25 Spray behaviors of single-hole and multi-hole injectors.

$P_{rail}=120$ MPa, $P_a=1.5$ MPa and $Q_{inj}=2$ mm³/hole.

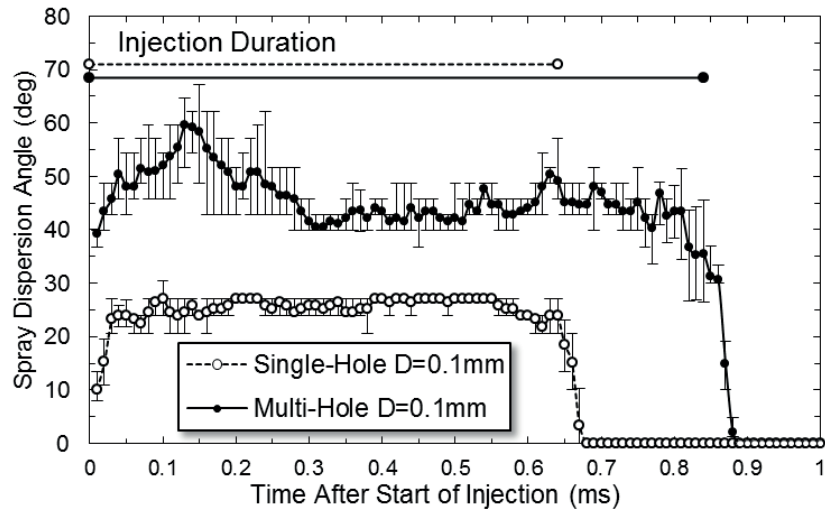
The penetration results are in accordance with the injection rate variations analysed previously, and different factors (sac pressure or effective flow area) dominate the spray tip penetrations of different kinds of nozzles in the initial stage of injection. Moreover, as the color arrows show, the reduction of the spray penetration of the single-hole nozzles caused by the decrease of the hole diameter is much larger than that of the multi-hole nozzles.

The spray angle of the multi-hole nozzle is wider than that of the single-hole one under the larger orifice condition. The maximum deviation appears at 0.1 ms ASOI as well, up to 10°. However, the spray angles of the nozzles with smaller holes are all much narrower than those of the nozzles with larger holes. Moreover, different from the penetration results, the reduction of the spray angle of the single-hole nozzles caused by the decrease of the hole diameter is much smaller than that of the multi-hole nozzles. Furthermore, the micro orifices can also reduce the difference of the spray angle between single-hole and multi-hole nozzles. Simulation results in the upcoming section can be used to explain this phenomenon in depth.

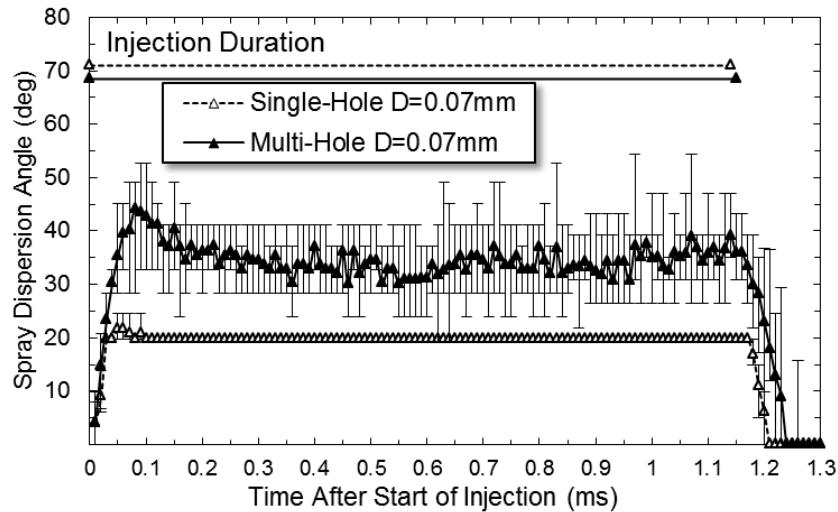
The difference between spray cone angles of the single-hole and multi-hole nozzles with larger orifices is also very obvious. It should be noted that the penetration of the multi-hole nozzle is shorter than 100 times the hole diameter at 0.1 ms ASOI; hence, only the spray angle can be measured, as shown in Figure 4.25-(c). At 0.2 ms ASOI the spray cone angle difference is small. However, after that, the multi-hole spray cone angle increases a great deal, which is mainly attributed to the more completed internal flow in multi-hole nozzles [Lai et al. 2011]. When it comes to the micro hole condition, the deviation of the spray cone angles between the single-hole and multi-hole nozzles is reduced greatly. Moreover, the same with the spray angle results, the reduction of the spray cone angle of the single-hole nozzles caused by the decrease of the hole diameter is much smaller than that of the multi-hole nozzles. The fuel jet enters into the chamber with the less cavitation level, reduced mass flow rate, momentum, and less turbulence due to the increased ratio of nozzle hole length to diameter, which result in the narrower spray cone angle, since the cavitation collapse and turbulence flow are two of the major mechanisms of the primary break-up [Baumgarten, 2006; Moon et al., 2014].

The comparison of the spray dispersion angle results from the close-up images are shown in Figure 4.26. Here, this angle is determined by 10 times of the hole diameter away from the nozzle tip. Under the hole diameter of 0.10 mm, the spray dispersion angle of the multi-hole nozzle is much wider than that of the single-hole one. When the hole diameter becomes 0.07 mm, the dispersion angles are all narrower than those of the larger hole diameter condition. The deviation between the

spray parameters of the single-hole and multi-hole nozzles is also reduced, and the spray behaviors become more stable relatively.



(a) Under hole diameter of 0.10 mm condition



(b) Under hole diameter of 0.07 mm condition

Figure 4.26 Close-up spray behaviors injected from single-hole and multi-hole injectors.

$$P_{\text{rail}}=120 \text{ MPa}, P_a=1.5 \text{ MPa and } Q_{\text{inj}}=2 \text{ mm}^3/\text{hole}.$$

The comparison of the single-shot and average spray dispersion angle results measured from the corresponding close-up images are shown in Figure 4.27. Under the hole diameter of 0.10 mm condition, the spray dispersion angle is much wider than that of the micro-hole one.

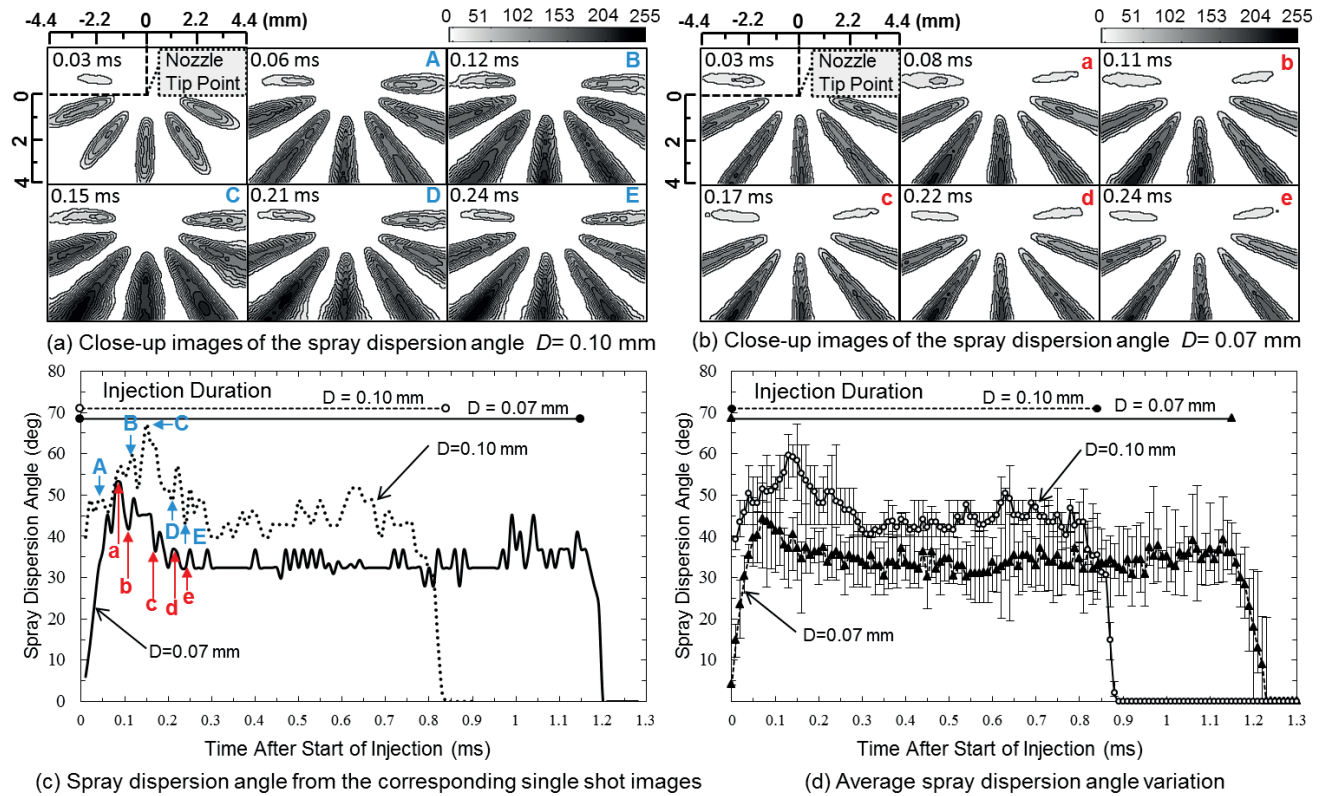


Figure 2.27 Close-up spray behaviors injected from different injectors The color arrows and capital letters are corresponding to the spray images at the typical timings during the initial stage of the injection duration $P_{rail}=120$ MPa, $P_a=1.5$ MPa and $Q_{inj}=2$ mm³/hole

Caused by the pulsating phenomenon, the curve of the spray dispersion angle has strong waves and fluctuations, especially in the initial stage of the injection duration (0.1-0.25 ms ASOI), as the color arrows and capital letters indicate in the figures. When the hole diameter is reduced to 0.07 mm, the spray dispersion angle becomes much narrower, and the fluctuation of the curve also decreases dramatically. It is impeded for the flow to entry into the narrower orifices from the sac, and the reduced flow transverse suppresses the vortex and cavitation level, which causes the relatively steady spray morphology and the narrower spray width of the micro-hole nozzle.

4.3 NON-EVAPORATING SPRAY EVOLUTION OF MULTI-HOLE NOZZLES

From the comparison between the single-hole and multi-hole nozzles, it is clear that the deviation is so large that it is really worthwhile to pay more attention to the multi-hole nozzles, which is closer to the realistic engine conditions. As a result, the injection processes and spray evolution of multi-hole nozzle will be discussed specially in this section. It is divided into two parts, where the first

one is concentrated on the different engine dynamic operation conditions (rail pressure and injection quantity), and the second part concentrates on the nozzle geometrical effect.

4.3.1 Under Different Engine Dynamic Operation Conditions

In fact, the effect of dynamic operation conditions (rail pressure and injection quantity) on multi-hole nozzle spray has already been discussed when conducting the comparison between the single-hole and multi-hole nozzles in last section. The injection rate, far-and near-field spray images, and the corresponding spray parameters under different rail pressure and injection quantity conditions have been shown there. The multi-hole nozzle is very sensitive to the variation of engine dynamic operation conditions, and a lot of comprehensive describe, explanation, and analysis are also conducted. Therefore, in this section, the nozzle geometrical effect on the spray characteristics of multi-hole nozzles will be paid more attention.

4.3.2 Relationship between Nozzle Geometrical Structure and Spray Characteristics

Nozzle hole diameter variation

In order to investigate the nozzle hole diameter variation effect on the injection process and spray properties of the multi-hole nozzles, three multi-hole nozzles with 0.07, 0.10, and 0.133 mm were selected, and they have the same geometry except for the hole diameter, as shown in Figure 4.28. The fuel was all injected at 120 MPa rail pressure, 1.5 MPa ambient pressure and 2 mm³ / hole. The injection rate, far-field spray images, and spray properties will be compared.

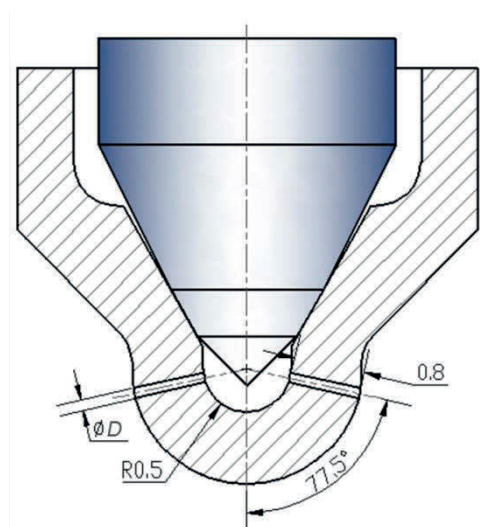


Figure 4.28 Nozzle tip configuration

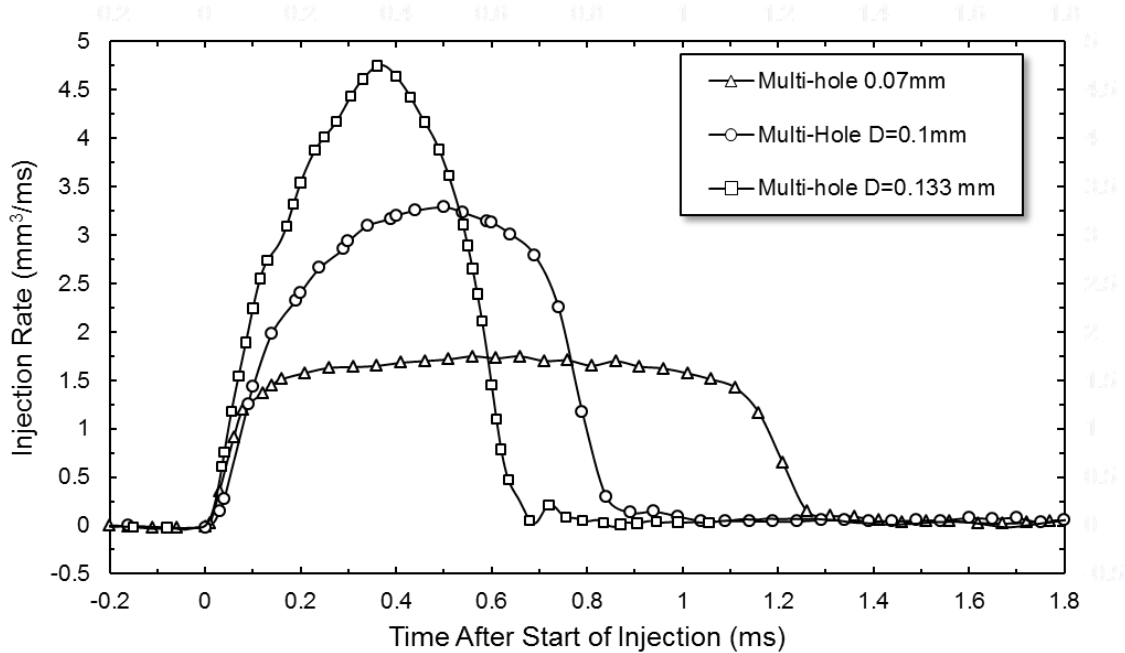


Figure 4.29 Injection rate of multi-hole nozzles with different nozzle hole diameter

The measured injection rate curves of the three different nozzles under the same conditions ($P_{\text{rail}}=120$ MPa, $P_a=1.5$ MPa, $Q_{\text{inj}}=2.0$ mm³/hole) are shown in Figure 4.29. There is apparent distinction between these three curves. Overall, the injection rate of the nozzle with 0.07 mm hole diameter is much lower than that of the nozzle with larger hole diameter. Consequently, the injection duration of the micro-hole nozzle is much longer when maintaining the same injection quantity per hole. It can be concluded that the hole diameter changes the regularity of the injection process conspicuously. Moreover, the attention should be paid to the initial stage of the injection duration, which is emphasized before. The injection rate of the nozzle with micro orifices is a little higher than that of the base one with 0.10 mm orifices in the initial stage of injection. However, under the 0.133 mm condition, the injection rate is the largest one all along the whole injection duration. As a result, all the phenomena described above reveal that the effect of micro holes plays entirely different roles in the injection rate at different injection stages. The injection rate is dominated by the hole diameter and sac pressure at the same time. Specifically, at the initial stage of injection, the relatively lower sac pressure discharge rate, the higher sac pressure and the consequent higher flow velocity inside the nozzle with micro holes mainly dominate the injection rate of this stage. However, the relatively larger effective flow area caused by the larger hole diameter, and the consequent higher mass flow rate inside the nozzle with 0.133 mm hole diameter mainly dominate the injection rate of the nozzle.

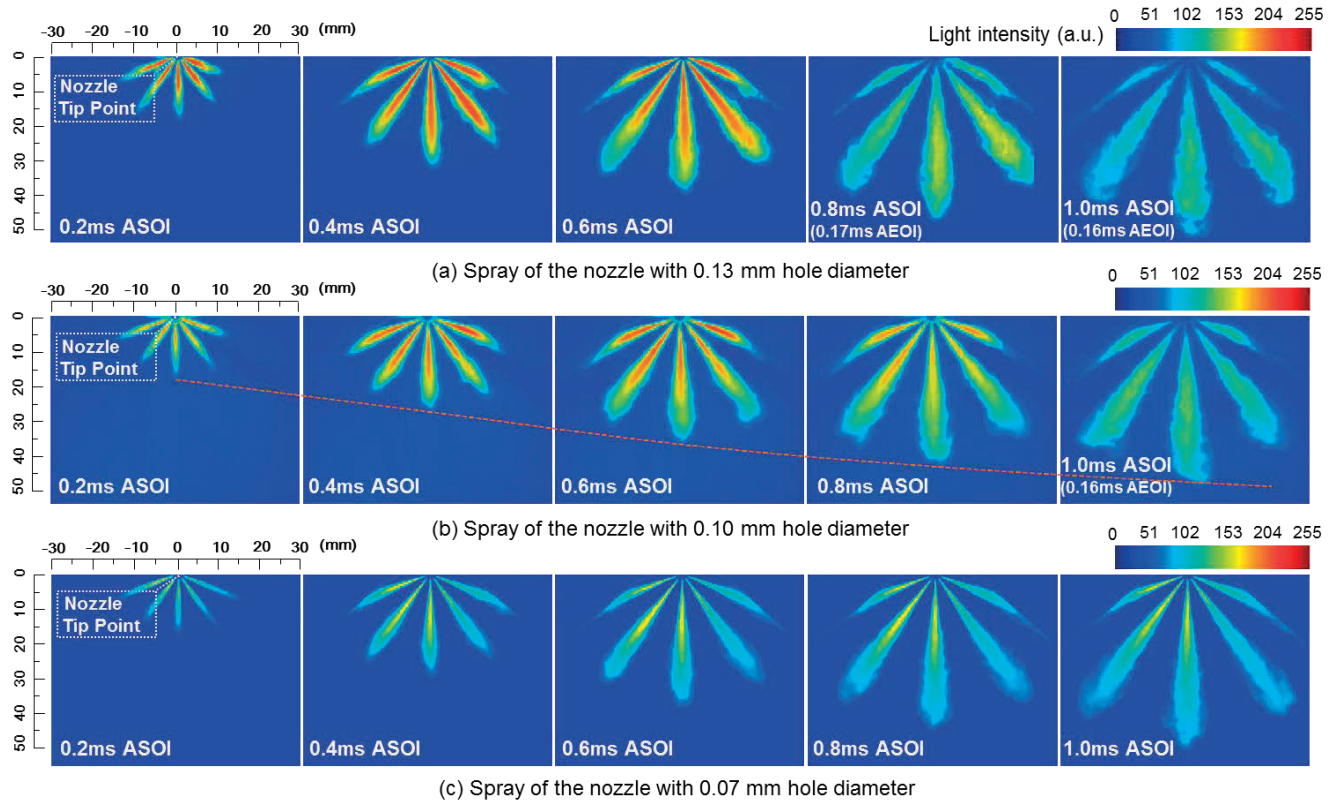


Figure 4.30 Spray images of multi-hole nozzles with different nozzle hole diameter

Typical false-coloured and temporal spray images of different nozzles are shown in Figure 4.30. Comparing the central sprays of the nozzles with different holes, which are shown in (a), (b), and (c), respectively, the global intensity of the spray emerging from the larger holes is much higher than that from the smaller ones, particularly in the beginning stage of injection. Furthermore, the high intensity even can extend to the downstream region of the larger-hole nozzle spray. All the distinctions described above can add additional evidence to verify that the fuel concentration is lower, the droplet size is smaller, and the atomization effect is better under the smaller hole diameter condition [Matsumoto et al., 2007]. This also indicates that, at the same timing ASOI, the fuel quantity injected from the larger-hole injector is larger than that from the smaller-hole injector, even the total injection mass per hole is held as constant. Second, as for the spray geometry and shape, the edges of the spray injected by the larger holes are irregular, and the spray plumes are flanked by evident wavelike contours. Therefore, it is safe to say that decreasing the hole diameter can supposedly reduce the uncontrollability and instability of the sprays emerging from multi-hole nozzles.

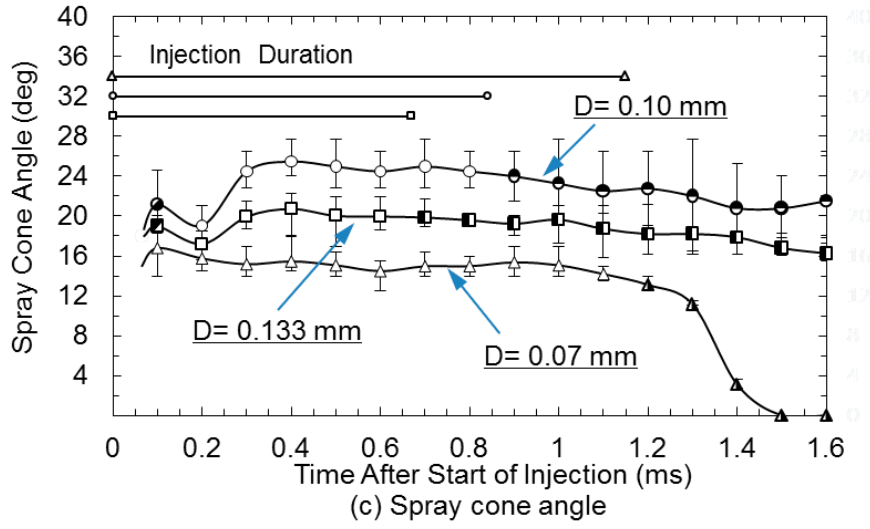
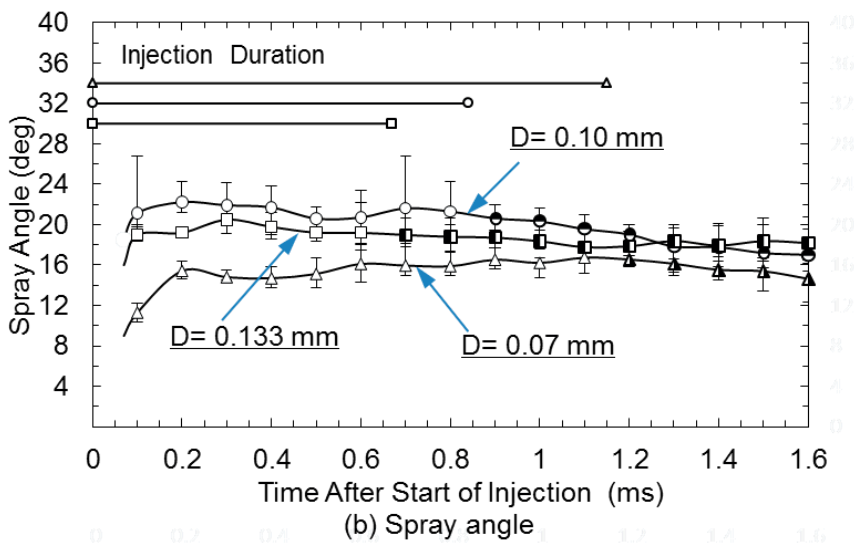
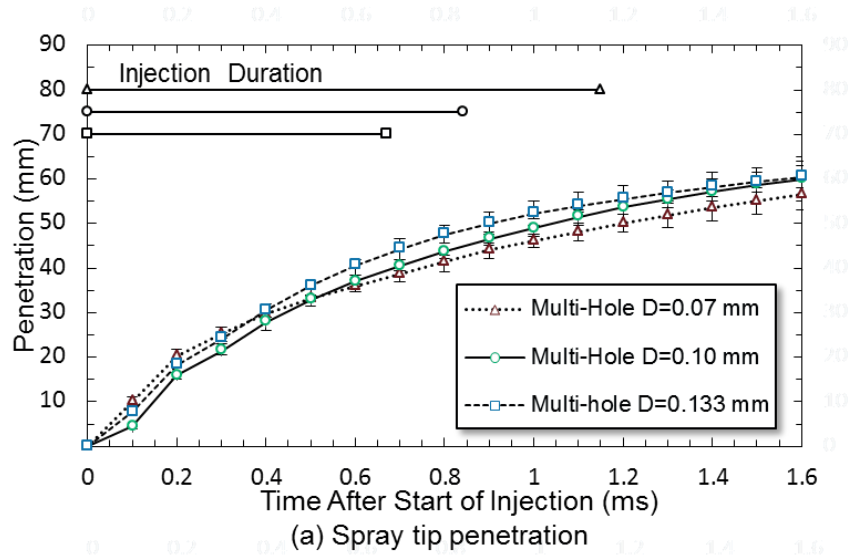


Figure 4.31 Spray parameters of multi-hole nozzles with different nozzle hole diameter

As for the corresponding spray tip penetration result, which is shown in Figure 4.31, it is in accordance with the injection rate variations analyzed previously. With the time elapses, the micro-hole nozzle spray tip penetration passes over the other two nozzle spray tip penetration, and it is the different factors (sac pressure or effective flow area) that dominate the spray tip penetration of different nozzles in different injection stages.

As is known to all, the injection strategy, including the injection timing, injection times and the injection quantity, is one of the basic adjustable factors in the calibration processes for the Diesel engine combustion system. Combing the results of injection rate and spray tip penetration, it is conceivable that the effects of the multi-hole diameter on the practical multi-hole nozzle injection processes and spray propagation should be given enough attention when optimizing the Diesel engine preference.

The spray deceleration and diffusion are associated with the transfer of the spray momentum to the turbulence energy. Temporal variation of the spray behaviours (spray angle, and cone angle) are also shown in Figure 4.31. It is obvious that the spray is the narrowest under the 0.07 mm orifice condition. However, the nozzle with 0.10 mm hole diameter has wider spray than the 0.133 mm one. Moreover, different from the penetration results, there is no overlap between the two spray angle curves of different nozzles. Furthermore, it seems that the micro orifices can exert more effect on the reduction of the spray angle than that on the spray tip penetration. The atomization effect and spray momentum can also affect the spray width very much. The simulation results in the upcoming chapter can be used to explain this phenomenon in depth.

The difference between the spray cone angles of the nozzles with different holes is also evident. At 0.2 ms ASOI the spray cone angle difference is small, because the 100 times hole diameter (10 mm) position is around the spray head area of the normal-hole nozzle spray, which can result in a small value of spray cone angle. However, after that, the spray penetrates long enough, and the normal-hole nozzle spray cone angle increases a great deal, which is mainly attributed to the more completed internal flow inside the nozzle [Baumgarten C., 2006]

According to the above discussion, because of the unique geometric structure of multi-hole nozzle, the injection rate, spray evolution, and spray parameters have special sensitivity to the nozzle hole diameter variation. Combing these phenomena with the interlaced relationship between the trends of the spray tip penetration and spray width of different nozzles, it is concluded that the effect of the hole diameter on different spray properties is discrepant.

Nozzle hole length variation

In order to investigate the nozzle hole length variation effect on the injection process and spray properties of the multi-hole nozzles, three multi-hole nozzles with 0.4, 0.6, and 0.8 mm hole length were selected, and they have the same geometry except for the hole length, as shown in Figure 4.32. The fuel was all injected at 120 MPa rail pressure, 1.5 MPa ambient pressure and 2 mm³/hole. The injection rate, far- and near-field spray images, and spray properties will be compared.

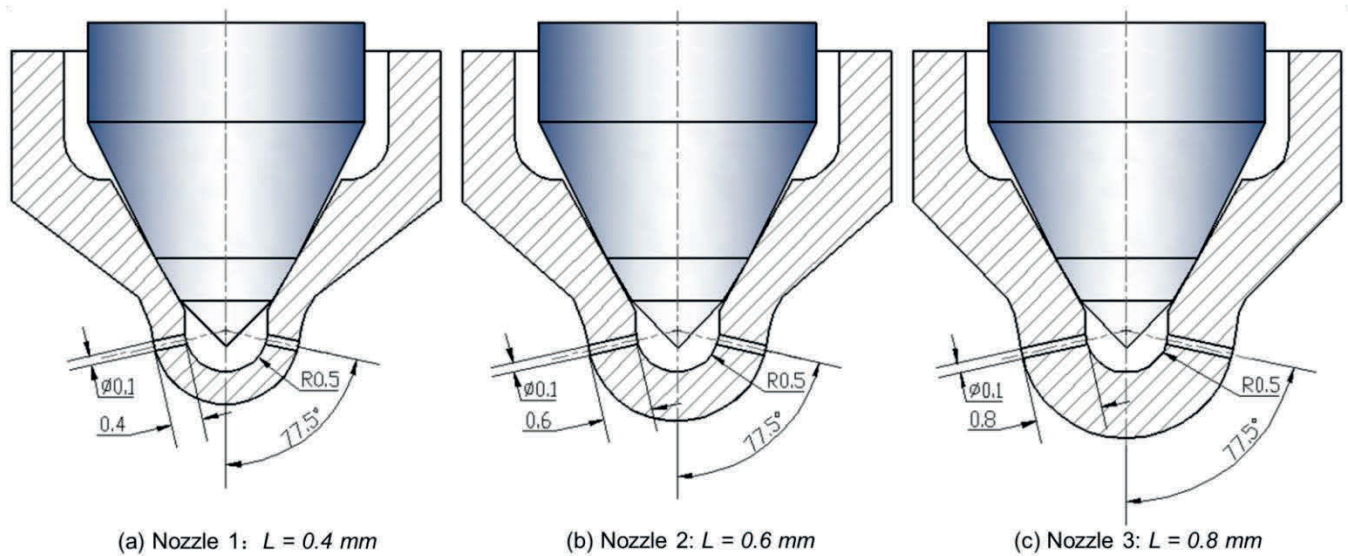


Figure 4.32 Configuration of the nozzles applied in the experiments

The measured injection rate curves are shown in Figure 4.33. Overall, with the decreasing of the nozzle hole length, the injection rate is decreased. During the main stages of the injection, the nozzle with 0.4 mm hole length has the lowest injection rate, while the nozzle with 0.8 mm hole length has the highest injection rate. Consequently, these three nozzles have different injection duration when maintaining the same injection quantity per hole. With the decreasing of the nozzle hole length, the injection duration is prolonged. When it comes to the post stages of the injection, caused by the shortest injection duration, the nozzle with 0.8 mm hole length finishes the injection first, and it presents low injection rate. However, because the nozzle with 0.4 mm hole length has the longest injection duration, it is the last one to finish the fuel injection. This is the reason why it presents high value of injection rate during this duration.

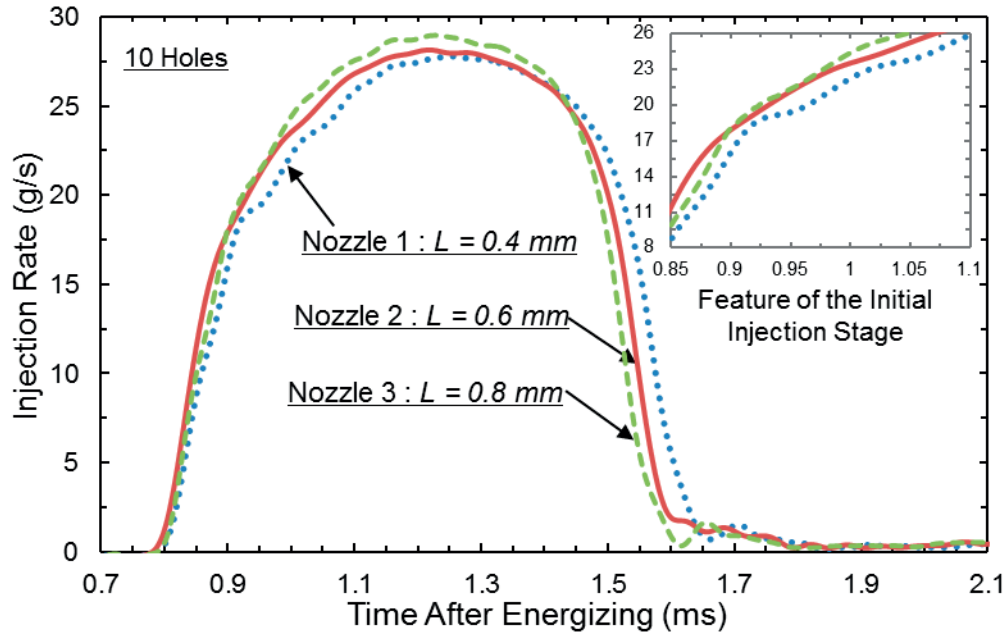


Figure 4.33 Injection rate results

However, according to the close-up view of the initial stage of the injection processes in the upper right corner of the figure, the nozzle with 0.6 mm hole length has the highest injection rate at the beginning, and then it is overtaken by that of the nozzle with 0.8 mm hole length. In fact, under the cavitated two-phase flow condition, it is known that the injection rate can be expressed simply as the following equation, considering that all the fluid is in liquid phase and flows out through an effective area with an effective injection velocity, \bar{V} .

$$Q_f = \rho_f * C_a * A * \bar{V} \quad (4.3)$$

Q_f means the injection rate, and ρ_f is the fuel density. A represents the theoretical flow area, whilst the effective flow area coefficient, C_a , incorporates the loss of flow section. It can be deduced that the injection rate is dominated by C_a and \bar{V} , simultaneously [Payri, R. et al, 2005]. Furthermore, the effective flow area coefficient mainly depends on the cavitation level on the hole exit, and the local average effective injection velocity has relationship with the hole length, which can alter the pressure drop, friction loss, and momentum loss of the fuel flow inside the hole. It is conceivable that the effective flow area should be decreased with the reduction of the hole length due to the void fraction on the hole exit, while the injection velocity should be increased inside the nozzle with shorter hole length because of the higher pressure drop, and less friction and momentum loss of the fuel flow inside the hole.

The injection rate of different nozzles is dominated by diverse factors at each injection stage. To be specific, compared with the other two nozzles, the injection rate of Nozzle 1 is dominated by the lower effective flow area during the whole injection duration. On the contrary, the reason why there is interlaced relationship of the injection rate between the Nozzle 2 and Nozzle 3 is that, compared with Nozzle 3 the higher injection velocity and lower effective flow area dominate the initial and middle stages of the injection of the Nozzle 2, respectively. This kind of analysis will be validated further using the internal flow computational results in the second part of this section.

Typical false-coloured and temporal far-field spray images of the three nozzles, which are converted from the raw black-and-white images, are shown in Figure 4.34. The original spray images can be used to measure the temporal spray properties variation, which will be presented in the next figure, while it is easier to observe the spray lineament in the false-coloured spray images.

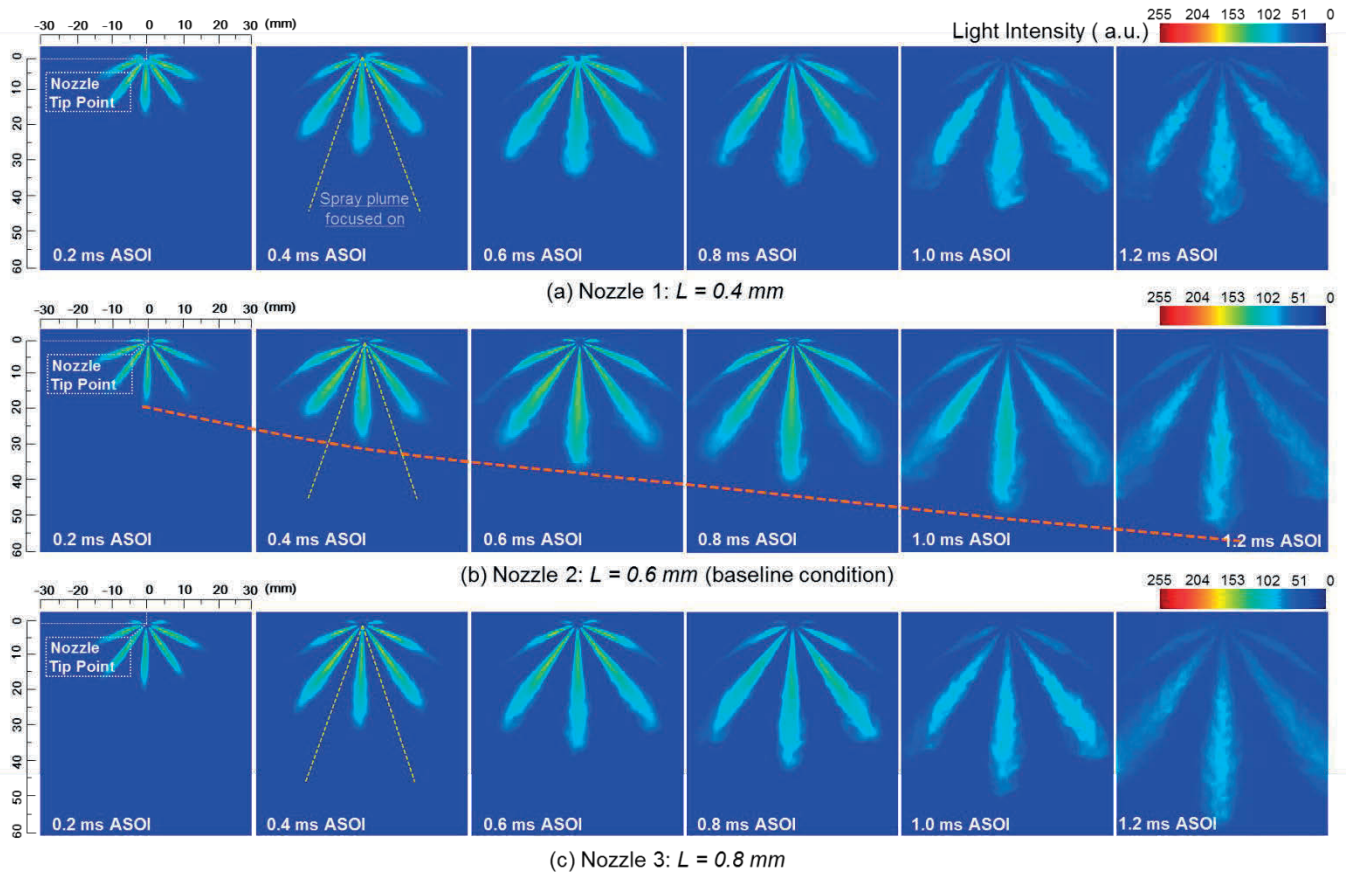


Figure 4.34 Far-field spray images

Paying attention to the geometry and shape of the central spray of different nozzles, with the decreasing of the nozzle hole length the spray becomes fatter and more buxom with wider spray tail, while the spray propagation distance is suppressed in somehow. The gradient of the spray scattering light intensity is also more prominent. Meanwhile, the edges of the central spray become more asymmetric and irregular, and the spray plumes are flanked by evident wavelike contours. Moreover, if taking the Nozzle 2 ($L = 0.6$ mm) as the baseline condition, the differences of the spray characteristics between the Nozzle 1 and Nozzle 2 are more evident than those between the Nozzles 3 and Nozzle2, which implies that the far-field spray characteristics are more sensitive to the nozzle hole length variation under the thinner sac wall thickness conditions. Except for the influence of the spray to spray interaction, it seems that all the unique spray morphology phenomena described above are contributed by the different internal flow characteristics consisting of intense turbulence and cavitation inside different nozzles. A deeper discussion will be conducted by combining the simulation result in the following sections.

The spray parameters can be used to illustrate the effect of the nozzle hole length from another view. In Figure 4.35, temporal variation of the spray behaviours is characterized in terms of the spray tip penetration, spray angle, and spray cone angle as a function of time after start of injection and different nozzles. The raw spray images were processed to calculate their properties by subtracting the background, rectification for the spray direction, images binarization, and detecting the spray edges and so on [Dong et al, 2016].

There are evident distinctions in the spray tip penetration results among these three nozzles. Compared with the baseline condition (Nozzle 2 : $L = 0.6$ mm), the Nozzle 1 has the shortest spray tip penetration, while the spray emerging from the Nozzle 3 can penetrate to the longest distance. However, the deviation between the Nozzle 1 and Nozzle 2 is more obvious than that between the Nozzle 3 and Nozzle 2. It also should be noticed that, as the close up view of the initial injection stage shows, there is interlaced relationship in the penetration result between Nozzle 2 and Nozzle 3, which is similar with that in the result of injection rate. The penetration of the Nozzle 3 is shorter at 0.1ms ASOI, while it goes over that of the Nozzle 2, and becomes a little longer during the middle and post stages of the injection. Afterward, caused by the longer injection duration, the penetration of the Nozzle 2 catches up that of the Nozzles 3 gradually after the end of injection.

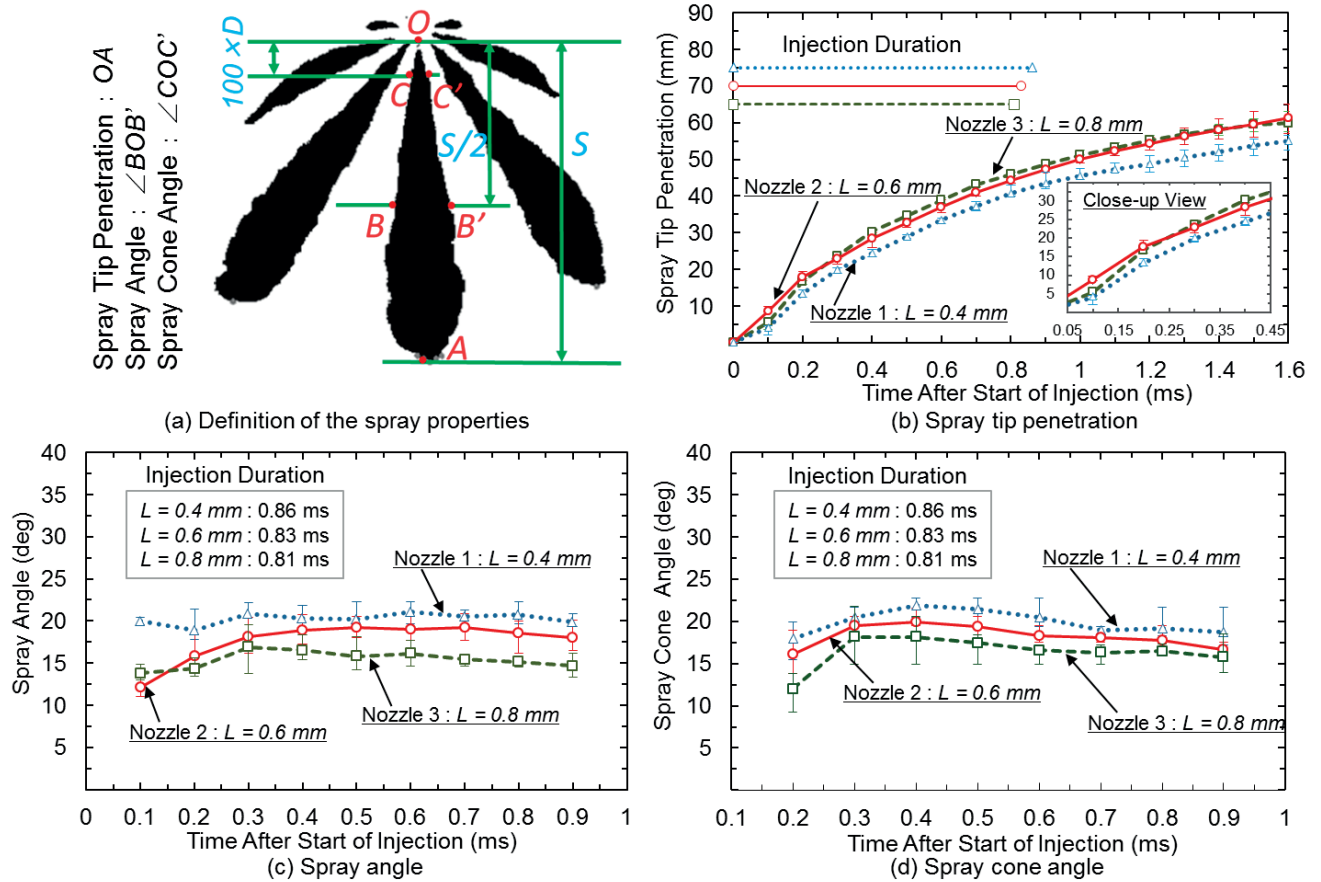


Figure 4.35 Macroscopic spray properties measured from the far-field spray images

The spray tip penetration can be affected greatly by the initial jet momentum flux [Payri et al., 2005], which is expressed in the following equation:

$$M_o = \rho_f * C_a * A * \bar{V}^2 \quad (4.4)$$

where M_o is the initial jet flow momentum flux on the orifice exit. As analyzed before, the effective flow area and the average injection velocity (value and direction) can dominate the injection processes of different nozzles at each of injection stages, simultaneously. Consequently, the initial spray momentum flux is dominated by them as well. The analysis above can be used to explain the deviation of the spray tip penetration of different nozzles presented in this figure.

When it comes to the spray angle and spray cone angle results, it should be emphasized that the spray tip penetration of the nozzles is still shorter than 100 times hole diameter at 0.1 ms ASOI, hence the spray cone angle result is plotted from 0.2 ms ASOI. Overall, with the decreasing of the nozzle hole length, the spray angle and spray cone angle all become larger, but the spray angle result also presents a interlaced relationship between the Nozzle2 and Nozzle 3 at the beginning of

the injection, which is attributed to the trade-off relationship between the spray tip penetration and the spray angle. The mechanism behind the wider spray width will be well explained by the internal flow simulation results in the following section.

In order to investigate the spray behaviors near the nozzle tip region in detail, high speed imaging of 100000 fps was applied to take a close-up view for this regime. Figure 4.36 shows the microscopic view of the near-field spray images of the nozzles with different hole length. The images are converted from the Mie scattering images in order to observe the near-field spray profile clearly.

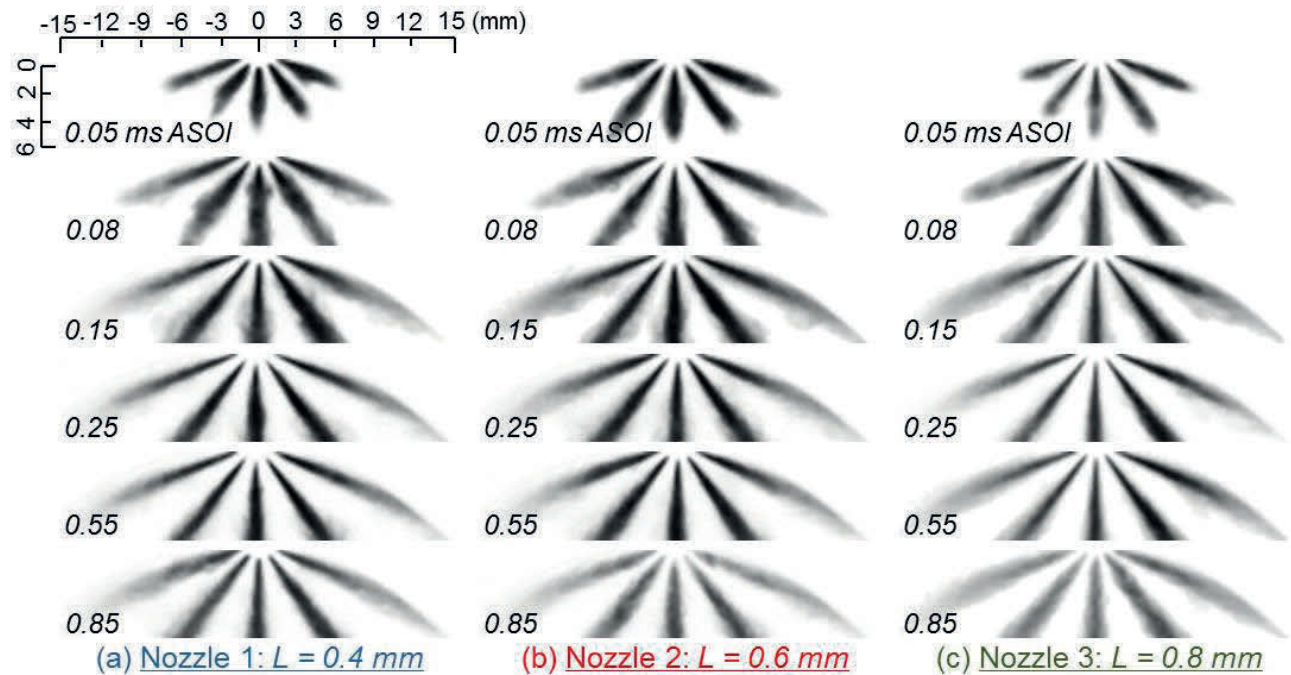


Figure 4.36 Microscopic spray images

According to the images of typical timings, sprays all pulsate out from the nozzle tip to the radial direction, and the edges of them fluctuate seriously, particularly at the initial stage of the injection (0.05-0.25 ms ASOI). The integrated speculations and reasonable explanations for this phenomenon can be excavated out by linking the previous results [Dong et al., 2015] and the current study. It is known that there is large vortex flow inside the sac of multi-hole nozzles due to the off-axis arrangement of the orifices, especially under the low needle lift condition [Dong et al., 2016]. The location of the unstable vortex cores vary with the needle moving, which results in that the unstable spiraling fuel flow patterns emerge out through the orifice with intense vortices and pulsated perturbations.

Among the central sprays of the three nozzles, compared with the baseline condition (Nozzle 2), the Nozzle 1 has the largest spray width, the most fluctuated spray profile, and the most obvious perturbations. There is also some cloudy drop shadow between the spray plumes in the image background. However, the spray of the Nozzle 3 is the thinnest one. It has much more stable and neater edges, and the background between the spray plumes is very clean and clear. According to the comparison analyzed above, it seems that the quality of the spray atomization effect can be improved by decreasing the nozzle hole length.

The comparison of the spray dispersion angle results measured from the close-up images are shown in Figure 4.37. Here, this angle is determined by 20 times of the hole diameter away from the nozzle tip. Caused by the pulsating phenomenon, there are all waves and fluctuations in these three curves, and the peak value appears around the initial stage of the injection. Furthermore, with the decreasing of the nozzle hole length, the near-field spray dispersion angle is increased, which is supposedly mainly attributed to the internal flow characteristics inside different nozzles.

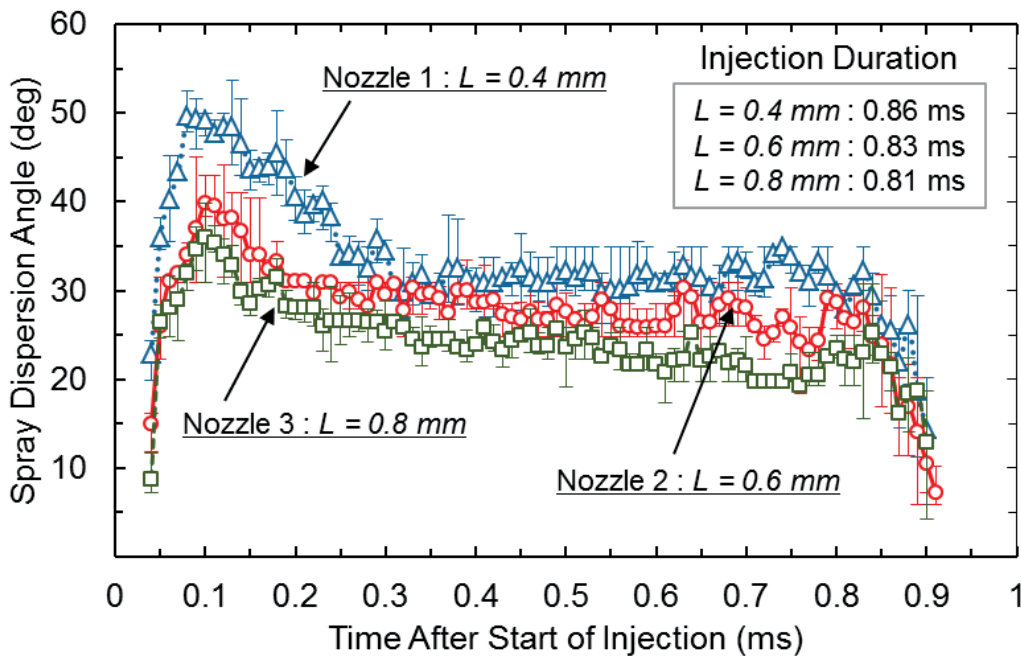


Figure 4.37 Spray dispersion angle measured from the microscopic images

4.4 CORRELATION OF EXPERIMENTAL RESULT AND EMPIRICAL PREDICTED MODEL FOR SPRAY TIP PENETRATION

As it is known that Hiroyasu and Arai [1990] developed the classic spray tip penetration prediction empirical equations more 25 years ago under the single-hole nozzle conditions, and it is necessary to confirm if it is still available for the modern injections, especially for the multi-hole nozzles under the high rail pressure conditions.

4.4.1 Comparison between Experimental Result and Classic Predicted Model

Under the single-hole nozzle condition

The experimental results under the baseline condition ($P_{rail}=120$ MPa, $P_a=1.5$ MPa, $Q_{inj}=2.0$ mm³/hole) is regarded as the validation standard here. The classic empirical equations are shown as below simply, which have already been introduced in detail in Chapter 1.

$$0 < t < t_b$$

$$S = \alpha \times \left(\frac{2 \times \Delta P}{\rho_f} \right)^{0.5} \times t \quad (4.5)$$

$$t_b < t < t_{inj}$$

$$S = \beta \times \left(\frac{\Delta P}{\rho_a} \right)^{0.25} \times (D \times t)^{0.5} \quad (4.6)$$

$$t_b = \frac{\beta^2}{2 \times \alpha^2} \times \frac{\rho_l \times D}{(\rho_a \times \Delta P)^{0.5}} \quad (4.7)$$

$a=0.39$, $b=2.95$ in the original paper

$$t > t_{inj}$$

$$S = \gamma \times t^{0.25} \quad (4.8)$$

$$\gamma = \frac{S_{inj}}{t_{inj}^{0.25}} \quad (4.9)$$

The comparison of experimental and empirical result of spray tip penetration is shown in Figure 4.38. It can be seen that the spray tip penetration is under estimated by the original equations, and there is something to do to increase the accuracy of the equations to match up with the modern diesel sprays.

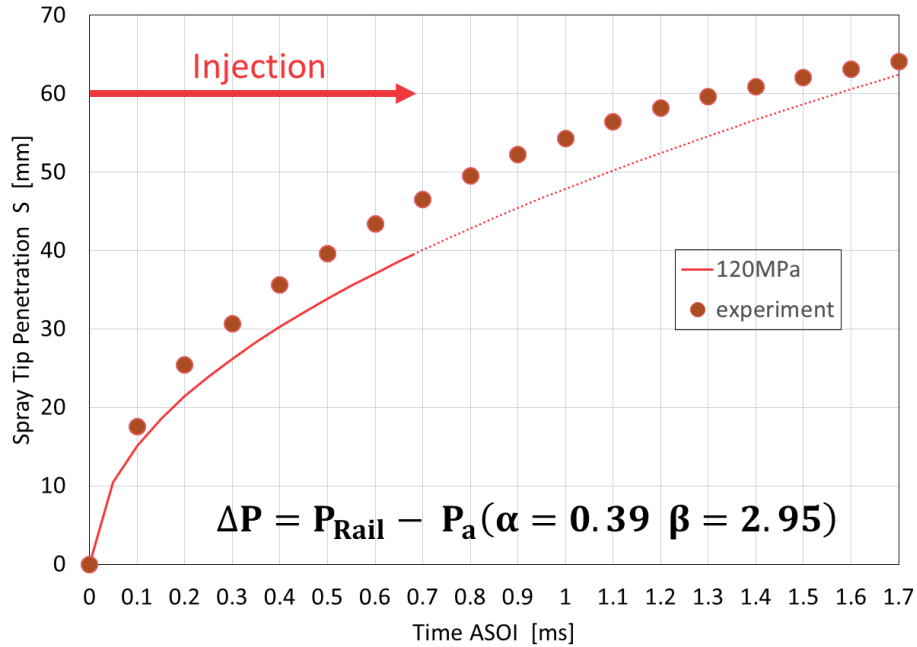


Figure 4.38 Comparison of experimental and empirical results of spray tip penetration

Under the multi-hole nozzle condition

The multi-hole nozzle spray tip penetration result shown in Figure 4.39 is also under the baseline condition. The comparison of experimental and empirical result of spray tip penetration shows that the spray tip penetration is also over estimated by the original equations.

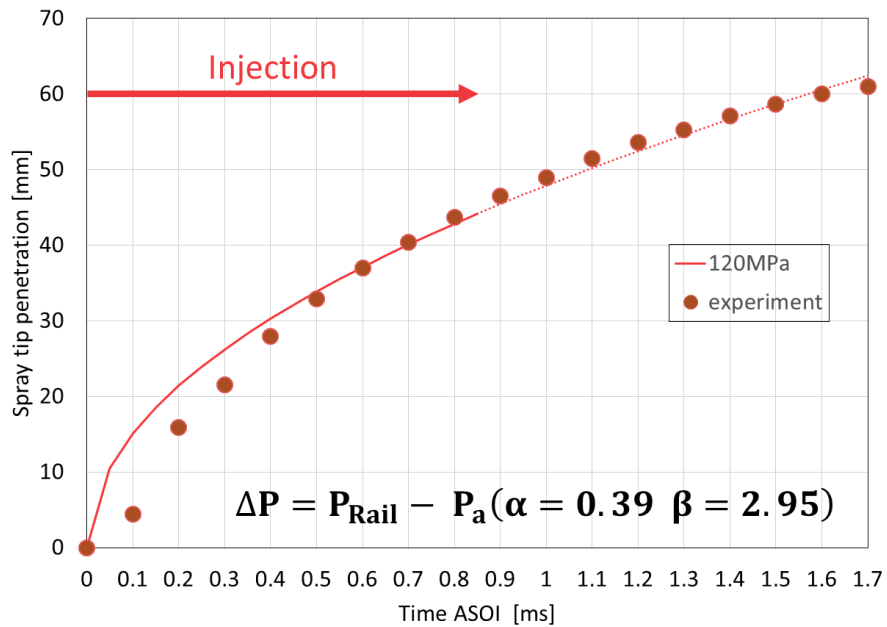


Figure 4.39 Comparison of experimental and empirical results of spray tip penetration

It should be noted that the rail pressure (120 MPa) is applied in the original equations to calculate the pressure drop, while as analyzed before, the pressure in the sac and the pressure in the rail is not the same one under the dynamic injection processes. Moreover, under the multi-hole nozzle condition, the sac pressure is very low at the beginning of the injection, and that is the reason why the original equation result is longer than the experimental results. It can be concluded that the classic empirical equations, which is developed under the quasi-steady conditions by using the single-hole nozzles are not available for the modern diesel spray, and it is necessary to improve them to make a contribute to the modeling of the current diesel sprays.

4.4.2 Correction of Spray Tip Penetration Prediction Equations

Correction of the equations for single-hole nozzle spray

There are two way to make corrections for the equations. The first one is to increase the corresponding coefficient ($\alpha = 0.39$ and $\beta = 2.95$) inside the original equations simply, the results shown in Figure 4.40 is an example of increasing the β to 3.4, and the predicted result can match up with the experimental result well.

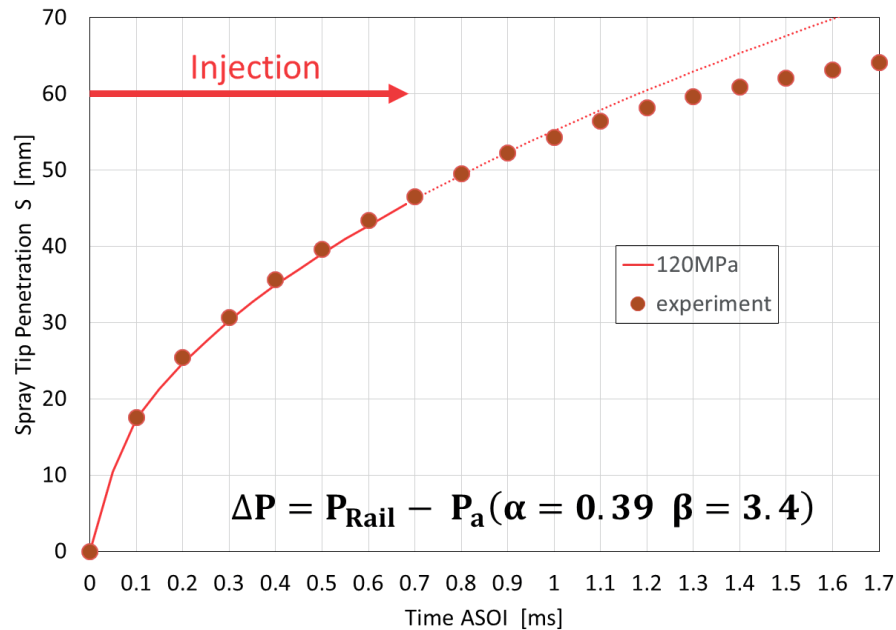


Figure 4.40 Increasing the corresponding coefficient inside the original equations

However, considering the physical significance of the empirical equation, the pressure drop calculation is the main point, and if the real pressure drop between the hole inlet and out let can be taken into the consideration, the empirical equation can be improved substantial. As a result, the rail pressure is instead of sac pressure at the corresponding timing during the injection duration in

the equations. As introduced before, according to the injection rate result, the sac pressure can be calculated by the Bernoulli's equation with appropriate discharge coefficient, just as shown in Figure 4.41.

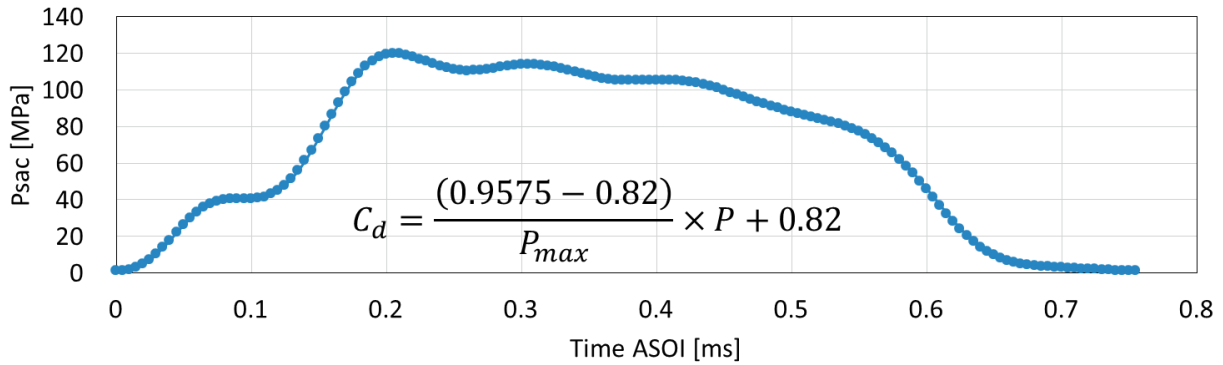


Figure 4.41 Sac pressure calculated by the Bernoulli's equation with appropriate discharge coefficient

In this way, the spray tip penetration can be calculated by applying the classic equations at each time, and the pressure drop is calculated by applying the corresponding sac pressure at each timing. The results are shown in Figure 4.42. The envelope line of all the results can be regarded as the calculated spray tip penetration results.

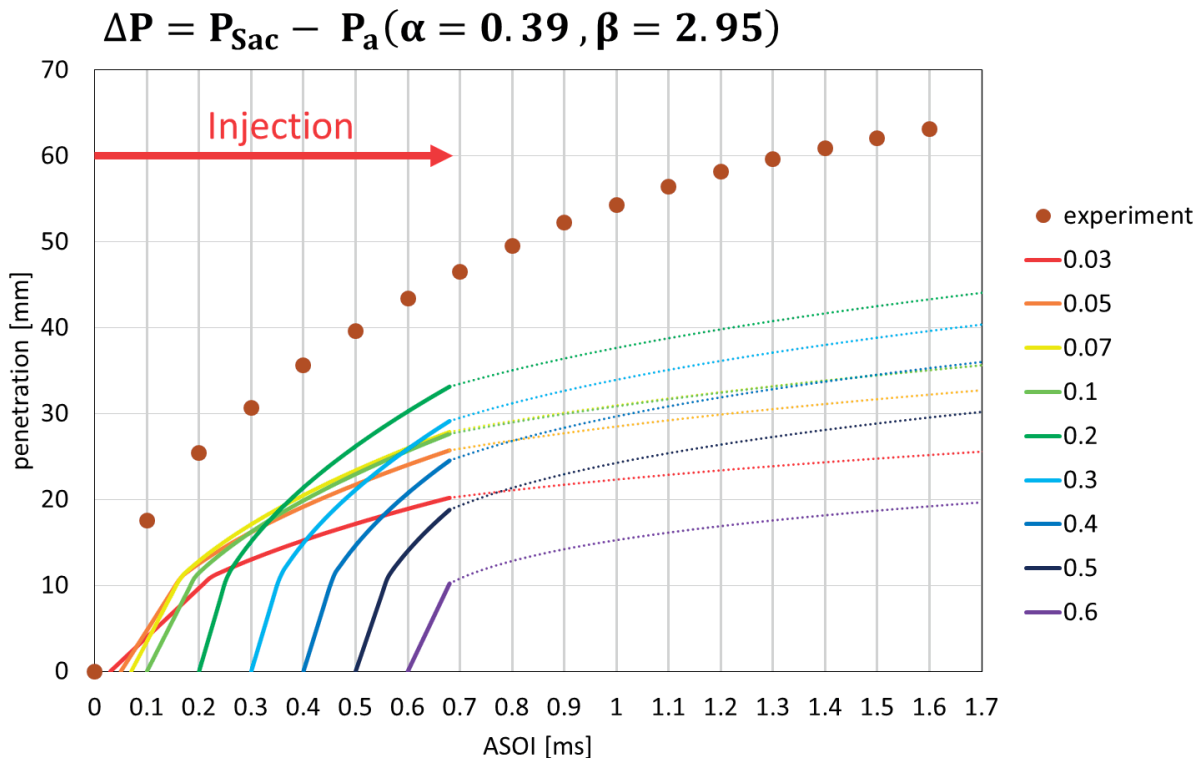


Figure 4.42 Spray tip penetration prediction by applying the time resolved pressure drop

However, the spray tip penetration is still under estimated, and the corresponding coefficient inside the original equation is still needed to be increased. The result shown in Figure 4.43 is one of the most ideal schemes, and the spray tip penetration equation after the end of injection is also adjusted. The experimental result is still under estimated because the nozzle hole discharge coefficient is very different to be measured, and the sac pressure is also affected by that. It is believed that if the accuracy of the time resolved discharge coefficient can be increased, the precision of the prediction will also be increased a lot.

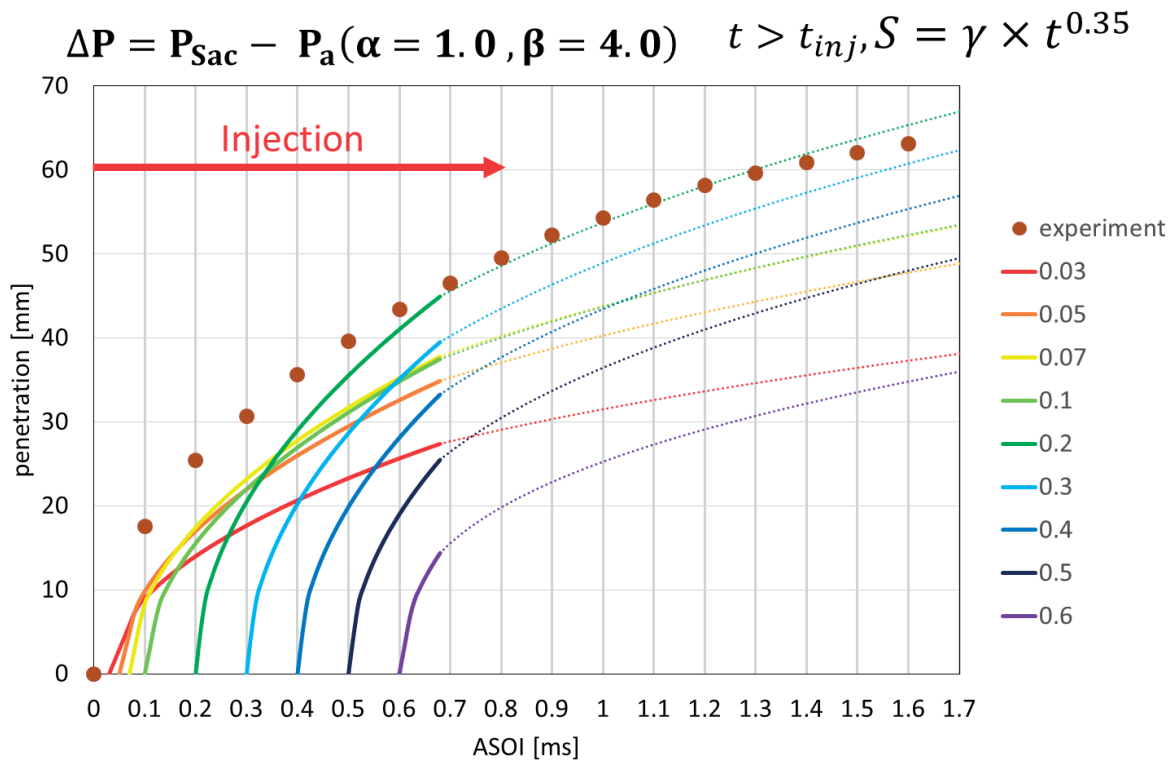


Figure 4.44 Spray tip penetration prediction by applying the time resolved pressure drop and adjusting the corresponding coefficient inside the equations

Correction of the equations for multi-hole nozzle spray

The same as single-hole nozzle, there are also two ways to make corrections for the equations of multi-hole nozzle spray tip penetration. However, the first one is to decrease the corresponding coefficient ($\alpha = 0.39$ and $\beta = 2.95$) inside the original equations simply, the results shown in Figure 4.44 is an example of decreasing the α to 0.13, and the predicted result can match up with the experimental result well.

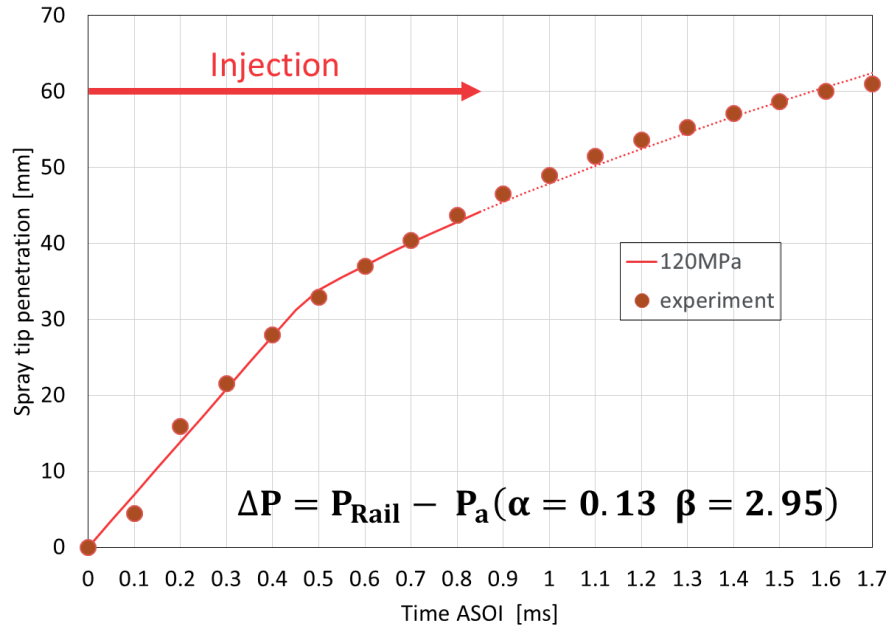


Figure 4.44 Decreasing the corresponding coefficient inside the original equations

However, as explained before, considering the physical significance of the empirical equation, the rail pressure is instead of sac pressure at the corresponding timing during the injection duration in the equations. Therefore, the other way is to take the time resolved pressure drop into the consideration. Figure 4.45 shows the calculated sac pressure variation of multi-hole nozzle based on the injection rate results. The calculation result of applying the original equations is shown in Figure 4.46. The sac pressure is lower relatively, and the envelope line of all the results is still lower than the experimental result.

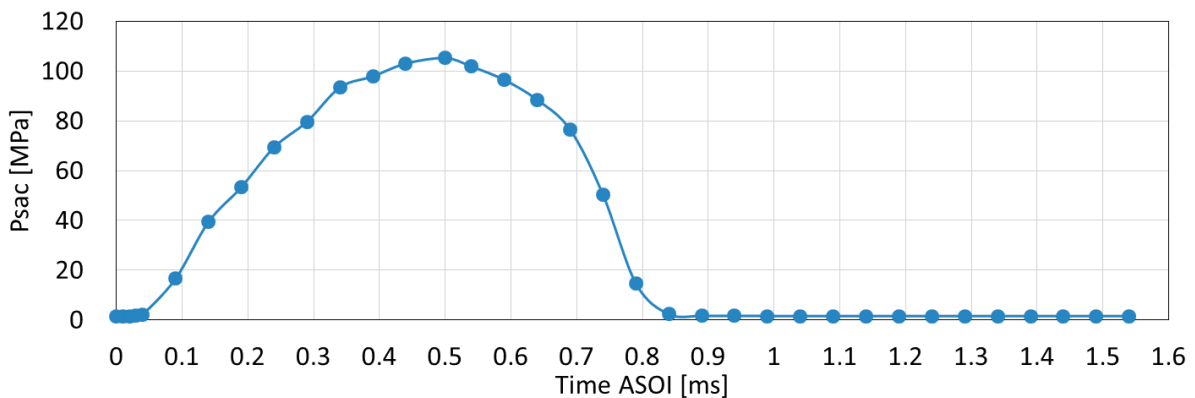


Figure 4.45 Sac pressure variation of multi-hole nozzles under the baseline condition

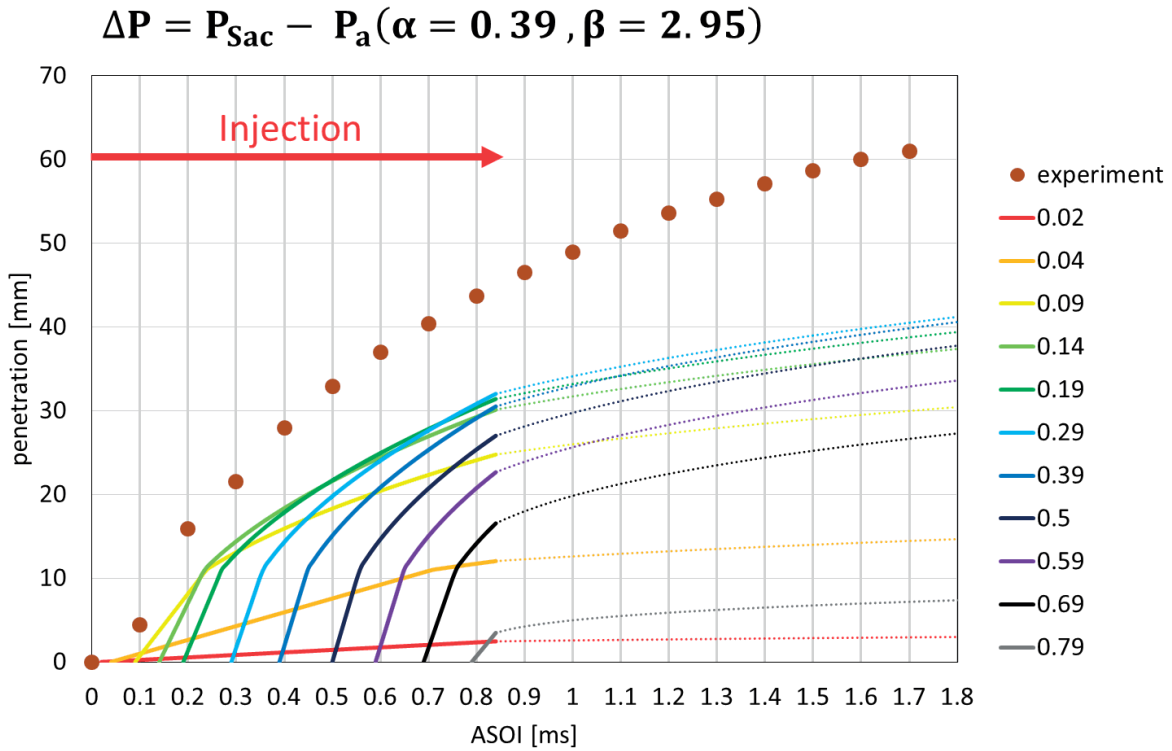


Figure 4.46 Multi-hole nozzle spray tip penetration prediction by applying the time resolved pressure drop

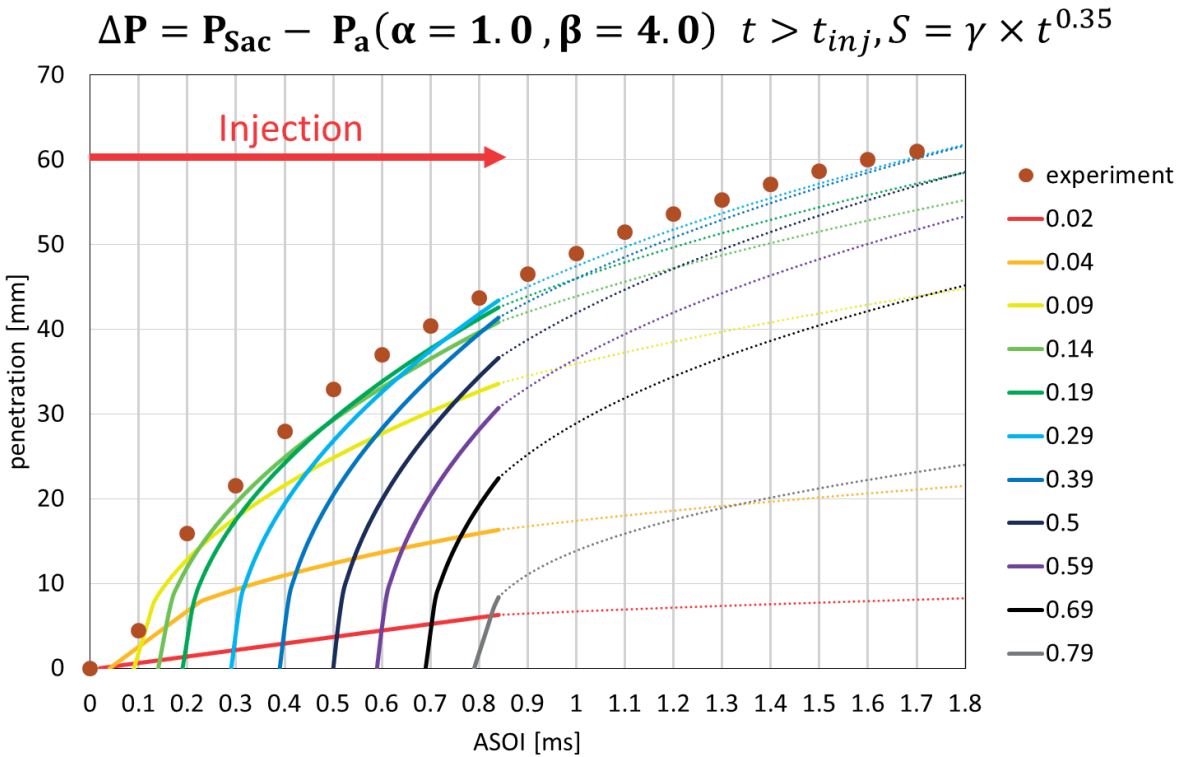


Figure 4.47 Multi-hole nozzle spray tip penetration prediction by applying the time resolved pressure drop and adjusting the corresponding coefficient inside the equations

However, because the spray tip penetration is still under estimated, and the corresponding coefficient inside the original equation is still needed to be increased. The result shown in Figure 4.47 is one of the most ideal schemes, and the spray tip penetration equation after the end of injection is also adjusted. The experimental result can be matched up with very well, and it is concluded that the correction of the equation is suitable for the multi-hole nozzle spray tip penetration prediction under this injection conditions. A lot of work still needs to do to extend the possibility of this correction to the wider conditions.

4.5 Summary

A comparison between the traditional single-hole nozzle and the modern practice multi-hole nozzles was conducted firstly, including the injection rate, spray behaviors and so on. After that, the characteristics of spray evolution of multi-hole nozzles under different engine operation and nozzle geometrical conditions were investigated and discussed in detail in this chapter. The empirical equations for the spray tip penetration of different nozzles were also improved in this chapter. The conclusion and summary are listed as follows:

1. According to the above discussion, because of the unique geometric structure, the multi-hole nozzle has a lower injection rate and sac pressure, shorter spray penetration, and wider spray angle and spray cone angle compared to those of the single-hole nozzle spray.
2. The injection rate and duration of the single-hole and multi-hole nozzles are both very sensitive to the rail pressure variation. However, the higher rail pressure has a greater effect on the multi-hole nozzle spray behaviours.
3. For both of the single-hole and multi-hole nozzles, with the decreasing of the injection quantity, except for the spray width, the other parameters are all reduced. However, the multi-hole nozzle is more sensitive than that of the single-hole nozzle.
4. Decreasing the nozzle hole diameter can reduce the deviation of spray characteristics between the single-hole and multi-hole nozzles. Multi-hole nozzle spray characteristics are more sensitive to the hole diameter variation.
5. The effects of the orifice length of the Diesel multi-hole nozzles on the fuel injection processes and far-and near-field spray behaviors under the constant injection quantity conditions were clearly demonstrated, relatively. With the decreasing of the hole length, the penetration is reduced, while the spray width is increased.

CHAPTER 5 INTERNAL FLOW CHARACTERISTICS OF MULTI-HOLE NOZZLES

In the current study, to aid the interpretation of the experiment results, the influences of the geometric structure of nozzles on internal flow and cavitation characteristics have been numerically investigated by the commercial CFD Code AVL-Fire Version 2013 (AVL). The computational study is used to illustrate the different internal flow characteristics inside the single-hole and multi-hole nozzles, with the aim of correlating the nozzle internal flow effect with the near-and far-field nozzle spray characteristics.

5.1 MESH BUILDING PROCESS, BOUNDARY CONDITIONS AND SIMULATION VALIDATION

The typical computational meshes of the single-hole and multi-hole nozzles are shown in Figure 5.1. As for the multi-hole nozzle with ten holes, considering the geometric periodicity, symmetry, and calculation timing, only one-tenth of the entire volumetric domain was selected. The typical settings for this computation have been listed in Table 5.1.

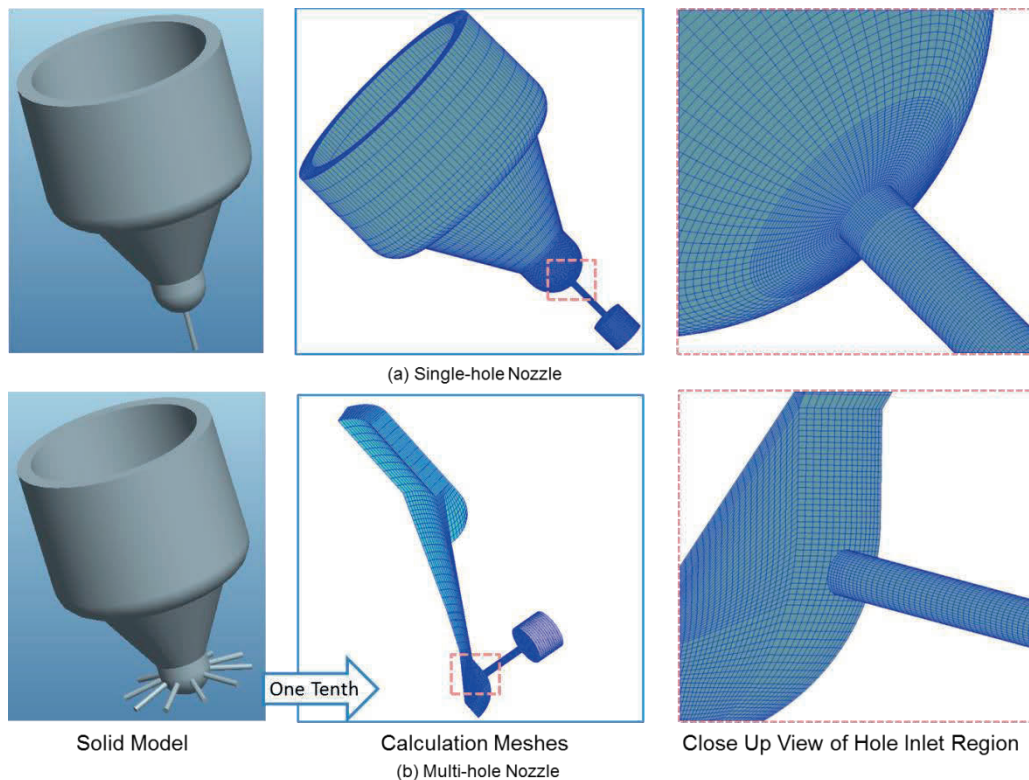


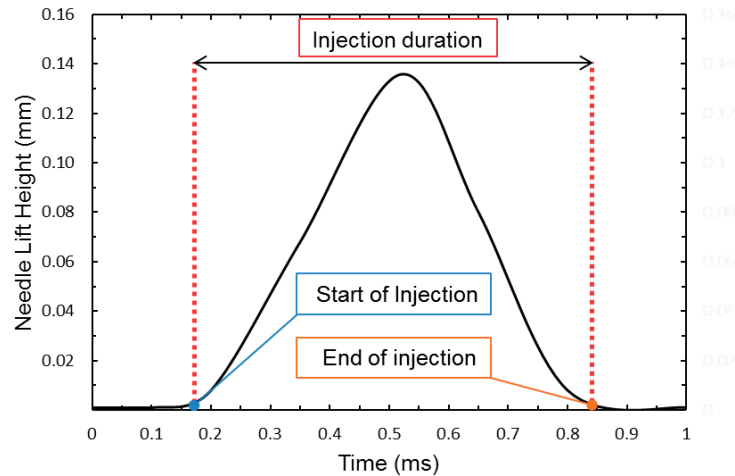
Figure 5.1 Computational meshes

Table 5.1 Computation setting

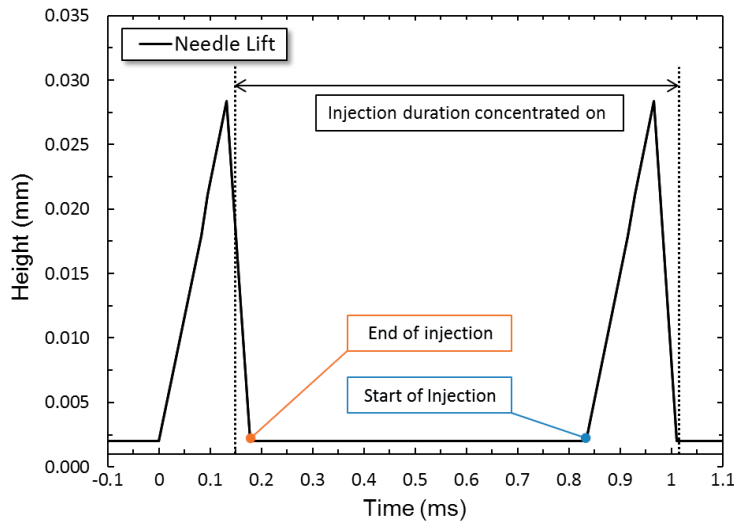
Item	Classification		Setting / Value
		K- ζ -F	
Model selection and Initial values	Turbulence model	Turbulence energy (m^2/s^2)	0.1
		Turbulence length scale (m)	0.000001
	Cavitation model	Linear cavitation model	
		Cavitation bubble density number	1.5×10^{18}
		Diesel saturated vapor pressure (Pa)	892
Initial boundary	Inlet boundary	Injection Pressure (MPa)	80 120 180
	Export boundary	Ambient Pressure (MPa)	1.5
Mesh information	The minimum cell size (mm)	Single-hole injector	6.01×10^{-4}
		Multi-hole injector	2.42×10^{-3}
	The maximum total grid number (cells)	Single-hole injector	697304
		Multi-hole injector	180000

Simulations of the three-dimensional unsteady multi-phase flow inside the nozzles were carried out using two-fluid model [Leng et al., 2015]. The liquid phase is assumed as incompressible, and both liquid and vapor phases are treated as continuous medium. The initial fuel temperature in the upstream was regarded as the same with the room temperature, while the setting for the liquid viscosity inside the nozzle was decreased compared with that under the atmospheric condition, because the increased fuel temperature and bubble density inside the nozzle caused by the high injection pressure was taken into the consideration. The conservation equations are solved separately for each phase. The mass and momentum exchange between phases are calculated by additional source item in the conservation equations. Moreover, the Reynolds Averaged Navier-Stokes Simulation (RANS) method and a four-equation k- ζ -f model [Hanjalic et al., 2014], based on the Durbin's elliptic relaxation concept [Durbin, 1991], were adopted to reproduce the turbulent flow inside the nozzles. This model introduces new transportation equations to describe the variable ζ which has relationship with turbulence viscosity. As a result, the property of anisotropic turbulence can be taken into the consideration. Furthermore, a Linearized Rayleigh model [Mulemane, A. et. al., 2004], in which the simplified bubble dynamic equation is employed to describe the evolution of a single bubble, was used to express the cavitation bubble behaviours within the nozzle. The initial pressure conditions, bubble density, turbulence kinetic energy, and turbulence length scale are all listed in Table 5.1. The two side boundaries of the 36° sector are set

as rotationally periodic boundaries, and all walls are set as adiabatic conditions. All the cells in the domain are set to have uniform initialization. Aiming to make comparisons, the same transient needle-lift curve measured from a similar type of multi-hole injector was applied for both the single-hole and multi-hole meshes, as shown in Figure 5.2.



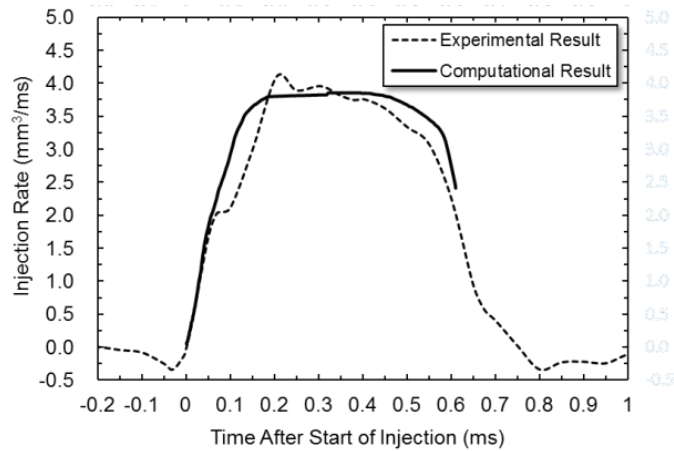
(a) Normal injection quantity



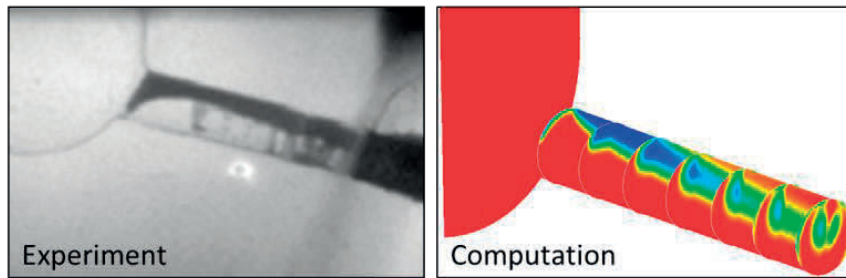
(b) Tiny injection quantity

Figure 5.2 The needle lift applied in the computation

A validation was performed on the adopted models before the further computational studies by taking the experimental results from the paper published by Blessing et al. [2003] as the criteria, which is shown in Figure 5.3, because the characteristics of the injector and experimental conditions in their work covered some feature of the current investigation. During the verification process, it proved that the mass flow rate, and the distribution and occurrence of the cavitation could be predicted accurately by this simulation. More information about the validation processes were presented in the previous research [Dong et al, 2016].



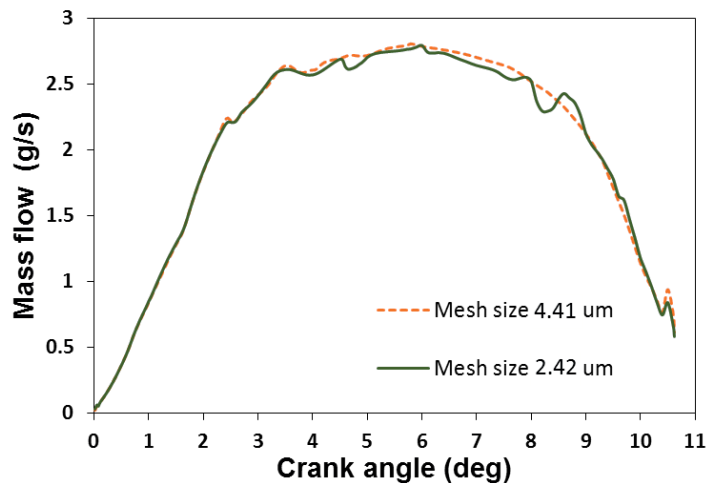
(a) Injection rate results from the experiment and computation



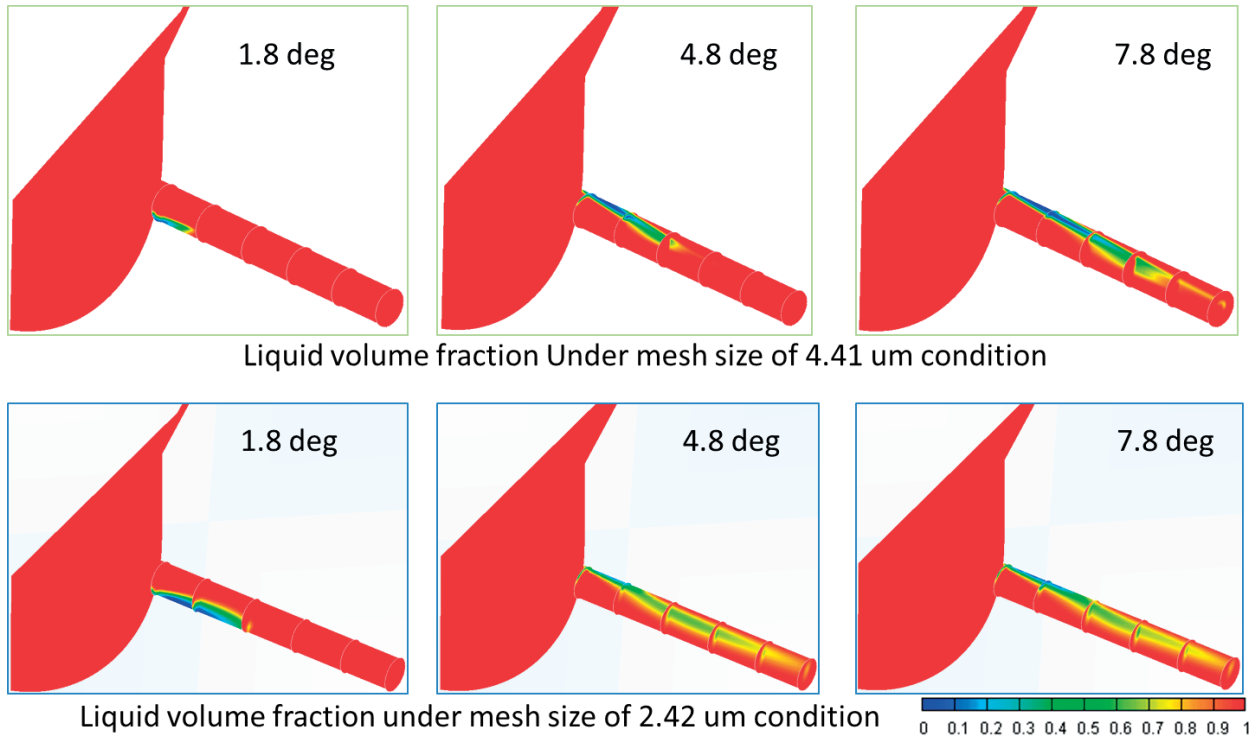
(b) Cavitation results from the experiment and computation

Figure 5.3 Validation of the computation setting

When considering the mesh size effect, the specific processes are shown here. The grid size (2.42 and 4.41 μm) effect on the result was also tested before the further simulation study. The result is shown in Figure 5.4. The first one is the mass flow rate comparison result, and it is found that there is not too much obvious deviation between the two curves. Consequently, at least it can be confirmed that the mass flow results are independent from the grid size variation relatively when the mesh size is under this order of magnitudes condition.



(a) Mass flow rate under different mesh size conditions



(b) Liquid volume fraction distribution under different mesh size conditions

Figure 5.4 Mesh size effect on the simulation results

The cavitation structure inside the nozzle at different timing under different mesh size conditions are shown in the Figure 5.4-(b). It can be seen that the cavitation structure is affected a little by the mesh size. After the comprehensive consideration about the calculation time and the validation of the simulation result, grid size ($\sim 2.5 \times 10^{-3}$ mm) was applied in the current study.

5.2 CHARACTERISTICS OF INTERNAL FLOW INSIDE SINGLE-HOLE AND MULTI-HOLE NOZZLES

In this section, the different internal flow characteristics between the single-hole and multi-hole nozzles under different injection quantity and nozzle hole diameter conditions will be discussed. The result will be applied to explain the spray behaviors observed in the experiments. Moreover, the experimental conditions are coincided with that in the non-evaporation spray observation experimental conditions. In this transient simulation analysis, as emphasized before, in order to make comparison, the same needle lift curve was implemented with the different nozzle configurations. Three timings, which represent the initial, full needle lift, and post stages of the injection will be focused on, respectively.

5.2.1 Computational Results via Full and Partial Mesh of Multi-hole Nozzle Geometry

There are ten hole in the multi-hole nozzles, which is applied in the current study, while as introduced before, only one tenth of the geometry is selected in most of the simulation, the processes is shown in Figure 5.5. In order to confirm the symmetrical characteristics of the internal flow inside the multi-hole nozzles, the calculation with full mesh is also conducted, and the result is compared with the partial mesh results.

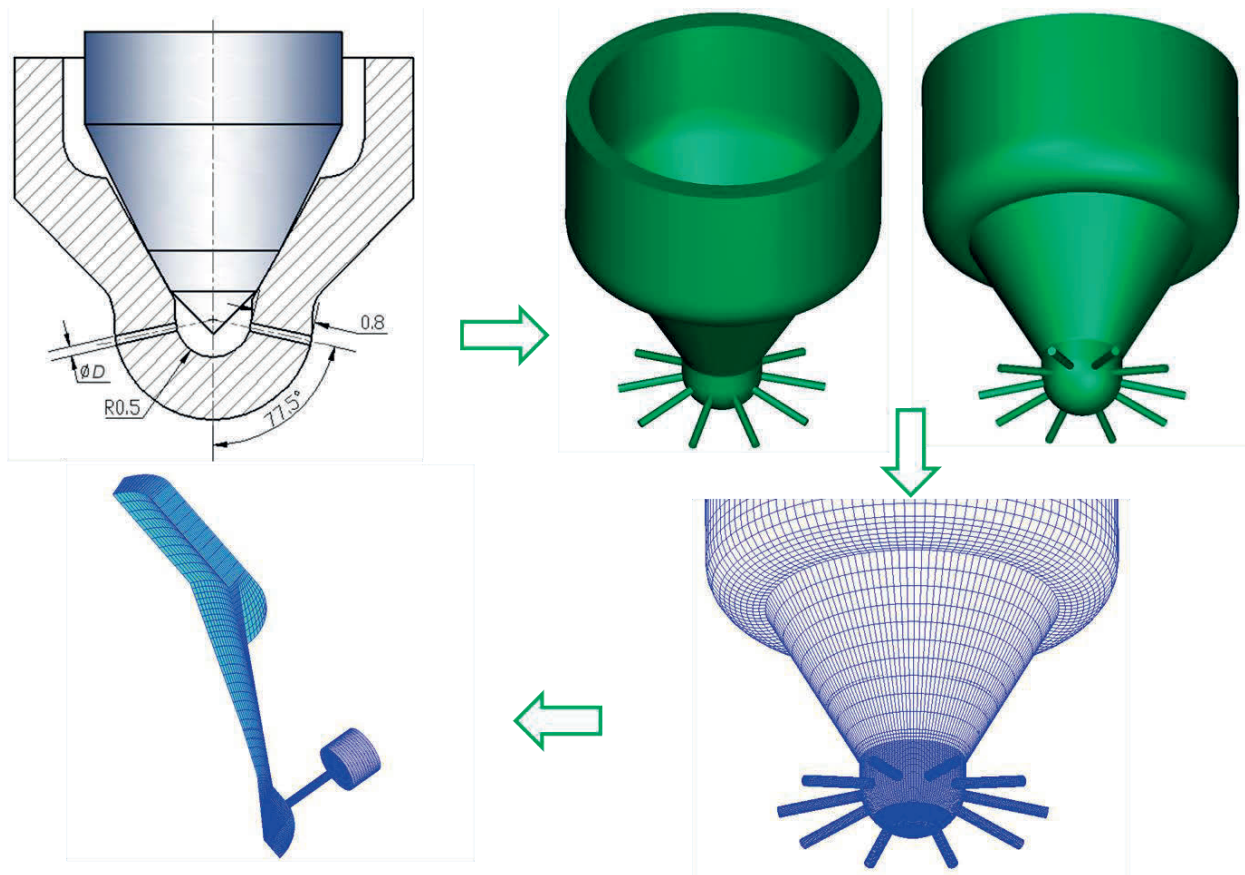


Figure 5.5 Processing method of calculation domain

The velocity and liquid volume fraction distribution inside the full mesh geometry is shown in Figure 5.6, and the symmetrical characteristic is obvious. The mass flow rate result is also shown in this figure. This is the discussion about hole to hole variation. The left figure is the temporal variation of mass flow rate on the exits of different holes. The deviation is quite small. The right chart shows the comparison of mass flow result calculated from the full and partial meshes. This result agrees with the cloud pictures. It can be concluded that the one-tenth mesh can predict the flow characteristics inside the multi-hole nozzle very well.

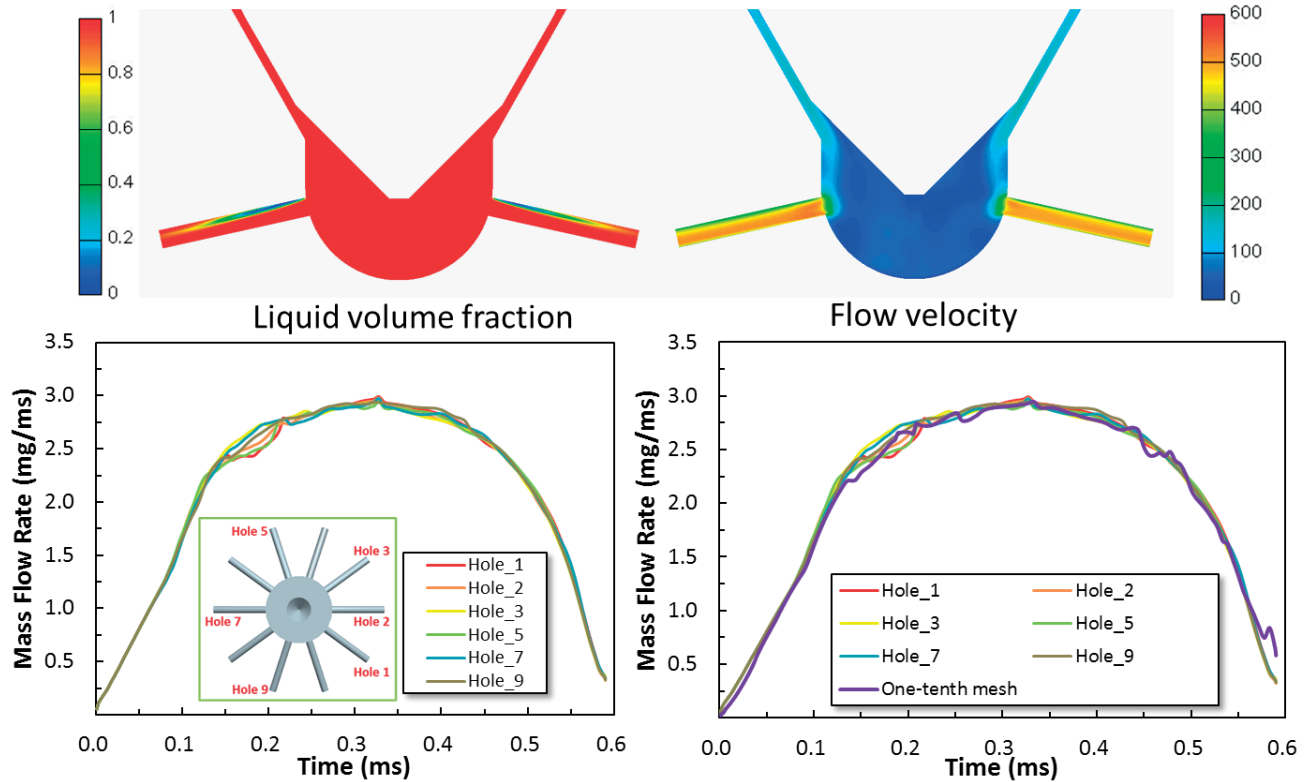


Figure 5.6 Internal flow results under full-mesh and partial mesh conditions

5.2.2 Global Comparison of Internal Flow between Single-hole and Multi-hole Nozzles

The simulation was conducted under the base line condition. The pressure variation in the sacs of the different nozzles at typical injection stages is shown in Figure 5.7. The rate of increasing pressure and peak value of the single-hole nozzle are both much higher than those of the multi-hole one, which coincides with the previous analysis.

The streamline variations are shown in Figure 5.8, and the flow in the sac and the hole volume are analyzed separately. Complicated streamlines with greater curvatures are generated in the sac of the multi-hole nozzle throughout the entire injection duration. These vortices were also observed by M. Gavaises et al. [2006], Lia et al. [2011], and Hayashi et al. [2014]. It has been proven that there are close correlations between the swirling motion in the sac and the string-type cavitation and spray cone angle. On the other hand, streamlines in the single-hole nozzle sac are smooth except at the beginning of injection, when the needle lift is very low. When attention is paid to the internal flow inside the nozzle hole volume, spiral and counter-rotating flows appear in the multi-hole region, especially during the time of full needle lift, whereas this is, by default, absent inside the

single-hole nozzle hole volume. Andriotis et al. [2008 and 2009] also found the same phenomenon, which could explain the wider multi-hole spray cone angle observed in the current experiments.

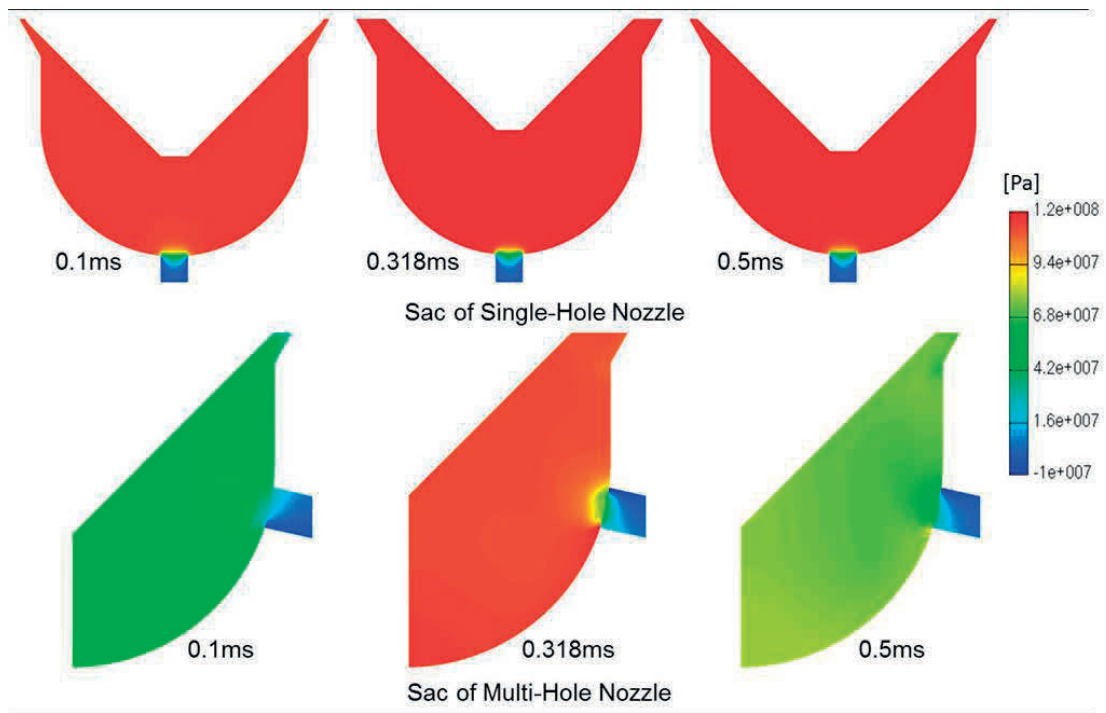
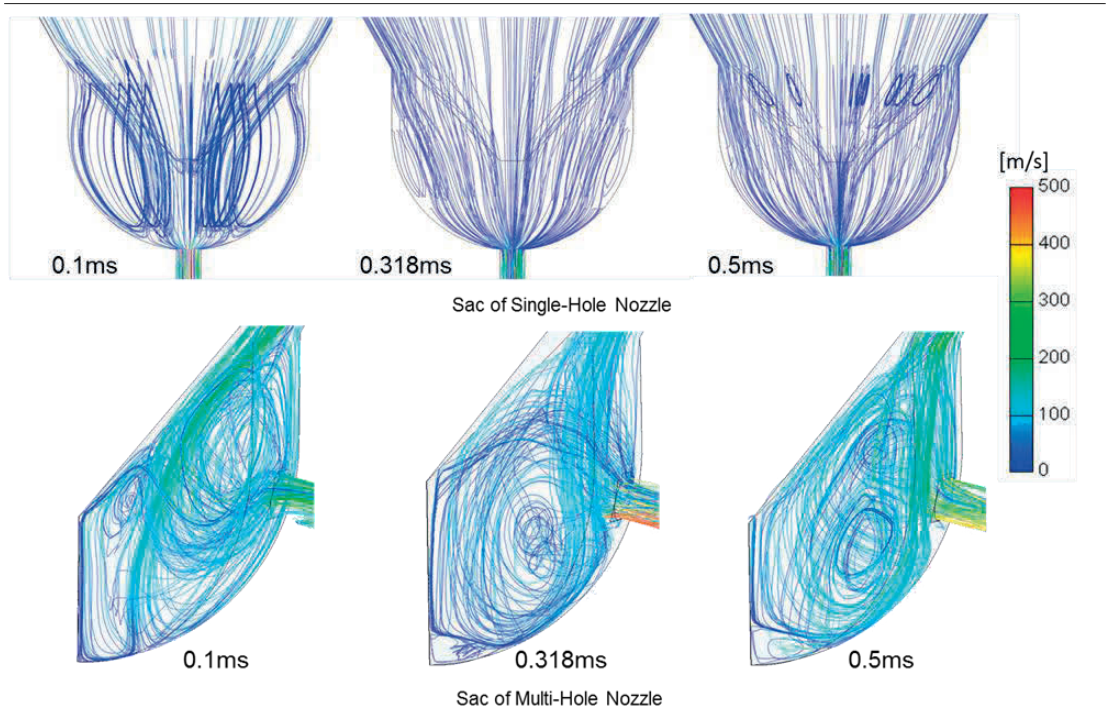
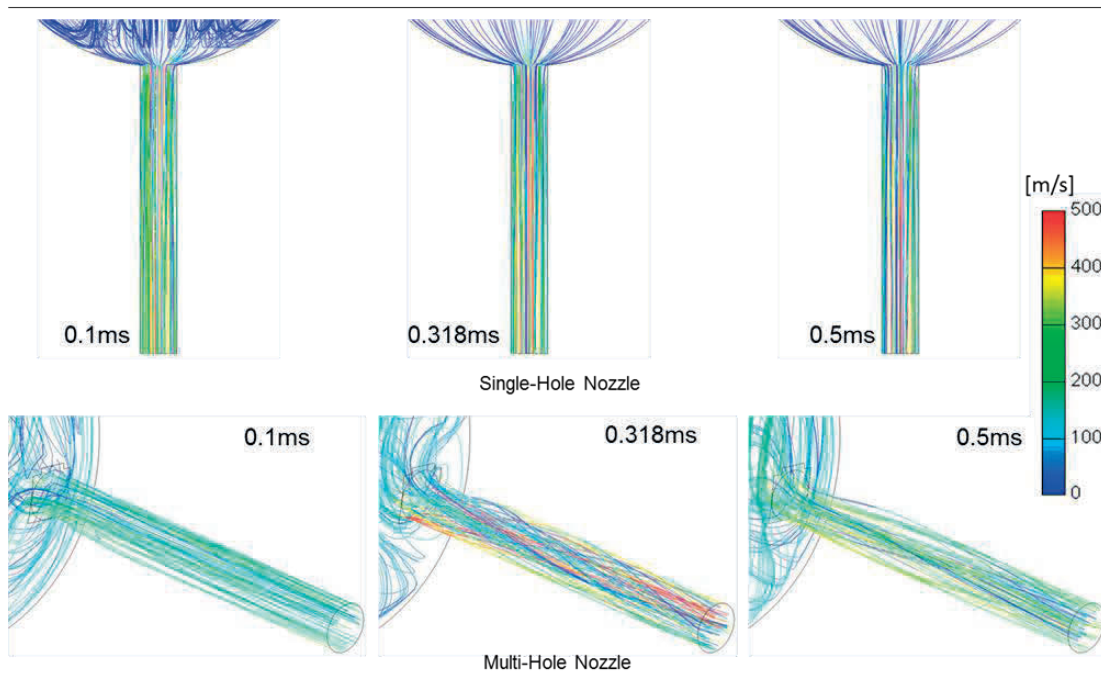


Figure 5.7 Pressure distribution in the sac at typical timing during the injection duration



(a) Streamline distribution in the sac at typical timing during the injection duration



(b) Streamline distribution in the hole at typical timing during the injection duration

Figure 5.8 Temporal variation of streamline in different nozzles

The velocity distribution is shown in Figure 5.9. The relatively axial-symmetrical features and high rate of increasing velocity in the single-hole nozzle are consistent with greater spray tip penetration and narrower spray cone angle measured in the experiment. Affected by its special configuration, the velocity distribution in the multi-hole nozzle is asymmetrical. With the needle moving, the asymmetrical low velocity region generated by the aspects changing of the flow direction moves from the lower reaches of the hole inlet to upper reaches. The lower velocity region is mainly occupied by the cavitation bubbles and counter-rotating flow. It can be concluded that the non-symmetric multi-hole nozzle spray is dominated by both the internal flow pattern and the Coanda effect, simultaneously.

In fact, the fuel injected from the exit section of the nozzle hole can be divided into three vectors, as shown in Figure 5.10. V_a has the same direction as the hole axis. The other two velocity components are on the outlet section plane, which are perpendicular to each other. The combination of these two components is defined as V_r . In this study, the ratio of V_r to V_a along the horizontal hole diameter line is focused on.

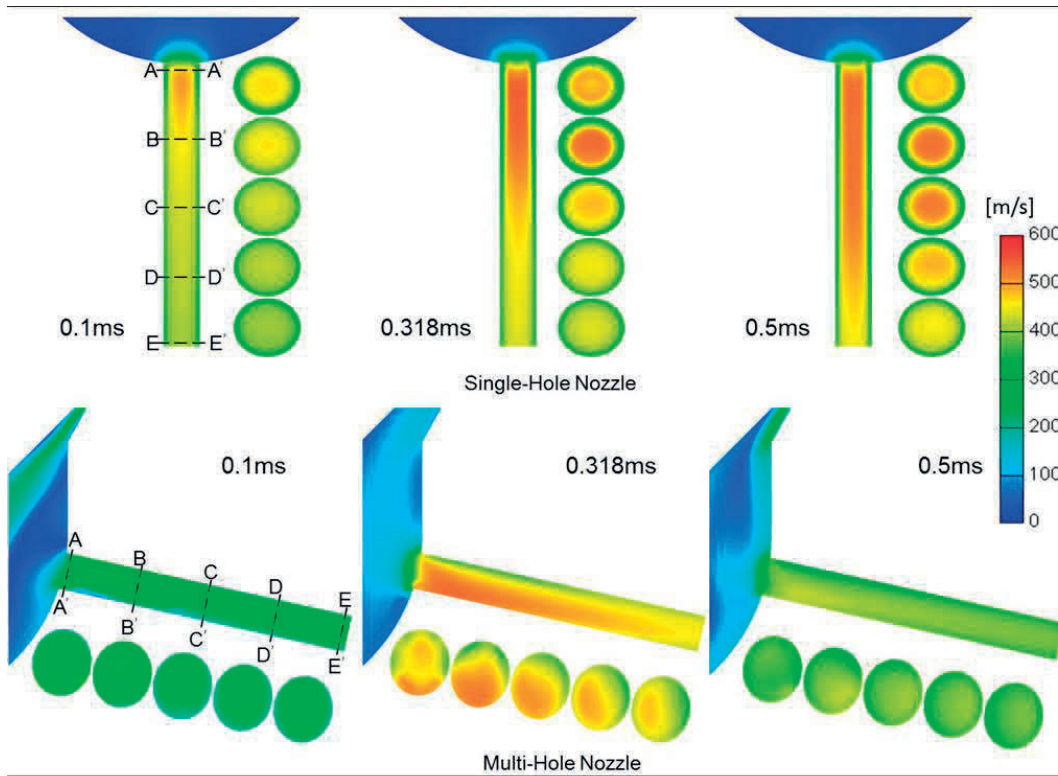


Figure 5.9 Velocity distribution in different nozzles at typical timing during the injection duration

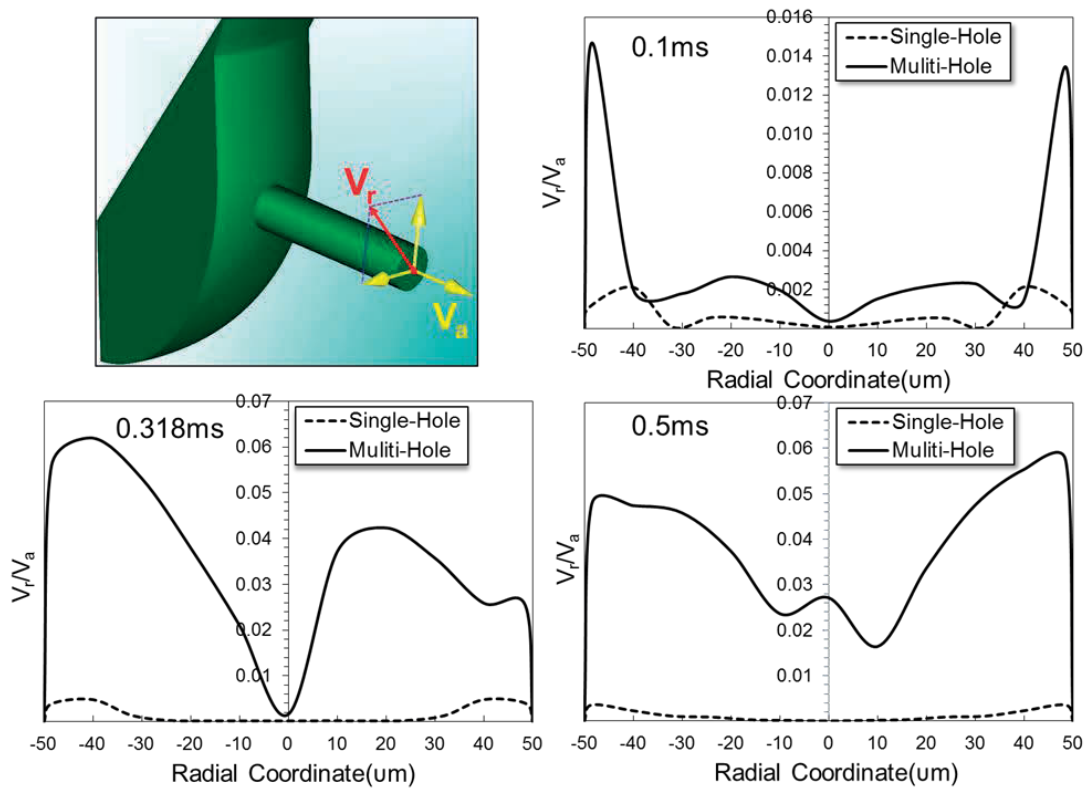


Figure 5.10 Ratio of velocity components variation on the outlet of different nozzles

At the initial stage of injection (0.1 ms) when the internal flow pattern inside the multi-hole nozzle has not been established completely, this ratio, calculated from the multi-hole nozzle, is not much higher than that of the single-hole one, except for at the boundary locations where the directions of velocity vectors play a significant role in the spray cone angle. As time elapses, the difference becomes prominent and expands from the boundary locations to the central area, which provides additional explanations of the wider spray cone angle of the multi-hole nozzle.

The temporal variations of the liquid volume fraction are shown in Figure 5.11. For the single-hole nozzle, the film-type cavitation generated by flow separation mainly appears in the upstream region around the wall of the nozzle hole, symmetrically, and rarely reaches the centre of the exit section. However, the cavitation position and intensity are all unstable inside the multi-hole nozzle. The string-type cavitation, which is generated by the spiral and streamwise counter-rotating vortices, can reach the central area of the exit section. The high mass and momentum exchange in the downstream region are more conducive to the wider spray cone angle [Kubitschek et al., 2008].

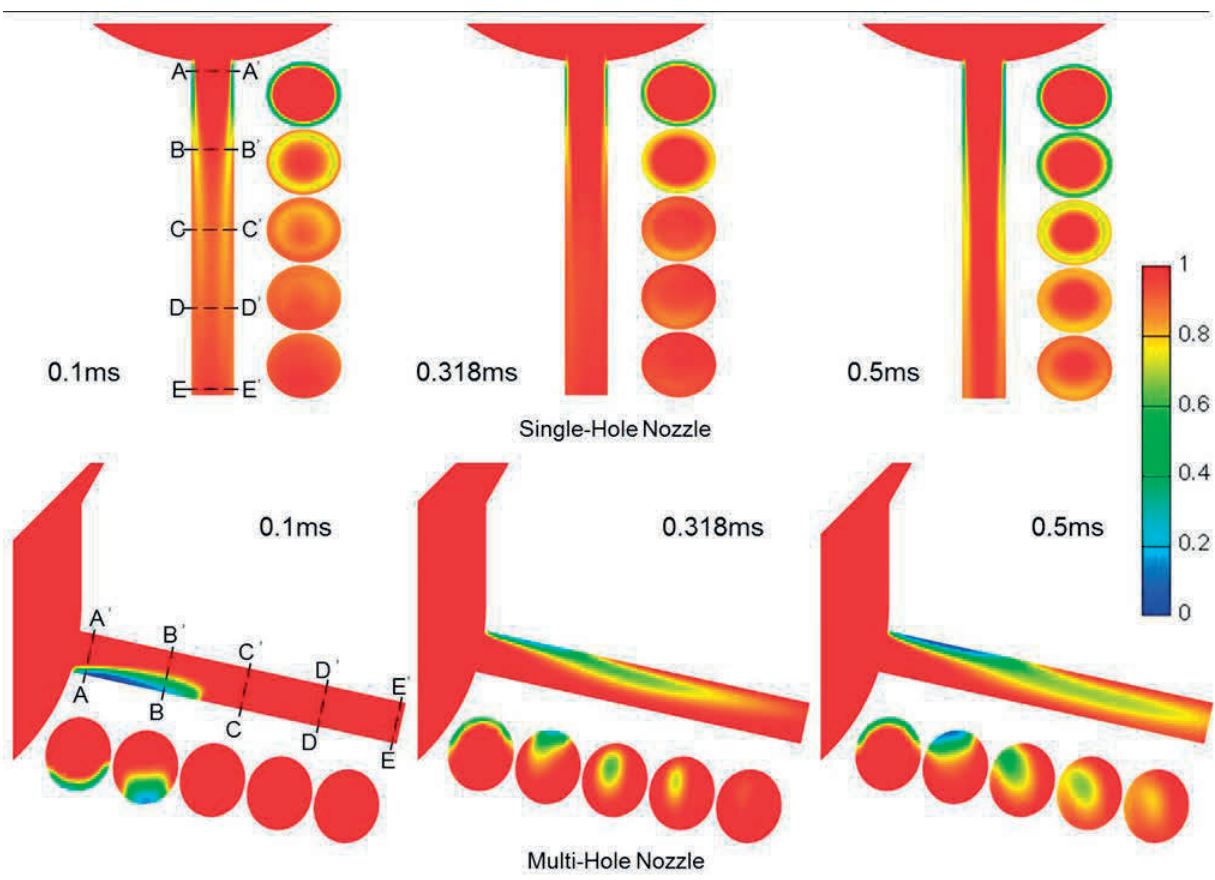


Figure 5.11 Temporal variation of liquid volume fraction distribution inside different nozzle holes

5.2.3 Under Tiny and Normal Injection Quantity Conditions

The internal flow simulation results conducted under the normal and tiny injection quantity conditions ($2 \text{ mm}^3/\text{hole}$ and $0.3 \text{ mm}^3/\text{hole}$) will be compared in this section. Figure 5.12 shows the average pressure variation inside the sac and the mass flow rate on the outlet sections of different nozzles during the calculation duration.

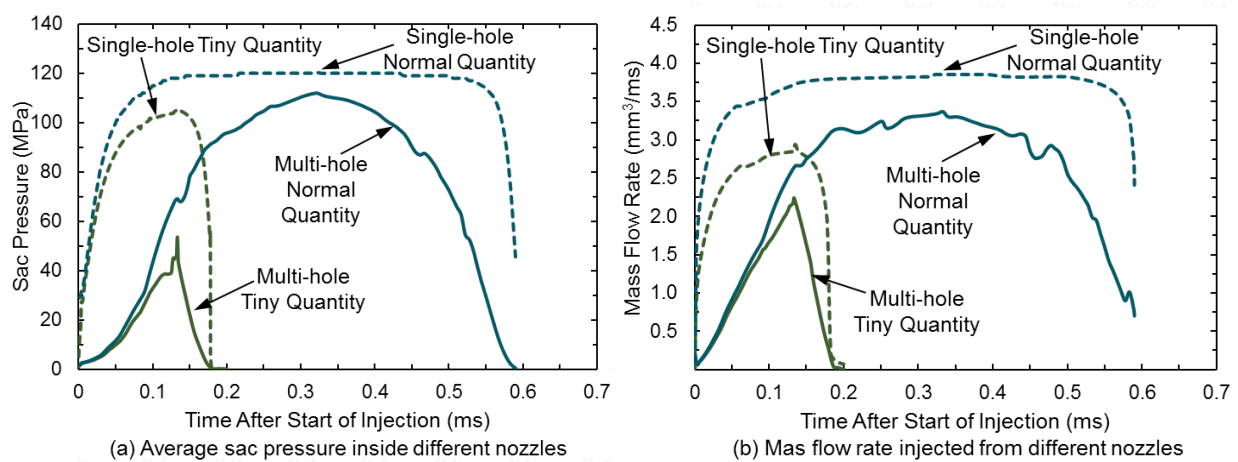


Figure 5.12 Calculation sac pressure and mass flow rate results under different quantity conditions

Because the eccentricity of the needle movement is not involved in the needle lift curves, the variation trend of the sac pressure and mass flow rate of the single-hole nozzle is smooth relatively. However, affected by the variable internal flow patterns and unstable cavitation structure and position [He et al., 2013], the sac pressure of the multi-hole nozzle has small waves under the two injection quantity conditions. As for the mass flow rate of the multi-hole nozzle, the fluctuation is obvious under the normal injection quantity condition, but the shape of the curve varies sharply under the tiny quantity condition. The overall relationship and trend of the calculation results are coincided with the experimental results, which are the averaged value in the measurement conducted ten times. In addition, under different injection quantity conditions, both the rate of increasing pressure and peak value of the single-hole nozzle are much higher than those of the nozzle with complex structure, and the mass flow rate results also present the same regularities. As a result, the simulation can be used to support the discussion about the experimental results in last chapter.

The different fuel flow velocity variation characteristics during the injection duration at the special monitoring points on the exit sections of different nozzles is shown in Figure 5.13. For the single-hole nozzle, four monitoring points along the horizontal hole diameter line were selected

symmetrically, and for the multi-hole nozzle, eight points were selected along the horizontal and vertical hole diameter lines, as shown in the figure. There is strong relationship between the outlet velocity variation and the near-field spray behaviours [Moon et al., 2015].

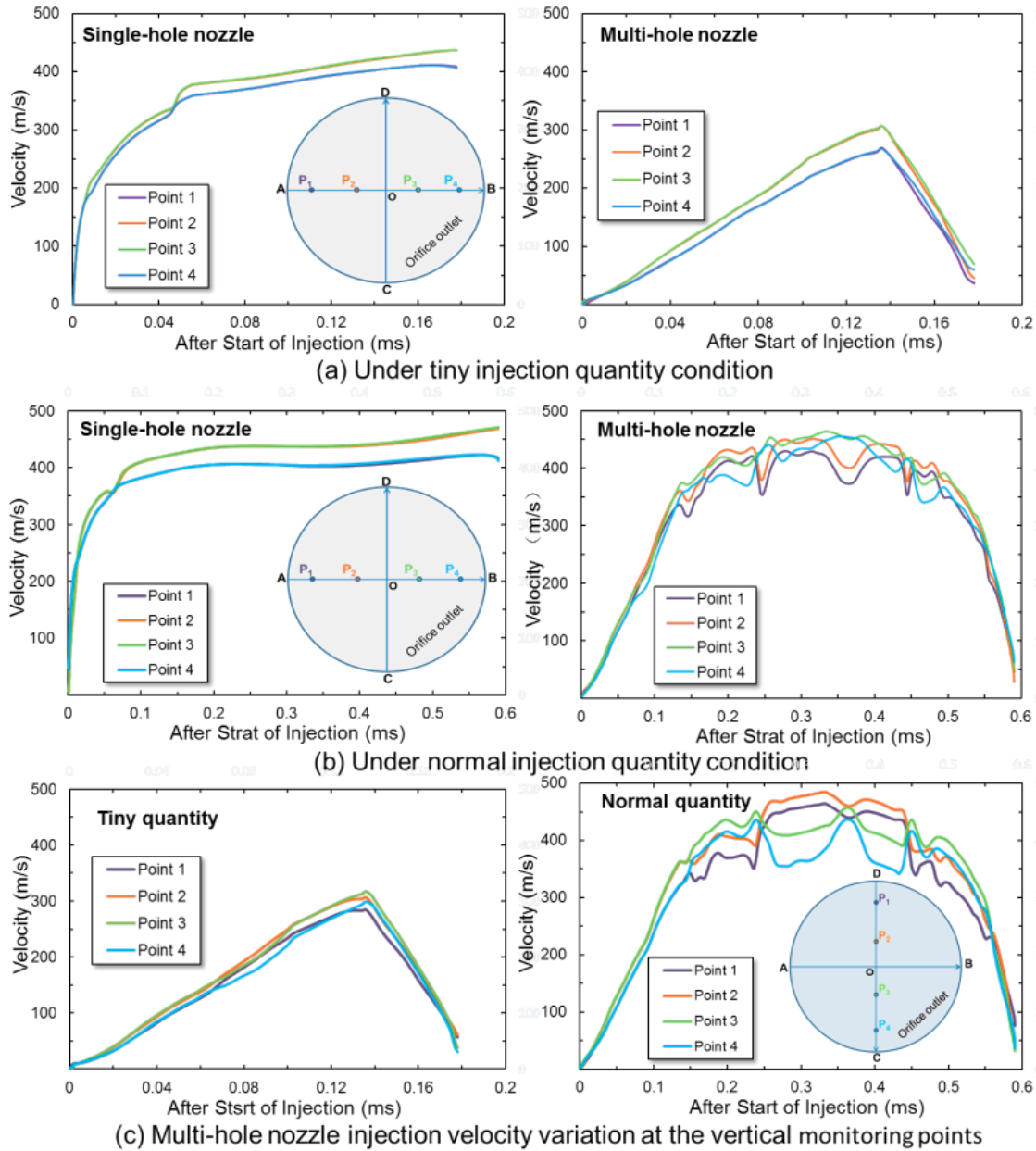


Figure 5.13 Velocity variation at the special monitoring points on the exits of different nozzles under different injection quantity conditions

Under both tiny and normal injection quantity conditions, caused by the higher sac pressure analyzed before, the injected fuel velocity of the single-hole nozzle increases dramatically as soon as the start of injection, and all maintains almost at the same high level until the end of

injection. Moreover, the velocity at the two inner points is higher than that at the outer points, while the curves are all very smooth, which implies that the flow inside the nozzle is stable relatively. On the other hand, in the case of the multi-hole nozzle, under the tiny injection quantity condition, the velocity increases slowly with the needle moving, and decreasing to the small value at the end of injection. The shape of the curve is smooth but sharp. However, under normal injection quantity condition, its value is much higher than that under the tiny quantity condition, and the velocity variation at the monitoring points all has serious fluctuation. Furthermore, there is antipodal and asymmetric trend of the velocity variation between two symmetrical monitoring points, especially along the vertical lines. These different flow instances can play a significant role in the spray behaviors, which is observed in the experimental results in last section. The discussion above can be used to explain the reason why there is larger deviation between the multi-hole nozzle spray tip penetration under different injection quantity conditions, compared with that of the single-hole one. The analysis about the distinct near field spray properties in last chapter can also be supported by this part of results.

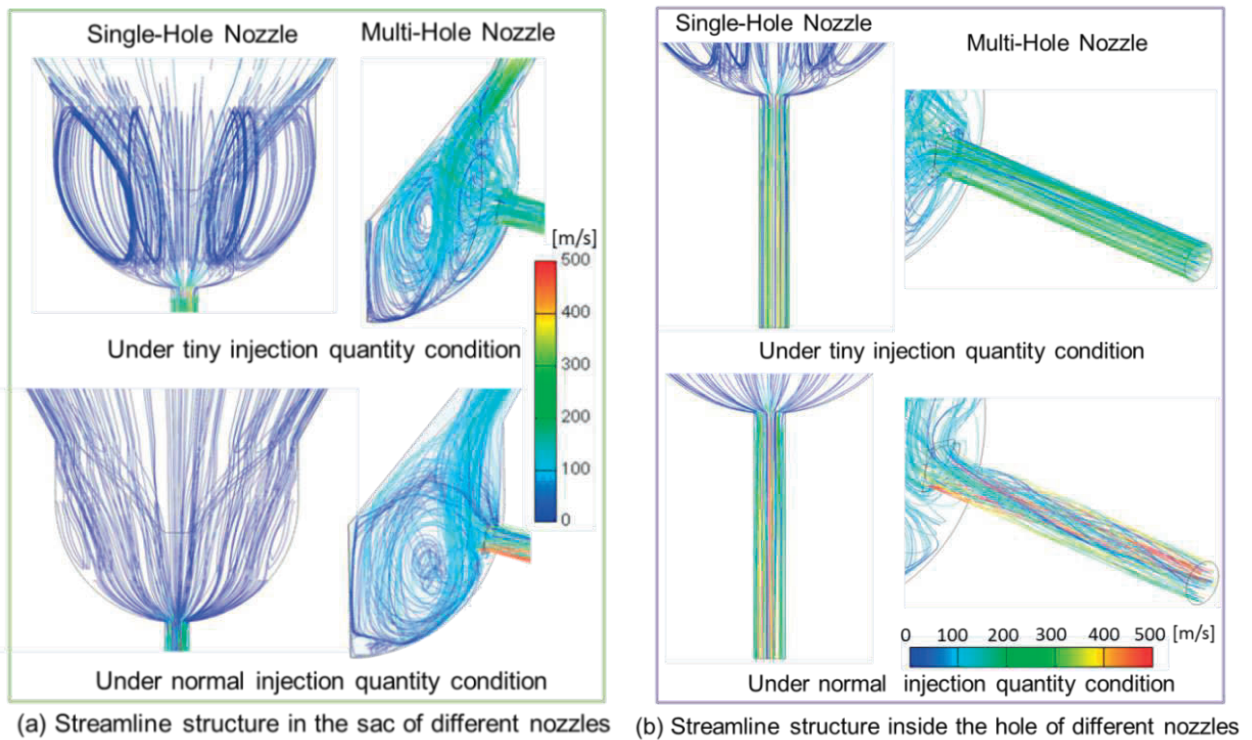


Figure 5.14 Streamline structure inside different nozzles at the full needle lift timing of different injection quantity conditions

The distinct streamline distribution inside different kinds of nozzles at the full needle lift timing are shown in Figure 5.14, and the flow in the sac and the hole volume are analyzed separately. They can intuitively reflect the local flow patterns inside the nozzles under different injection quantity conditions. Under the tiny injection quantity condition, there are large vortices in the sac volume of the single-hole nozzle, which are caused by the low needle lift height, narrower charging area, and the unique upstream flow direction. However, the streamline structure in the sac is very smooth under the normal injection quantity condition, when the needle lift is high enough. This difference may have relationship with the relatively unstable single-hole nozzle spray observed under the tiny quantity condition in the experiment. As for the multi-hole nozzle, although there are all vortices in the sac under the two kinds of injection quantity conditions, the number, construction, and position of the vortex are all more complicated under the tiny injection quantity condition. The pulsated near-field spray behaviours in the experiment may be caused by this issue. Making comparison between the single-hole and multi-hole nozzles, the difference in the streamline structure is more prominent under the normal injection quantity conditions, because under high needle lift condition, the flow patterns is mainly affected by the nozzle hole structure and hole position [Lai et al., 2011].

When the attention is paid on to the nozzle hole region, caused by the central axis layout of the hole, there is smooth, stable, and neat streamline inside the hole of the single-hole nozzle under different injection quantity conditions. However, there is absolutely different streamline construction inside the hole of the multi-hole nozzle under tiny and normal injection quantity condition. Affected by the lower velocity, there is almost no intense turbulent and vortex in the hole under tiny quantity condition, while the complicated streamlines with greater curvatures and counter rotating flow are observed inside the its hole volume under the normal quantity condition, which should have strong relationship with the near field spray width and the first breakup processes [Cycil et al., 2015]. It can be also concluded that the difference in the streamline structure inside holes between the single-hole and multi-hole nozzles is more apparent under the normal injection quantity conditions, which attributes to the wider multi-hole nozzle spray angel, spray cone angle, and unstable spray profiles results in the experiments.

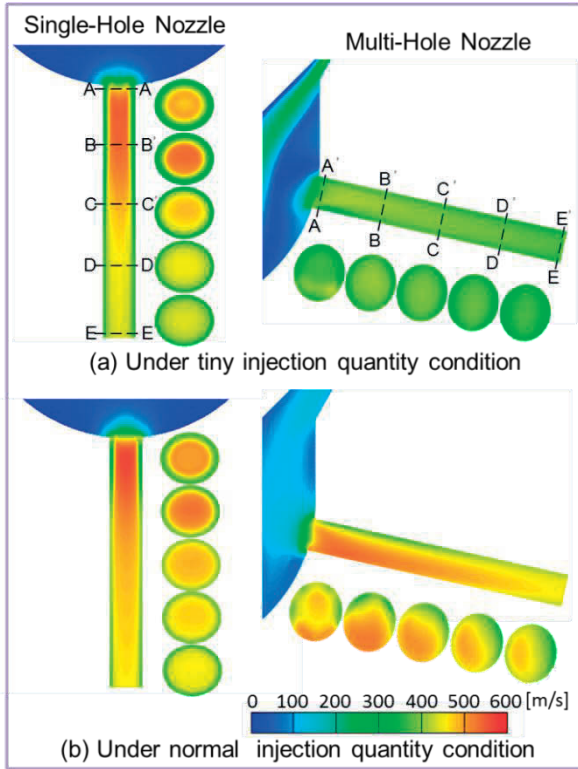


Figure 5.15 velocity distribution

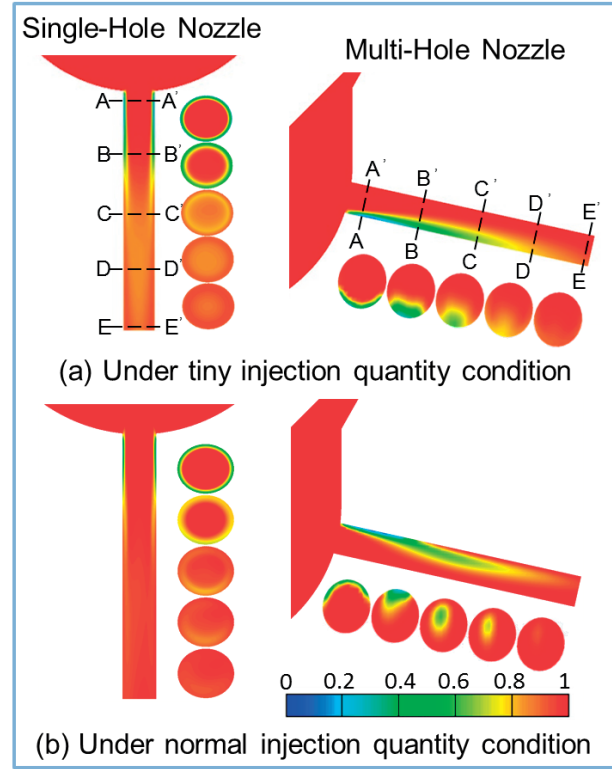


Figure 5.16 Liquid volume fraction distribution

The velocity characteristics inside different nozzles at the full needle lift timing under tiny and normal injection quantity conditions is shown in Figure 5.15. The velocity distribution inside the single-hole nozzle is symmetric, and it is higher than the asymmetrical flow velocity inside the multi-hole nozzle, especially under the tiny injection quantity condition. This is mainly caused by the lower sac pressure and sharp bend and change of flow direction of the multi-hole nozzle. It also can be concluded that compared with the single-hole nozzle, the flow velocity inside the multi-hole nozzle is more sensitive to the variation of the injection quantity condition.

The different cavitation shape and collapse position inside the holes can also have a strong effect on the spray break up [Payri et al., 2012]. Meanwhile, the needle lift could alter the cavitation and turbulent inside both of the single-hole and the multi-hole nozzles [Margot et al., 2010 and 2011]. The structure of the liquid volume fraction under different needle lift and injection quantity conditions is shown in Figure 5.16. For the single-hole nozzle, the film-type cavitation generated by flow separation mainly appears in the upstream region around the wall of the nozzle hole symmetrically, and rarely reaches the centre of the exit section. Caused by the large vortex structure in the sac, its cavitation intensity is higher under the tiny injection quantity condition, which can attribute to the waved spray contours observed in the experiments. However, the

cavitation position and intensity are all unstable inside the multi-hole nozzle. It should be noted that there is absolutely distinct cavitation structure inside the multi-hole nozzles under different injection quantity conditions. For the tiny one, caused by the lower needle lift, the high pressure fuel, which flows into the low pressure sac volume, can reach to the bottom of the sac, and then flow into the hole entrance with generating large vortex inside the sac. The cavitation is mainly caused by the flow separation, and located in the lower part of the hole volume. On the contrary, the string-type cavitation, which is generated by the spiral and streamwise counter-rotating flow, can be observed under the normal injection quantity condition. Moreover, the position of the cavitation is in the upper part of the nozzle hole geometric, and it can even reach the central area of the exit section. All of the unstable cavitation structure described above inside the multi-hole nozzle can be used to explain its unique and fickle spray behaviors observed in the experiment. There is also significant difference in the cavitation behaviors between the single-hole and multi-hole nozzles under both tiny and normal injection quantity conditions. The cavitation in the multi-hole nozzle is asymmetric and unstable compared with that in the single-hole nozzle, and it can be conceivable that the higher mass and momentum exchange in the downstream region of the multi-hole nozzle volume are more conducive to the wider spray cone angle plotted in last chapter.

It is known that the intense turbulent flow pattern injected from the nozzle hole plays a significant role in the primary breakup process of the spray, which can also result in stronger liquid/ambient gas interactions, lower spray velocity, and wider spray diffusion. Figure 5.17 shows the normalized turbulence kinetic energy (TKE) along the horizontal hole diameter line of different nozzles at the full needle lift timing under different injection quantity conditions.

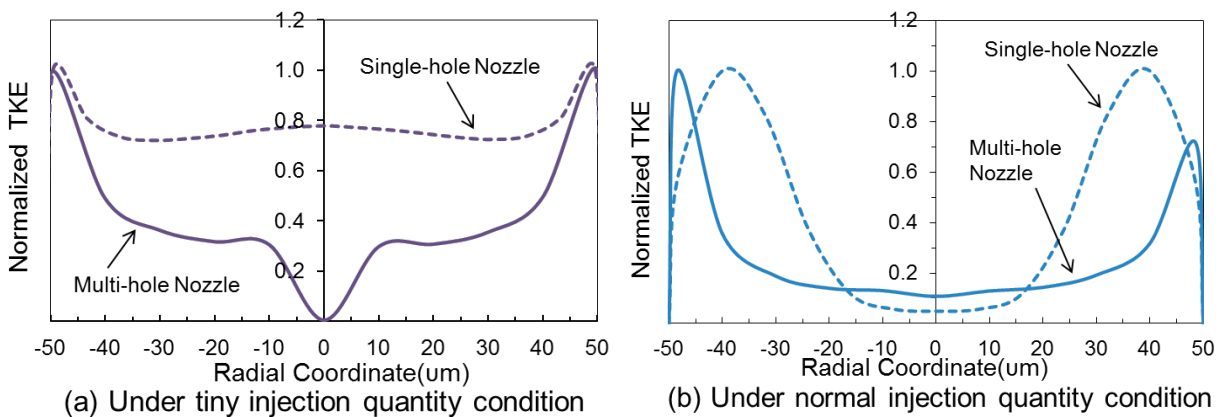
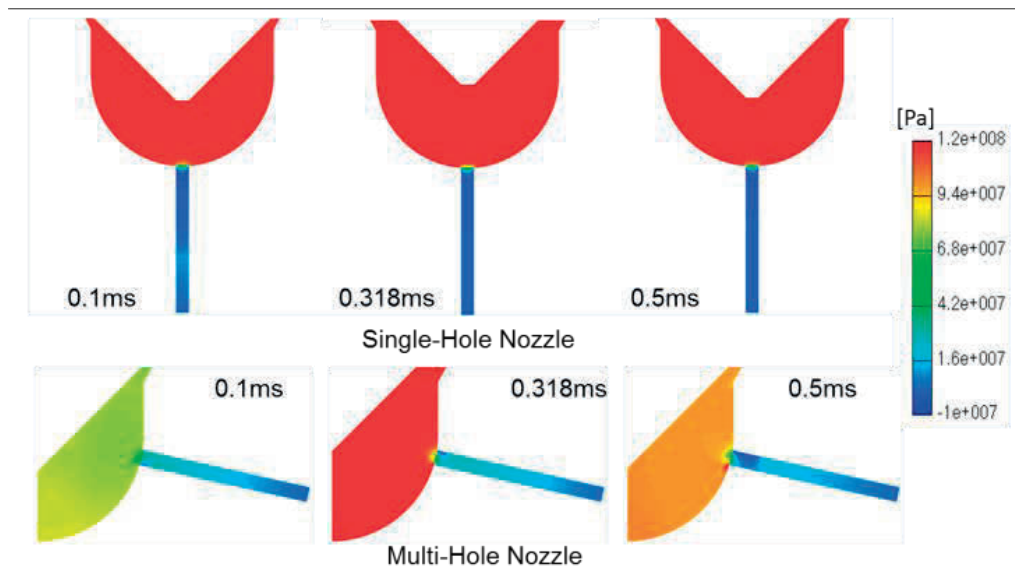


Figure 5.17 Normalized turbulence kinetic energy on the outlet of different injectors

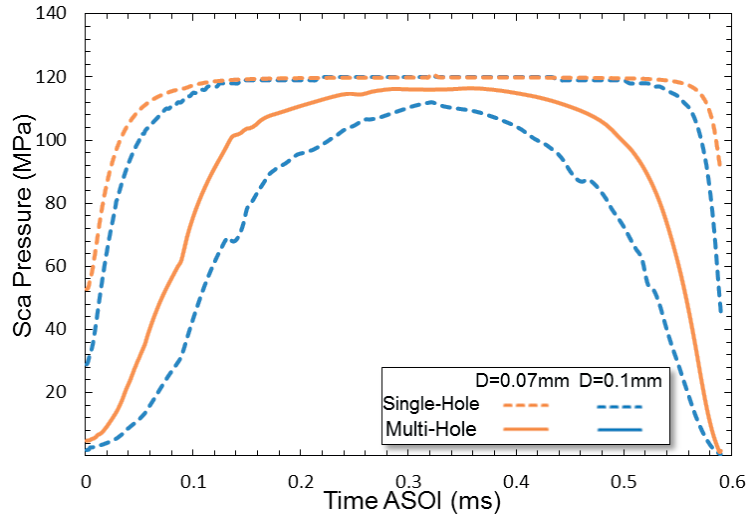
Under the tiny injection quantity condition, the gradient of this value of the multi-hole nozzle is much larger than that of the single-hole nozzle, which indicates that the spray behaviors of the multi-hole nozzle in the boundary locations are more unstable, resulting in the wider spray angle and cone angle. Meanwhile, under the normal injection quantity condition, although the gradient of this value is all obvious, its peak value appears more closer to the nozzle hole wall of the multi-hole nozzle, which predicts that at the boundary location, the interaction between multi-hole nozzle spray and the ambient air should also be more serious, and the multi-hole nozzle should have a wider spray angle and cone angle.

5.2.4 Effect of Micro Nozzle Hole Diameter

The simulation condition is corresponding to the Mie scattering experimental conditions. The 0.10 mm and 0.07 mm hole diameter is applied in the study. The pressure variations in different nozzles on typical injection stage are shown in Figure 5.18- (a). The time resolved pressure variation in the sac of different nozzles is shown in Figure 5.18-(b). Overall, the rate of increasing pressure in the single-hole nozzles is much higher than that of the multi-hole ones. Attention should be paid to the multi-hole nozzle with micro holes. Its sac and hole pressures are all higher than those of the multi-hole one with larger orifices at each injection stage, which coincides with the experimental analysis.



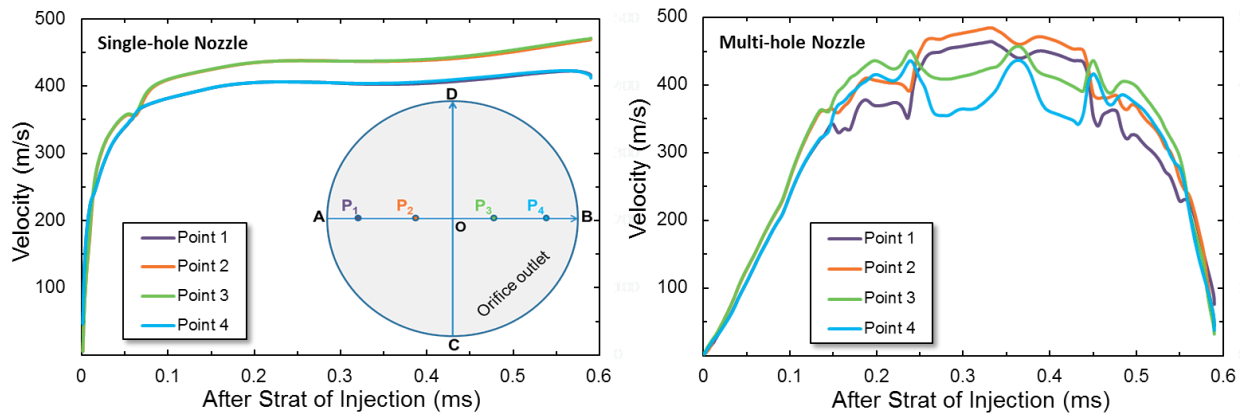
(a) Pressure distribution under hole diameter of 0.07 mm condition



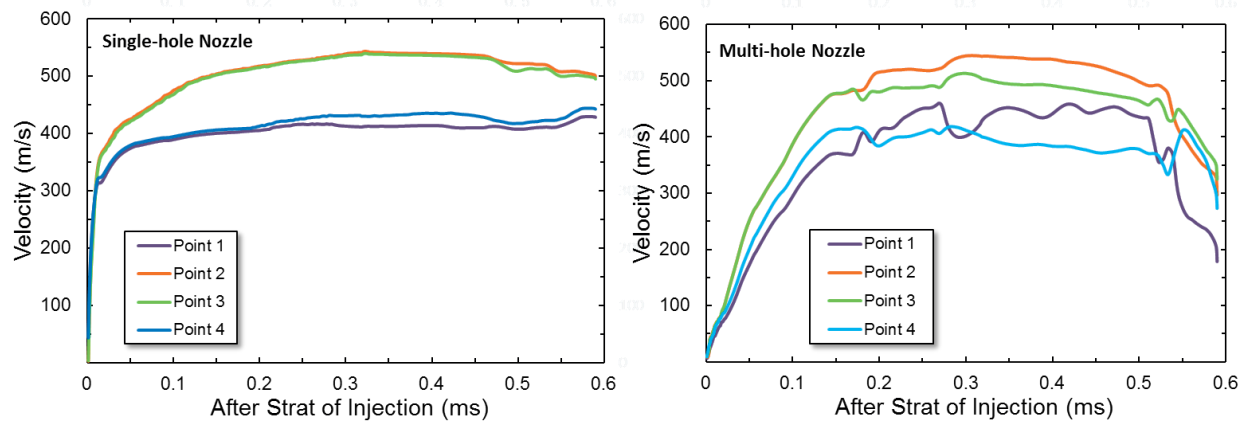
(b) time resolved pressure variation in the sac of different nozzles

Figure 5.18 Comparison of pressure variation under different hole diameter conditions

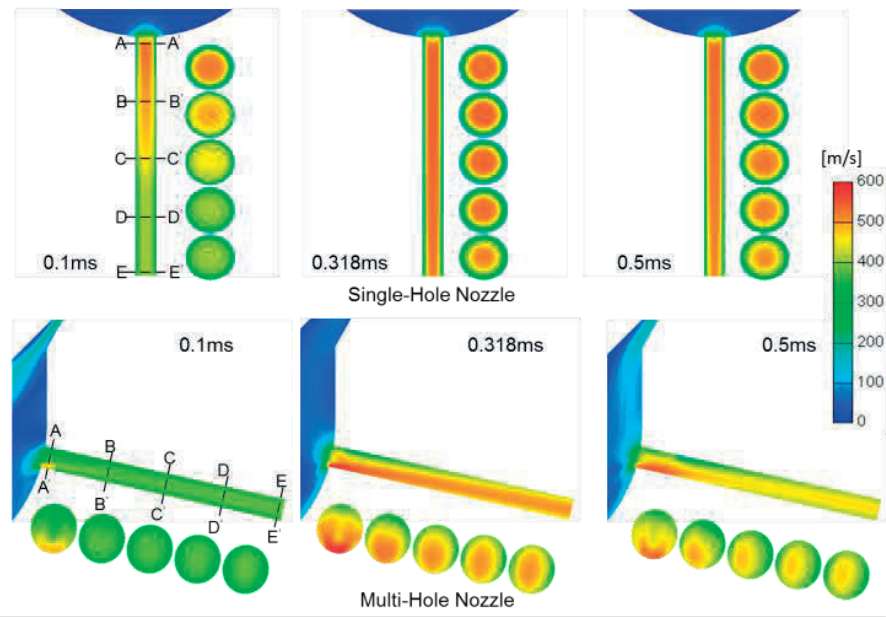
The temporal velocity variation on the outlets of the four nozzles is shown in Figure 5.19. Four monitoring points (P_1 , P_2 , P_3 and P_4) were set along the horizontal diameter line (Line A-B) symmetrically.



(a) Under hole diameter of 0.10 mm condition



(b) Under hole diameter of 0.07 mm condition



(c) Velocity distribution in different nozzles Under hole diameter of 0.07 mm condition

Figure 5.19 Temporal variation of fuel velocity at the monitoring points on the orifice outlets

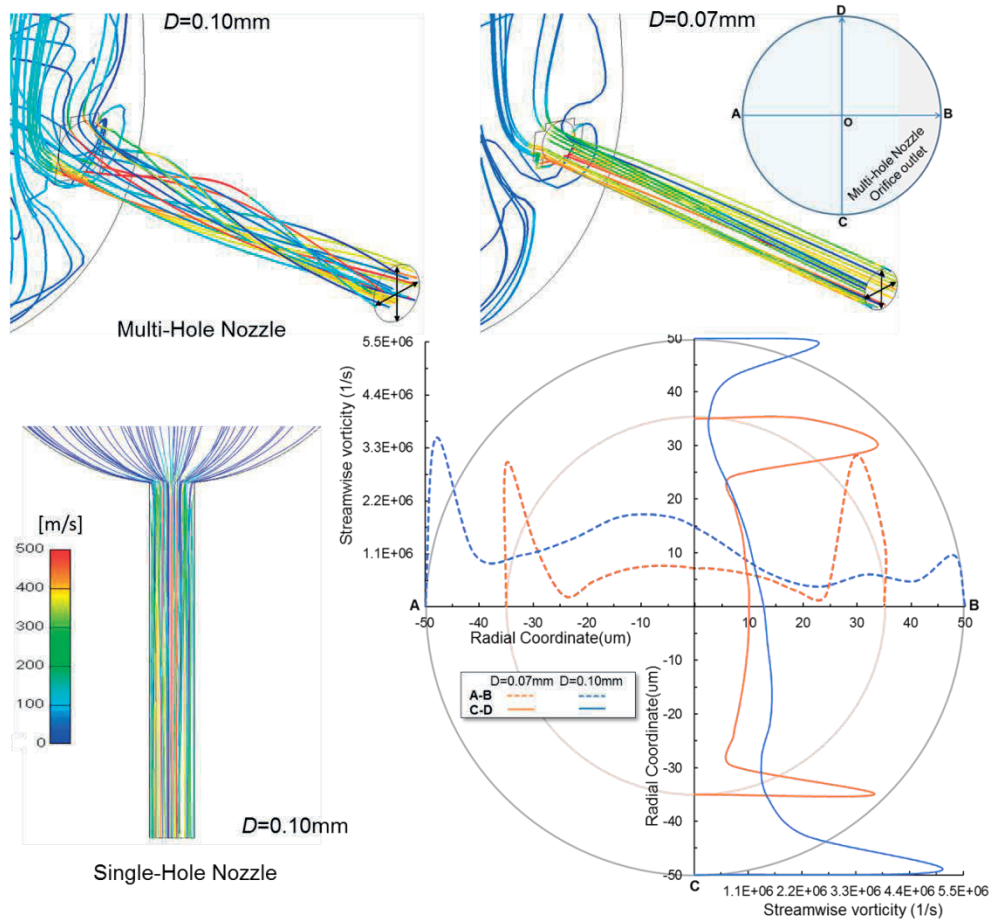


Figure 5.20 Streamline and streamwise vorticity distribution along the horizontal and vertical diameter lines on outlets of different multi-hole nozzles at full needle lift timing

The streamlines and vorticity distributions along the orthogonal orifice lines, shown in Figure 5.20, can provide another view to interpret the instance observed in the experiments. Under the larger orifice condition, much more complicated streamlines with higher stream-wise vorticity, stronger curvatures and counter-rotating flow are generated inside the hole volume of the multi-hole nozzle. This spiral flow is also observed by Gavaises and Andriotis [2006], Lai et al. [2011], and Hayashi et al. [2014]. It has been proven that there are close correlations between this swirling motion and the wider spray cone angle. However, the streamline inside the single-hole nozzle is very smooth. When attention is paid to the nozzles with micro orifices, the vorticity decreases, and the streamline is stable and smooth relatively even inside the multi-hole nozzle. This agrees with the reduced deviation of the spray behaviors between single-hole and multi-hole nozzles with the smaller hole diameter.

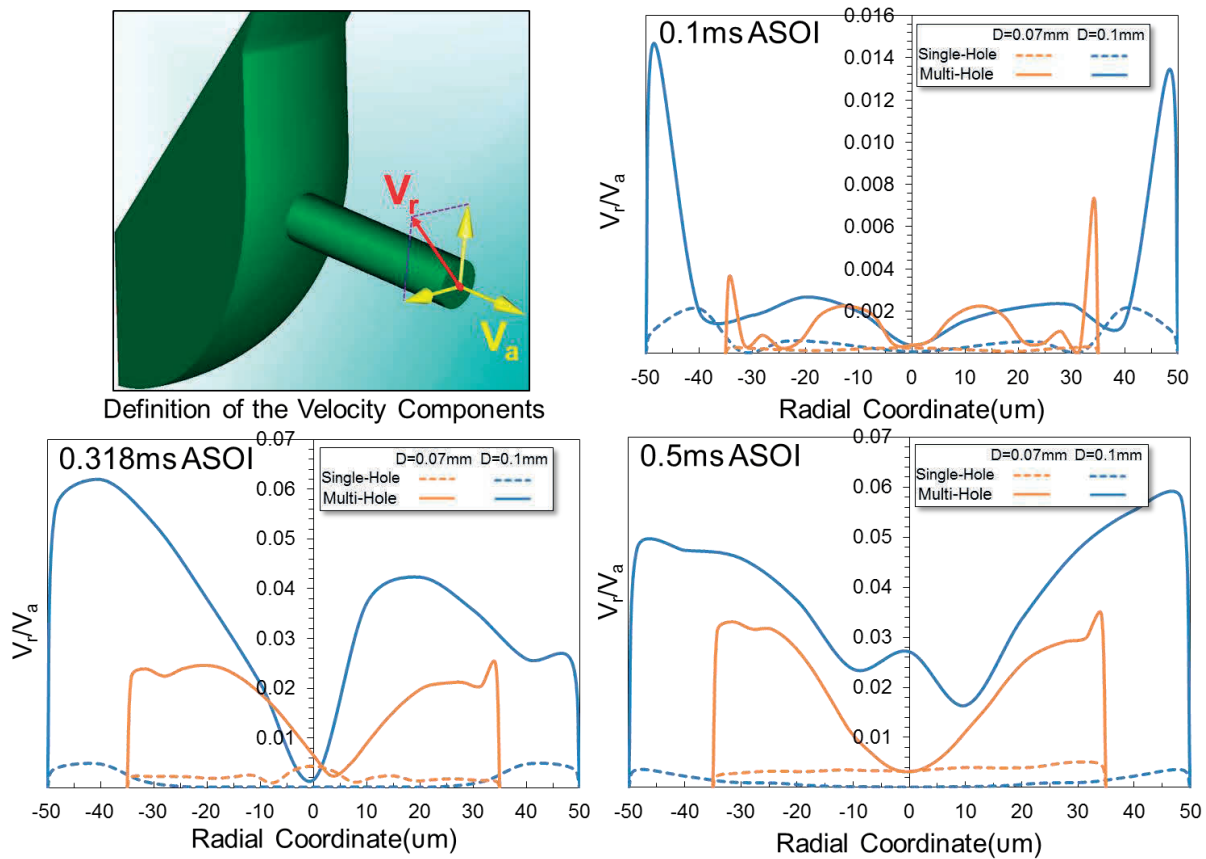


Figure 5.21 Variations of the ratio of velocity components (V_r/V_a) on the outlet of different nozzles at typical timings

In fact, the fuel injected from the exit section of the nozzle hole can be divided into three vectors as shown in Figure 5.21. The definition of different velocity components is already

introduced before. On the whole, this ratio calculated from the multi-hole nozzle at three typical timings is all much higher than that of the single-hole one, which provides additional explanations for the reason why the multi-hole nozzle has the wider spray cone angle. Furthermore, it can be seen that this kind of difference is reduced relatively under the micro orifices condition, which verifies previous analysis about the experimental results.

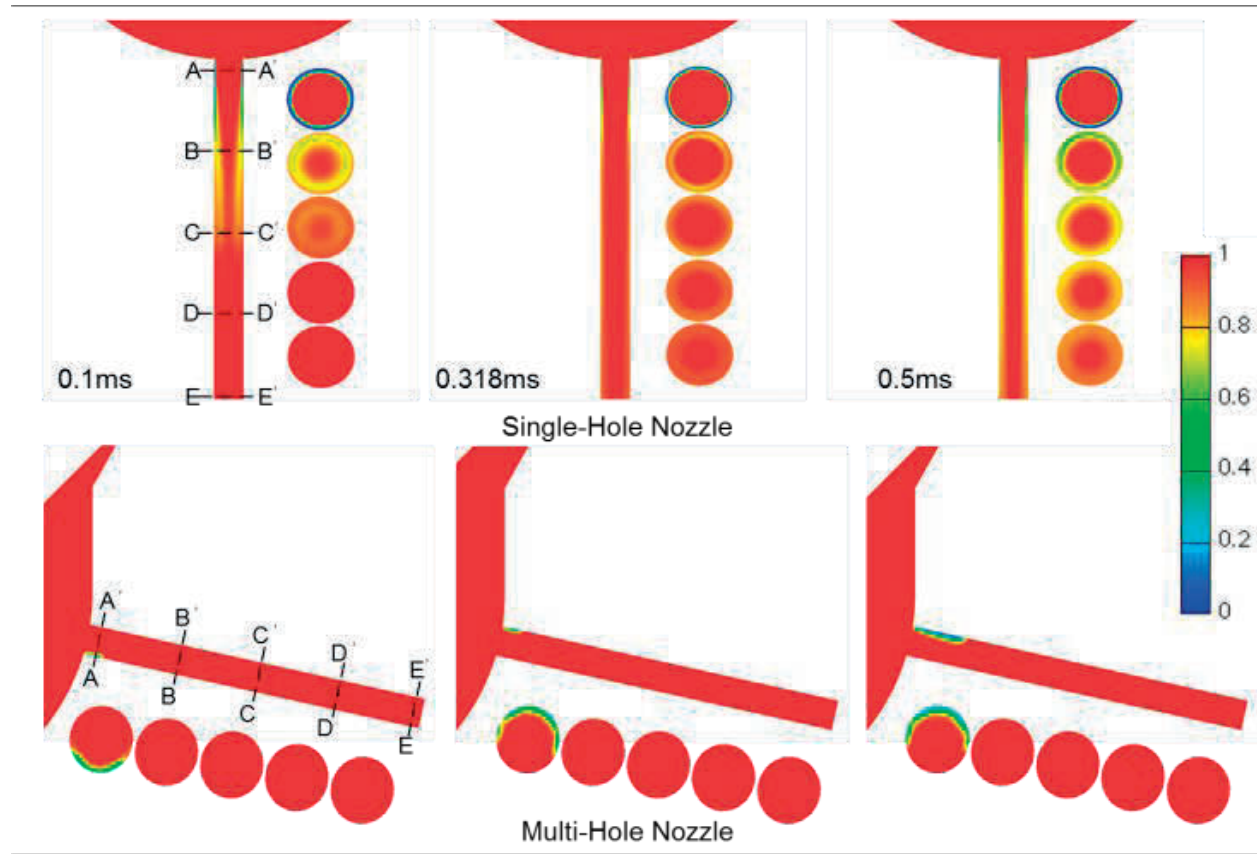


Figure 5.22 Temporal variation of liquid volume fraction distribution inside different nozzle holes

The temporal variations of the liquid volume fraction are shown in Figure 5.22. The difference between single-hole and multi-hole nozzles is already discussed under the normal diameter conditions. However, under the smaller hole diameter condition shown in Figure 5.22-(c), the cavitation intensity is much smaller than that of the nozzles with the larger orifices. This is attributed to the higher pressure and smoother flow structure inside the hole volume of the multi-hole nozzle with the micro orifices.

5.2.5 Internal Flow and Spray Transient around the End and Start of Injection

It is well known that the spray penetration and the mixing process are mainly affected by the nozzle configuration and the shape of fuel injection ramps, especially under the short multiple injection strategies, which is generally applied in the direct injection engines [Pickett, L., 2013]. Moreover, the internal flow and the spray transient around the end and the start of injection during the multiple injection instances have significant impact on engine performance and emissions under the concept of the conventional diesel combustion and HCCI engines [Musculus, M., 2009].

Figure 5.23 shows the calculated mass flow rate of different kinds of nozzles. The increasing rate, decreasing rate, and the maximum value of the mass flow rate of the single-hole nozzle are all much higher than those of the multi-hole nozzle, which coincides with the experimental result analyzed before. The averaged sac pressure inside different nozzles around the end of injection is presented in Figure 5.24.

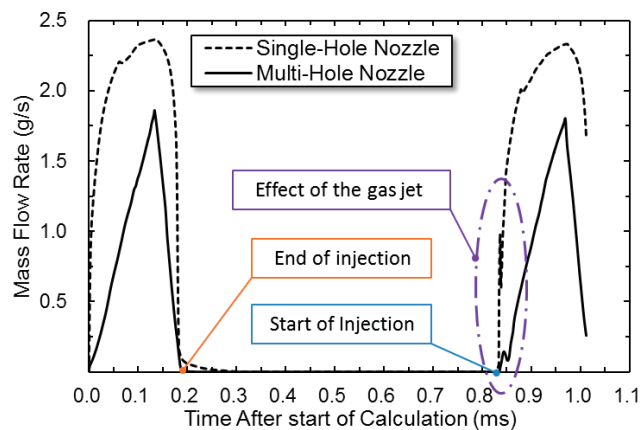


Figure 5.23 Calculated mass flow rate

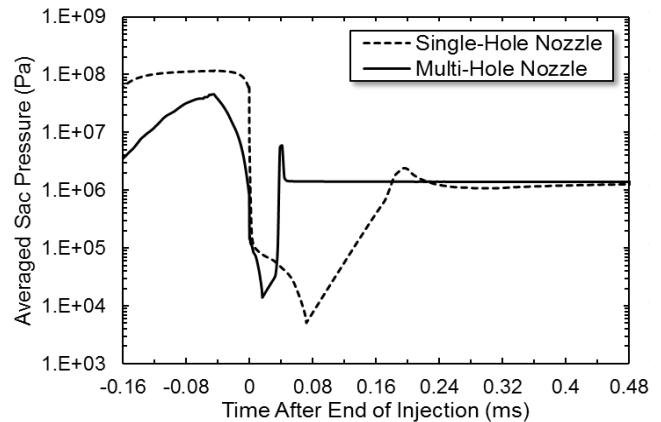
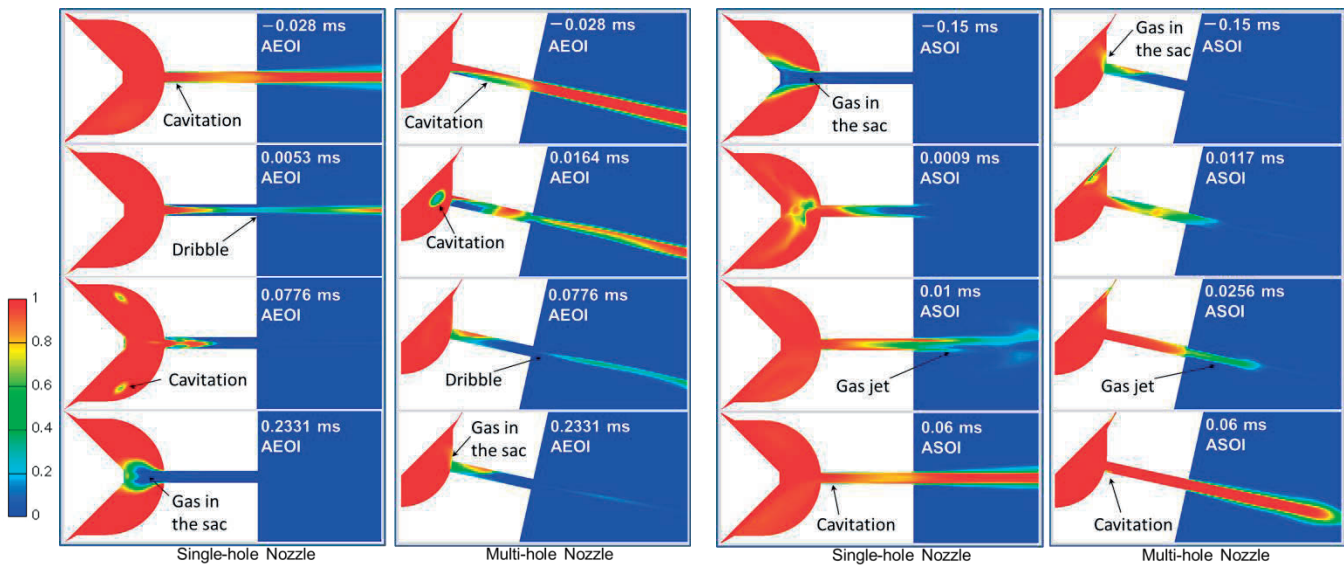


Figure 5.24 Averaged sac pressure variation

The sac pressure of the single-hole nozzle is almost steady before the end of injection, but the sac pressure of the multi-hole nozzle varies with the needle moving. The sac pressure of the two nozzles all reaches a minimum after the close of the needle, which can generate the void fraction and cavitation in the sac and hole volume. Affected by the lower flow velocity in the hole and the lower pressure decreasing rate in the sac, the minimum sac pressure of the multi-hole nozzle is higher than that of the single-hole one. The original high velocity liquid column decreases due to the low pressure upstream, and the rupture occurs forming dribbles. After that, the ambient gas is drawn into the low pressure sac volume, and this back flow refill the sac volume. As shown in Figure 5.23, the sac pressure increases to the level of the ambient pressure after this fluctuation. It

is known that the theoretical flow area of the single-hole nozzle is one tenth of that of the multi-hole nozzle. As a result, it takes relatively longer time for the single-hole nozzle to finish this process.

Figure 5.25-(a) shows the internal flow and spray transient around the end of the tiny mass injection of the single-hole and multi-hole nozzles. Overall, during the closing process of the needle, the liquid jet decelerates dramatically, and the rupture of the liquid column occurs with the formation of the dribbles consequently. It is shown that this kind of rupture and dribbles can enhance the flow instabilities, small-scale turbulence, and the air entrainment, and finally generate the local over-mixing region, which is one of the significant source of the soot and unburned-hydrocarbons emissions [Bruneaux, G., 2005; Hu, B., et al., 2010]. After that, the ambient gas is drawn into the sac through the open orifice and refills the sac volume promptly as the analyzing about Figure 5.24.



(a) Around the end of injection

(b) Around the start of injection

Figure 5.25 Spray transient: the phenomena around the start and end of the injection

However, there are a lot of distinctions between the single-hole and the multi-hole nozzles. The cavitation distribution in the single-hole nozzle before the end of injection is symmetric, and the cavitation level is lower, but due to the off-axis arrangement of the orifice and the low needle lift, the cavitation in the multi-hole nozzle mainly appears in the lower part of the hole volume. The appearing timing of the jet rupture and the dribbles of the multi-hole nozzle is later than that of the single-hole nozzle due to the lower sac pressure and the lower jet velocity. Affected by the different arrangement of the hole, it is easier for the ambient gas to entry into the sac of the single-hole nozzle, but only few gas can entry into the sac of the multi-hole nozzle along the inclined holes.

Figure 5.25-(b) shows the internal flow and spray transient around the start of the tiny mass injection of the single-hole and multi-hole nozzles. On the whole, the start of a new injection event is consequently affected by the presence of the residual gas in the sac. With the needle lifting up, the liquid fuel fills the nozzle sac and hole volume, and pushes previously ingested gas out of the orifice (as presented Figure 5.23), and the initial plume is mainly the gas jet with fine turbulent structures. Gradually, the liquid jet tip reached the gas tip, and it is conceivable that the simultaneous fuel and air mixing process occurring with the expelled gases can change the mixing process with the fresh air and the vaporization rate of the first part of the injection.

There are also some obvious differences between the single-hole and multi-hole nozzles around the start transit of the tiny mass multiple injection. The velocity of the gas jet and the liquid jet of the multi-hole nozzle is all lower than that of the single-hole one, since the increase rate of the sac pressure is different as analyzed before. The appearing timing and the locations of the cavitation are different as well. It is expected that the phenomena analyzed above have strong relationship with the different spray behaviors observed in the experiments.

According to the results of the internal flow of the different nozzles, except for the spray to spray interactions, it is the unique properties of the internal flow in multi-hole nozzles that affect their spray behaviors. These spray properties are also affected a lot by the orifice diameter. It is observed that the internal flow pattern inside the multi-hole nozzle with the smaller orifice is more similar to that inside the single-hole nozzle.

5.3 INTERNAL FLOW VARIATION OF MULTI-HOLE NOZZLES

The comparison of internal flow characteristics between single-hole and multi-hole nozzles was conducted in last section, it is obvious that the multi-hole nozzles have the unique properties. As a result, the multi-hole nozzle internal flow will be discussed further in this section.

5.3.1 Under Different Dynamic Operation Conditions

In fact, the effect of one kind of dynamic operation condition (injection quantity) on multi-hole nozzle spray has already been discussed when conducting the comparison between the single-hole and multi-hole nozzles in last section. The multi-hole nozzle is very sensitive to the variation of injection quantity, and a lot of comprehensive description, explanation, and analysis are also conducted. Therefore, in this section, the other one operation condition (injection pressure) will be paid more attention. The conditions are also corresponding to the Mie scattering experimental conditions. Under normal and tiny quantity conditions, three kinds of injection pressures were

conducted. The result will be shown in the following paragraphs, and the nozzle hole length is 0.6 mm, the diameter is 0.10 mm. The needle lift curves for normal and tiny quantity conditions are shown in Figure 5.26.

The mass flow rate on the hole exit for normal and tiny injection quantity under three different injection pressure conditions is shown in Figure 5.27. The mass flow rate increases with the rail pressure increasing. The fluctuation of the mass flow rate curves under the large injection quantity is obvious, while the curve is smooth under the small quantity condition. The shape of the mass flow rate curve under the small injection quantity is sharp, while the shape under large quantity condition is slick relatively.

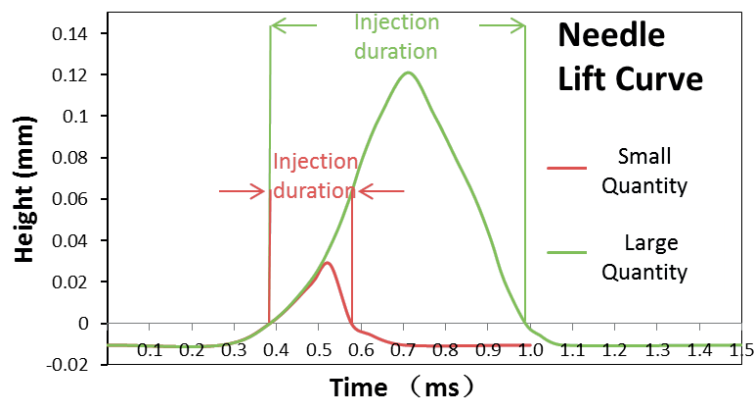


Figure 5.26 Needle lift curve applied in the simulation

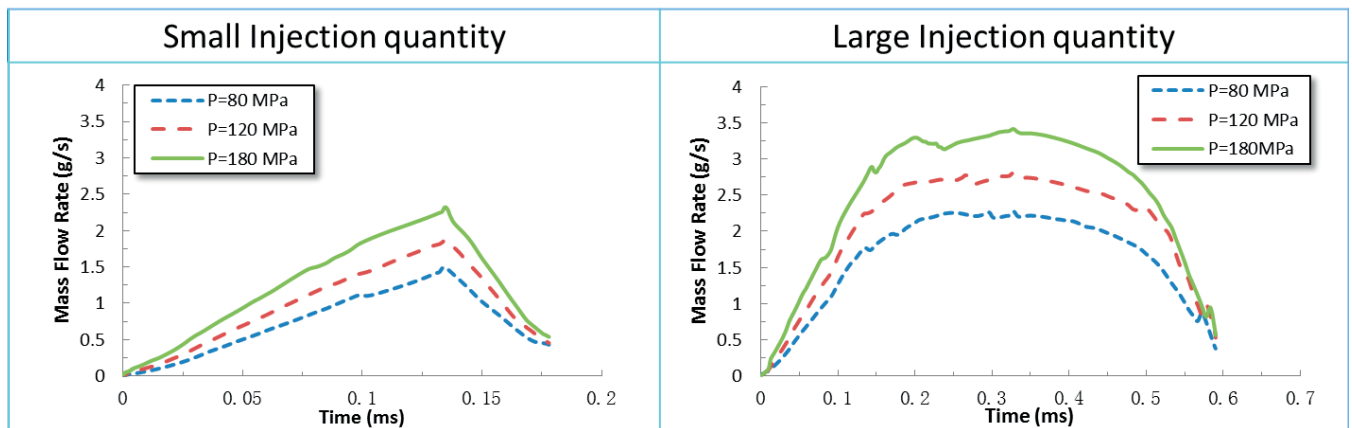


Figure 5.27 Mass flow rate under different conditions

Figure 5.28 is the pressure distribution inside the nozzle at the full needle lift timing under different injection quantity and injection pressure conditions.

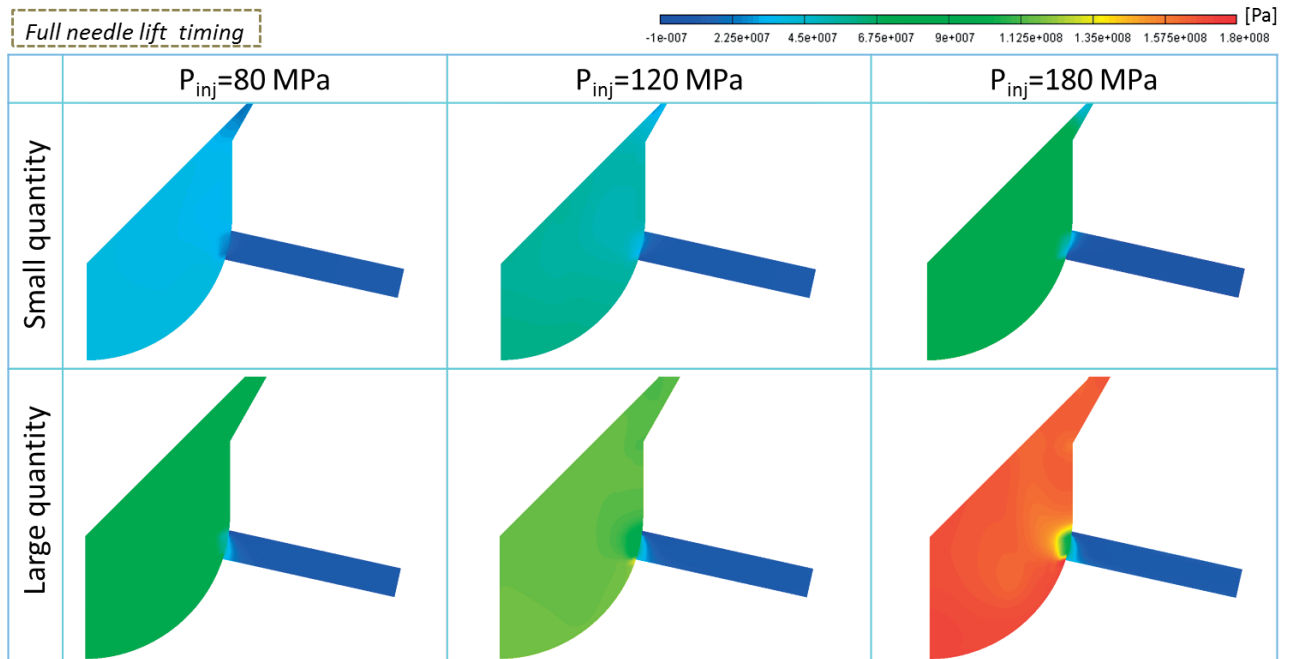


Figure 5.28 Pressure distribution inside nozzles under different conditions

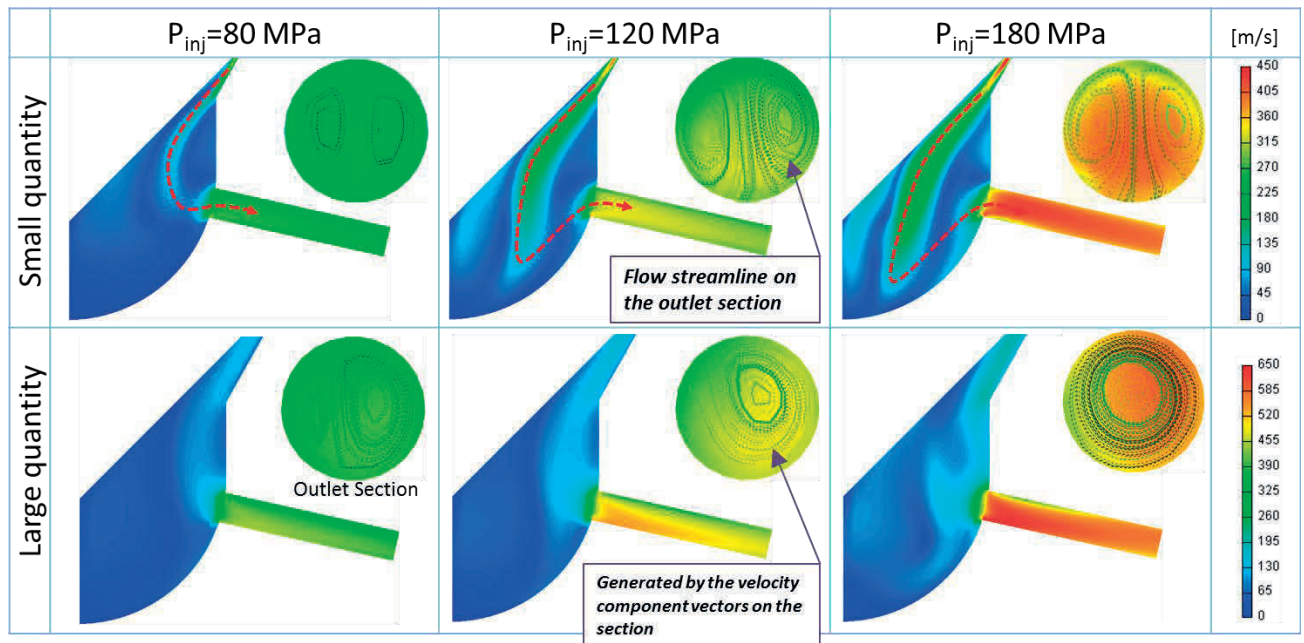


Figure 5.29 Velocity distribution inside nozzles under different conditions

The upper row is the small injection quantity condition. The lower row is the normal injection quantity condition. With the increasing of the injection pressure, the sac pressure is increased. Moreover, the sac pressure under large injection quantity condition is all higher than

that of the lower injection quantity condition, because the injection duration is longer and the needle lift is higher.

The velocity distribution inside the nozzle is shown in Figure 5.29. The outlet section is all presented in the figure. The dash line means the flow streamline on this section, it is made from the flow velocity component vectors on the section. With the increasing of injection pressure, the velocity is increased. The main flow path in the sac is also changing with the injection pressure, like red dash line shows. It is easier for the main flow to reach to the bottom of the sac under higher pressure condition.

It also should be noted that under small injection quantity condition, there are two vortexes on the outlet section, while under larger injection quantity conditions, there is only one main vortex structure on this section, especially under higher injection pressure condition.

The streamline distribution at the full needle lift timing is shown in Figure 5.30. Under small injection quantity condition, as color arrow shows, the flow goes along three ways, and the vortex position in the sac is affected by the injection pressure obviously. Under large injection quantity condition, the flow entries into the hole along these two ways, and the way of the flow entering into the hole does not change so much with the pressure variation.

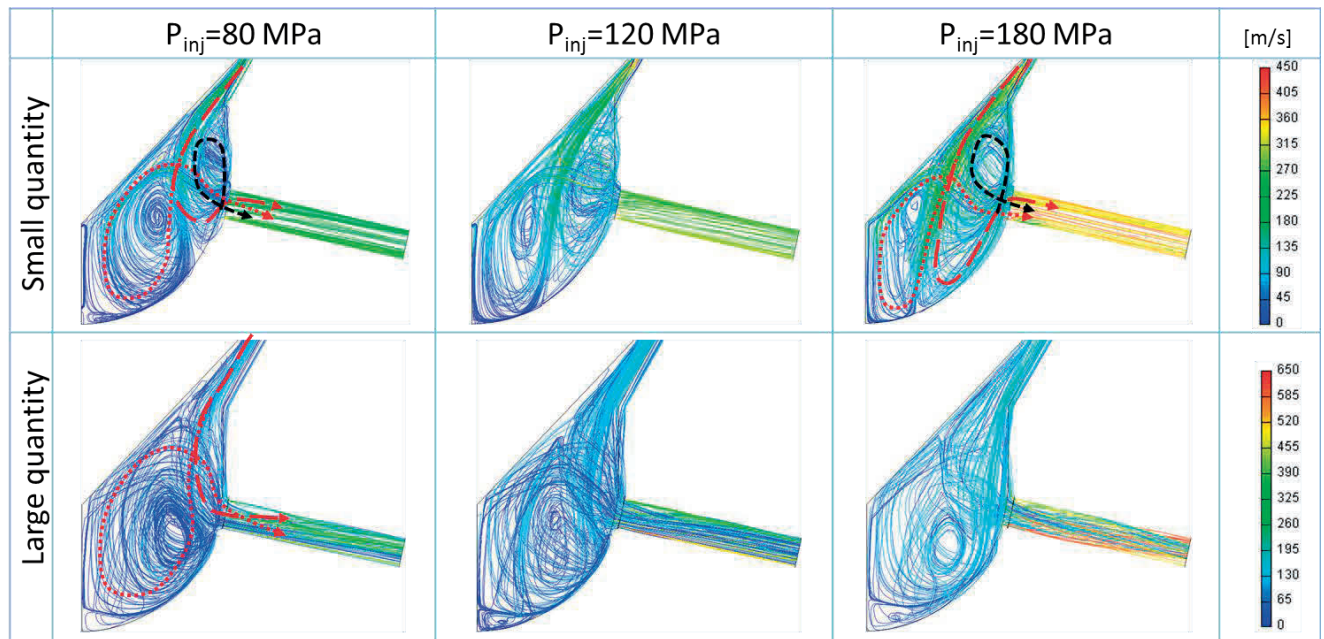


Figure 5.30 Streamline structure inside nozzles under different conditions

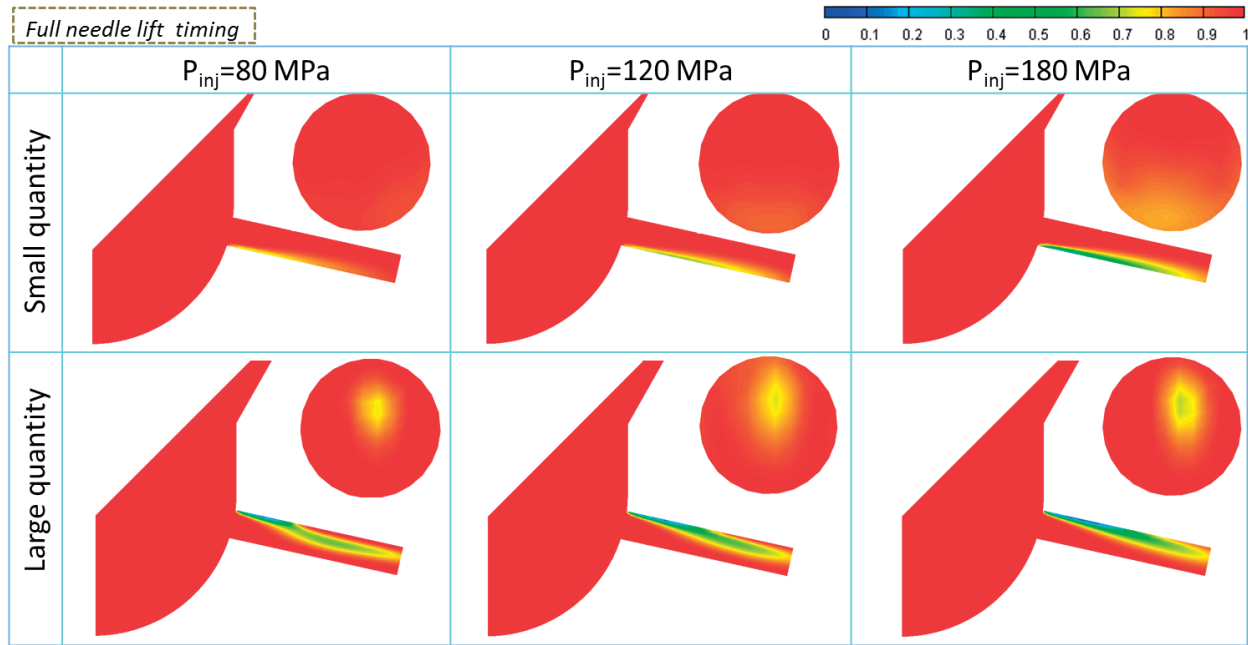


Figure 5.31 Liquid volume fraction inside nozzles under different conditions

The cavitation distribution under different conditions is presented in Figure 5.31. Overall, with the injection pressure increasing, the cavitation level is increased. Under small injection quantity condition, affected by the flow direction in the sac, the cavitation mainly appears in the downside region of the hole volume. However, under large injection quantity condition, the cavitation appears in the upside region of the hole volume at the full needle lift timing, and it can reach to the outlet of the hole.

5.3.2 Relationship between Nozzle Geometrical Structure and Internal Flow Properties

In this section, the effect of several factors on the internal flow properties of multi-hole nozzles will be discussed one by one, including the K factor, hole inlet roundness, hole diameter, and hole length.

Effect of K factor of the nozzle hole

The definition of the K factor of Nozzle hole is shown in Equation 5.1, and the parameter is indicated in Figure 5.32. The specific parameters of the nozzles applied in the study in shown in Table 5.2

$$K = \frac{D_i - D_o}{D_o} \quad (5.1)$$

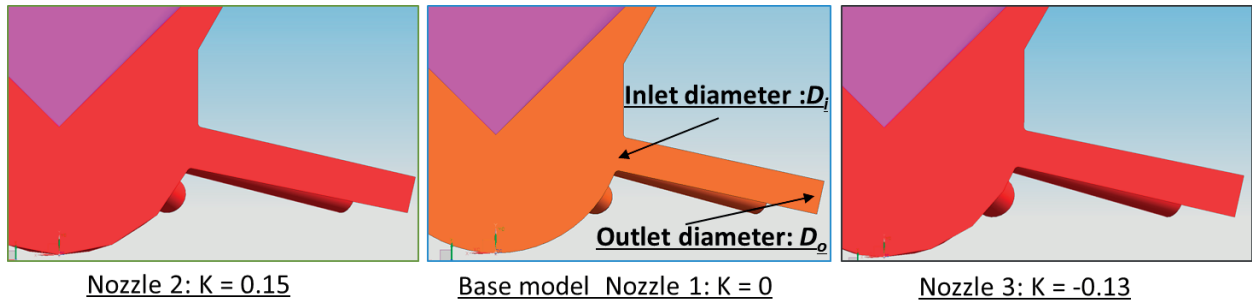


Figure 5.32 Schematic of different nozzles with conical holes in the study

The mass flow rate result calculated from three kinds of nozzles is presented in Figure 5.33. The left figure is the liquid flow rate on the nozzle hole outlet section, the right one is the vapor mass flow rate on the nozzles exits during the calculation, which is a reflection of cavitation. It can be seen that $K = 0.15$ condition has the highest liquid mass flow rate, while $K = -0.13$ condition has the most fluctuated liquid mass flow rate. Furthermore, $K = 0.15$ condition has the lowest vapor mass flow rate, and $K = -0.13$ condition has the highest vapor mass flow rate. This result can be explained by the cloud pictures in Figure 5.34.

Table 5.2 Nozzle Parameters

Item	Base	Conical hole	
<i>NO.</i>	1	2	3
Hole inlet diameter (mm)	0.133	0.153	0.133
Hole outlet diameter (mm)	0.133	0.133	0.153
K factor	0	0.15	-0.13
L (mm)	0.8	0.8	0.8
Inlet R (um)	16	16	16

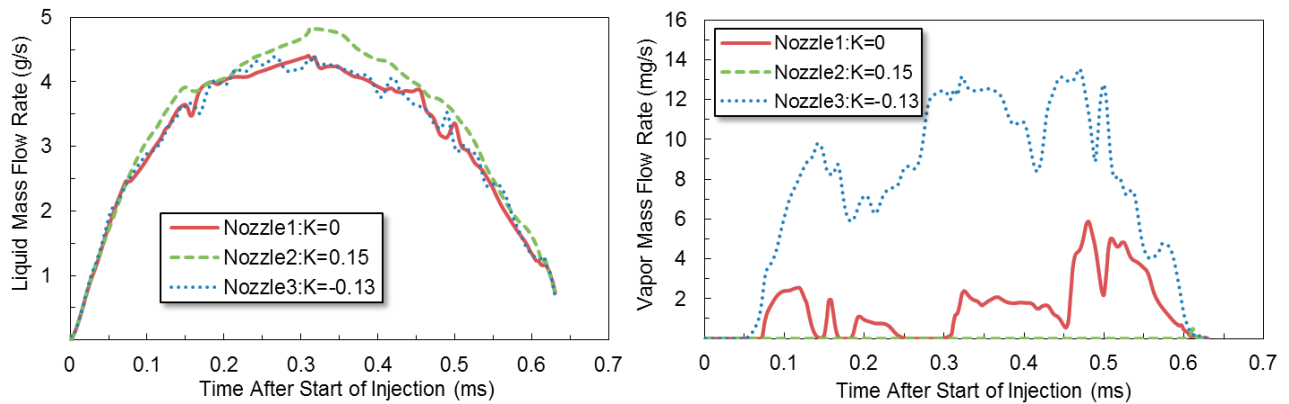


Figure 5.33 Mass flow rate result calculated from three kinds of nozzles

The pressure, velocity, and cavitation distribution inside different nozzles at the full needle lift timing is shown in Figure 5.34. Nozzle 2 has the lowest sac pressure, but highest hole pressure, hence the highest injection velocity, which is the reason why it has the highest mass flow rate. The cavitation level inside the Nozzle 3 is the highest, while caused by the higher pressure inside the nozzle hole, and the Nozzle 2 can suppress the cavitation, which is coincided with the vapor mass flow rate in Figure 5.33.

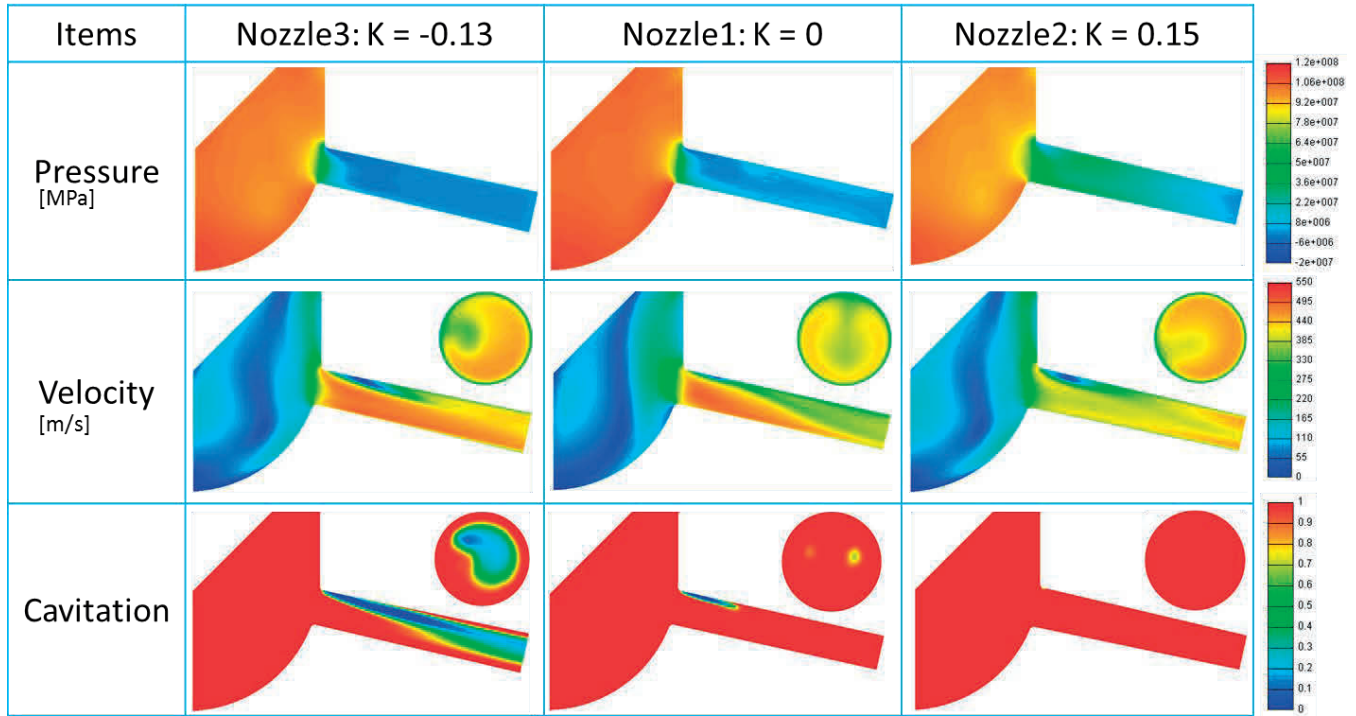


Figure 5.34 Pressure, velocity, and cavitation distribution inside different nozzles

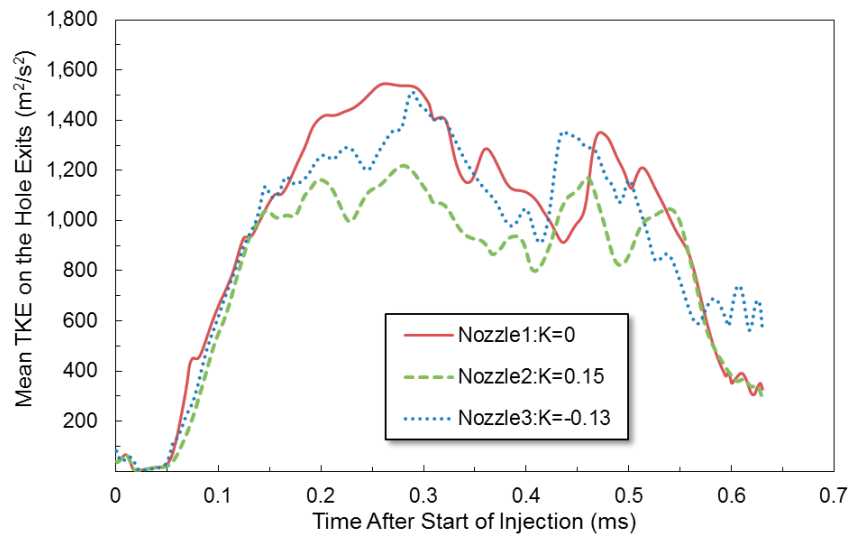


Figure 5.35 Average turbulent kinetic energy variation on the hole exits of three nozzles

The average turbulent kinetic energy variation on the hole exits of three nozzles is shown in Figure 5.35. There are two peaks of the average turbulence kinetic energy during the injection duration, which is corresponding to the nozzle lifting up and down, respectively. Nozzle 2 has the lowest level, which is caused by the small cavitation inside the hole.

Effect of nozzle hole inlet roundness

The nozzle hole inlet roundness is another important factors that alter the nozzle internal flow and spray behaviors. The nozzles with 0.8 mm hole length, 0.133 mm hole diameter, and different hole inlet roundness, which is shown in Figure 5.36, are applied in the investigation. The same needle lift cure was selected, and the discussion will be conducted in next page. Because it is easier for the fuel to entry into the hole with larger roundness, with the increase of the hole inlet roundness, the sac pressure is decreased, which can be seen in detail in Figure 5.37.

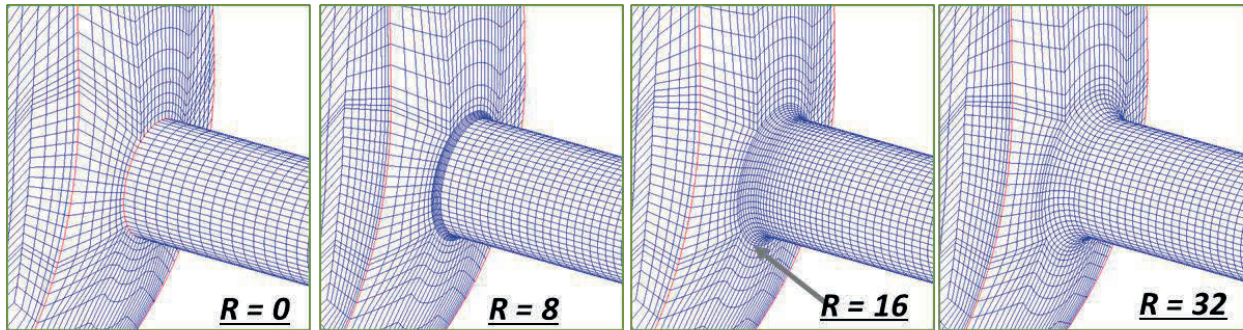


Figure 5.36 Nozzles meshes for calculation with different hole inlet roundness

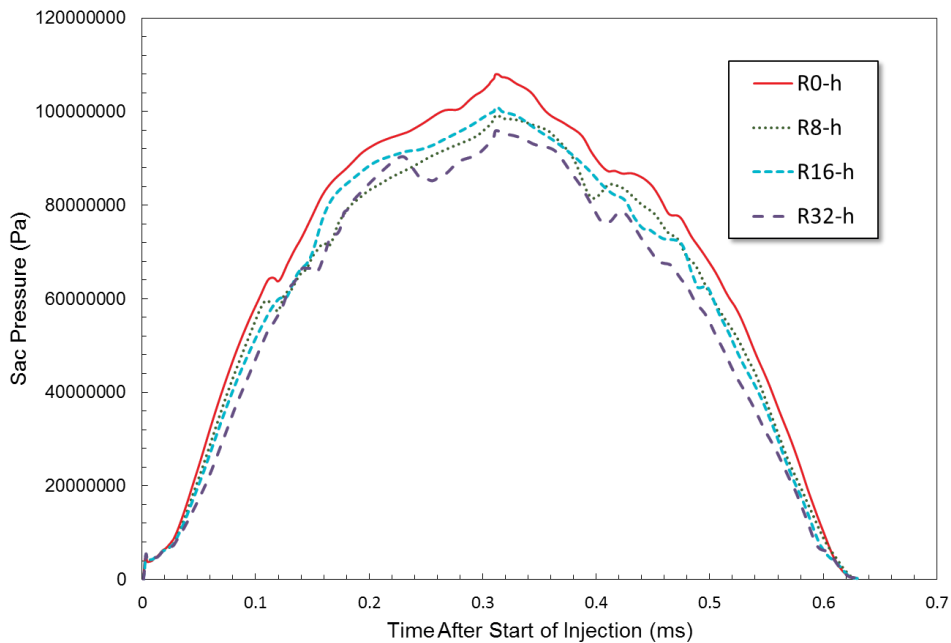


Figure 5.37 Sac pressure variation of different nozzles

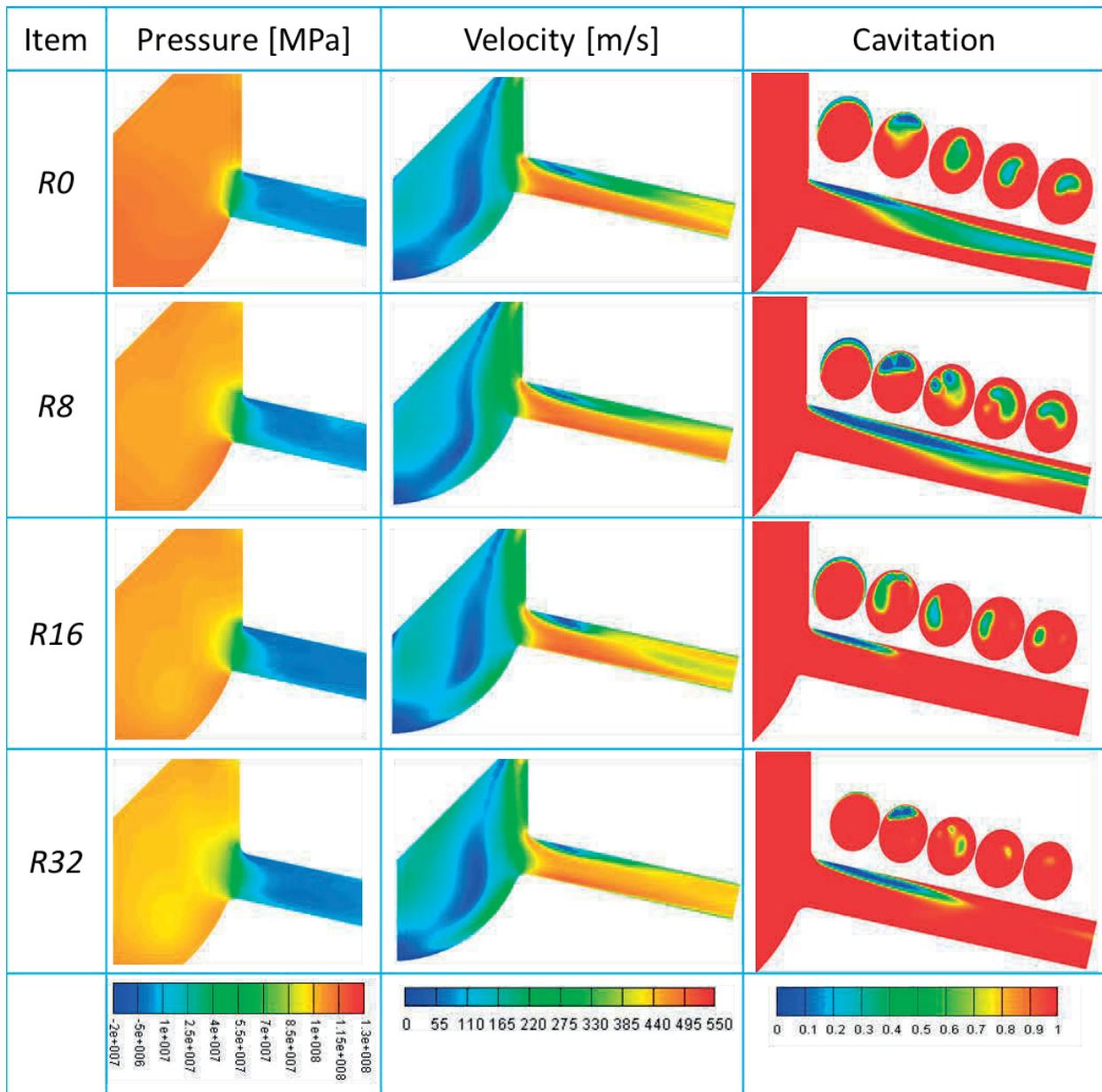


Figure 5.38 Pressure, velocity, and cavitation distribution inside different nozzles

The pressure, velocity, and cavitation distribution inside different nozzles at the full needle lift timing is shown in Figure 5.38. Because it is easier for the fuel to entry into the hole with larger roundness, with the increase of the hole inlet roundness, the sac pressure is decreased, which can be seen in detail in Figure 5.37. This trend is more obvious in the upstream region of the hole entrance. By increasing the hole inlet roundness, it can reduce the cavitation level, because the flow separation is reduced under the smoother hole inlet edge conditions, which can also be proved by the velocity pictures.

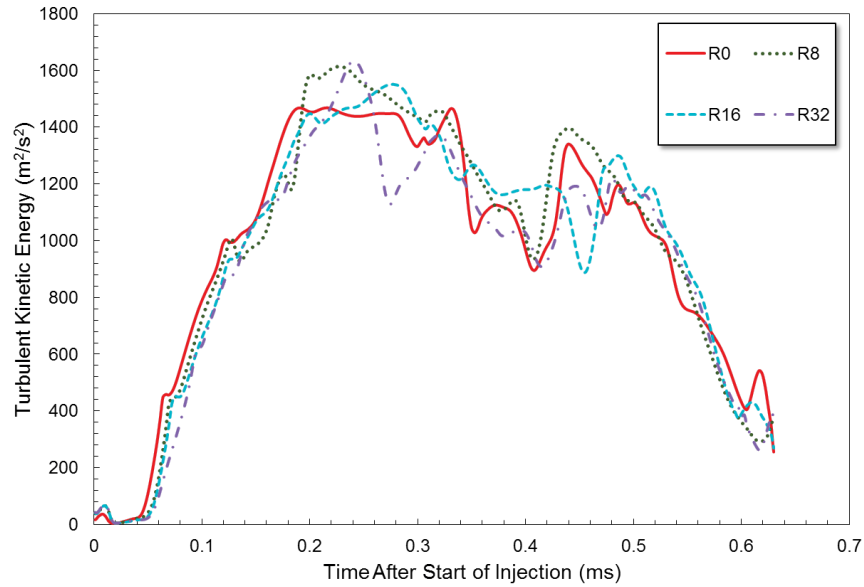
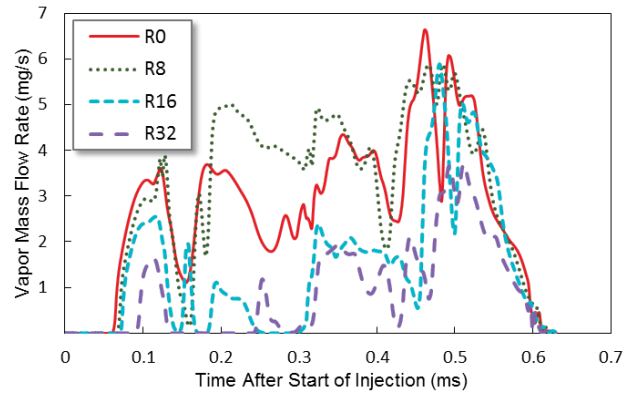
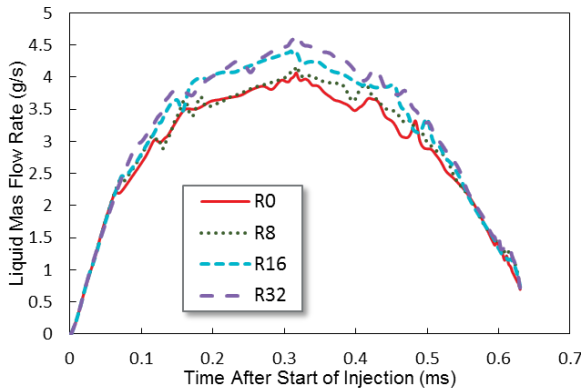
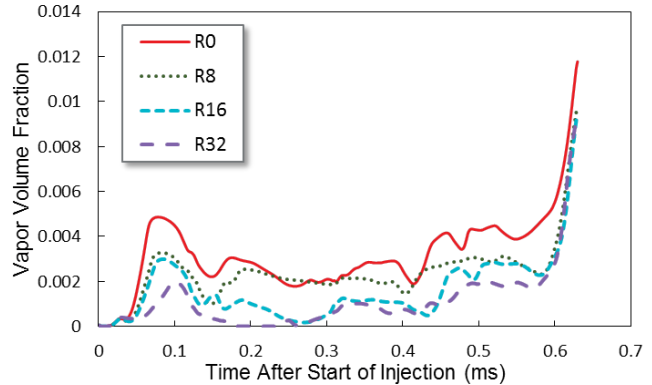
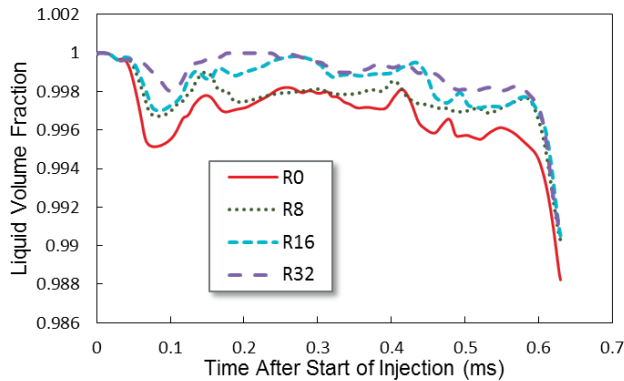


Figure 5.39 Average turbulent kinetic energy variation on the hole exits of four nozzles

There is not too much deviation in the average turbulent kinetic energy variation on the hole exits of four nozzles (see Figure 5.39), while it seems that the sharp hole edge can produced much more turbulence inside the hole.



(a) Mass flow rate on the hole exit of different nozzles



(b) Liquid and vapor volume fraction inside different nozzles

Figure 5.40 Mass flow rate and volume fraction of Liquid and vapor phase of different nozzles

The liquid and vapor mass flow rate on the nozzle hole exits of different nozzles is presented in Figure 5.40, and liquid and vapor volume fraction is also shown in this figure. With the increase of the hole inlet roundness, the liquid mass flow ratio on hole exit is enhanced, and the vapor mass flow is reduced consequently. The volume fraction of different phase is in accordance with the trend above.

Effect of nozzle hole diameter

When it comes to the nozzle hole diameter, although the micro hole diameter effect has already been discussed in last section, the hole diameter variation influence will be discussed more here under three different nozzle hole diameter conditions. The whole setting is corresponding to the baseline condition of Mie scattering experiments, and the nozzle hole length is 0.8 mm, and the diameter is 0.07 mm, 0.10mm, and 0.133 mm, respectively.

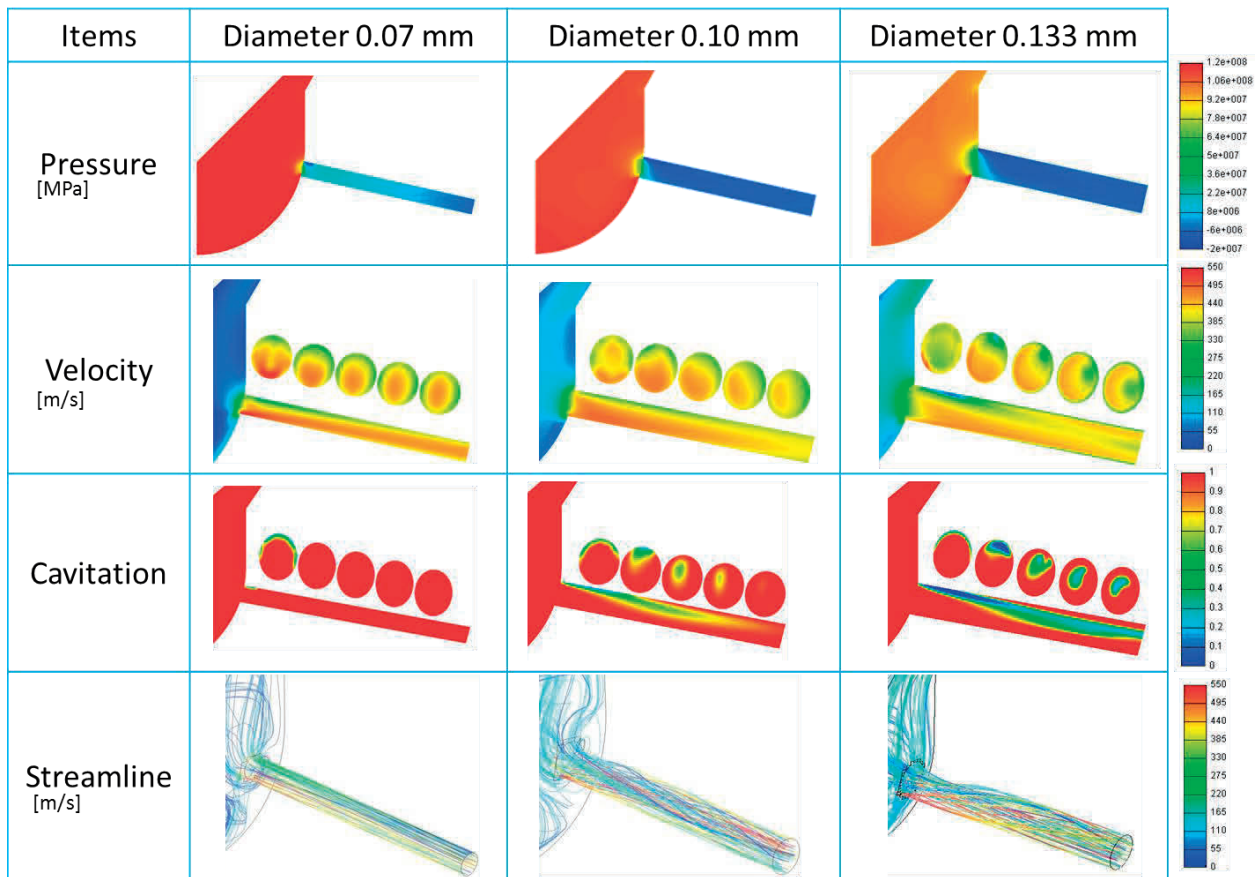


Figure 5.41 Pressure, velocity, cavitation, and streamline distribution inside different nozzles

The pressure, velocity, cavitation, and streamline distribution inside different nozzles at the full needle lift timing is shown in Figure 5.41. With the increasing of hole diameter, the sac pressure is decreased, because the discharge area is increased. The time resolved sac pressure variation is

shown in Figure 5.42, which is corresponding to the cloud pictures. Furthermore, the velocity inside the nozzle hole is also decreased with the increasing of hole diameter, which is affected by the pressure distribution. The corresponding mass flow rate in Figure 5.42 is also coincided with this analysis. The cavitation level inside different nozzles also presents interesting phenomenon. As discussed before, the smaller hole diameter can suppress the cavitation development inside the hole. The liquid volume fraction result inside the nozzles, which is shown in Figure 5.42 also can validate this discussion. As for the streamline, there are all spiral flow structure inside large diameter holes. Combing the experimental result in Chapter 4, the spray width is dominated by the jet atomization and the spray momentum. The atomization is affected by the turbulent, cavitation, and the interaction of liquid jet and ambient gas. The lower pressure inside 0.133 mm hole deteriorated the atomization compared with the 0.101 mm hole, and the spray momentum is too high to conducted the energy transform, which all results in the narrower spray width.

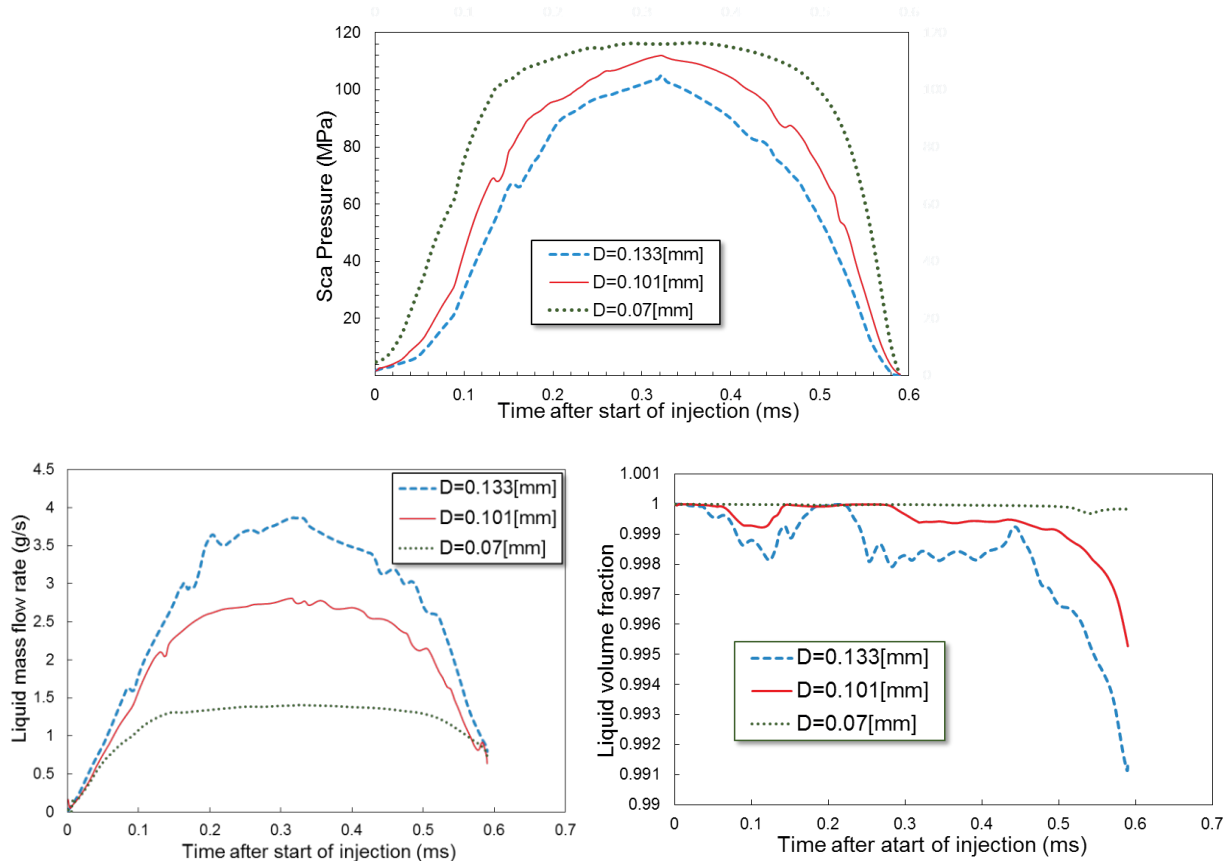


Figure 5.42 Sac pressure, mass flow rate and liquid volume fraction variation of different nozzles

Effect of nozzle hole length

Corresponding to the Mie scattering experiments, the nozzle internal flow under different nozzle hole length condition is also reproduced under the same operation conditions. In order to

make comparison, the same needle lift curve, which is measured in the experiment, is shown in Figure 5.43. The internal flow calculation result will be correlated with the experimental results.

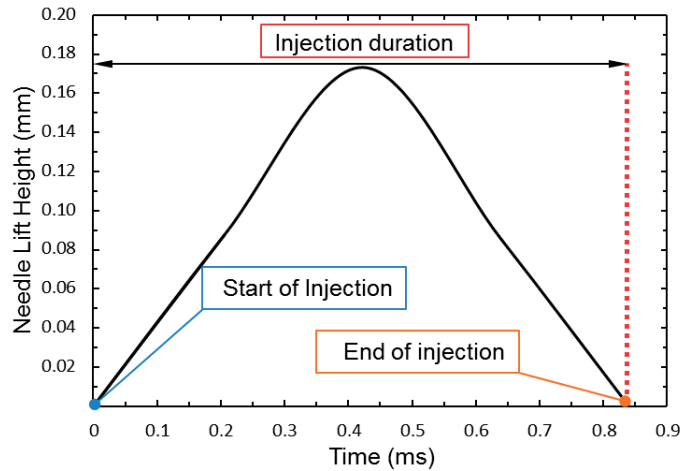


Figure 5.43 Needle lift curve measured in the experiment

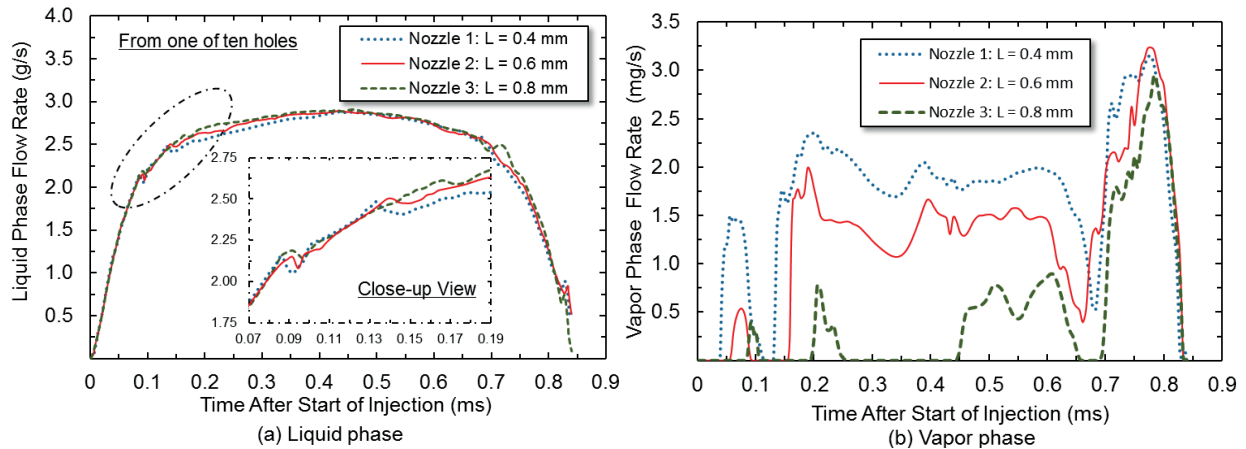


Figure 5.44 Injection rate result in the computational study

The calculated mass flow rate on the orifice exits of the nozzles with different hole length is shown in Figure 5.44. As for the liquid mass flow rate, it can be seen that the Nozzle 1 has the lowest liquid mass flow rate, while the Nozzle 3 is the highest one. Although the difference is not so much apparent due to the application of the same needle lift curve, the trend is coincided with that in the experimental result. According to the close-up view for the initial injection stage, the Nozzle 1 firstly has fluctuation due to the appearance of the cavitation, and there is also some interlacement between the curves of the Nozzle 2 and Nozzle 3.

The vapor mass flow rate of these three nozzles can further validate the previous analysis for the injection rate results in the experiments. Almost during the whole injection duration, the vapor mass flow rate of the Nozzle 1 is the highest one, especially at the initial and middle stages of

the injection. However, the Nozzle 3 has little vapor mass flow except for the post stage of injection, when the needle is almost closed. This phenomenon indicates that it is easier for the cavitation to reach the outlet of the nozzle with shorter hole length, and the effective flow area can be reduced with the reduction of the nozzle hole length. The flow dynamics results inside different nozzles in the following paragraph will provide more interpretation for the phenomena observed in the experiments.

The fuel flow velocity inside the nozzle orifices is another important factor that can affect the fuel injection rate and the spray propagation. The streamline structure and the velocity distribution inside different nozzles at 0.4 ms ASOI (around full needle lift) are shown in Figure 5.45-(a) and (b), respectively. Complicated streamlines with great curvatures are generated in the sac of the nozzles. When attention is paid to the internal flow inside the nozzle hole volume, the spiral and counter-rotating flow appears in the hole region, which is caused by the complex flow patterns in the upstream of the hole entrance, where is within the sac volume.

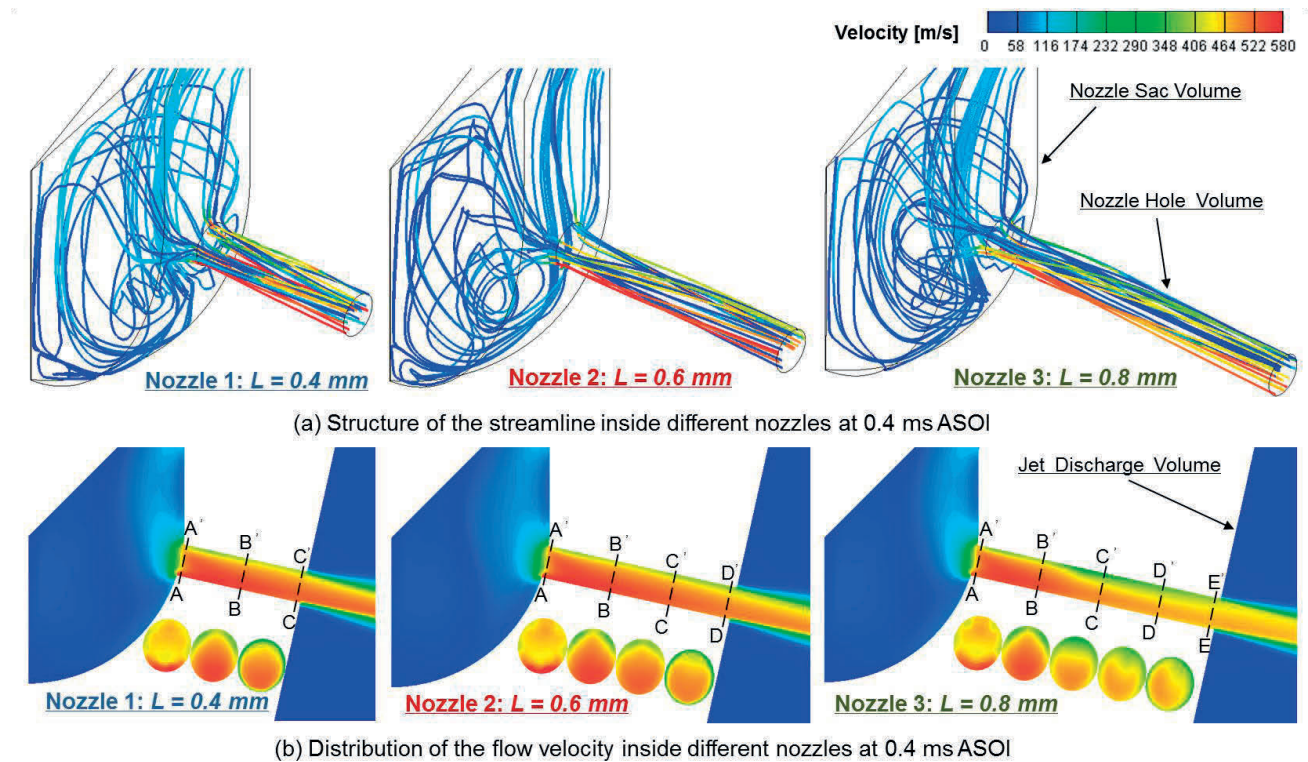


Figure 5.45 Characteristics of the flow velocity inside different nozzles

However, it seems that with the increasing of the hole length, the development of the spiral flow can be suppressed by the longer hole, and the streamline structure in the hole exit part becomes smoother, more straight, and orderly, which has much relationship with the different near-field spray width observed in the experiments.

There is also distinction in the fuel flow velocity properties inside different nozzles. The velocity distribution inside the hole volume is asymmetric, which is generated by the aspects changing of the flow direction due to the special configuration of the multi-hole nozzles. Furthermore, with the increasing of the hole length, the fuel injection velocity is reduced obviously, which agrees with the analysis in the experimental section. It is the multiple factors (effective flow area and injection velocity) that dominate the fuel injection rate and the spray tip penetration of different nozzles, simultaneously.

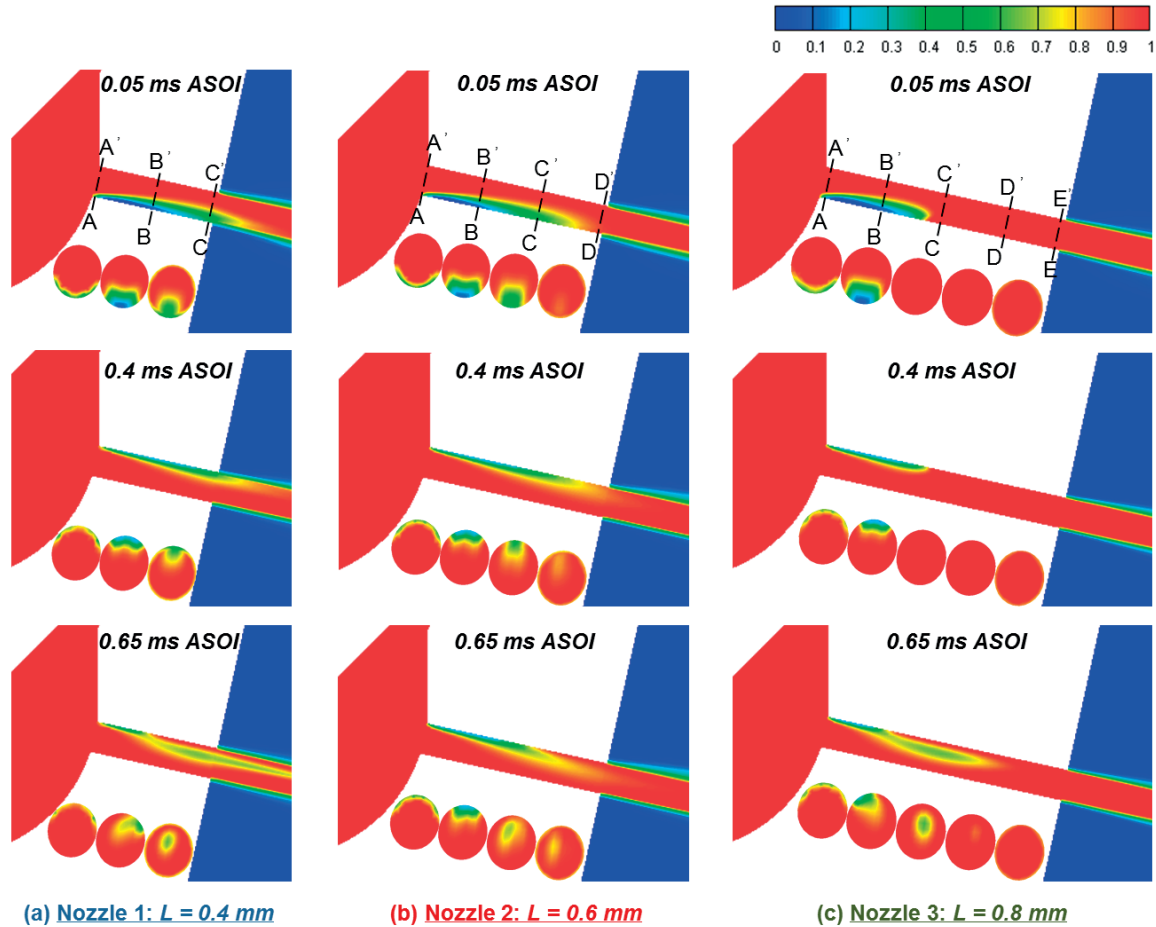


Figure 5.46 variation of the liquid volume fraction within the computation domains

The temporal variations of the liquid volume fraction inside these three nozzles are shown in Figure 5.46. Generally, the cavitation position and intensity are all unstable inside different nozzles. At the beginning of the injection, caused by the lower needle lift, the high-pressure fuel, which flows into the low-pressure sac volume, can reach to the bottom of the sac, and then flows into the hole entrance with generating large vortex inside the sac. As a result, the cavitation appears in the lower reaches of the hole inlet, which is mainly caused by the flow separation. With the needle moving, the position of the cavitation moves to upper reaches of the hole inlet, and there is

even string-type cavitation inside the nozzle hole, which is generated by the spiral and streamwise counter-rotating vortices inside the hole. With the decreasing of the hole length, it is easier for the cavitation to reach the hole exit, which can reduce the fuel discharge coefficient, injection rate, injection jet momentum, and the spray tip penetration [Payri, F., 2004]. However, the higher mass and momentum exchange in the downstream region, which is caused by the cavitation collapse, should be more conducive to the wider spray dispersion angle and the near-field spray perturbations observed in the experiments.

The specific velocity distribution on the nozzle hole exits at the full needle lift timing under different nozzle hole length conditions is shown in Figure 5.47. The definition of velocity vectors is already introduced. In this figure, the two velocity components along the orthogonal hole diameter lines ($A-B$ and $C-D$) are analyzed separately, just as shown in Figure 5.47-(b) and (c), respectively.

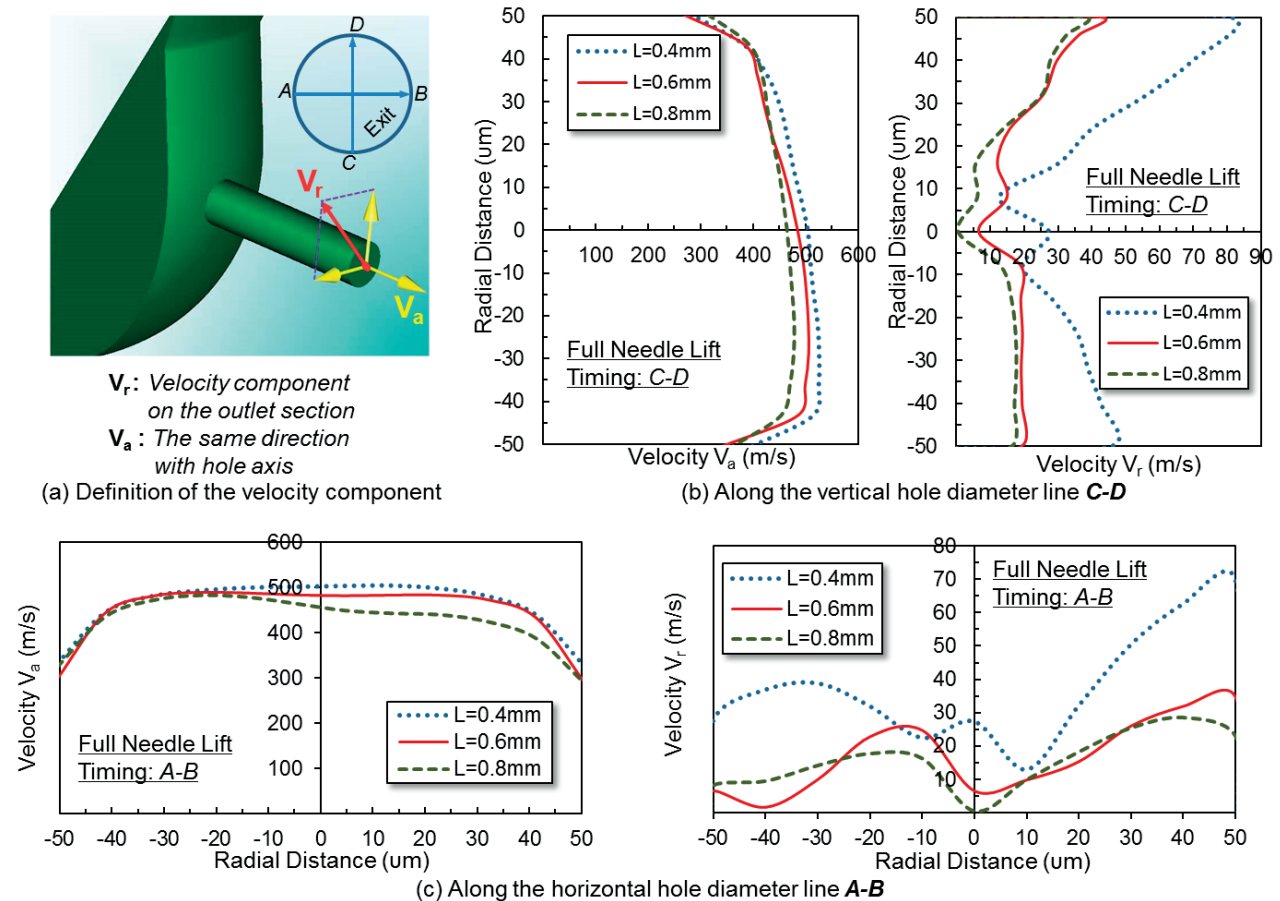


Figure 5.47 Velocity distribution on the hole exits at the full needle lift timing under different hole length conditions

Along the vertical hole diameter line ($C-D$), with the decreasing of the nozzle hole length, V_a is increased relatively. The same trend can be found along the horizontal line, and the deviation in these three profiles is more apparent along the right portion of $Line A-B$, which should be attributed to the unstable and asymmetrical flow patterns inside the nozzle hole volume. As for the distribution of V_r , it is very asymmetric, and the Nozzle 1 has the highest value no matter along the $Line A-B$ or $C-D$, which is responsible for the widest spray dispersion angle and waved spray profiles in the experiments. Moreover, the difference in V_r between Nozzle 1 and Nozzle 2 is more prominent than that between Nozzle 3 and Nozzle 2, which is also in accordance with what observed and discussed in the experimental results.

Except for the cavitation, the turbulent flow generated during the injection duration is another significant factor that affects the spray first breakup. The average turbulent kinetic energy (TKE) variation on the hole exits of different nozzles during the injection duration is presented in Figure 5.48-(b).

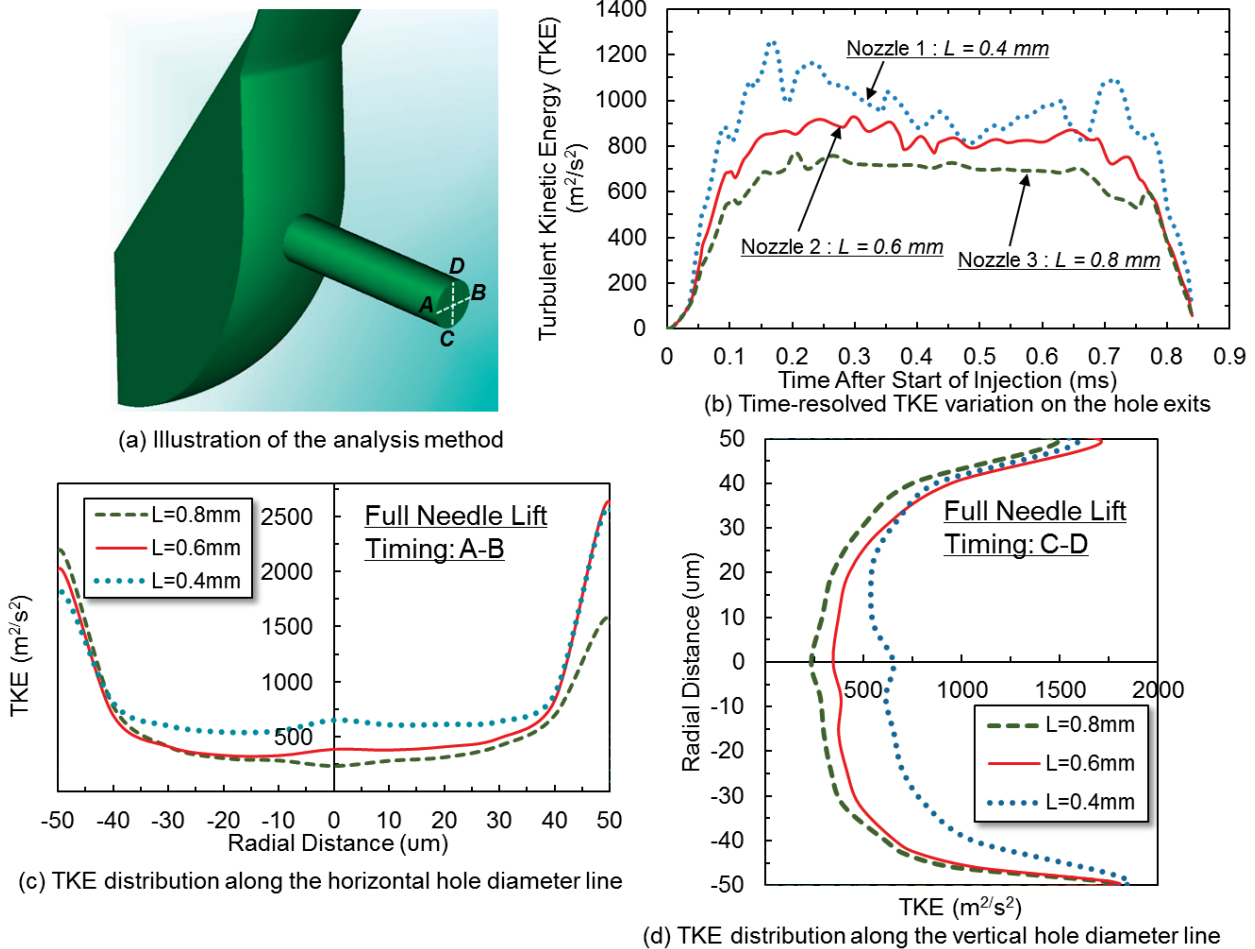


Figure 5.48 Variation and distribution of turbulent kinetic energy on the hole exits

The Nozzle 1 has the highest TKE almost during the whole injection process, while the value of the Nozzle 3 is the lowest one. Moreover, the TKE distribution along the orthogonal hole diameter lines (*A-B* and *C-D*) on the hole exits at the full needle lift timing is plotted in Figure 5.48-(c) and (d), respectively. There is also obvious distinction among these three nozzles, especially along the vertical line (*C-D*). The deviation in TKE results provide more interpretation for the different spray lineament observed in the experiments.

5.4 CORRELATING NOZZLE GEOMETRICAL DESIGN AND INTERNAL FLOW WITH SPRAY BEHAVIORS

It is well known that the turbulence intensity increases with the enhancement of the dissipation of the transfer of the spray momentum to turbulence energy, resulting in more intense liquid/gas interactions, lower spray velocity, and wider spray diffusion. The computational maximum turbulent intensity of the outlet at different injection timings and the corresponding experimental spray cone angle results under the baseline condition are plotted in Figure 5.49. The results show that the turbulence intensity at the exit of the multi-hole nozzle is higher than that of the single-hole one; consequently, the spray cone angle is wider. In fact, the turbulent intensity of the single-hole nozzle does not increase so much as it looks in the Figure, because the abscissa value of this figure is multiplied by 100 to increase its visualization and understandability. Moreover, it should be noted that the spray cone angle is affected by the turbulent intensity and the cavitation level simultaneously. The obviously increased spray cone angle is also attributed by the high cavitation level inside the multi-hole nozzle, which has been discussed previously.

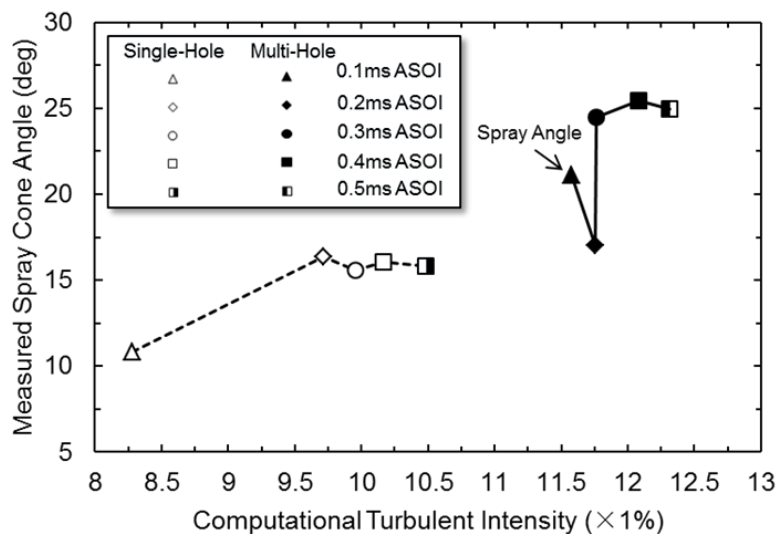


Figure 5.49 The computational maximum turbulent intensity of the outlet at different injection timings and the corresponding experimental spray cone angle results under the baseline condition

The characteristics of internal flow patterns inside the nozzles with different nozzle hole length are discussed in previous sections, and their effects on the corresponding spray behaviors is correlated with the experimental results in Figure 5.50.

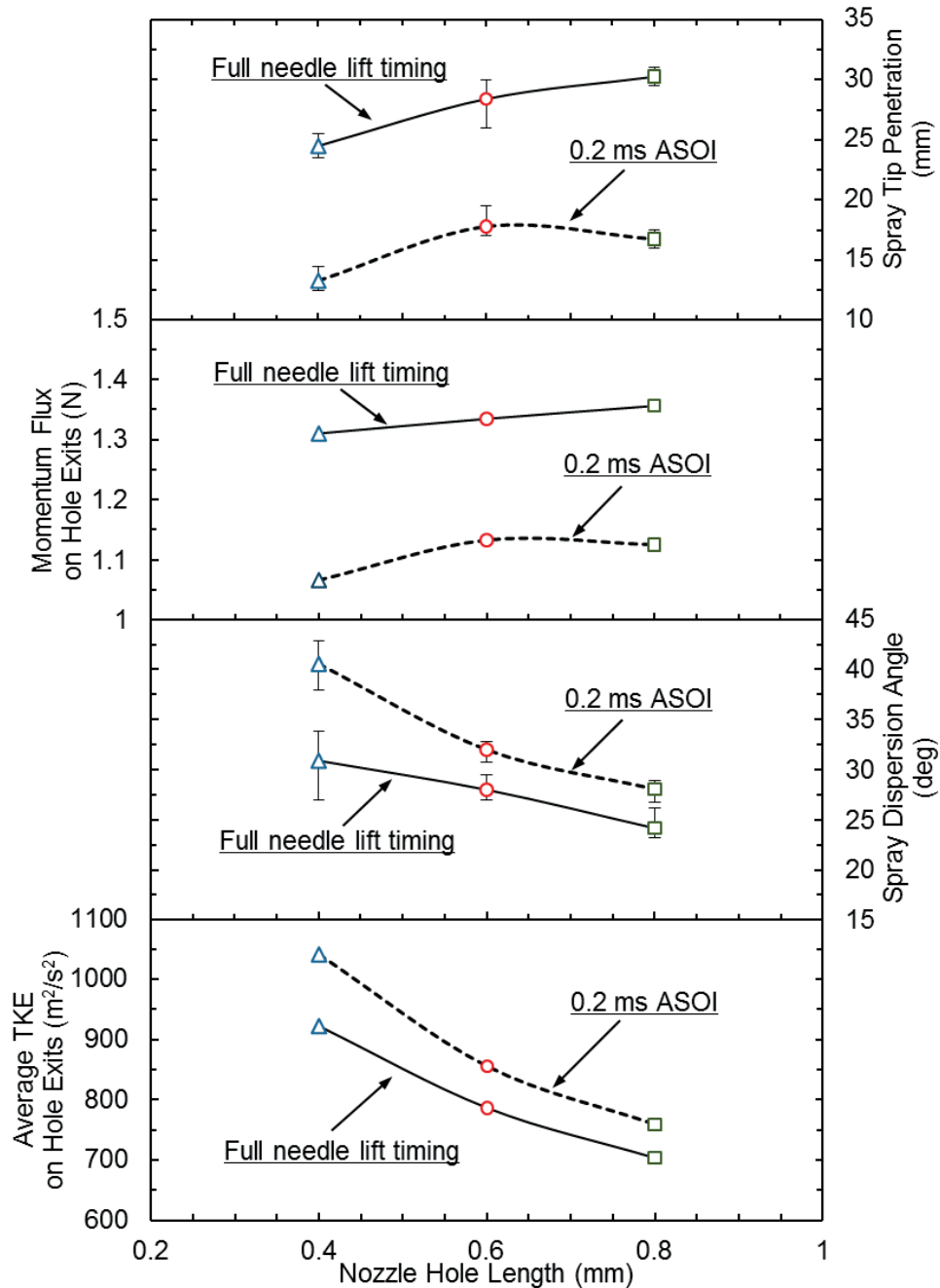


Figure 5.50 Correlation between the internal flow and the spray properties at typical timings

As for the computational results, the average turbulent kinetic energy and momentum flux on the nozzle hole exits at the typical timings (0.2 ms ASOI and full needle lift timing) under different nozzle hole length conditions are plotted in this figure. The corresponding spray tip

penetration and spray dispersion angle results measured from the experimental images at the same timings are also presented here. The correlation can validate the analysis in the previous sections, and it is the unique properties of the internal flow inside different nozzles that mainly dominate the corresponding spray behaviors.

In this study, the multi-hole nozzles with different parameters are listed in Table 5.3. In order to investigate the correlation between the nozzle geometrical design, internal flow, and spray behaviors, the parameters is normalized to the ratio of nozzle hole length to diameter. At the quasi-steady stage of the injection duration of baseline condition, the experimental spray cone angle and the calculated hole exit turbulent kinetic energy under different normalized nozzle parameter conditions is plotted in Figure 5.51.

Table 5.3 Normalized Parameters of multi-hole nozzles

Nozzles	Hole length (mm)	Hole diameter (mm)	Ratio of length to diameter
1	0.8	0.07	11.429
2	0.8	0.10	8.000
3	0.8	0.133	6.015
4	0.4	0.101	3.960
5	0.6	0.101	5.941
6	0.8	0.101	7.921

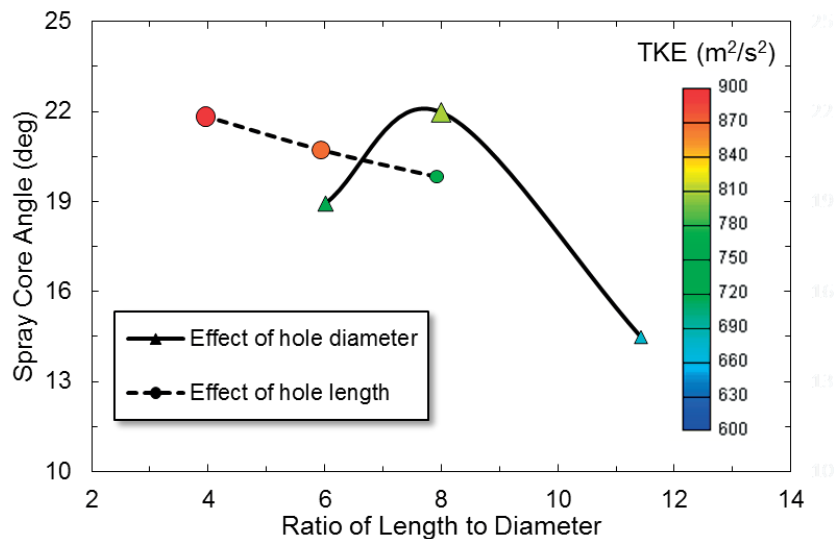


Figure 5.51 Correlation between the nozzle geometrical design, internal flow, and spray behaviors

With the increasing of the ratio, the spray cone angle is decreased, and the turbulent kinetic energy is also reduced. However, it should be note that when considering the hole diameter, the

multi-hole nozzle presents a kind of special regularity, and the spray cone angle and TKE reach to the highest at the ratio of 8. As explained before, the sac pressure of the nozzles with different hole diameter also plays a significant role in the spray width, because the sac pressure and hole diameter not only affect the turbulent and cavitation, but also control the injection velocity and spray momentum. The internal flow and the aerodynamics factors can alter the liquid jet break up , simultaneously. When looking for the optimum geometrical nozzle design, the injection duration and injection quantity, which is dominated by the ratio of hole length to diameter, should also be concerned, because the nozzle must match up with the whole engine control concept and system.

5.5 SUMMARY

In this chapter, the internal flow characteristics inside single-hole and multi-hole nozzles was compared firstly, after that, the multi-hole nozzles were paid more attention. The dynamic operation condition and nozzle geometrical effect were investigated under the same condition with the Mie scattering experiment. Finally, the internal flow and experimental result were correlated. The main conclusions are listed as follows:

1. Sprays from the multi-hole nozzle are dominated by the lower sac pressure, vortex flow in the sac, complex spiral flow structure inside the hole, and Coanda effect between the adjacent spray plumes. The computational results of these two flow configurations reveal that the rate of increasing sac pressure is higher in the single-hole nozzle. However, the swirling motion only forms inside the sac and hole of the multi-hole nozzle, which can generate string-type cavitation. This complex flow structure also produces a stronger turbulence intensity and larger velocity component at the hole exit. Consequently, the enhanced interfacial instability and wider spray cone angle of the multi-hole nozzle are observed in the Mie scattering images.
2. The distinctions in the internal flow patterns between the single-hole and multi-hole nozzle show different sensitivity under the tiny and normal injection quantity conditions. For some of the parameters, including the sac pressure, injection velocity, turbulence kinetic energy distribution on the nozzle exit, the deviation of them between different nozzles is much larger under the tiny injection quantity condition. However, the difference in the streamline structure, injection rate, and injection duration between the single-hole and multi-hole nozzles is more apparent under the normal injection quantity condition. Moreover, the deviations in the cavitation structure are always large and obvious under both of the two injection quantity conditions.
3. The influence of the micro hole diameter on the internal flow and injection processes of the single-hole and multi-hole injectors is prominent. The reduced effective flow area suppresses the

cavitation and turbulence flow, alters the injection rate, and prolongs the injection duration. Affected by the lower sac pressure discharge rate and reduced deviation of the internal flow, the difference of the spray properties between single-hole and multi-hole nozzles with micro orifices are reduced significantly.

4. The deviations of a series of internal flow properties of the multi-hole nozzle between the tiny and normal injection quantity conditions are much more prominent than those of the single-hole nozzle. Moreover, the rail pressure variation can exert more effect on the multi-hole nozzle internal flow under the tiny injection condition.

5. The simulation results indicate that there are also obvious differences in the internal flow and the spray transient around the end and the start of the pilot injections between the single-hole and the multi-hole nozzles. The dribbles of the multi-hole nozzle spray around the end of the pilot injection appear later than that of the single-hole one. It is easier for the ambient gas to entry into the sac of the single-hole nozzle, which can affect the properties of initial spray jet.

6. The hole taper ratio, hole inlet roundness, and the hole diameter variation effect on the internal flow are investigated, and the conical hole, smoother inlet edge can increase the injection rate and reduce the cavitation level inside the multi-hole nozzles. The hole diameter variation affects the sac pressure directly. With the increasing of the hole diameter, the cavitation level is increased, while the sac pressure and injection velocity is reduced, which is important for the spray break up.

7. The distinctions in the internal flow patterns and injection processes of the multi-hole nozzles under different hole length conditions are prominent. The nozzle hole length can affect the development of the flow patterns and the local cavitation inside the hole. Consequently, the void fraction, flow turbulent kinetic energy, and the injection velocity components on the hole exits, which are regarded as key mechanism governing the emerging spray properties, change significantly with the variation of the nozzle hole length. It is safe to say that decreasing the nozzle hole length can enhance the level of cavitation and turbulence inside the hole, increase the injection velocity and spray width, and promote the spray perturbation and break up, while it decreases the fuel effective flow area and the spray propagation length, relatively. Moreover, the changes summarized above are not linearly, and different parameters have variable sensitivity to the nozzle hole length variation.

8. The internal flow properties, experimental results, and the nozzle geometrical design concept is discussed. The spray modeling processes under engine operation conditions and the optimized design of diesel multi-hole injectors may get some clue and benefit from the data presented in this chapter.

CHAPTER 6 NUMERICAL COMPUTATIONAL STUDY OF MULTI-HOLE NOZZLE SPRAY

6.1 MESH BUILDING PROCESS, BOUNDARY CONDITIONS, AND SIMULATION VALIDATION

In this chapter, the spray of single-hole and multi-hole nozzles will be reproduced by the simulation method, and the meshes for calculation are shown in Figure 6.1. The single-hole and multi-hole nozzles have specially meshes to simulate the spray evolution. The specific setting and conditions for the simulation is shown in Table 6.1. The condition is corresponding to the Mie scattering experiments in Chapter 4. The break up models and parameter settings has already been introduced in Chapter 3, and the specific comparison results will be shown in the next section.

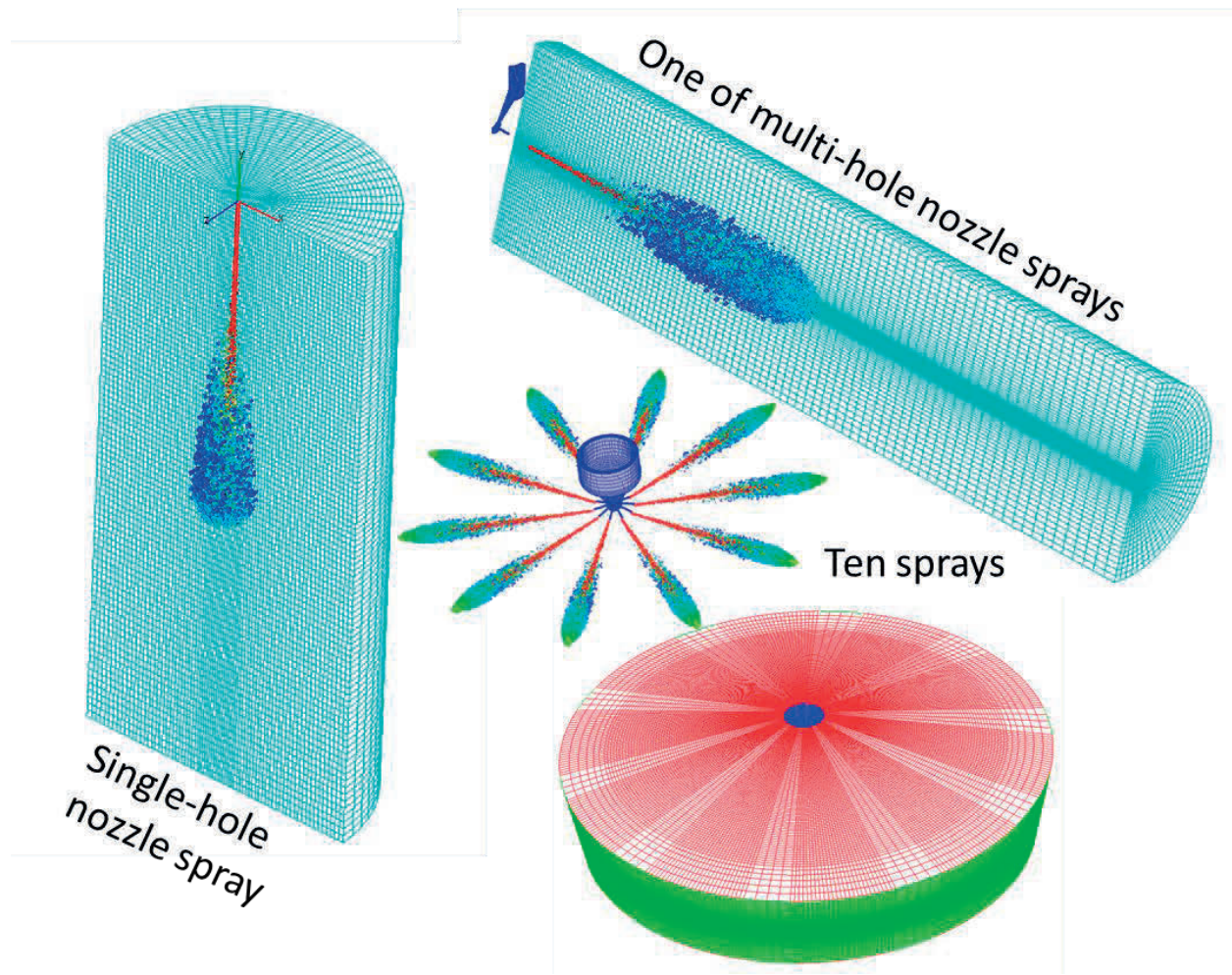
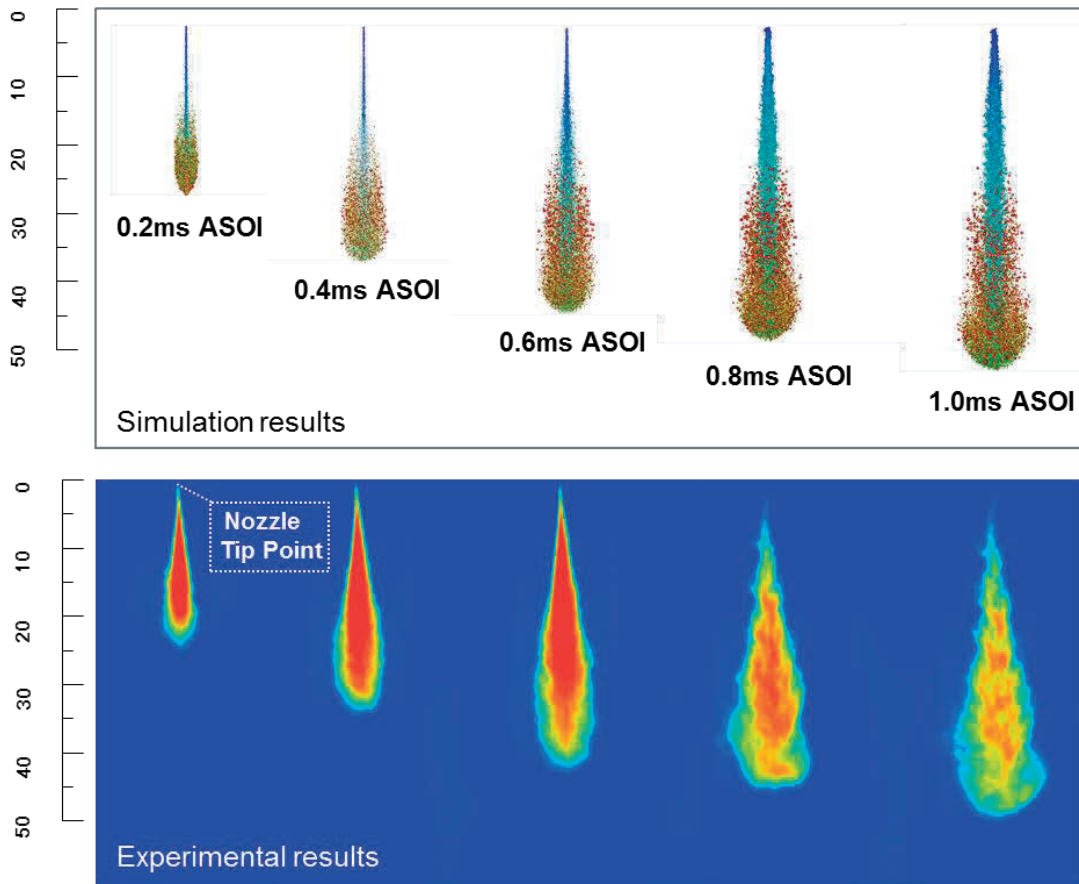


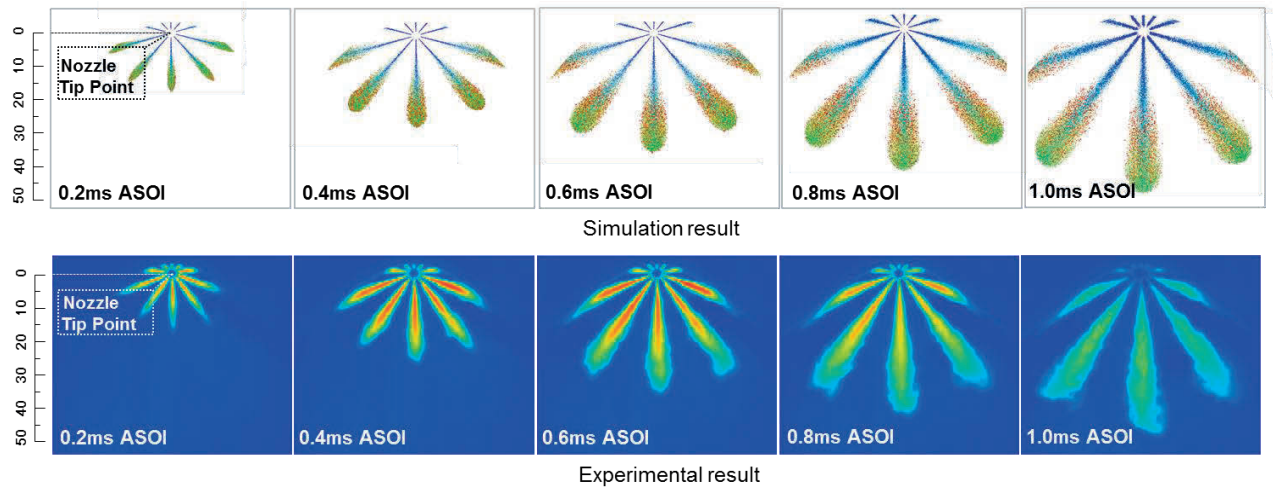
Figure 6.1 The meshes for calculation of sprays emerging from single-hole and multi-hole nozzles

Table 6.1 Computation setting and conditions

Item	Classification		Setting / Value
Model selection and Initial values	Turbulence model		K- ζ -F
	Break up models	The first break up	Core coupled with nozzle internal flow files
		The second break up	KH-RT
Initial boundary	Inlet boundary	Injection Pressure (MPa)	80, 120, 180
	Export boundary	Ambient Pressure (MPa)	1.5
Computational condition	Dynamic conditions	Injection quantity (mm ³ /hole)	0.3, 2
	Geometrical conditions	Nozzle hole diameter (mm)	0.07, 0.10, 0.133
Mesh information	The minimum cell size (mm)	Single-hole spray	0.25
		Multi-hole spray	0.15
	The maximum total grid number (cells)	Single-hole spray	217600
		Multi-hole spray	240000



(a) Spray simulation validation for single-hole nozzle



(B) Spray simulation validation for multi-hole nozzle

Figure 6.2 Spray simulation validation by comparing with the high speed video images

Before the further calculation, the validation for the spray simulation is conducted for both single-hole and multi-hole nozzles. The comparison of spray appearance between the experimental and numerical results is shown in Figure 6.2, and the single-hole nozzle spray and multi-hole nozzle spray are presented separately. It can be seen that the morphology of the sprays are in accordance with each other, and the spray tip penetration comparison result, which is shown in Figure 6.3, can further validate the accuracy of this simulation study.

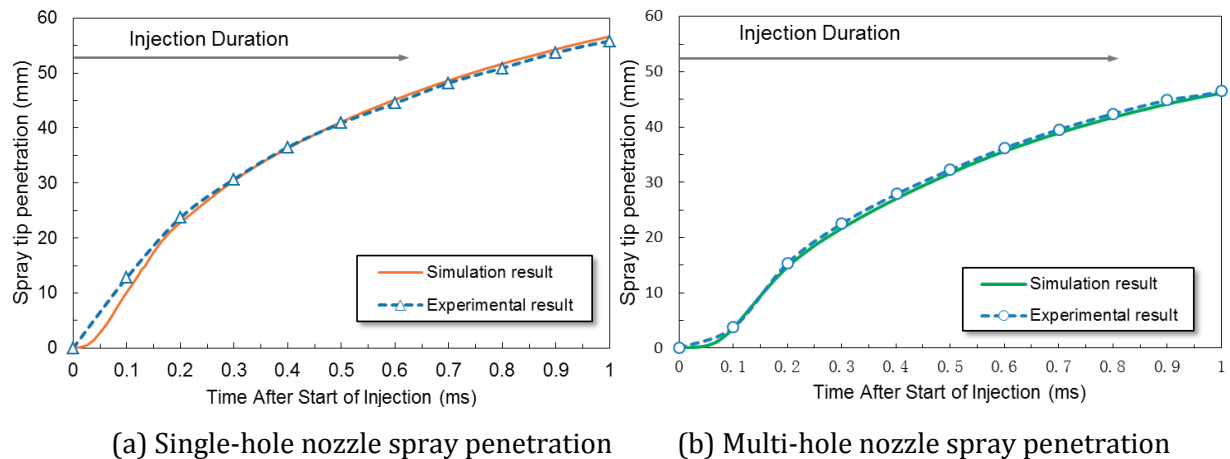


Figure 6.3 Comparison on spray penetration between experimental and numerical results

6.2 COUPLING OF MULTI-HOLE NOZZLE INTERNAL FLOW RESULTS WITH SPRAY SIMULATION

As introduced in Chapter 3, two steps concept was applied in the simulation of nozzle spray in this study, the specific process is shown in Figure 6.4. The internal flow information under different conditions can be obtained in Chapter 5, and those files is inserted into the first break up model as the boundary conditions.

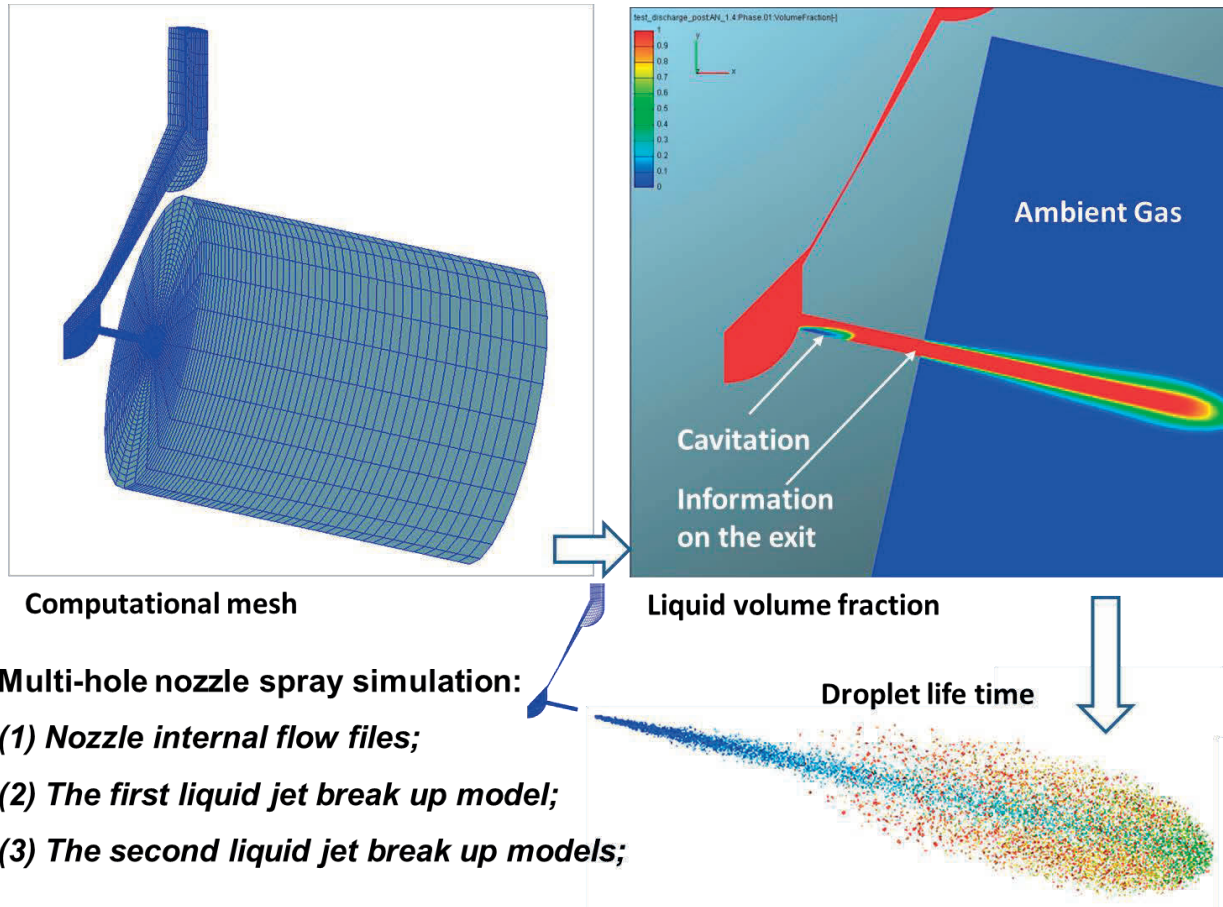


Figure 6.4 Spray simulation method applied in the current study

The comparison of the spray results by applying different simulation methods, including the traditional two methods and the current method, are shown in Figure 6.5. The color bar is neglected, because of the timings selection. The color in this figure is corresponding to the droplet lifetime, and the size means the droplet size. All of the parameters setting are the same except for the quantity of the break up information introduced into the boundary conditions. It can be seen that when only the second break up model is applied, the droplet is too large, while when the first and the second break up models are applied, and the break up is enhanced much more, especially in

the downstream region. However, the droplet size near field nozzle hole region is also too large, which is beyond the nozzle diameter. When the internal flow information is inserted into the first break up models, the spray presents well atomization characteristics, and it proves that this method is the best way to reproduce the spray evolution, with the consideration of nozzle geometry and internal flow effects on the first break up processes. The time resolved Sauter mean diameter of the spray under different conditions shown in Figure 6.6 can support the analysis before.

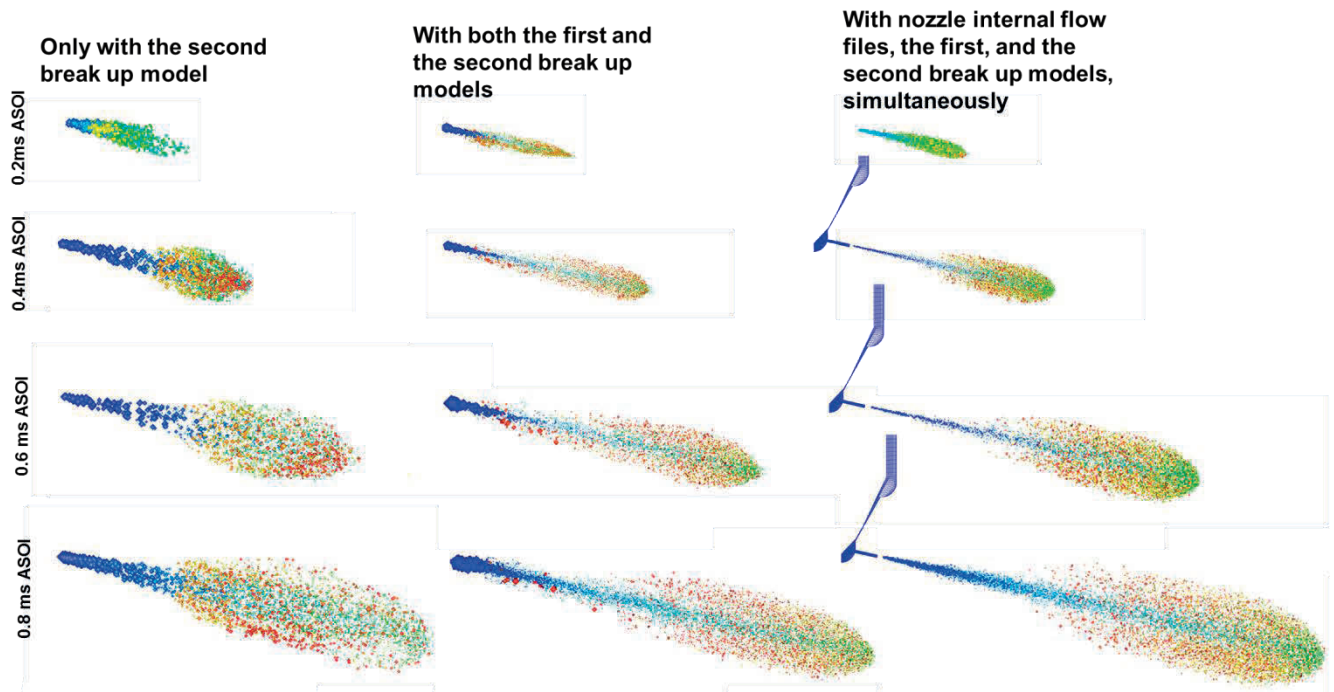


Figure 6.5 Comparison of spray results by applied different simulation methods

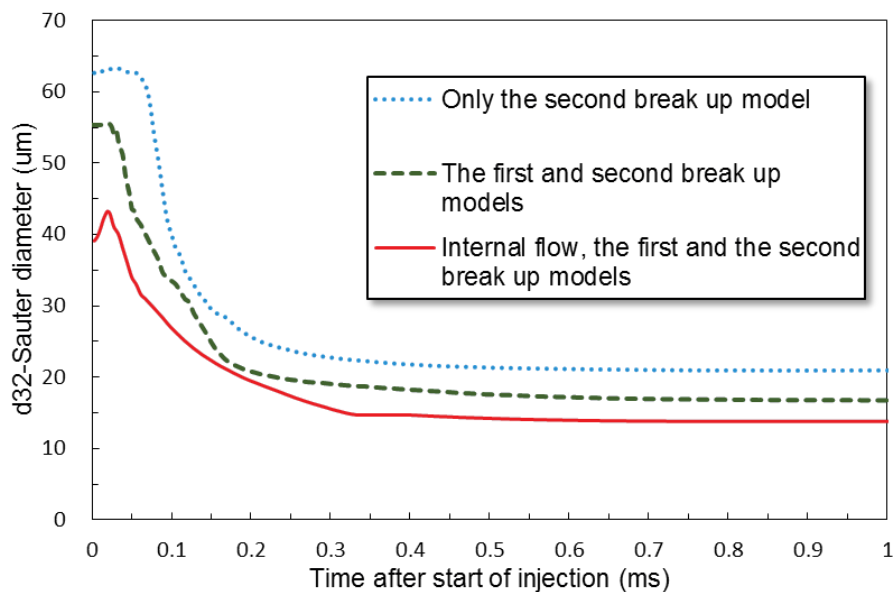


Figure 6.6 Time resolved Sauter mean diameter of the spray under different condition

6.3 COMPARISON OF SPRAY SIMULATION RESULT BETWEEN SINGLE-HOLE AND MULTI-HOLE NOZZLES

The experimental spray evolution results have already been shown in Chapter 4, the single-hole and multi-hole nozzle sprays are compared there. In order to explain the experimental result in detail, the internal flow simulation inside different nozzles was reproduced in Chapter 5. In this section, the numerical simulation spray result of single-hole and multi-hole nozzles under the baseline condition will be compared in further.

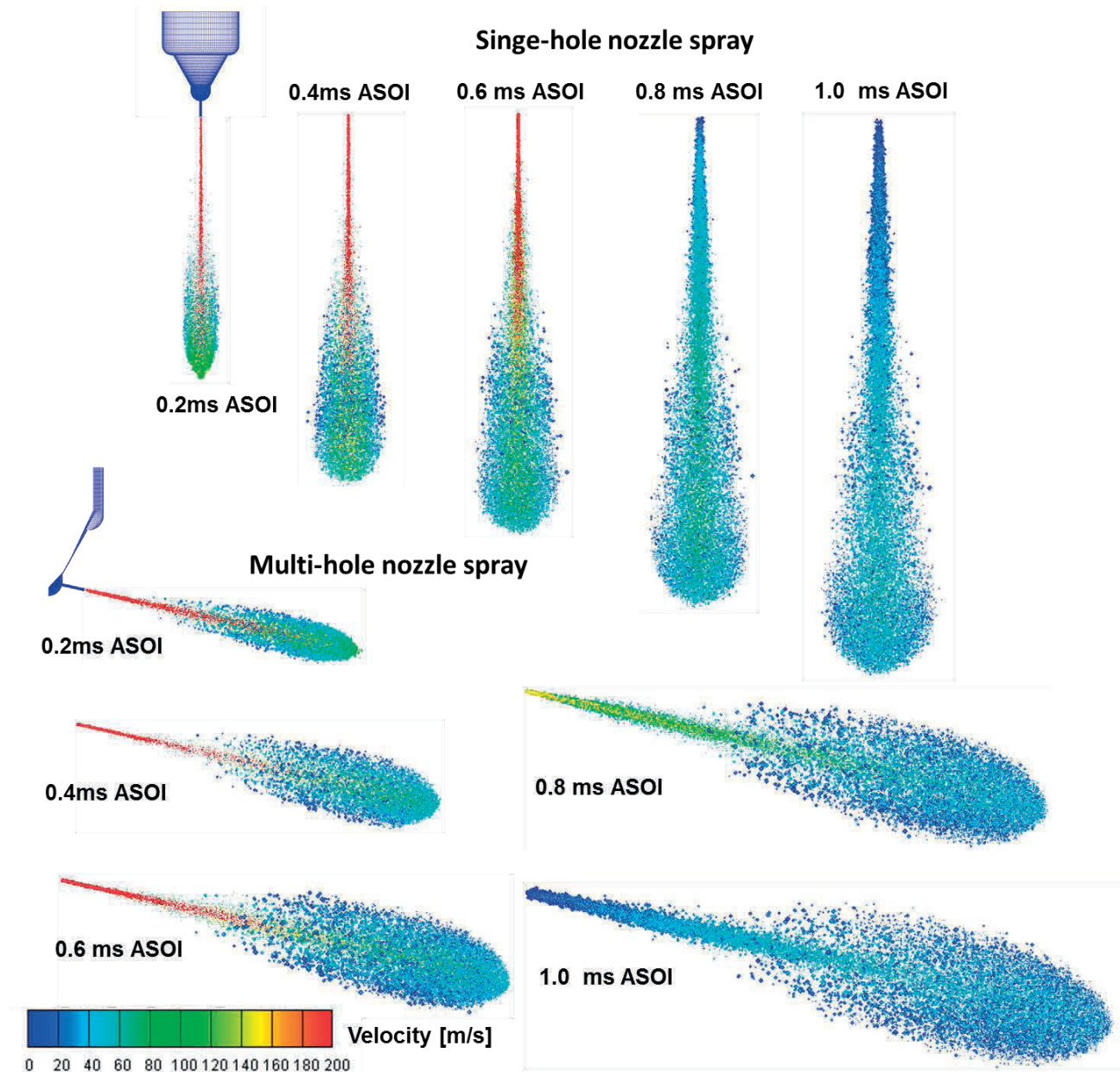


Figure 6.7 Comparison of single-hole and multi-hole nozzle spray

The comparison of spray appearance between single-hole and multi-hole nozzles is shown in Figure 6.7. The typical timing selection is the same with that in Chapter 4. The single-hole nozzle spray has higher velocity than the multi-hole one, and it is also thinner than the multi-hole nozzle spray. The spray tip penetration comparison result, which is shown in Figure 6.8, is coincided with the analysis before. The single-hole nozzle spray penetrates much longer than the multi-hole one.

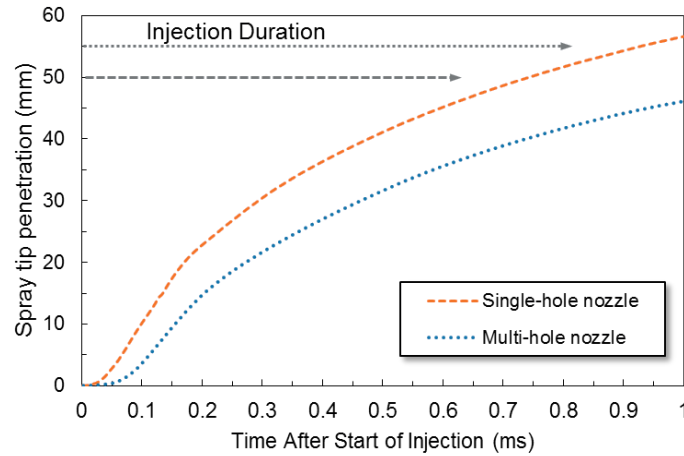
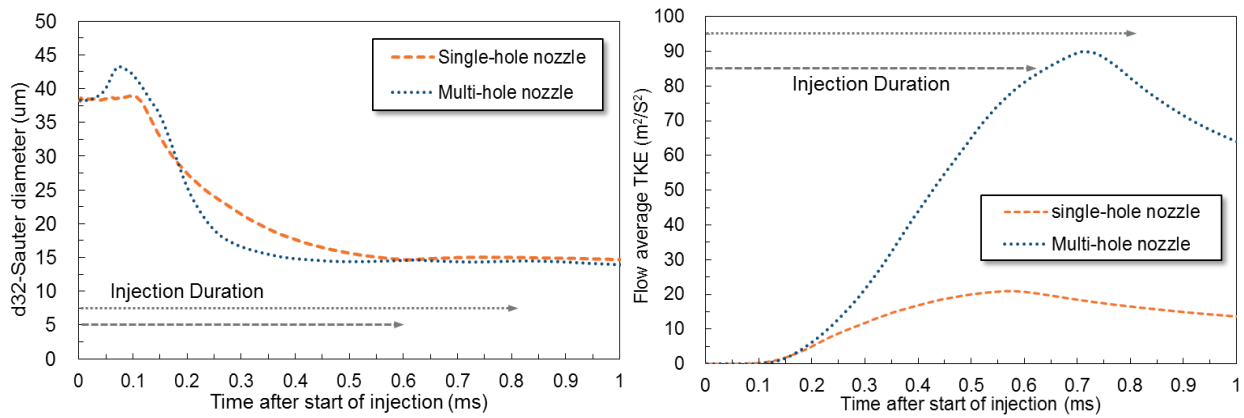


Figure 6.8 Comparison of single-hole and multi-hole nozzle spray tip penetration

The Sauter mean diameter of the droplet inside single-hole and multi-hole nozzle spray is shown in Figure 6.9-(a). The interesting phenomenon is that at the beginning of the injection, the d_{32} of the single-hole nozzle is smaller than that of the multi-hole one, which is attributed to the higher sac pressure, better atomization of the single-hole. However, during the middle stage, the multi-hole nozzle spray has smaller d_{32} , under the end of the timing. The strong turbulent and cavitation inside the multi-hole nozzle can attribute to this issue. The average turbulent kinetic energy in the flow field of different nozzle sprays (shown in Figure 6.9-(b)) can provide another view in the comparison of atomization characteristics of single-hole and multi-hole nozzles



(a) Sauter mean diameter result

(b) Flow average turbulent kinetic energy

Figure 6.9 Comparison in Sauter mean diameter and flow average TKE of single-hole and multi-hole nozzle spray

6.4 CHARACTERISTICS OF MULTI-HOLE NOZZLE SPRAY

6.4.1 Ambient Flow and Spray Interaction of Multi-Hole Nozzle Spray

In this section, the simulation for the whole ten spray plumes is conducted to observe the spray interactions and the ambient gas flow under the base line condition. As shown in figure 6.10, the upper row is the schematic of multi-hole nozzle spray, which can not be observed in the current view in the experiments. The color means the lifetime of the droplets. The spray distribution is symmetrical and the droplets at downstream and on the periphery of the sprays have longer lifetime. The lower row shows the spray droplet velocity distribution and ambient gas flow field.

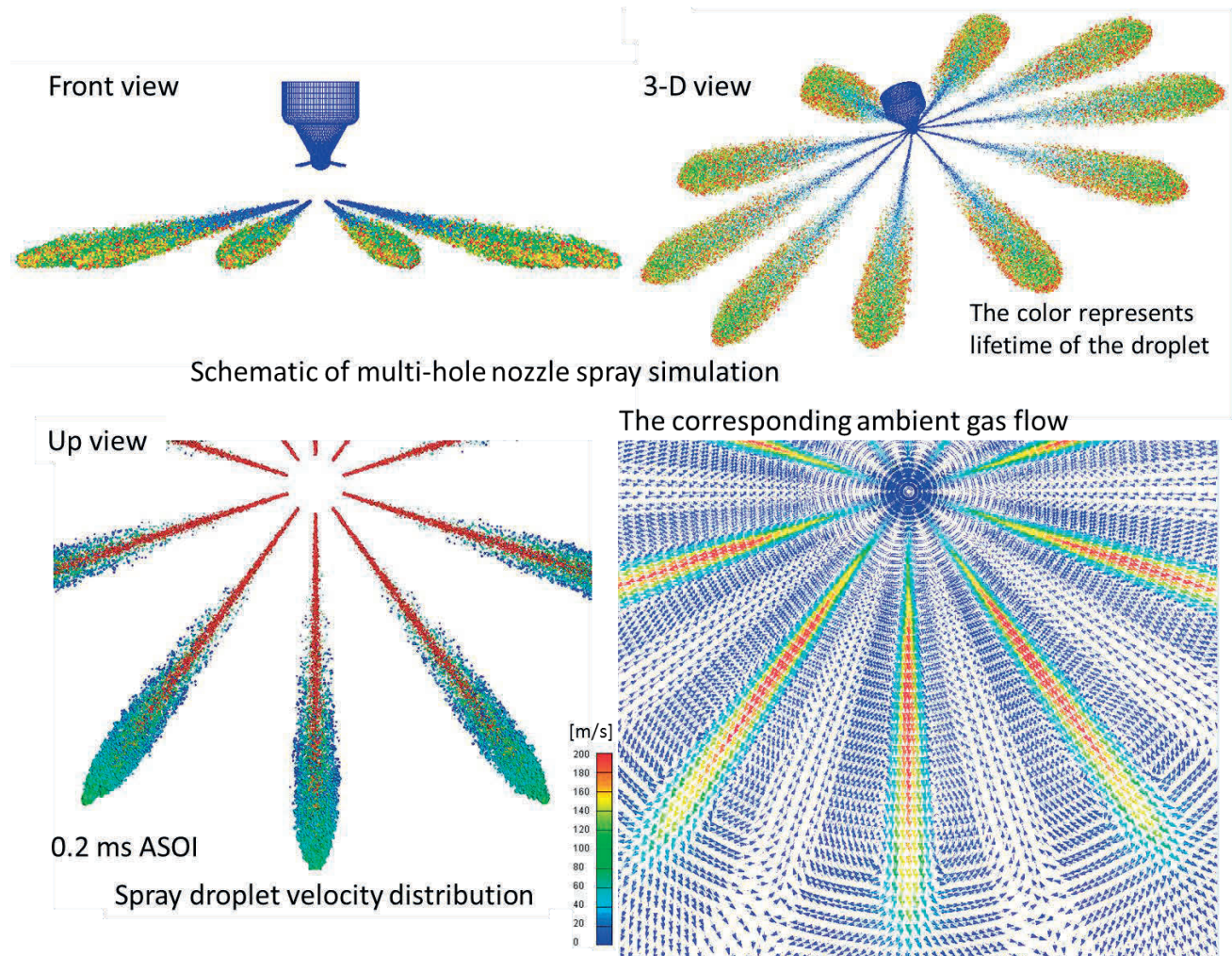


Figure 6.10 Multi-hole nozzle spray simulation result and the ambient gas flow between that sprays

The inner core of the spray has higher velocity at the beginning of the injection (0.2 ms ASOI), and the droplets on the periphery of the spray has the lowest velocity, due to the aerodynamic effect. The ambient gas between the spray plumes entrains into the adjacent sprays, simultaneously, which have significant effect on the mixture formation and fuel evaporation.

6.4.2 Under Different Rail Pressure Conditions

In this section, the rail pressure effect on the multi-hole nozzle spray evolution will be discussed, and the injection pressure is selected as 80 MPa, 120 MPa, and 180 MPa. The injection quantity is kept constant as 2 mm³/hole . The spray droplets velocity at typical timing during the injection duration is shown in Figure 6.11.

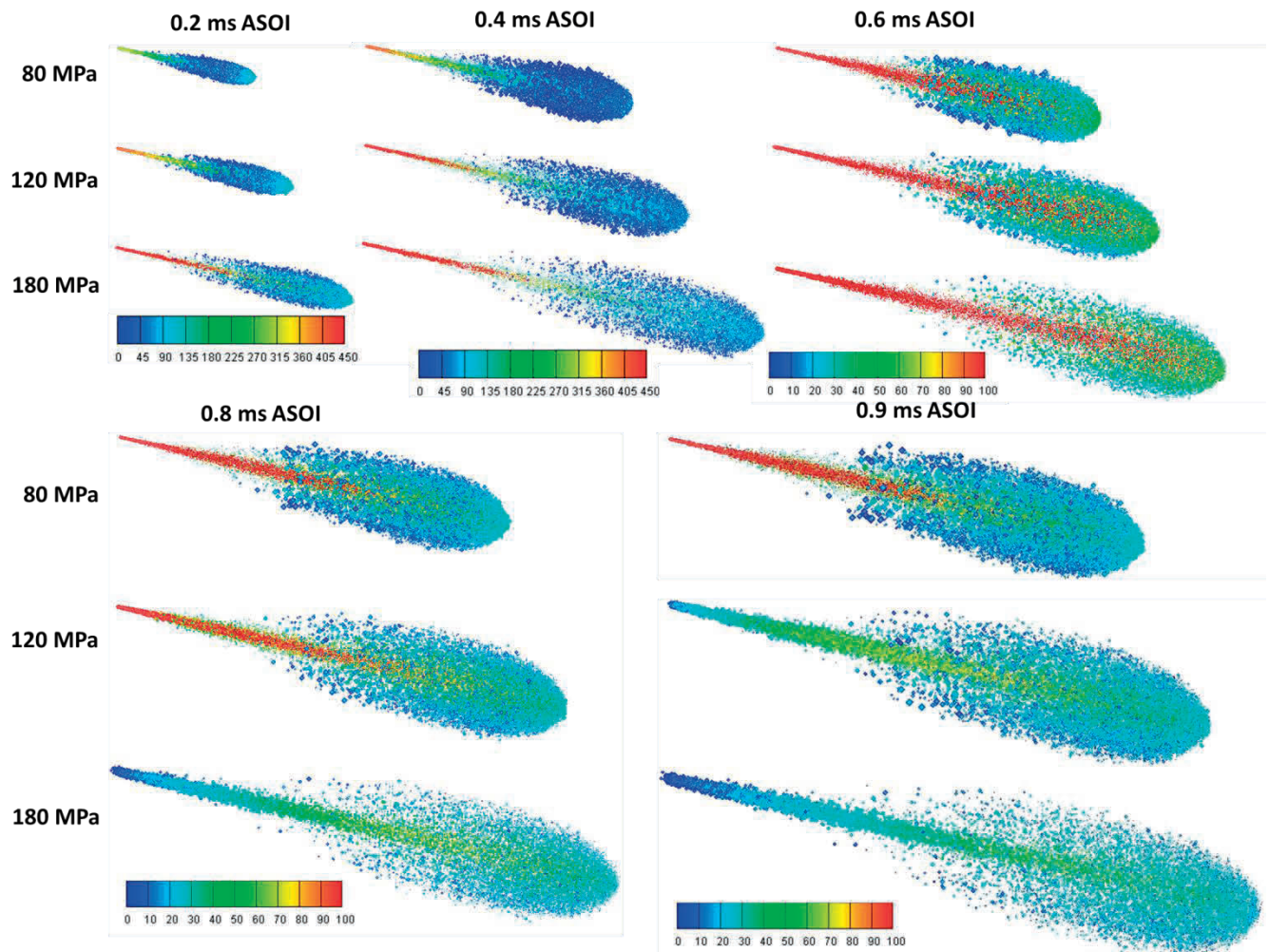


Figure 6.11 Spray evolution under different rail pressure conditions (velocity m/s)

In the near nozzle region, with the increasing of the rail pressure, the injection velocity is increased, while the droplet size is reduced. Paying attention to the downstream of the spray, the droplets in the periphery of the spray have lower velocity and larger size. Moreover, at 0.8 ms ASOI, the injection under 180 MPa condition is already finished, and at 0.9 ms ASOI only under the 80 MPa pressure condition, the injection is still happening. As a result, the droplet velocity become lower, and the liquid jet near the nozzle hole becomes thicker.

The comparison of spray tip penetration is shown in Figure 6.12, and it is obvious that with the increasing of the rail pressure, the penetration is increased a lot. The comparison of Sauter mean diameter and average turbulent kinetic energy (TKE) in the flow field under different conditions are presented in Figure 6.13, respectively.

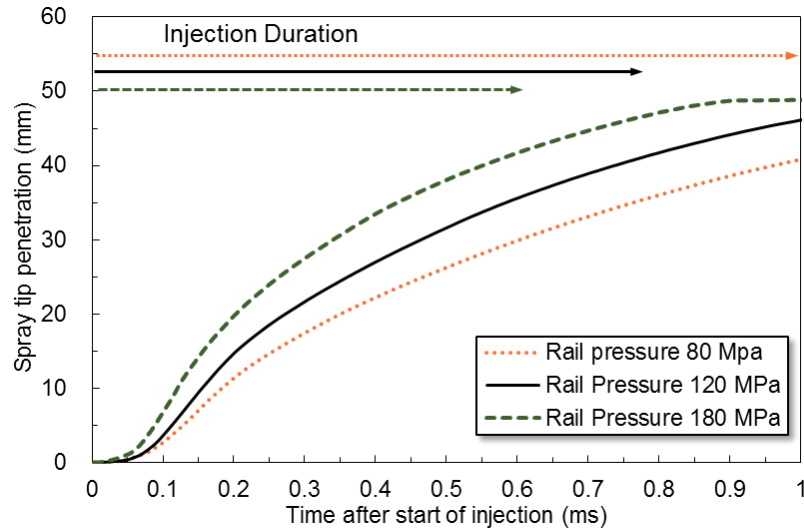
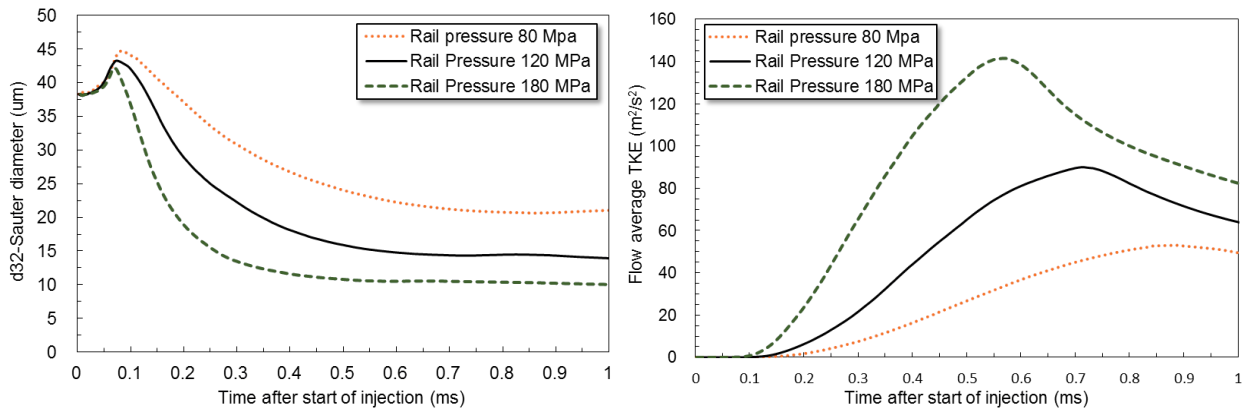


Figure 6.12 Comparison of spray tip penetration under different rail pressure conditions



(a) Sauter mean diameter result

(b) Flow average turbulent kinetic energy

Figure 6.13 Comparison in Sauter mean diameter and flow average TKE under different rail pressure conditions

The droplet size is decreased a lot with the increasing of the rail pressure, which is coincided with the spray images in Figure 6.11. Average TKE result also shows the interesting trend, and the higher rail pressure can generate much higher TKE than the lower rail pressure one, which implies that the interaction and velocity deviation between the liquid droplet and the ambient gas are more apparent. That is another reason that why the break up processes, especially for the second break up process, are more prevalent under the higher pressure condition.

6.4.3 Sensitivity of Spray Properties to Nozzle Hole Diameter Variation

In this section, the nozzle hole diameter effect on the multi-hole nozzle spray evolution will be discussed, and the hole diameter is selected as 0.07 mm, 0.10 mm, and 0.133 mm, which are corresponding to the Mie scattering experiments in Chapter 4. The injection quantity is also kept constant as 2 mm³/hole. The spray droplets velocity at typical timing during the injection duration is shown in Figure 6.14.

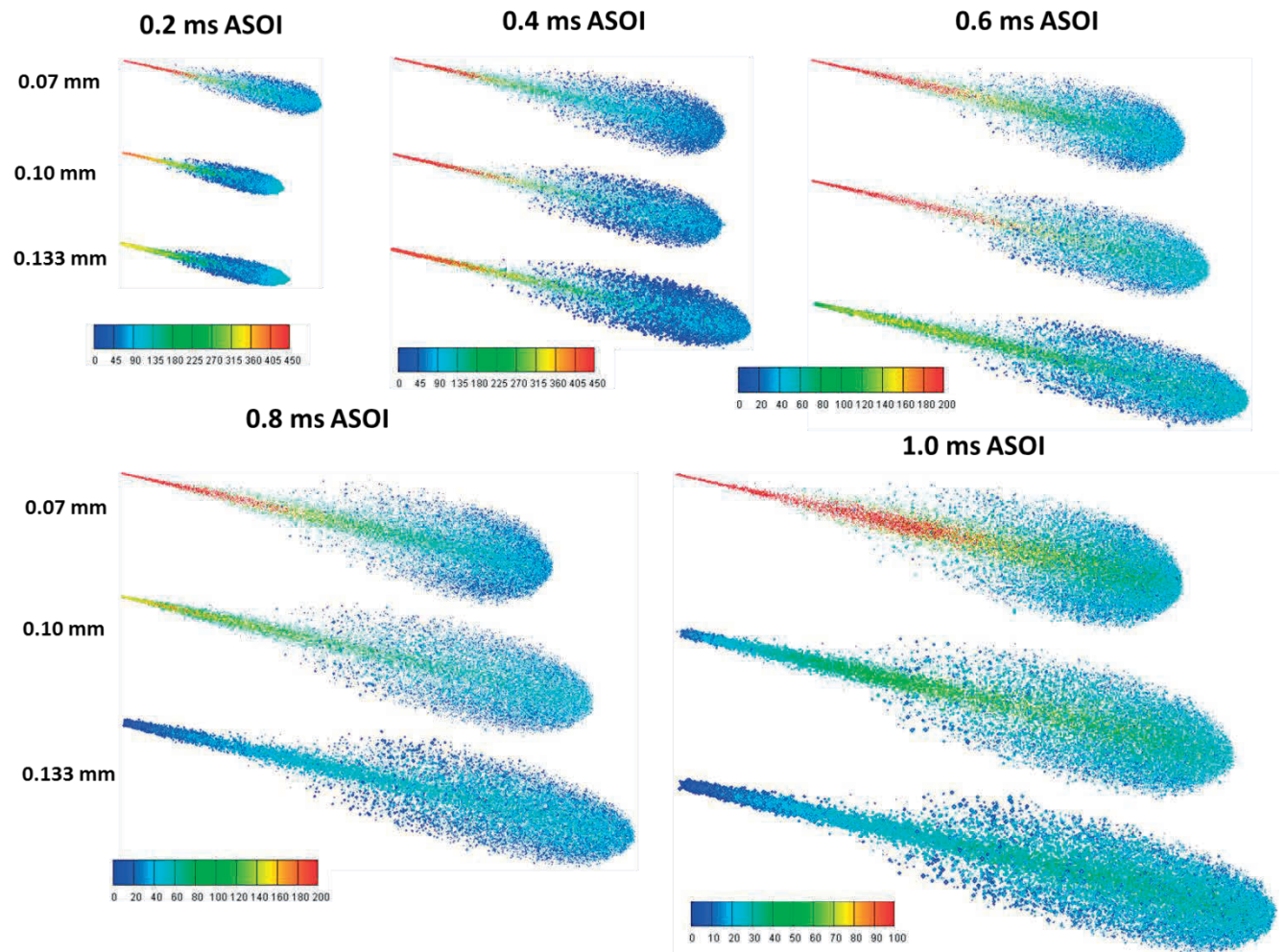


Figure 6.14 Spray evolution under different nozzle hole diameter conditions (velocity m/s)

In the near nozzle region, with the decreasing of the hole diameter, the injection velocity is increased, while the droplet size is reduced. Moreover, the spray tip penetration is also increased at the beginning of the injection (0.2 ms ASOI). Paying attention to the downstream of the spray, the droplets in the core of the spray have higher velocity and larger size. Moreover, the injection duration is shortened by the hole diameter increasing, hence at 0.8 ms ASOI, and 1.0 ms ASOI, the droplet velocity become lower, and the liquid jet near the nozzle hole becomes thicker.

The comparison of spray tip penetration is shown in Figure 6.15, and it is obvious that there is overlap in the result, which is in accordance with the discussion in Chapter 4. The comparison of Sauter mean diameter and average turbulent kinetic energy (TKE) in the flow field under different conditions are presented in Figure 6.16, respectively.

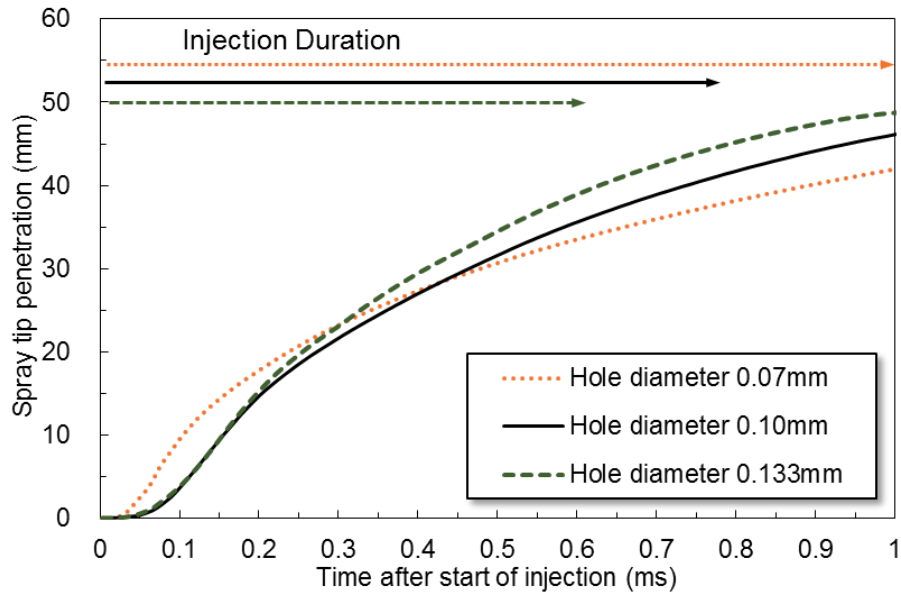
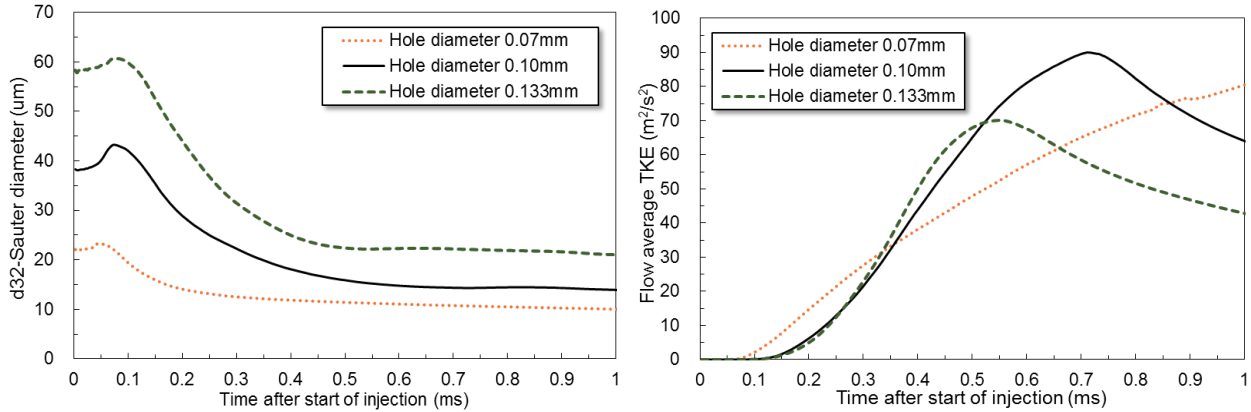


Figure 6.15 Comparison of spray tip penetration under different hole diameter conditions



(a) Sauter mean diameter result

(b) Flow average turbulent kinetic energy

Figure 6.16 Comparison in Sauter mean diameter and flow average TKE under different hole diameter conditions

The droplet size is decreased a lot with the decreasing of the hole diameter, which is coincided with the spray images in Figure 6.13. The average TKE result also shows the interesting over trend, which is also coincided with the spray width result in Chapter 4, the TKE is a reflection of spray momentum transferring to the turbulent energy, which is important to the jet break up.

The spray liquid mass and velocity dominant the spray momentum emerging from different holes at the same time, hence there is overlap relationship in the average flow field TKE results.

6.5 SUMMARY

The spray simulation results are introduced in this chapter, and the internal flow simulation results are inserted into the break up models as the boundary conditions. The comparison of single-hole and multi-hole nozzles spray is firstly discussed. The effect of rail pressure and hole diameter on the spray evolution is also analyzed in detail, the main conclusions are shown as follows.

1. The coupling between the internal flow and spray simulation is the best way to reproduce the spray evolution inside the chamber, and this method can provide more detail boundary information to the break up models and take the nozzle geometrical design effect on the spray characteristics into the consideration. As a result, the accuracy of the numerical work can be increased a lot.
2. The comparison result can validate the analysis in last two chapters, the multi-hole nozzle has lower injection velocity, shorter spray tip penetration, better atomization, wider spray propagation, smaller droplet size, and higher flow field turbulent level. As a result, it is necessary to pay more special attention to the practical multi-hole diesel sprays.
3. The multi-hole nozzle spray interaction and the ambient gas flow between the sprays is also discussed in this chapter, and distribution of the ten sprays is symmetrical, and the ambient gas between the spray plumes entrains into the adjacent sprays, simultaneously, which have significant effect on the mixture formation and fuel evaporation.
4. Increasing the rail pressure can enlarge the injection velocity, spray tip penetration, and flow field turbulent level, while it can decrease the injection duration and droplet size, and the spray width is also reduced a little by the increase of the rail pressure.
5. The spray properties are very sensitive to the variation of nozzle hole diameter. The micro hole and the normal larger hole can exert very special effect on the spray evolution. There is overlap trend in the spray tip penetration and flow field turbulent level, while the droplets size decreases, and the injection velocity increases monotonously with the reduction of the hole diameter.

CHAPTER 7 SPRAY EVOLUTION AND MIXTURE FORMATION OF MULTI-HOLE NOZZLES UNDER EVAPORATION CONDITIONS

7.1 INTRODUCTION

The multi-hole nozzle spray evolution under non-evaporating conditions has been discussed in Chapter 4. In order to further investigate the spray properties of multi-hole nozzles, the spray evolution under the evaporation condition will be discussed in this chapter.

7.1.1 Experimental Conditions

The experimental conditions and the nozzles applied in this part are all corresponding to the conditions in Chapter 4, and the specific description is shown in Table 7.1. In order to reproduce the engine TDC ambient condition, the temperature is set as 780K, and the ambient pressure is 3.9 MPa, which can maintain the same ambient density in Chapter 4. As introduced in Chapter 2, the fuel is the tracer test fuel, and the properties are listed as below. The single-hole and multi-hole nozzle spray evaporation characteristics under different injection pressure and quantity conditions will be discussed and analyzed one by one. Under each condition, the fuel is injected four times, while the spray images shown in this chapter are the single-shot images without average.

Table 7.1 Experimental conditions

Injection Conditions		
Fuel (Tracer LAS Test Fuel)	Density (20 °C, 1 atm) : ~767 kg/m ³ Boiling Point (1 atm) : ~235 °C Kinetic Viscosity (20 °C, 1 atm) : ~2.48 (10 ⁻⁶) m ² /s	
Injector	Single-Hole	Multi-Hole
Injection Quantity: Q_{inj} (mm ³ /hole)	2.0*	0.3 2.0*
Rail Pressure: P_{inj} (MPa)	120*	80 120* 180
Ambient Condition		
Ambient Gas	Nitrogen	
Ambient Pressure : P_a (MPa)	3.9	
Ambient Temperature : T_a (K)	780	
Ambient Density : ρ_a (kg/m ³)	17.4	

* Baseline condition

7.1.2 Image Processing and Technical Validation

The multi-hole nozzle spray is not hundred percent vertical inside the chamber, as introduced in Chapter 2, hence the axisymmetric image processing method, which is called as onion-peeling

deconvolution method, cannot be employed to calculate the vapor concentration here. As a result, if using the LAS technique on the non-axisymmetric spray [Tadokoro, T. et al., 2006], such as the multi-hole or impinged spray, an extended LAS data processing method for non-axisymmetric sprays, which was proposed by Gao et al. [2007] and Zhang et al. [2004], has to be applied. The flow chart of the extended LAS image processing is illustrated in Figure 7.1.

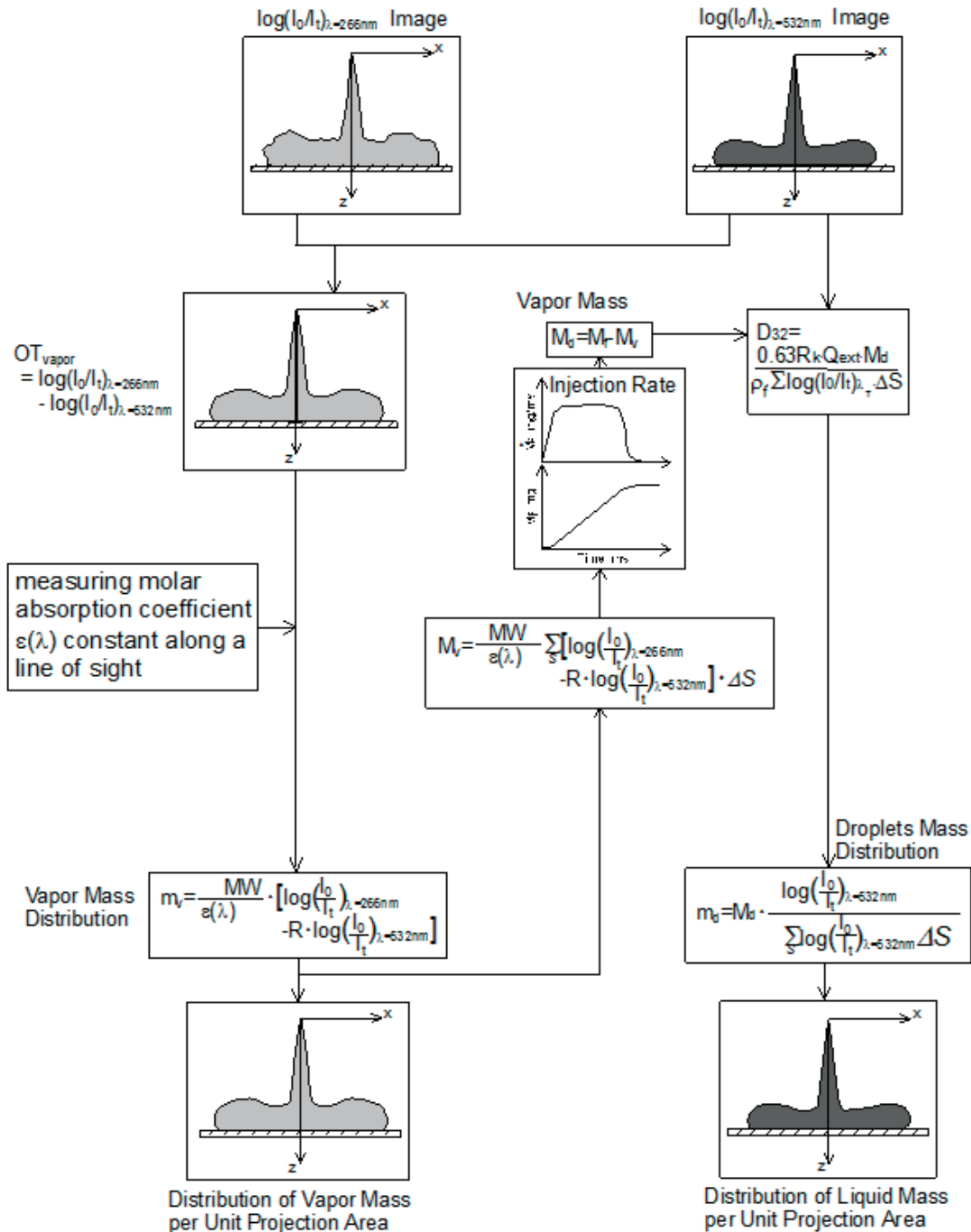


Figure 7.1 Flow Chart of Analysis of Mass Distribution

This method suggested that the vapor mass in a light path was probably obtained by the integrating light extinction rate from the absorption wavelength at per unit area along the light direction. Based on the introduced in Chapter 2, the integrated value of vapor phase mass \overline{C}_V in the light path at per unit cross-sectional area can be expressed in Equation 7.1.

$$\overline{C}_V = \int_L C_V dL = \frac{M}{\varepsilon} \int_L \log\left(\frac{I}{I + dI}\right)_{V_{abs}} dL$$

$$\overline{C}_V = \int C_V dl = \frac{MW \cdot \log(I_o/I_t)_{V_{abs}}}{\varepsilon} \quad (7.1)$$

In this case, it is assumed that the molar absorption coefficient is a constant in the direction of light path, the vapor mass M_V [kg] in the fuel spray can be obtained by integrating the average vapor concentration in whole spray area, and as shown in following.

$$M_V = \int \overline{C}_V dS = \int \frac{MW \cdot \log(I_o/I_t)}{\varepsilon} \times 10^2 \quad (7.2)$$

by this way, the accumulative mass of vapor and its distribution, as well as the liquid phase can be measured quantitatively within the non-axisymmetric spray.

Before the further application of this method, the validation was conducted by two ways. The first one is to compare the laser attenuation of UV and Visible beams under the non-evaporation condition to confirm the theory assumption and the setting of the laser beams. The single-hole nozzle spray and multi-hole nozzle spray were tested, which are shown in Figure 7.2 and Figure 7.3, respectively. It is proved that the laser attenuation of UV and Visible beams are corresponding to each other along the typical and important lines.

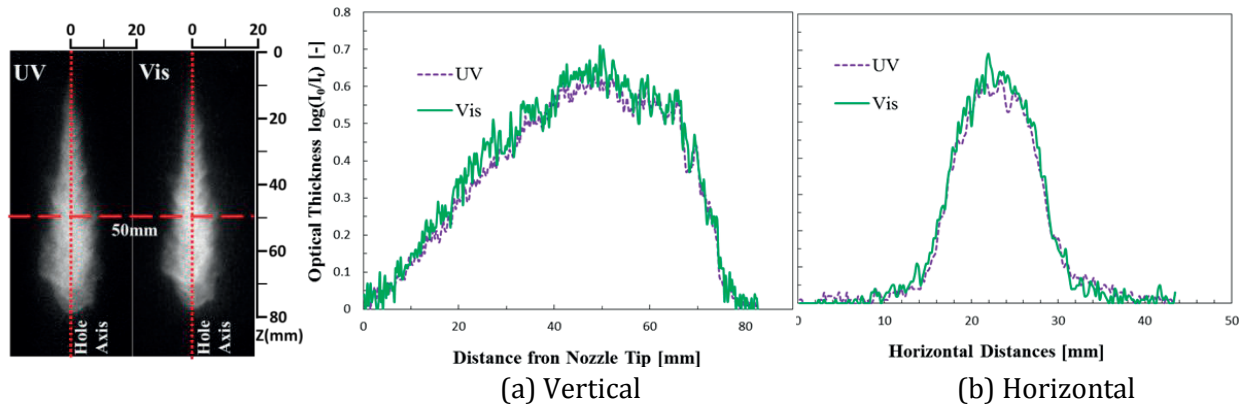


Figure 7.2 Distribution of attenuation on the Vertical and Horizontal Axis
 $P_{inj}=100\text{MPa}$ $M_f=2.97\text{mg}$ $P_a=1.4\text{MPa}$ $T_a=300\text{K}$ Test Fuel : Tracer LAS Fuel

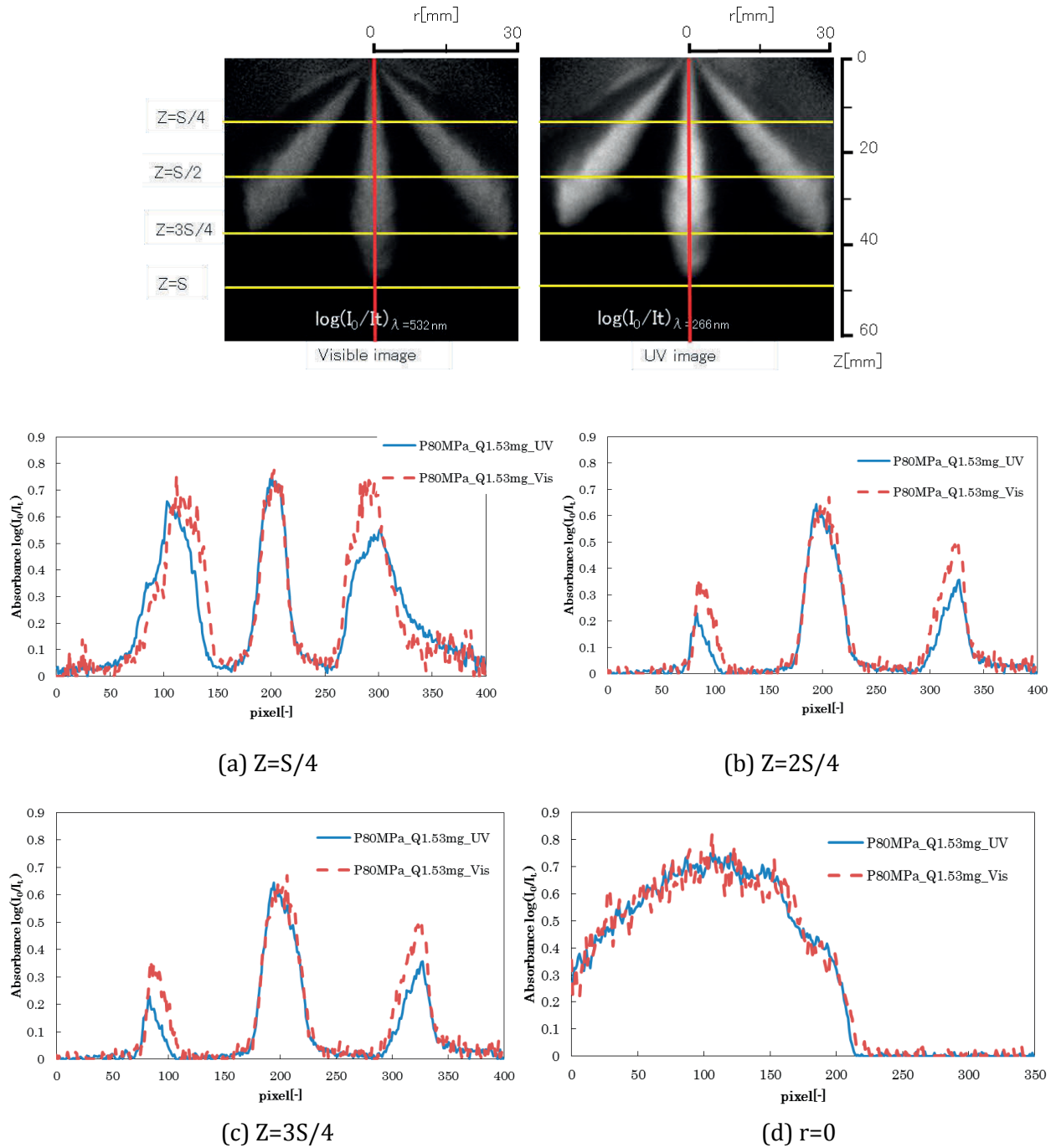


Figure 7.3 Distribution of attenuation on the Vertical and Horizontal Axis

$P_{inj}=80\text{MPa}$ $M_f=1.53\text{mg}$ $P_a=1.5\text{MPa}$ $T_a=300\text{K}$ Test Fuel : Tracer LAS Fuel

The second step is to validate this method using the vapor mass of single-hole and multi-hole nozzle spray under the evaporation condition, which are shown in Figure 7.4 and Figure 7.5, respectively. The result reveals that the error is within 10% under all the conditions, hence this method is believable to have high accuracy in the prediction for the spray evaporation properties.

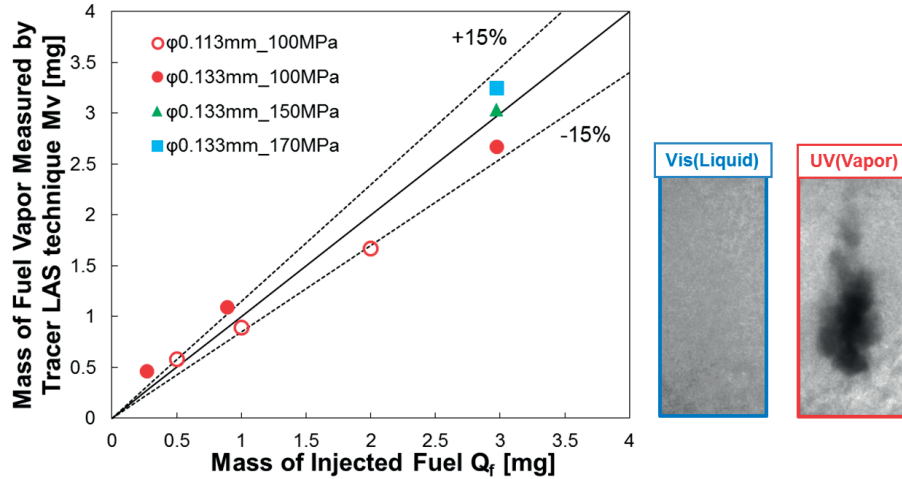


Figure 7.4 Measurement accuracy comparison between vapor mass at fully vaporized and injection mass from single-hole nozzle, Pa=3.6MPa Ta=760K

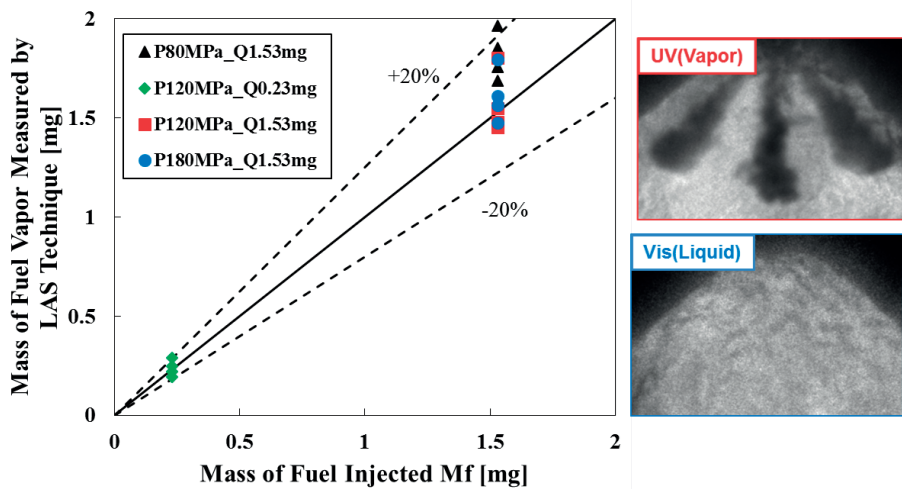


Figure 7.5 Measurement accuracy comparison between vapor mass at fully vaporized and injection mass from multi-hole nozzle, Pa=3.9MPa Ta=780K

7.2 EVAPORATING SPRAY CHARACTERISTICS OF SINGLE-HOLE AND MULTI-HOLE NOZZLES

In this section, the properties of spray evaporation emerging from single-hole and multi-hole nozzles will be compared under the baseline condition (120 MPa rail pressure, 780 K, 1.5 MPa ambient pressure, and 2 mm³/hole injection quantity). The micro hole diameter effect will also be discussed in the second part of this section, which is corresponding to the contents in Chapter 4 and chapter 5.

7.2.1 Global comparison in the evaporation spray between different nozzles

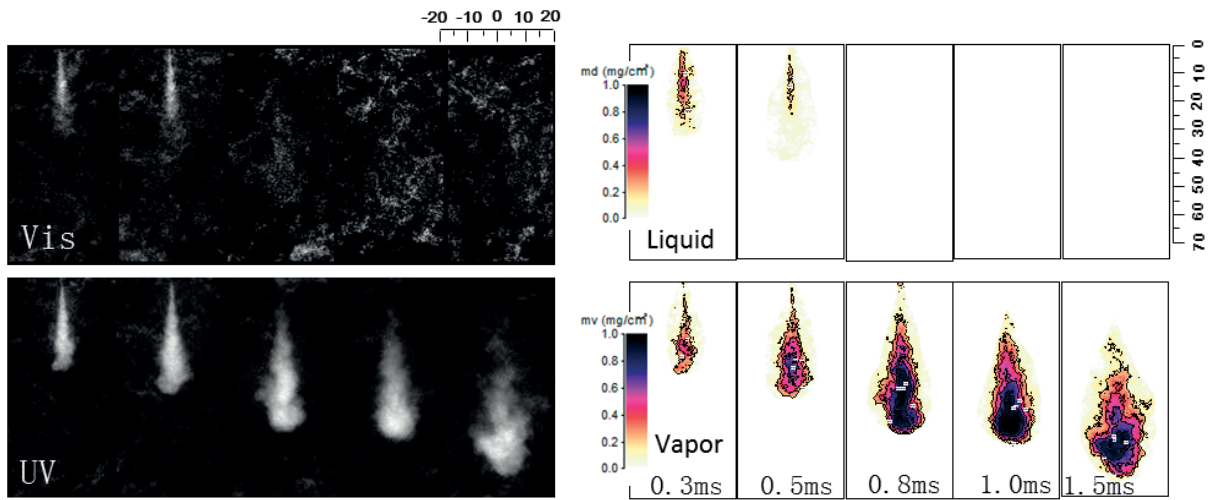


Figure 7.6 Optical thickness images and distribution of vapor and liquid phase of single-hole nozzle spray $D=0.10$ mm $P_{inj}=120$ MPa $M_f=1.53$ mg/hole

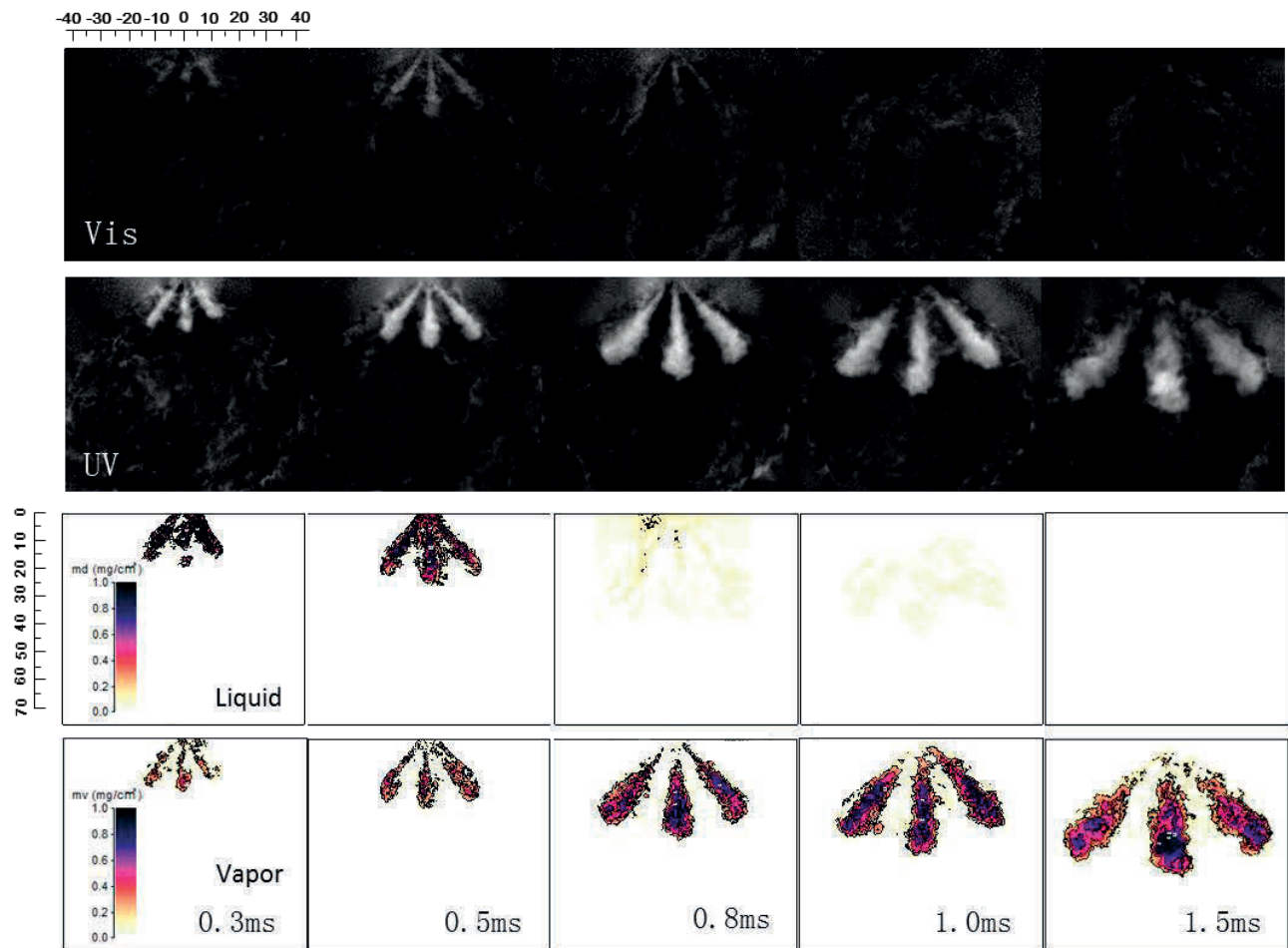


Figure 7.7 Optical thickness images and distribution of vapor and liquid phase of multi-hole nozzle spray $D=0.10$ mm $P_{inj}=120$ MPa $M_f=1.53$ mg/hole

The single-hole and multi-hole nozzle have the same hole length and diameter (0.8 mm and 0.10 mm), which are the same with the previous chapters. The optical thickness images and distribution of vapor and liquid phase of different nozzles at the typical timings are shown in Figure 7.6 and Figure 7.7 respectively. The same with the phenomenon observed under the non-evaporating condition, the single-hole nozzle spray has longer spray tip penetration, larger spray volume, which is attributed by the higher sac pressure and injection rate. Affected by the different injection duration, the vapor mass distribution and fuel evaporation ratio also present interesting rules. The comparison is plotted in Figure 7.7 and Figure 7.8 respectively. The vapor mass of single-hole nozzle spray is larger than that of the multi-hole one, which is mainly caused by the different injection rate. Moreover, the fuel spray evaporation ratio of single-hole nozzle is also a little higher, which has relationship with the ambient gas entrainment under different conditions. The result published by Hayato et al. [2014] can be used to explain the mechanism behind this result.

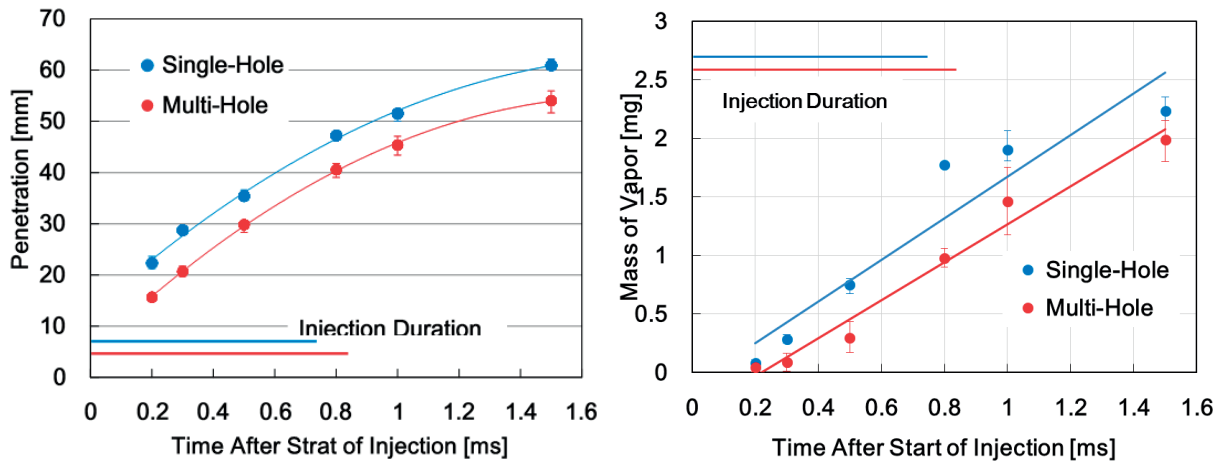


Figure 7.8 Comparison of spray tip penetration and evaporated fuel between different nozzles

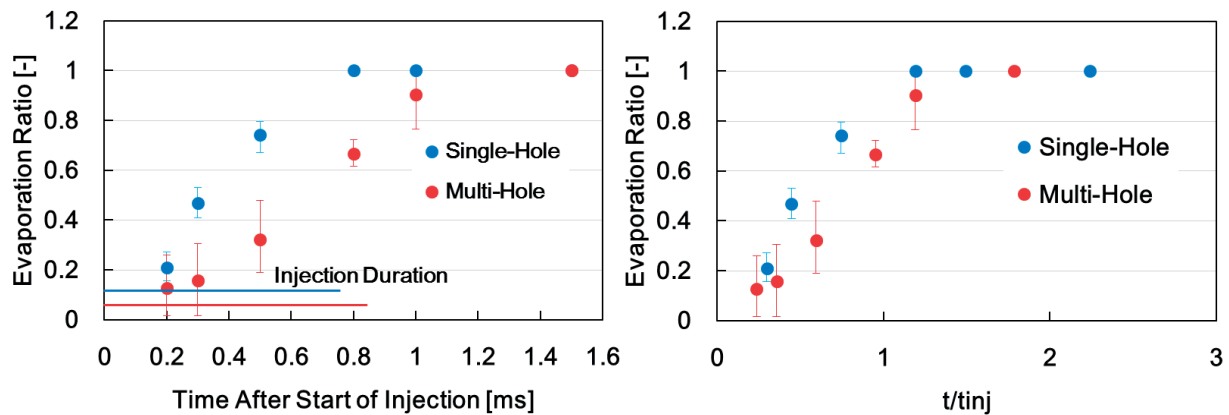


Figure 7.9 Comparison of spray evaporation ratio between different nozzles

The schematic of their measurement is shown in Figure 7.10, and ambient gas flow velocity can be obtained under the multi-hole and single-hole spray conditions. The comparison of ambient gas flow velocity components is presented in Figure 7.11.

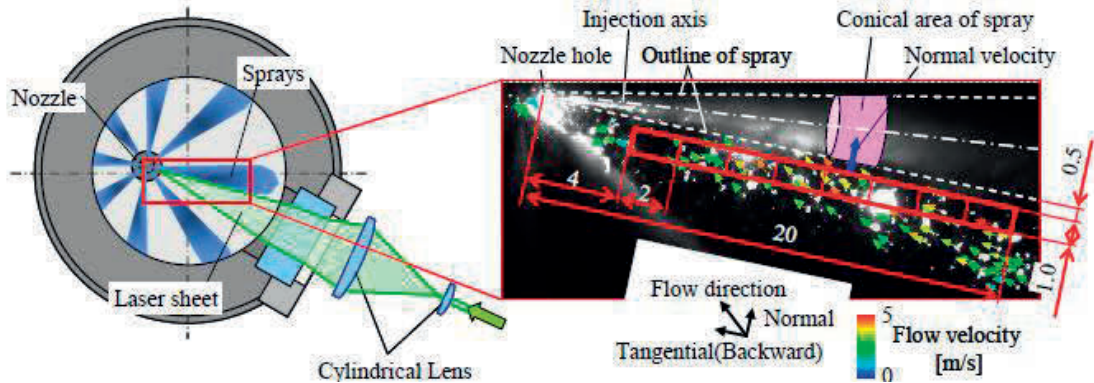


Figure 7.10 Measurement section of air flow rate into spray [Hayato et al. 2014]

It is believed that the ambient gas entrainment of the multi-hole nozzle spray is insufficient compared with that of the single-hole nozzle spray. There are ten spray plumes under the multi-hole condition, and the ambient gas between the spray plumes can enter into the spray, simultaneous, which create the low pressure region between the spray plumes. The ambient gas downstream will come into the low pressure region, where the countercurrent is observed. As a result, the difference in the ambient gas flow velocity components is very obvious in Figure 7.11.

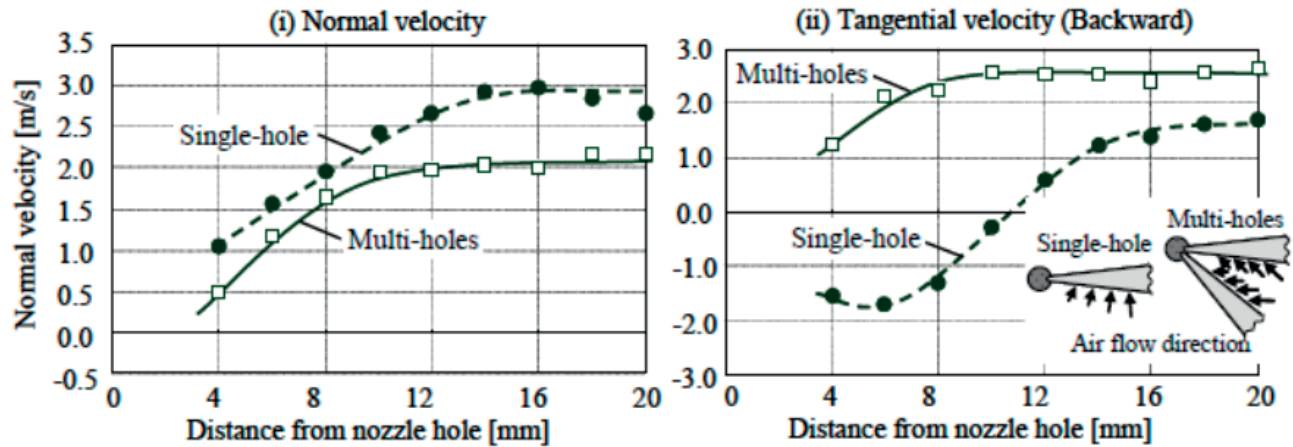


Figure 7.11 Variation of normal and tangential velocity between single-hole and multi-hole [Hayato et al. 2014] 8 holes, $P_{inj}=200$ MPa, $M_f=55$ mm³/8 holes

The simulation results in the current study, which is shown in Figure 7.12, also present the same regularity, and it can prove the analysis in last paragraph. The ambient flow velocity is quite different, which can affect the ambient entrainment significantly, as shown in the Figure. Moreover, the low injection velocity and shorter penetration is also not beneficial for the gas entrainment.

Different ambient gas entrainment properties can alter the fuel evaporation process. Therefore, there is different evaporation ratio under the single-hole and multi-hole nozzle sprays.

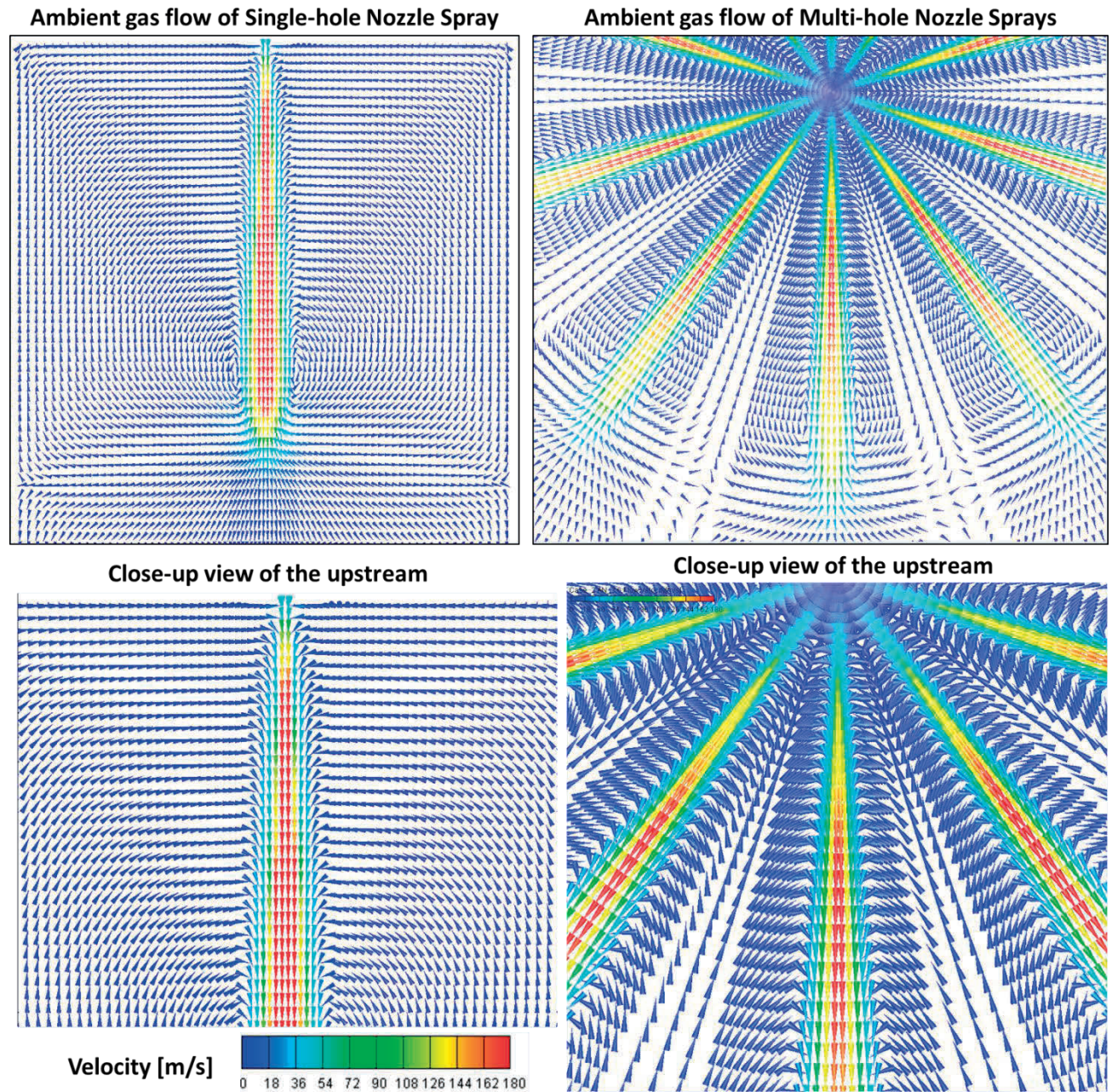


Figure 7.12 Comparison of ambient flow characteristics between single-hole and multi-hole spray

7.2.2 Effect of Micro Nozzle Hole Diameter on Mixture Formation Process

The comparison between the single-hole and multi-hole nozzle under the micro hole diameter condition (0.07 mm). The experimental conditions are the same with baseline condition.

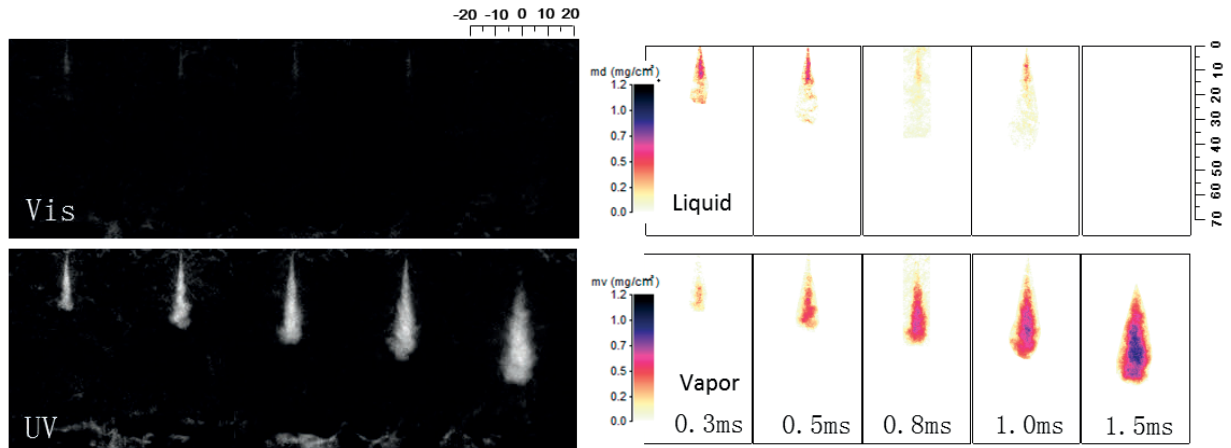


Figure 7.13 Optical thickness images and distribution of vapor and liquid phase of single-hole nozzle spray $D=0.07\text{mm}$ $P_{inj}=120\text{MPa}$ $M_f=1.53\text{ mg/hole}$

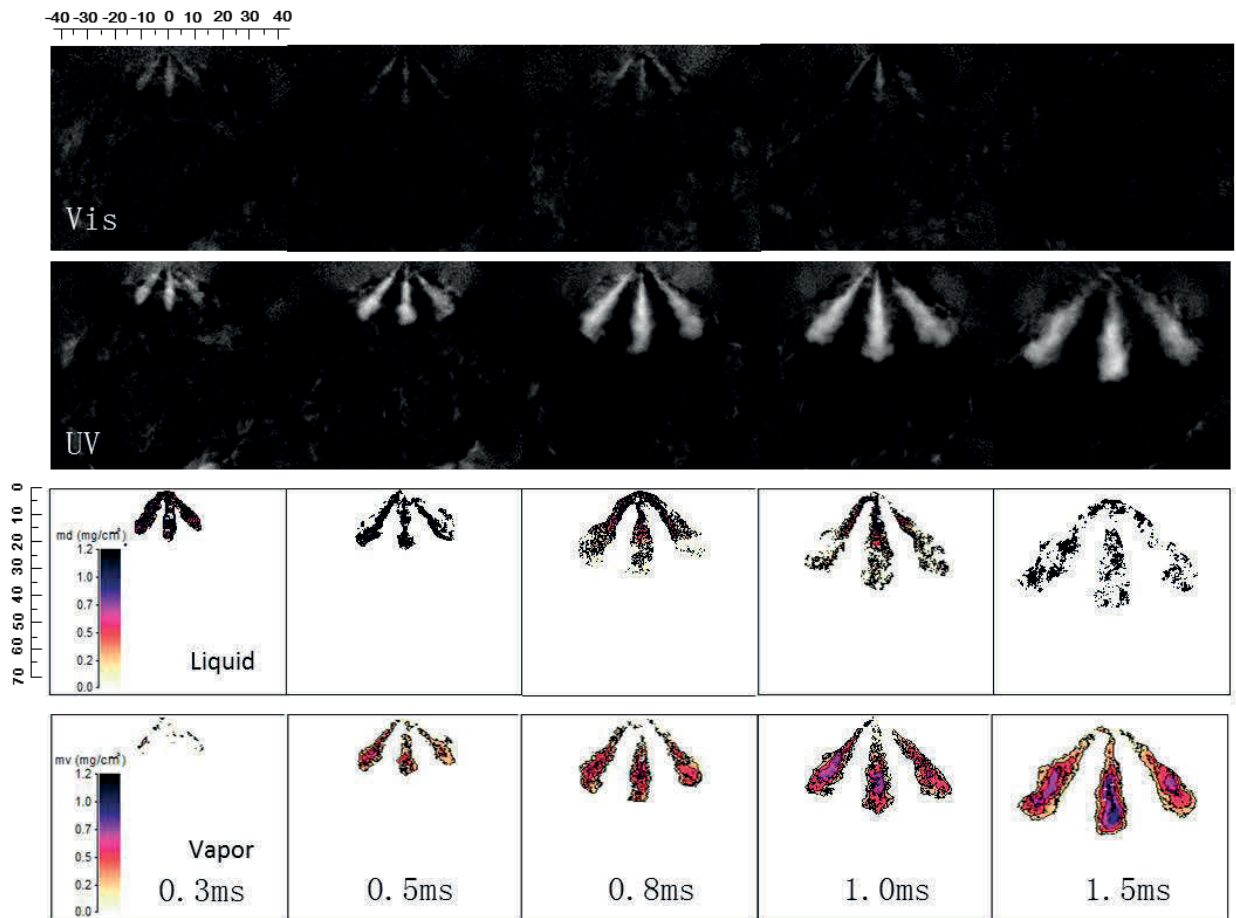


Figure 7.14 Optical thickness images and distribution of vapor and liquid phase of multi-hole nozzle spray $D=0.07\text{mm}$ $P_{inj}=120\text{MPa}$ $M_f=1.53\text{ mg/hole}$

The optical thickness images and distribution of vapor and liquid phase of the sprays emerging from different nozzles are shown in Figure 7.13 and 7.14, respectively.

The corresponding spray tip penetration comparison under different hole diameter condition is shown in Figure 7.15. It is seen that the deviation in the spray tip penetration between the two nozzles, is decreased much under the micro hole condition. The result is coincided with the analysis in Chapter 4. The reduced sac pressure discharge rate mainly attributes to this issue.

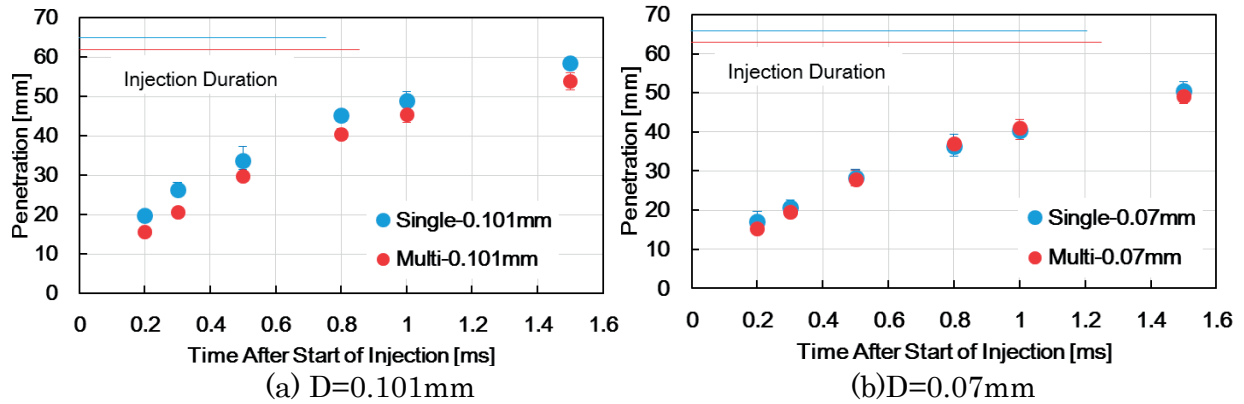


Figure 7.15 Comparison of spray tip penetration between different nozzles under normal and micro hole diameter conditions

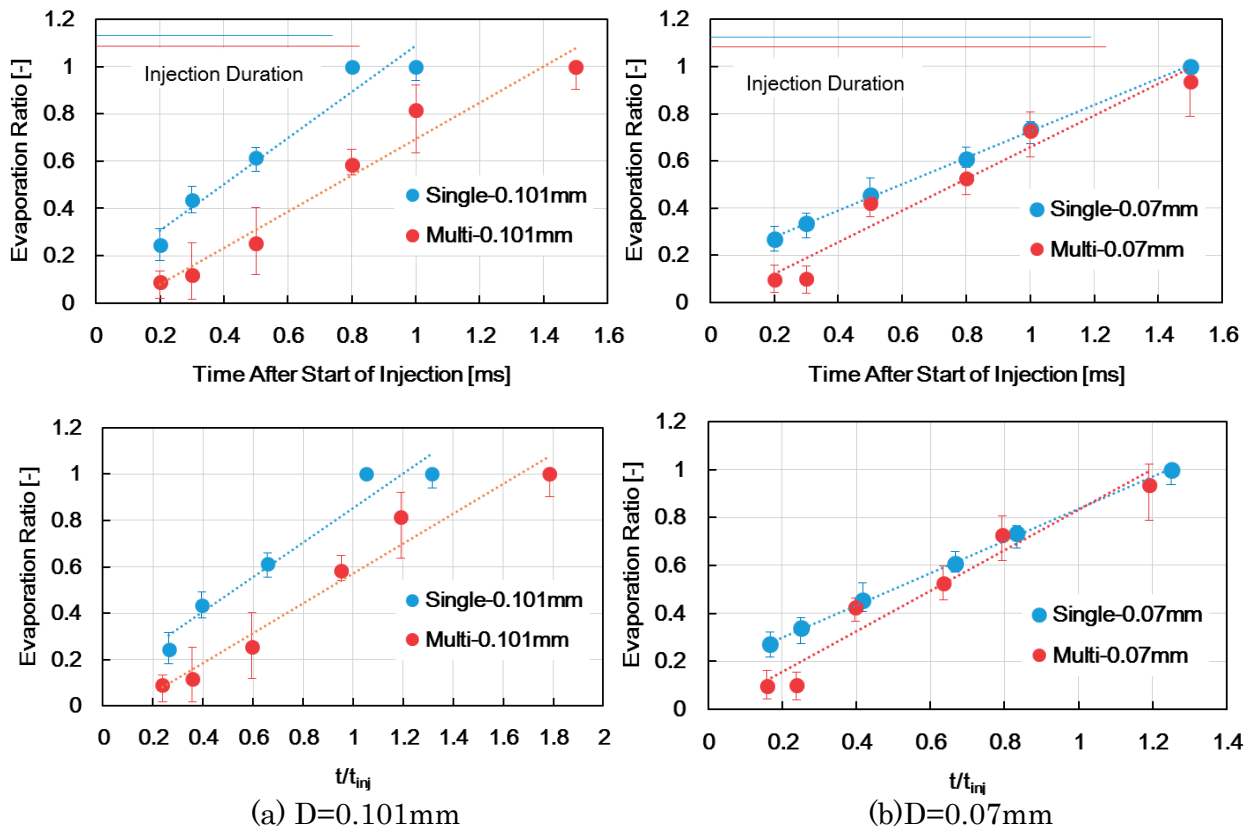


Figure 7.16 Comparison of spray evaporation ratio between different nozzles under normal and micro hole diameter conditions

Moreover, the comparison of fuel spray evaporation characteristics under different hole diameter condition is shown in Figure 7.16. The evaporation ratio is shown in real timing and normalized timing. The single-hole nozzle spray also has higher evaporation ratio than that of the multi-hole one under the micro hole condition, while the deviation is not so large. This can be explained by the reduced distinction between the single-hole and multi-hole nozzle spray and internal flow properties discussed in Chapter 4 and 5.

7.3 EVAPORATING SPRAY EVOLUTION AND MIXTURE FORMATION PROCESSES OF MULTI-HOLE NOZZLES

The multi-hole nozzle spray evolution under different dynamic operation and geometrical conditions will be discussed in this section. The first part will focus on the effect of rail pressure and injection quantity on the multi-hole nozzle spray evaporation characteristics.

7.3.1 Liquid and Vapor Phase Distribution under Different Dynamic Operation Conditions

Firstly, the fuel was injected into the high pressure and high temperature chamber under the constant quantity (2 mm³/hole) and different rail pressure conditions (80,120,180 MPa). The optical thickness images of UV laser beam are shown in Figure 7.17.

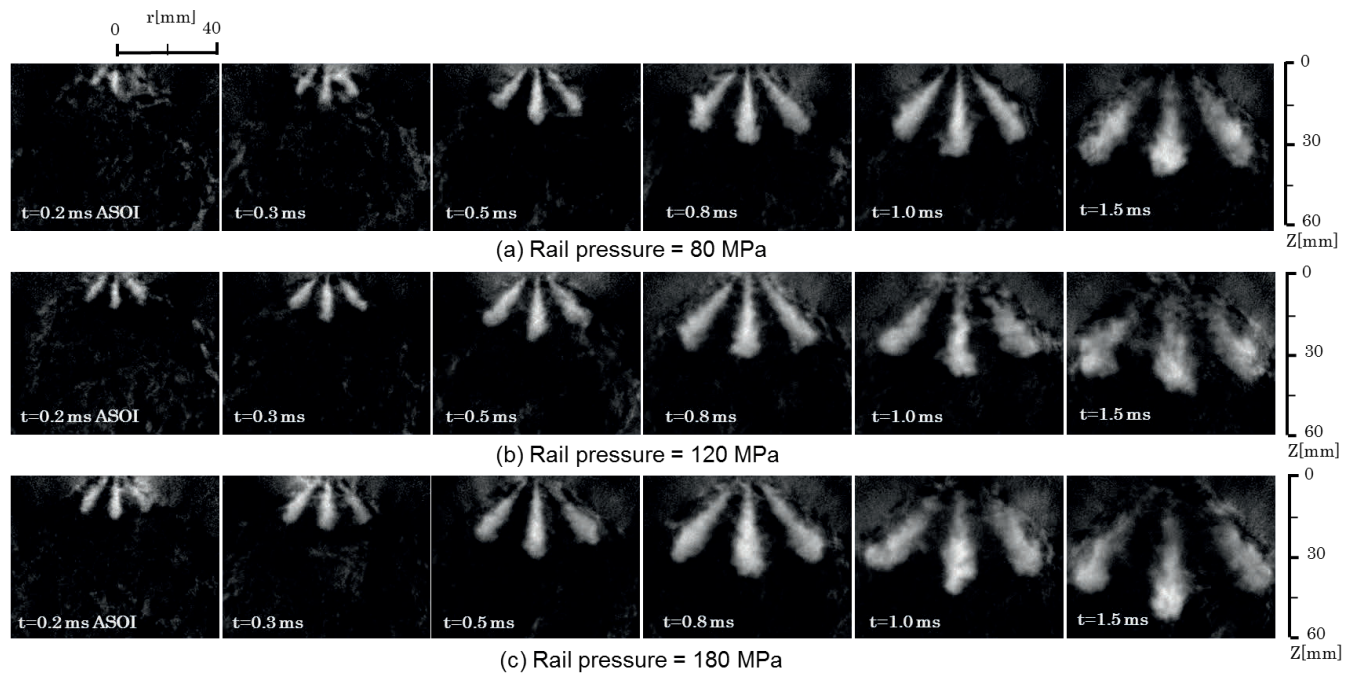


Figure 7.17 Optical thickness images of UV beam of multi-hole nozzle spray under different rail pressure conditions. $D=0.10$ mm, $P_{inj}=80, 120, 180$ MPa, $M_f=1.53$ mg/hole.

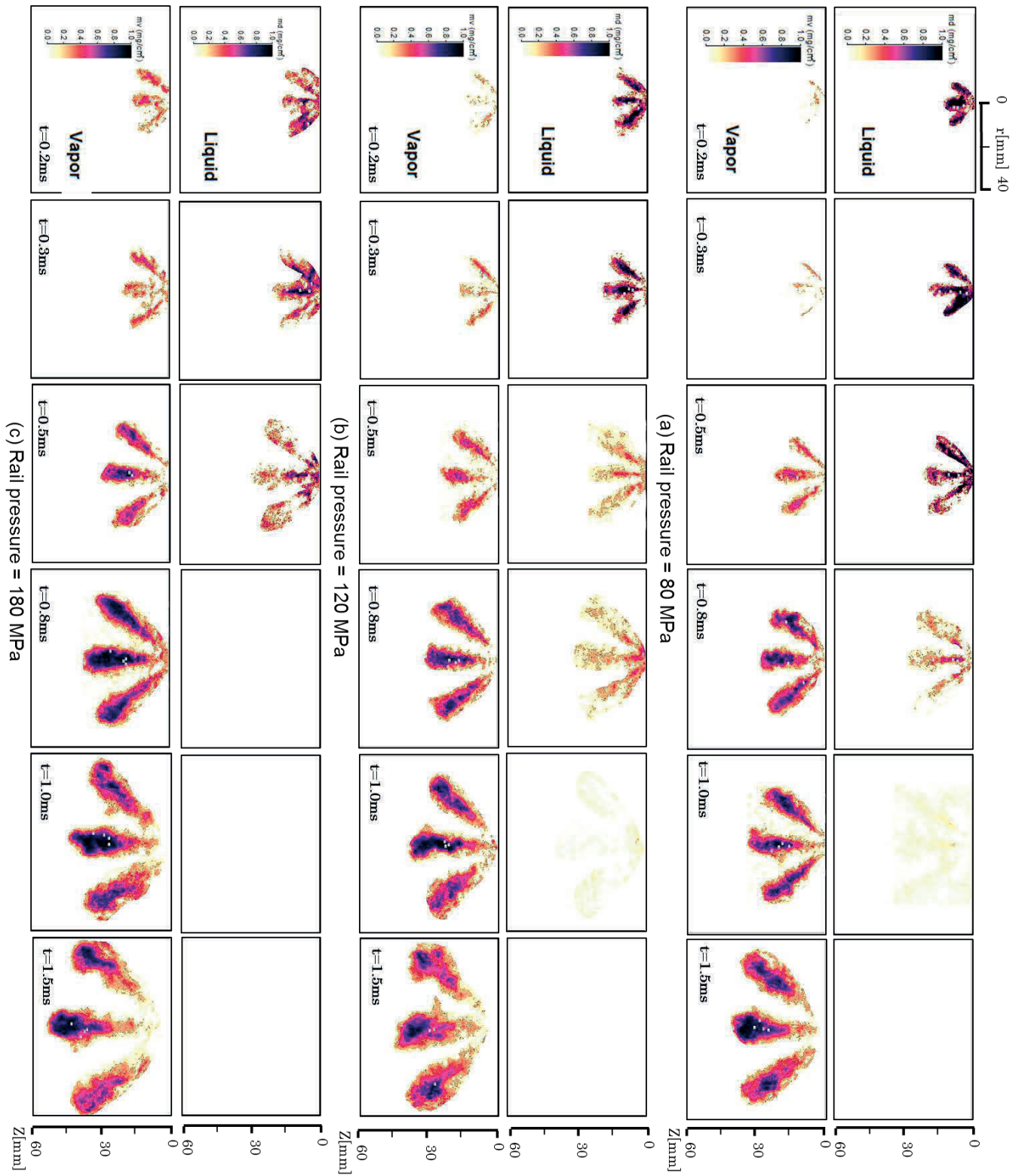


Figure 7.18 Distribution of vapor and liquid phase of multi-hole nozzle spray under different rail pressure conditions. $D=0.10$ mm, $P_{inj}=80, 120, 180$ MPa, $M_f=1.53$ mg/hole.

The comparison of distribution of vapor and liquid phase of multi-hole nozzle spray at the typical timing under different rail pressure conditions is shown in Figure 7.18. It seems that with the rail pressure increasing, the spray is enhanced. The comparison of spray liquid and vapor phase penetration under different rail pressure conditions is shown in Figure 7.19. With the increasing of the rail pressure, both of the liquid penetration and vapor penetration are increased. It should be noted that the under the lower rail pressure condition, affect by the slow evaporation rate, the liquid penetration is higher than the vapor penetration. However, under the high pressure condition, this deviation is reduced a lot.

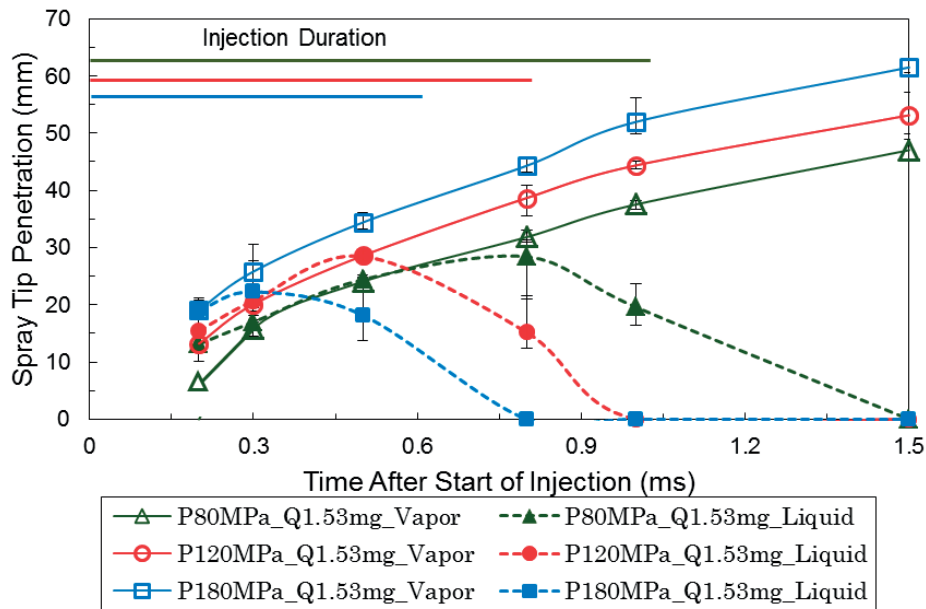


Figure 7.19 Spray liquid and vapor phase penetration under different rail pressure conditions

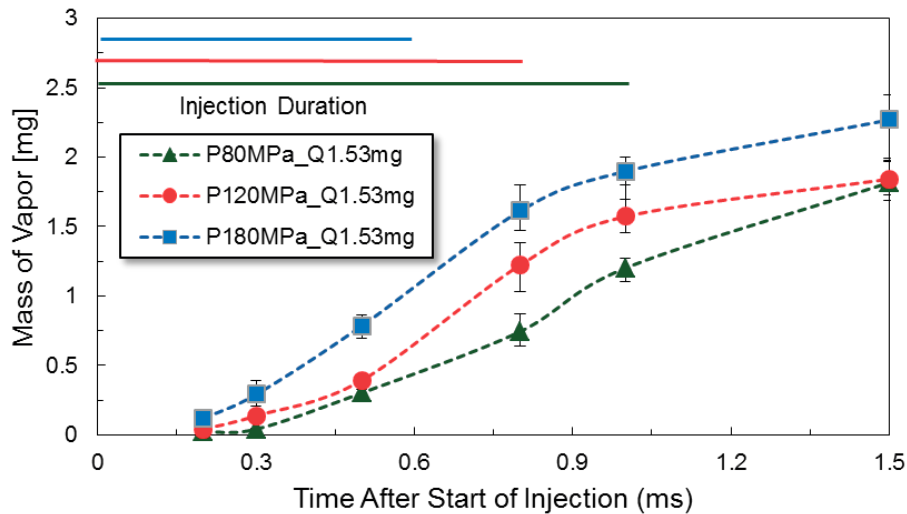


Figure 7.20 Comparison of vapor phase mass of the spray under different rail pressure conditions

The comparison of vapor phase mass of the spray under different rail pressure conditions is presented in Figure 7.20. The fuel evaporation ratio result is shown in Figure 7.21. With the increase of the rail pressure, the vapor phase fuel mass and the fuel evaporation ratio is increased, which confirmed that the rail pressure is a significant factor that alters the spray evaporation.

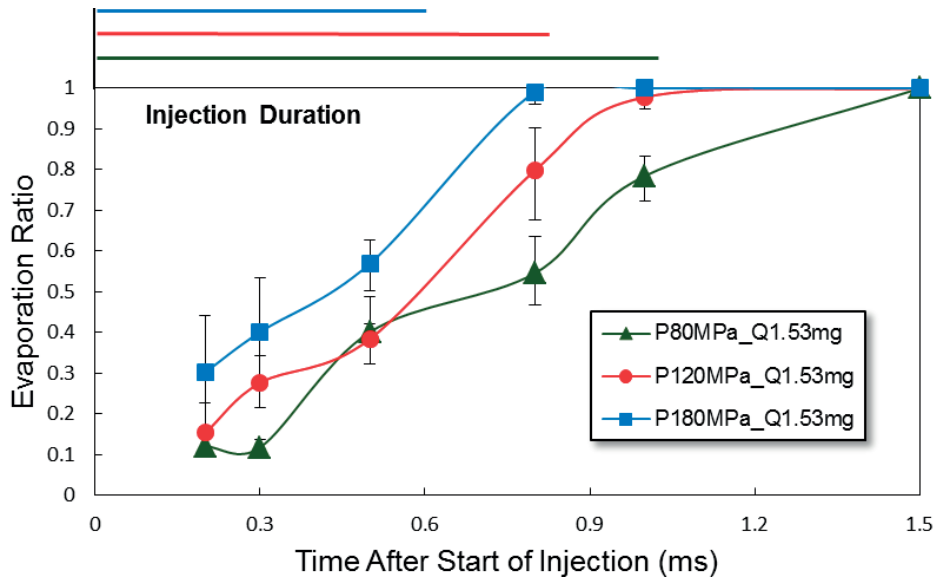


Figure 7.21 Comparison of fuel evaporation ratio under different rail pressure conditions

The injection quantity effect will be discussed in the following paragraphs, and the fuel was injected into the high pressure and high temperature ambient condition under the baseline rail pressure (120 MPa), normal and tiny quantity (0.3 mm³/hole and 2mm³/hole) conditions.

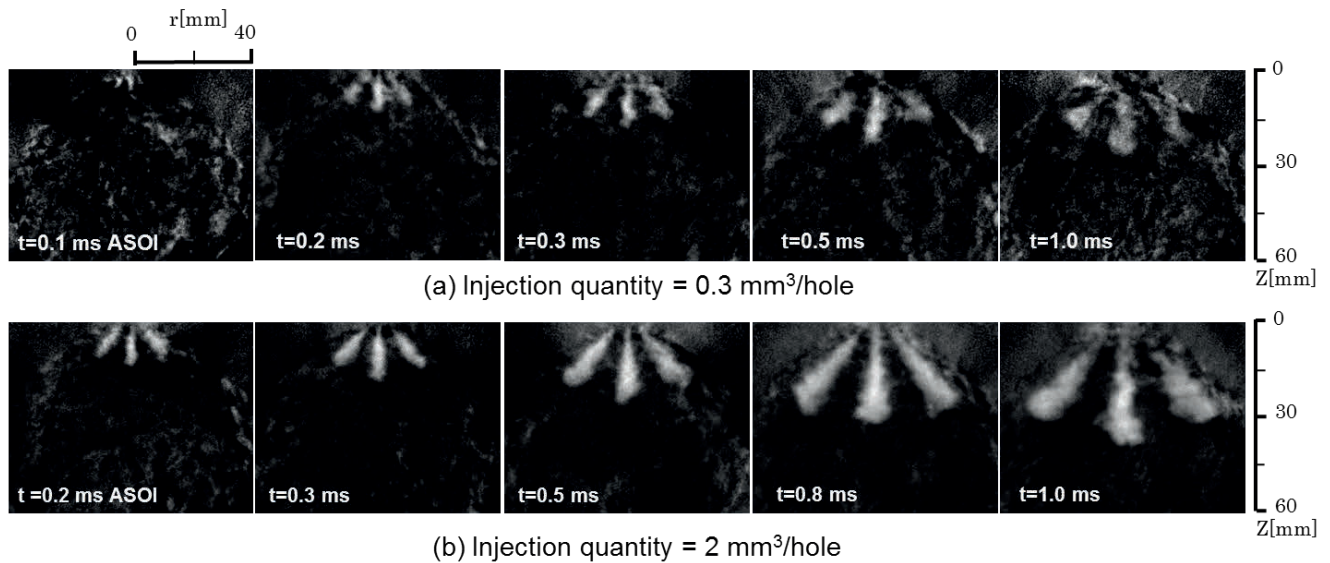


Figure 7.22 Optical thickness images of UV beam of multi-hole nozzle spray under different injection quantity conditions. $D=0.10$ mm, $P_{inj}=120$ MPa, $M_f=0.23$ and 1.53 mg/hole.

Under the tiny injection quantity condition, affected by the supper low fuel quantity and the noise of the high pressure and high temperature image background, the quantity of the spray image is not so much high. As a result, the spray in the upper raw of Figure 7.22 is not so easy to distinguish from the background noise, compared with the normal quantity condition.

The comparison in distribution of vapor and liquid phase of multi-hole nozzle spray at the typical timings between different injection quantity conditions is shown in Figure 7.23. The corresponding liquid and vapor phase spray tip penetration and the time-dependent vapor phase mass quantity are plotted in Figure 7.24 and Figure 7.25, respectively. Under the tiny quantity condition, affect by the lower spray momentum, the vapor phase penetration is shorter than that of the liquid one. However, under the normal quantity condition, affect by the higher spray momentum and evaporation, the vapor phase penetration is always longer than that of the liquid phase one. During the injection duration of tiny quantity condition, the vapor mass is a little larger than that of the normal condition, which can support the analysis above.

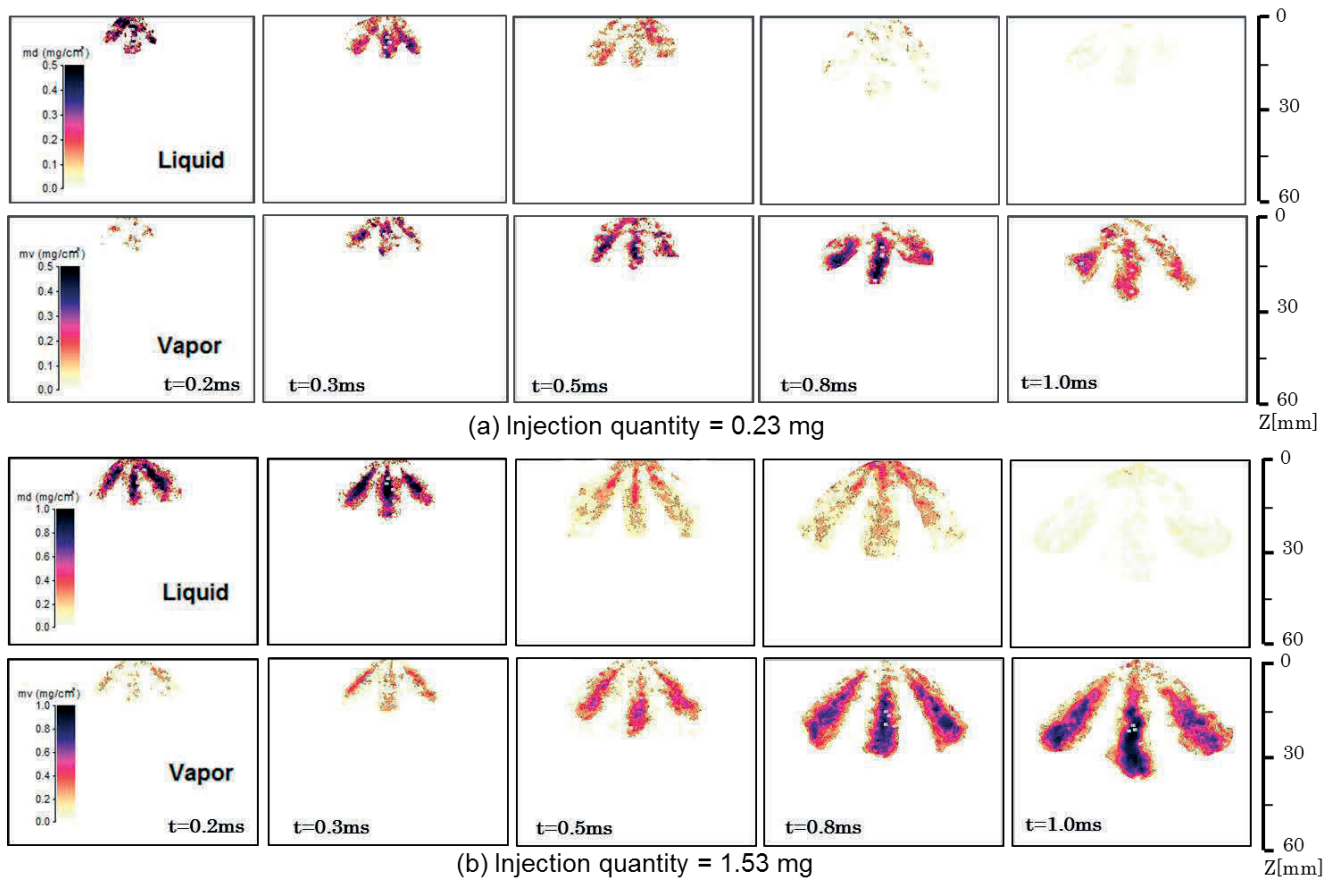


Figure 7.23 Distribution of vapor and liquid phase of multi-hole nozzle spray under different injection quantity conditions. $D=0.10$ mm, $P_{inj}=120$ MPa, $M_f=0.23$ and 1.53 mg/hole

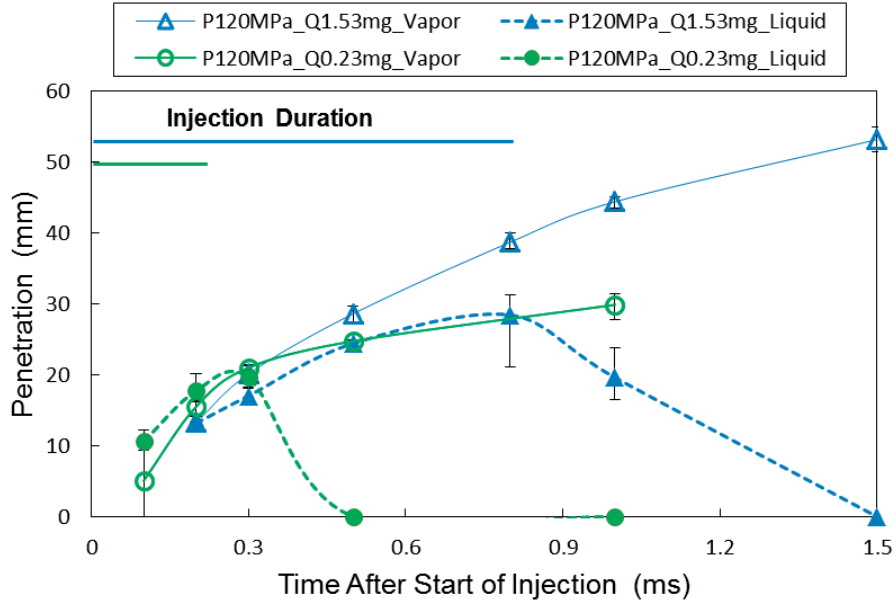


Figure 7.24 Liquid and vapor phase spray tip penetration under different injection quantity conditions. $D=0.10$ mm, $P_{inj}=120$ MPa, $M_f=0.23$ and 1.53 mg/hole

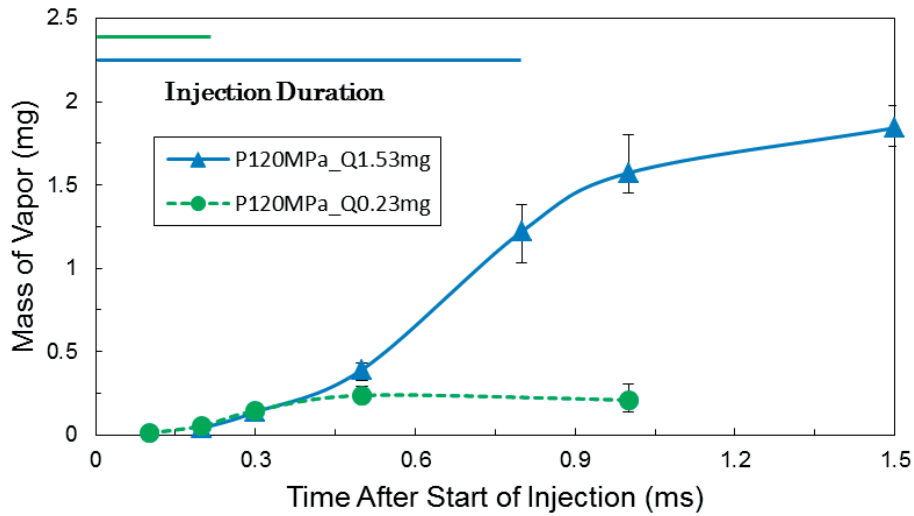


Figure 7.25 Time-dependent vapor phase mass quantity variation

The time-resolved spray evaporation ratio under different injection quantity condition is shown in Figure 7.26. The fuel is evaporated faster under the lower injection quantity condition. However, when it comes to the normalized fuel spray evaporation ratio, the tiny quantity has lower evaporation speed. The lower injection velocity and shorter spray tip penetration under the tiny quantity condition can deteriorate the ambient gas entrainment. Therefore, the normalized evaporation ratio is reduced. When the multiple injection strategies are applied in the engine operation condition, the phenomenon discussed here should be taken into the consideration.

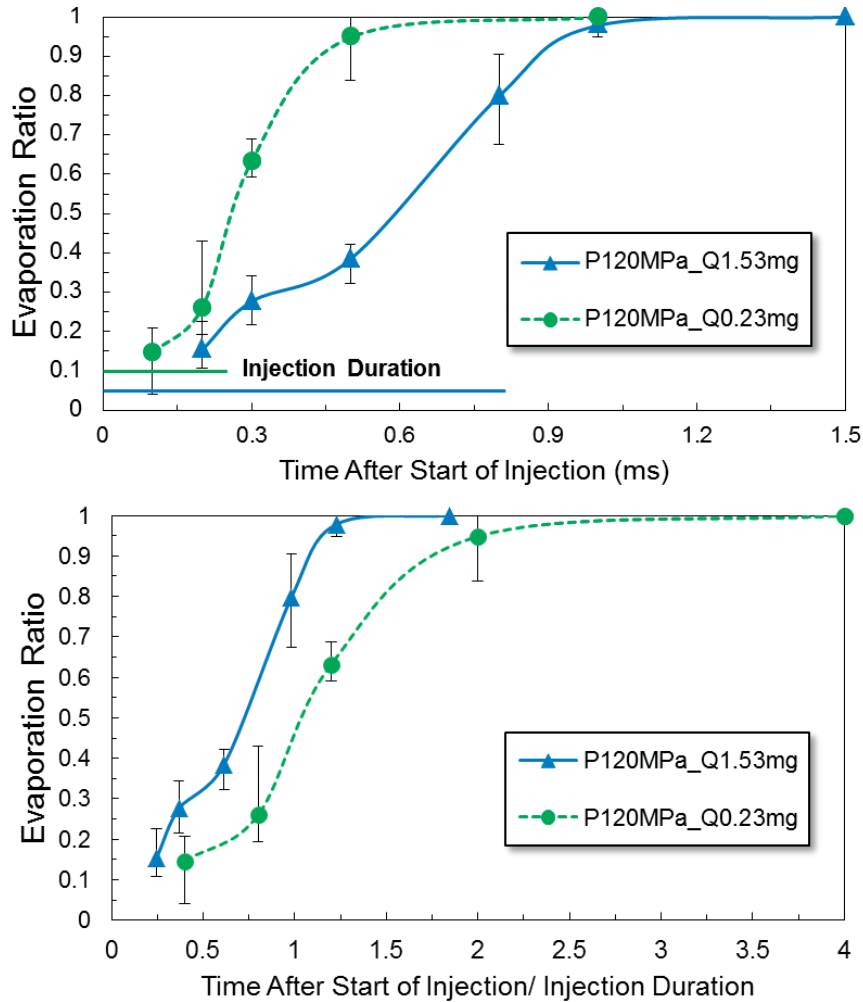


Figure 7.26 Comparison of spray evaporation ratio between different nozzles under normal and micro hole diameter conditions

7.3.2 Effect of Multi-hole Nozzle Geometrical Design on Evaporating Spray Characteristics

In this section, the effect of multi-hole nozzle geometrical design on the spray evaporation characteristics will be discussed. Specifically, corresponding to the non-evaporation conditions in Chapter 4, the effect of nozzle hole diameter and nozzle hole length variation is focused on.

Firstly, the spray evolution emerging from the multi-hole nozzles with different hole diameter (0.07 mm, 0.10 mm, and 0.133 mm) under the baseline condition is recorded at the typical timings during the injection duration. The Optical thickness images of UV beam of multi-hole nozzle spray under different hole diameter conditions. The distribution time-resolved variation of liquid and vapor phase of multi-hole nozzle spray under different hole diameter conditions are shown in Figure 7.28 and Figure 7.29, respectively.

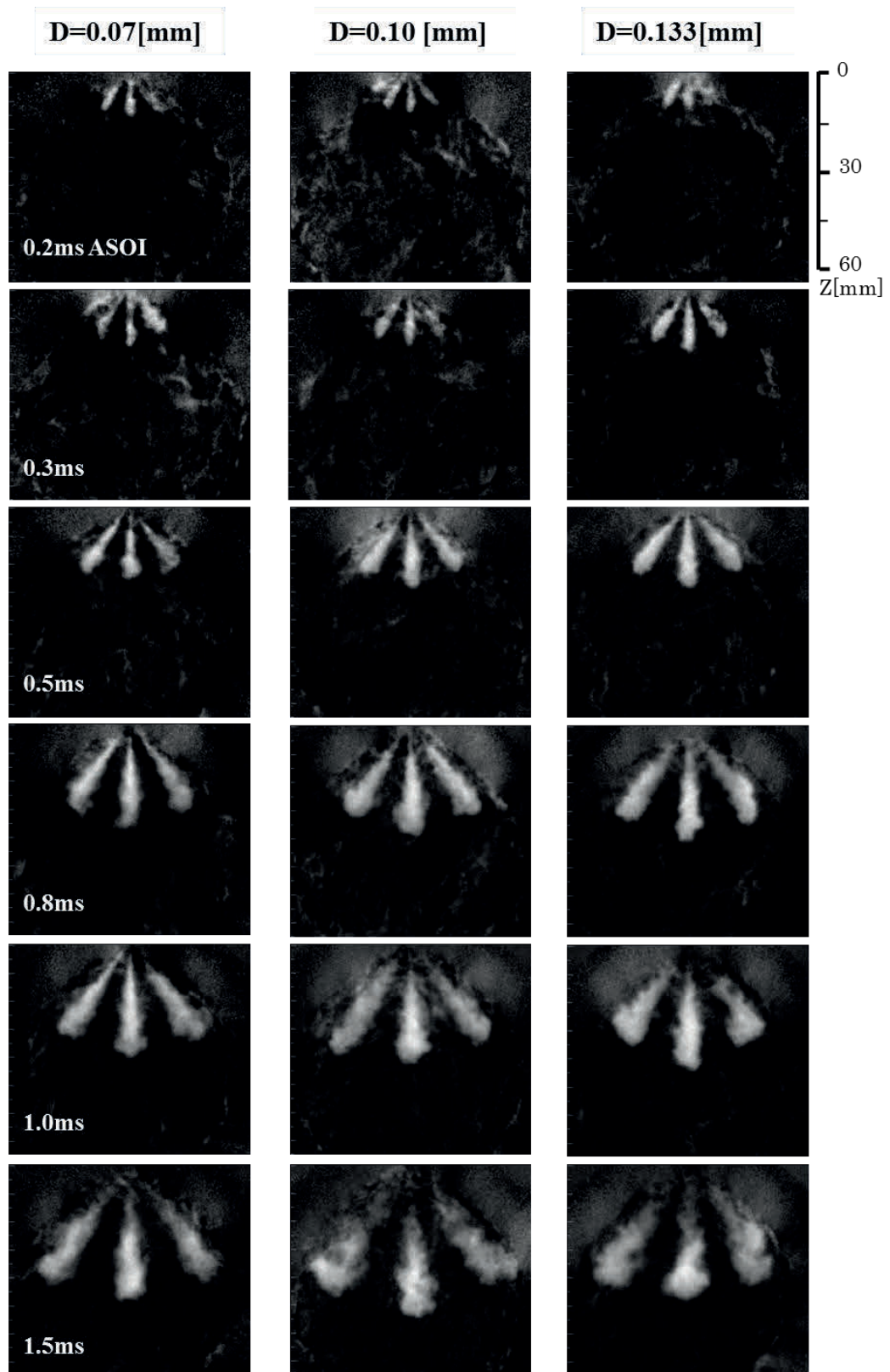


Figure 7.27 Optical thickness images of UV beam of multi-hole nozzle spray under different hole diameter conditions. $D=0.07$, 0.10 , and 0.133 mm, $P_{inj}=120$ MPa, $M_f= 1.53$ mg/hole.

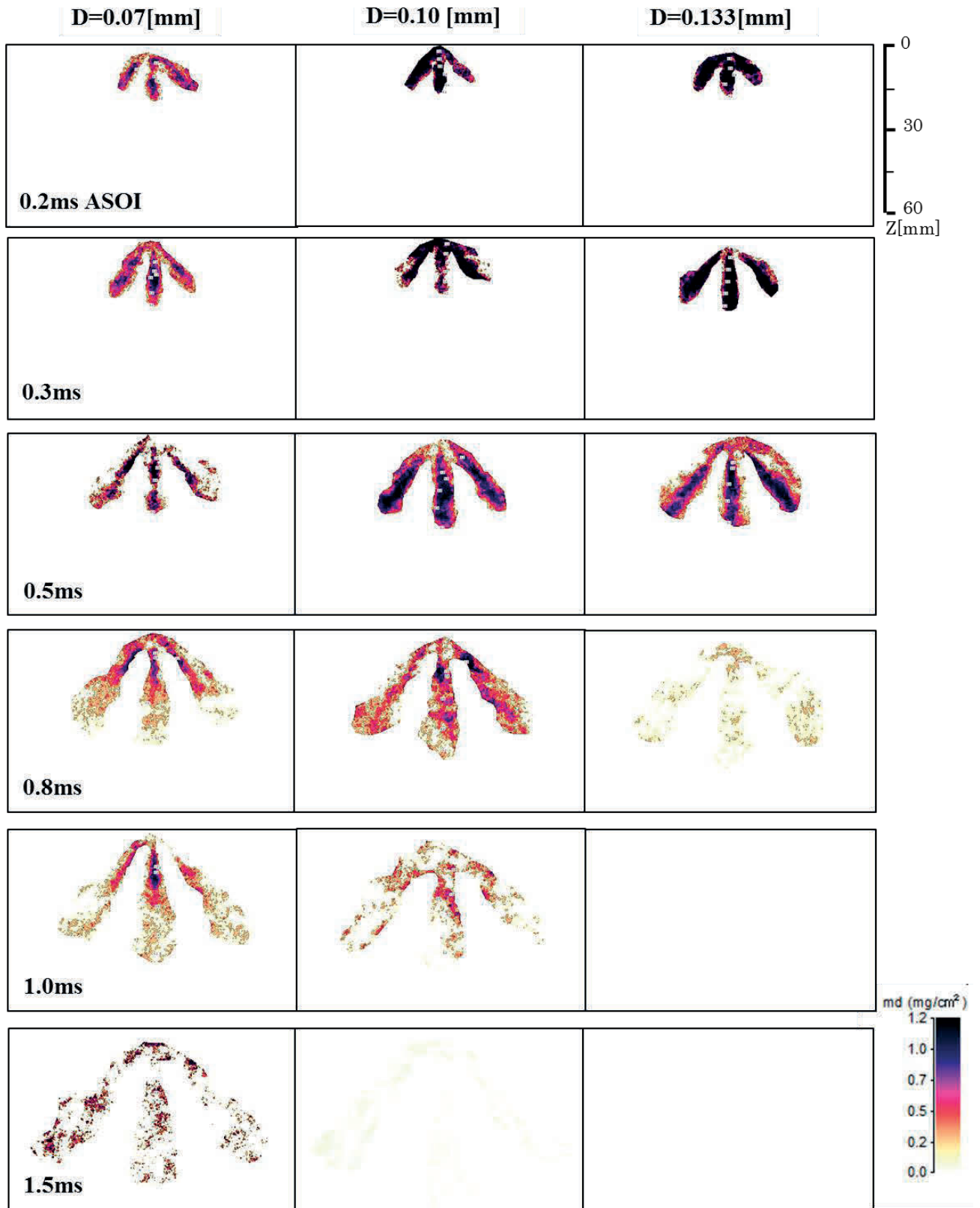


Figure 7.28 Distribution of liquid phase of multi-hole nozzle spray under different hole diameter conditions. $D=0.07, 0.10, \text{ and } 0.133 \text{ mm}$, $P_{inj}=120 \text{ MPa}$, $M_f= 1.53 \text{ mg/hole}$.

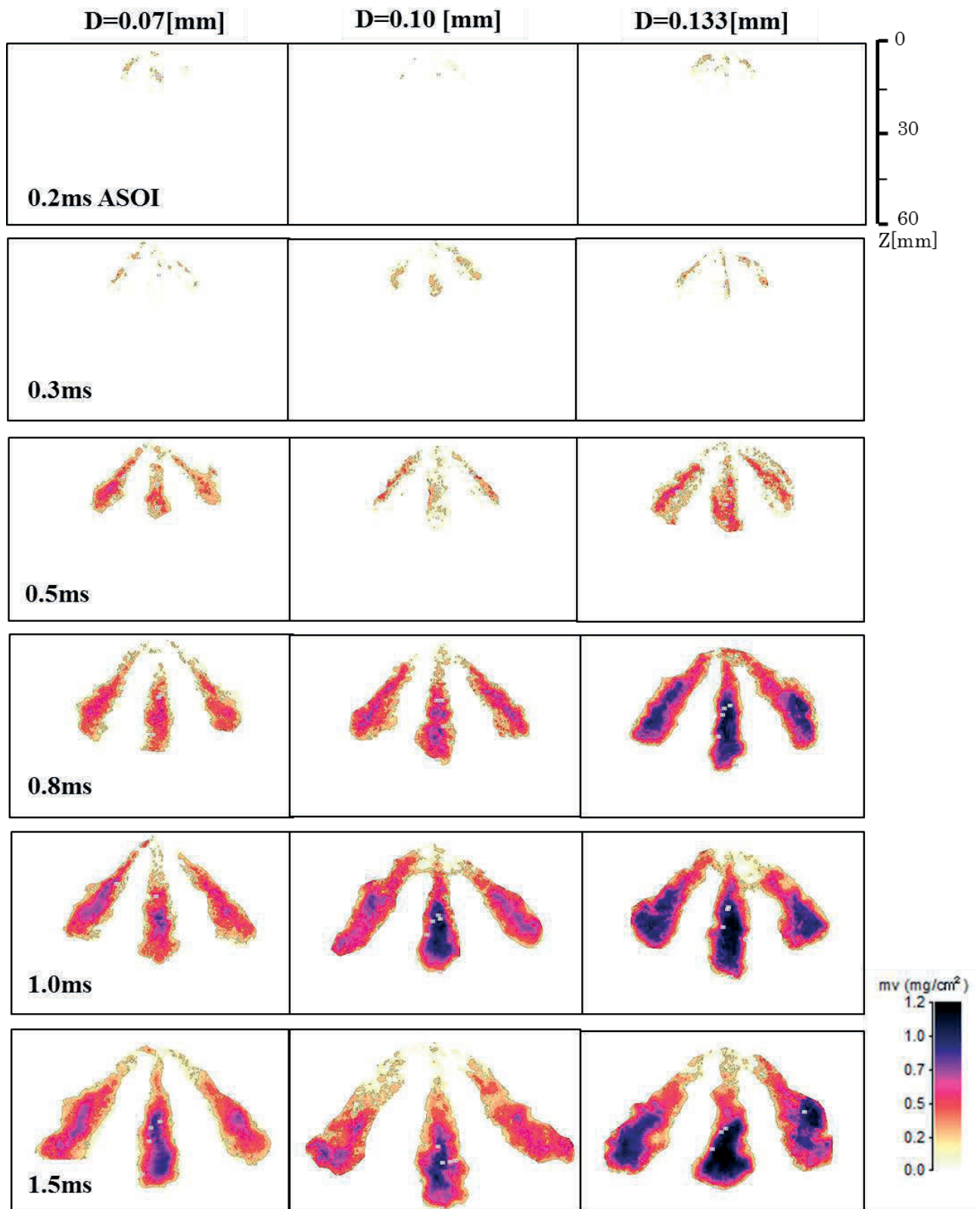


Figure 7.29 Distribution of vapor phase of multi-hole nozzle spray under different hole diameter conditions. $D=0.07, 0.10, \text{ and } 0.133 \text{ mm}$, $P_{inj}=120 \text{ MPa}$, $M_f= 1.53 \text{ mg/hole}$.

In order to maintain the same injection quantity, with the decrease of the hole diameter, the injection duration is prolonged. It is seen that the larger hole diameter can produce the denser liquid phase distribution at the beginning of the injection stage, which is corresponding to the higher injection rate. After that, the larger hole diameter can produce denser vapor phase at the end of injection, which is attributed to the shorter injection duration. The vapor phase spray tip penetration result is plotted in Figure 7.30. The result is the same with what analyzed in Chapter 4, the micro hole diameter can produce the longest penetration at the beginning of the injection because of the highest sac pressure. After that, the 0.133 mm hole has the longest penetration because the largest jet momentum, while the penetration of the micro hole spray becomes the smallest one, and the deviation becomes larger and larger.

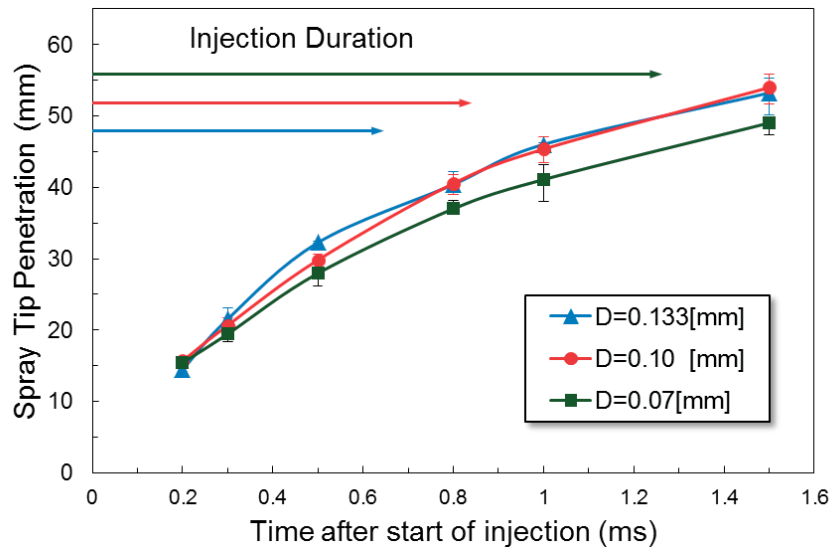


Figure 7.30 Comparison of spray tip penetration under different hole diameter conditions

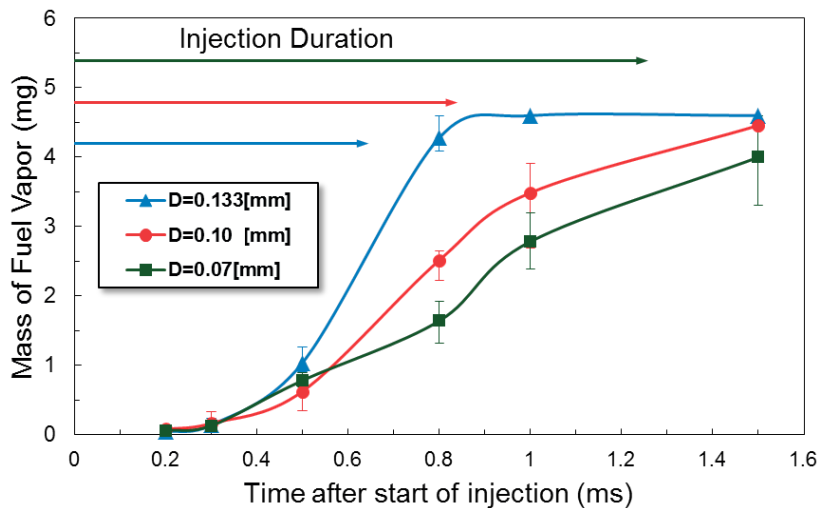


Figure 7.31 Time-resolved mass of fuel vapor phase under different hole diameter conditions

The time-resolved mass of fuel vapor phase under different hole diameter conditions are plotted in Figure 7.31. Moreover, the corresponding spray evaporation ratio is comparison is shown in Figure 7.32. Affected by the different injection rate and injection duration, there is intersection between different curves. The 0.133mm hole can generate the lowest vapor phase at the first half of the injection duration, while the highest vapor mass can be observed at the post stage of the injection. The micro hole nozzle has higher vapor phase mass at the beginning of the injection, while the increasing rate is slow with the time elapsing, which is caused by the lower injection rate. During the first half of the injection duration, spray emerging from the nozzle with micro holes has the highest evaporation ratio. However, the nozzle with 0.133 mm hole diameter is the lowest one. Because of the shortest injection duration, it increases fast to 100%. The normalized fuel evaporation ratio presents very clear trend that it increases with decreasing the hole diameter.

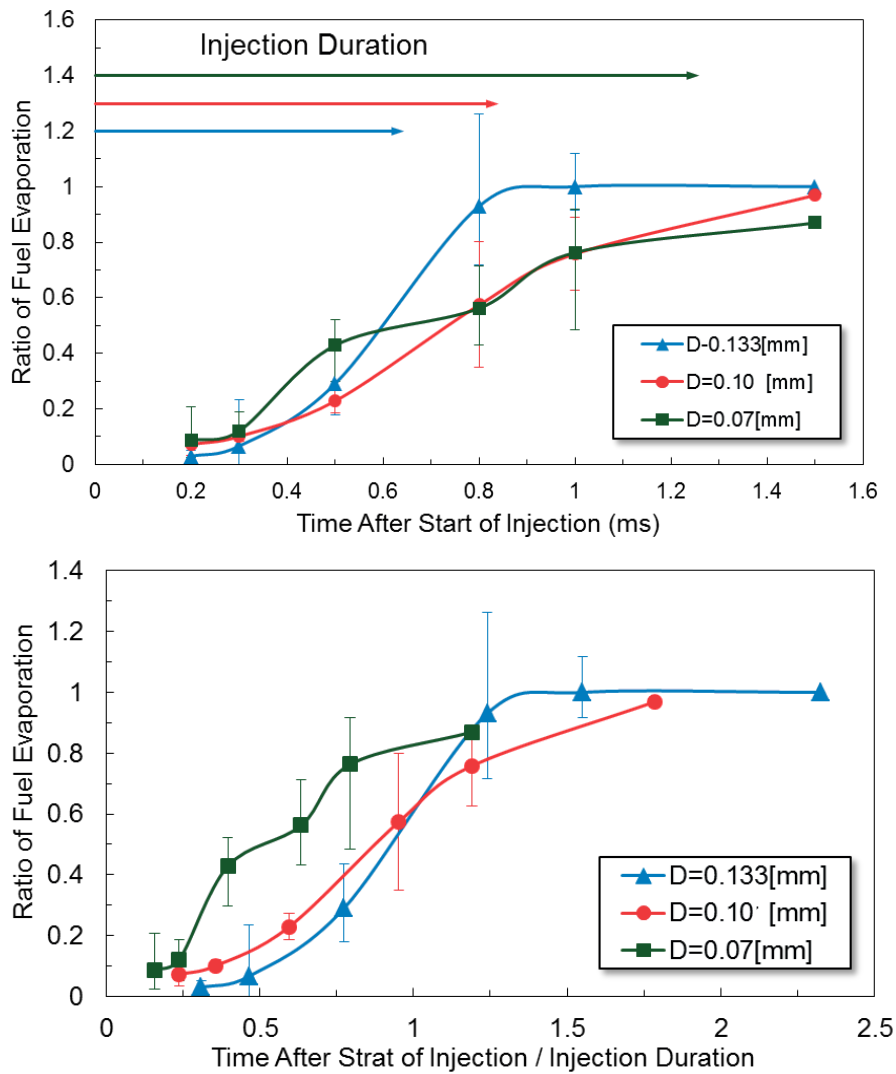


Figure 7.32 Comparison of evaporation ratio of the spray emerging from different nozzles

The effect of hole length variation on the spray evaporation processes is also investigated, and the conditions are corresponding to the contents in Chapter 4 and Chapter 5.

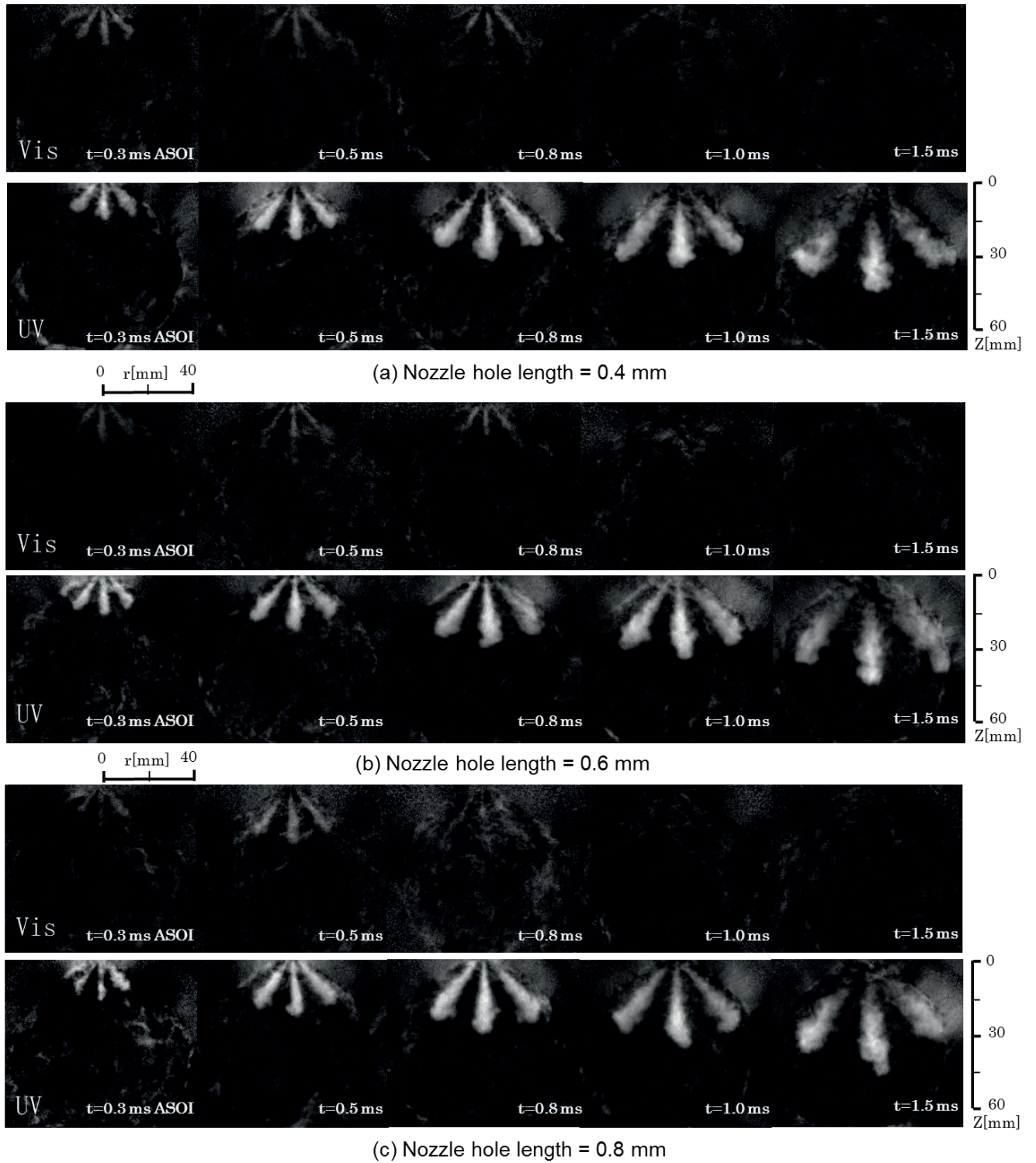


Figure 7.33 Optical thickness images of UV beam of multi-hole nozzle spray under different hole length conditions. $D=0.10$ mm, $L= 0.4, 0.6, 0.8$ mm, $P_{inj}=120$ MPa, $M_f= 1.53$ mg/hole.

The optical thickness images, and liquid and vapor phase distribution comparison results under different hole length conditions are shown in Figure 7.32 and Figure 7.33, respectively.

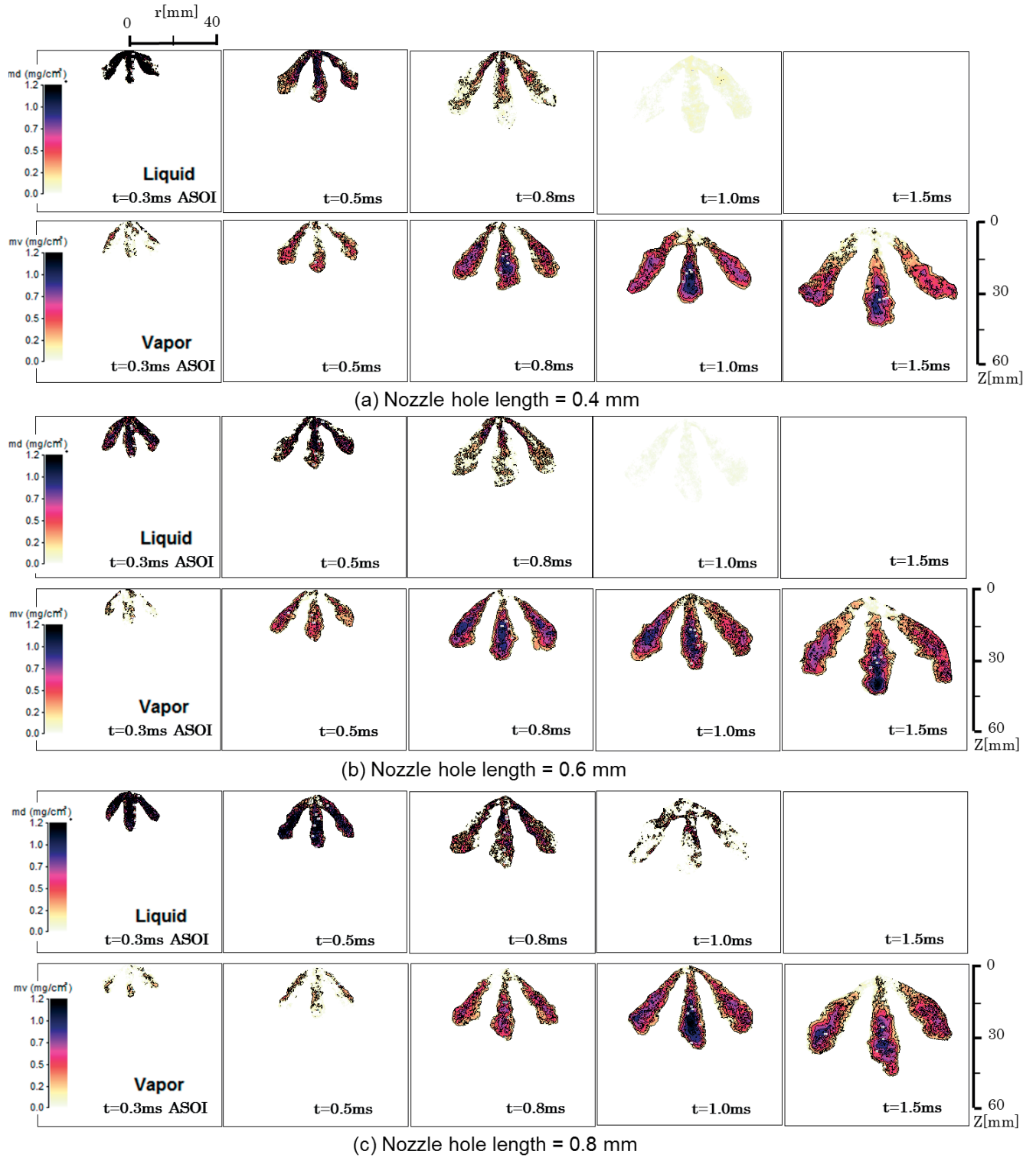


Figure 7.34 Distribution of liquid and vapor phase of the spray under different hole length conditions. $D=0.10$ mm, $L=0.4, 0.6, 0.8$ mm, $P_{inj}=120$ MPa, $M_f=1.53$ mg/hole.

With the decrease of the hole length, the same with the non-evaporation condition, the spray width is increased, while spray the tip penetration is decreased, which can be observed quantitatively in Figure 3.35. However, if the attention is paid to the first stage of the injection, the nozzles with 0.6 mm and 0.8 mm hole length almost have the same spray tip penetration, and the nozzle with 0.4 mm hole length always has the shortest penetration. The same with Chapter 4's result, the injection velocity and effective flow area of different nozzles affect the jet moment and spray tip penetration, simultaneously.

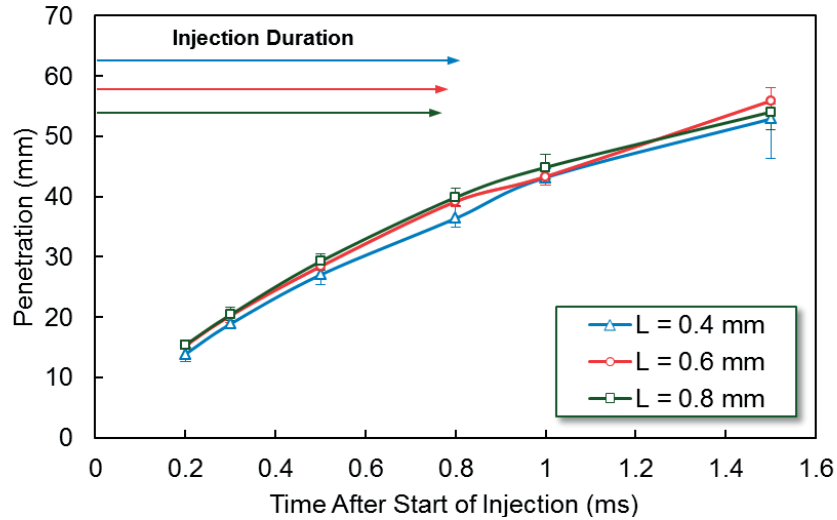


Figure 7.35 Comparison of spray tip penetration under different hole diameter conditions

Combining the results in Figure 7.34 and Figure 7.36, the spray emerging from the nozzle with 0.6 mm hole diameter has the highest vapor mass, and the fuel evaporation ratio result, which is shown in Figure 7.37, can also validate the description.

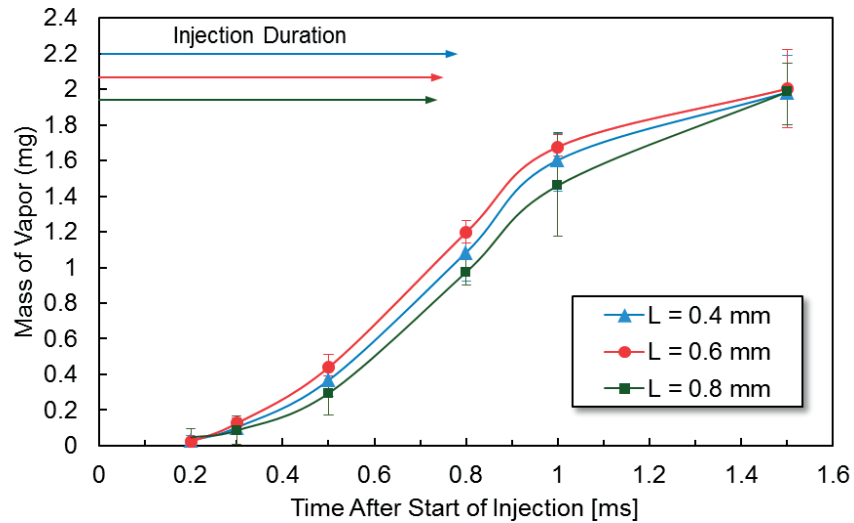


Figure 7.36 Time-resolved spray vapor mass variation under different hole diameter conditions

As analyzed before, the air entrainment is affected by the jet injection velocity, spray tip penetration, and spray width. Under the multi-hole nozzle spray condition, the lack in the ambient gas between the spray plumes is also another important factor.

The spray emerging from the nozzle with 0.8 mm hole length has the lowest injection velocity and narrowest spray width. Therefore, it has the lowest evaporation ratio. However, the evaporation ratio of spray emerging from the nozzle with 0.4mm is a little lower than that under the 0.6 mm length condition, although it has the widest spray angle and highest injection velocity. It should be noted that the spray under 0.4mm hole length condition has the shortest spray tip penetration, which is not beneficial for the gas entrainment. Moreover, the widest spray width may cause the lack of ambient gas, compared with the other two conditions. When it comes to the 0.6 mm condition, the spray has enough penetration, injection velocity, and appropriate spray width. Combing the comprehensive factors, the spray emerging from the nozzle with 0.6 mm hole diameter is evaporated fastest under the current study conditions.

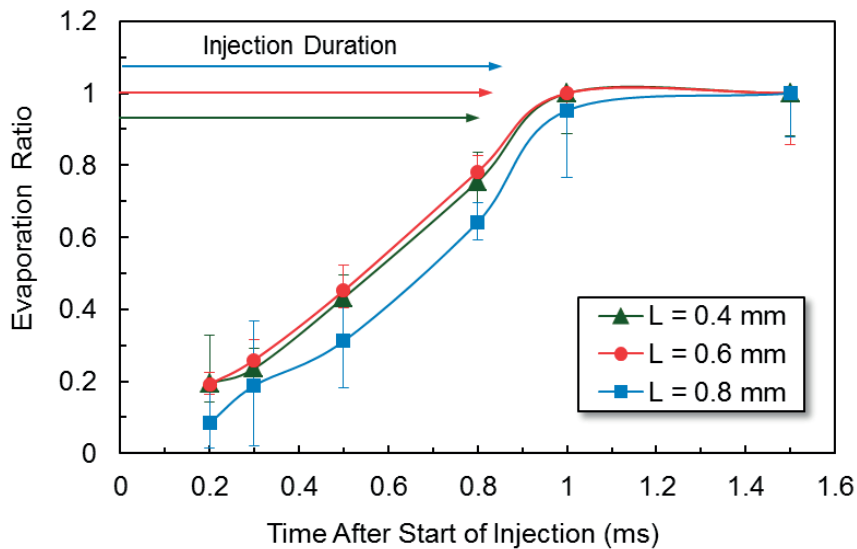


Figure 7.37 Comparison of time-resolved fuel evaporation ratio

7.4 DISCUSSION ON RELATIONSHIP OF NOZZLE GEOMETRICAL DESIGN, INTERNAL FLOW, NEAR-FIELD SPRAY AND MIXTURE FORMATION CHARACTERISTICS

In this study, the multi-hole nozzles with different parameters are listed in Table 5.3. In order to investigate the correlation between the nozzle geometrical design, internal flow, and spray evaporation properties, the parameters is normalized to the ratio of nozzle hole length to diameter.

At the quasi-steady stage of the injection duration of baseline condition, the relationship between the experimental spray evaporation ratio, the calculated average turbulent kinetic energy on the hole exits, the Sauter diameter of the droplet, and different normalized nozzle geometrical design concept is plotted in Figure 7.38.

The variation of hole diameter and hole length can exerts distinct effect on the spray evaporation characteristics, because different factors dominate the evaporation processes under different conditions. When the hole length is adjusted, the cavitation and turbulent dominate the break up process, as shown in the figure, with the increasing of the ratio, the TKE is increased a lot. As analyzed before, the internal flow and the air entrainment processes affect the evaporation, simultaneously. As a result, the ratio of 6 has the fastest evaporation ratio. On the contrary, when the hole diameter is adjusted, the droplet size is the main factor that dominates the evaporation process. With the increasing of the ratio, the droplet size is decreased very much. As a result, the evaporation ratio is also increased a lot.

In a word, the internal flow and the aerodynamics factors can alter the liquid jet break up, spray propagation, and the ambient gas entrainment, simultaneously. When pursuing the optimum geometrical nozzle design, the hole length, hole diameter should be considered from a comprehensive view. Moreover, the injection rate, injection duration, and injection quantity are also dominated by the ratio of hole length to diameter. The durability and manufacture process of the nozzle with special parameter are also significant factors when converting the design to the real products.

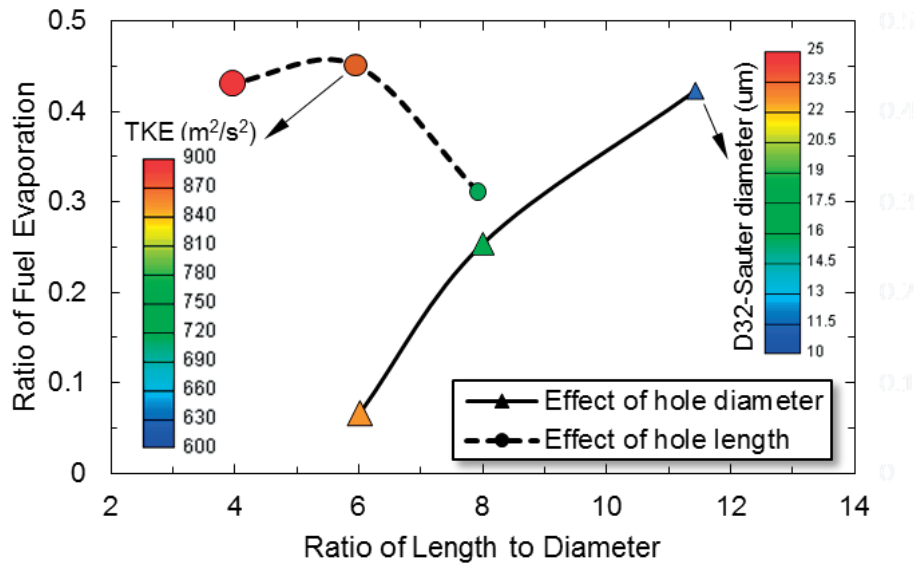


Figure 7.38 Correlating the nozzle geometrical design and experimental results with the numerical results.

7.5 SUMMARY

The spray evolution processes of the multi-hole nozzles under the evaporating conditions were discussed in this chapter. Firstly, the possibility and accuracy of the LAS measurement application on the multi-hole nozzle spray was confirmed. After that, the spray evaporation characteristics of single-hole and multi-hole nozzle was compared under the normal and micro hole diameter conditions. Furthermore, the multi-hole nozzle spray evaporation characteristics were investigated under different dynamic engine operation and nozzle geometry conditions. Finally, the spray evaporation properties and nozzle geometry design were correlated with the numerical results in the previous chapters. The main concludes are summarized as follows.

1. The possibility of the application of LAS technic on the evaporating spray of multi-hole nozzle, which is always implemented under the single-hole nozzle spray condition, is confirmed, and the accuracy of the measurement is also evaluated from different views. It is proved that this technic is also appropriate to the multi-hole nozzle spray, and the error of the measurement is with 10%.
2. Comparing the spray under the evaporating condition between the single-hole and multi-hole nozzles. The multi-hole nozzle spray has shorter spray tip penetration and lower evaporation speed. The different ambient gas flow and entrainment characteristic mainly contribute to this issue.
3. When decreasing the hole diameter to the micro level, the deviation between the single-hole and multi-hole nozzle spray evolution processes is reduced significantly.
4. With the increasing of the rail pressure, the spray tip penetration is increased, and the deviation between the liquid and vapor phase penetration is reduced. The spray evaporation ratio is also increased under the higher rail pressure condition.
5. Under the tiny injection quantity condition, the liquid phase spray tip penetration is longer than the vapor phase one, while under the normal quantity condition, the deviation in the different phase penetration is reduced a lot. Even the time-resolved spray evaporation ratio of tiny quantity condition is higher, it is much lower than the normal quantity condition when the injection duration is normalized.
6. The multi-hole nozzle evaporating spray tip penetration is increased with the increasing of the hole diameter. However, the spray evaporating speed is decreased under the larger hole diameter condition. The higher sac pressure and smaller droplet size is contributed to the evaporation.

7. Adjusting the nozzle hole length can alter the spray evaporating characteristics. The appropriate injection velocity, spray tip penetration and spray width, which is emerged from the nozzle with 0.6 mm hole length and 0.101mm hole diameter, has the fastest evaporating performance.

8. The internal flow, jet break up, and the aerodynamics effect should be taken into the optimum geometrical design of multi-hole nozzles simultaneously. Different from the single-hole nozzle spray, the ambient gas flow, entrainment characteristic, and the interaction of the adjacent spray plumes should be taken into the consideration. Two of the most important factors, hole diameter and hole length, can exerts different effect on the spray evaporation process. As a result, all of the factors should be evaluated comprehensively, as well as including the whole engine operation variation and the corresponding control strategies.

CHAPTER 8 CONCLUSIONS

In the current study, the differences in the internal flow and spray evolution between the traditional single-hole nozzle injector and the realistic multi-hole diesel injector (10 holes) were investigated experimentally and numerically. Furthermore, the characteristics of spray morphology, evolution processes, and evaporation characteristics emerging from the practical diesel multi-hole nozzles were compared and analyzed during the transient injection processes in detail. The high-speed video observation method and Laser Absorption Scattering technical were implemented under different engine dynamic operation and nozzle geometrical conditions to visualize the non-evaporating and evaporating spray, respectively. The effect of rail pressure (80, 120, 180 MPa) and injection quantity (0.3, 2.0mm³/hole) were paid attention to firstly, and then the multi-hole nozzles with different orifice diameter (0.07, 0.10, 0.133 mm), and different hole length (0.4, 0.6, 0.8 mm) were selected to acquire a better understanding about the nozzle geometrical design effect on spray behaviors. Moreover, the relationship between the different nozzle internal flow properties and the corresponding spray behaviors was investigated by the numerical simulation method systematically under the same conditions of the experiments. Additionally, the effect of multiple fuel injection, nozzle hole inlet roundness (0, 8, 16, 32 μ m), and *K* factor of the hole (-0.13, 0, 0.15) on the multi-hole nozzle internal flow properties was discussed deeply as well. The main conclusions are summarized in this chapter.

8.1 FINDINGS OF THE CURRENT STUDY

The motivation and significance of this study were introduced, and a review of the previous research in this field was conducted to give more background information of the current study in Chapter1. After that, the experimental and numerical approaches applied in this research were introduced in very detail in Chapter 2 and Chapter 3, respectively. The discussion and analysis about the results were from chapter 4. The main findings are classified as following.

8.1.1 Comparison between Single-hole and Multi-hole Nozzles

The comparisons between the traditional single-hole nozzle and the modern practice multi-hole nozzles were conducted firstly in each chapter from a variety of views, including the nozzle internal flow, non-evaporating spray, and evaporation spray, and so on. The injection pressure, injection quantity, and the micro orifice effects were also taken into the consideration.

In chapter 4, the comparison in the injection processes and spray evolution between single-hole and multi-hole nozzles was conducted under the room temperature condition. The empirical equations for the spray tip penetration of different nozzles were also improved in this chapter. Because of the unique geometric structure, the multi-hole nozzle has a lower injection rate and sac pressure, shorter spray penetration, and wider spray angle and spray cone angle compared to those of the single-hole nozzle spray. The injection rate and duration of the single-hole and multi-hole nozzles are both very sensitive to the rail pressure variation. However, the higher rail pressure has a greater effect on the multi-hole nozzle spray behaviours. For both of the single-hole and multi-hole nozzles, with the decreasing of the injection quantity, except for the spray width, the other parameters are all reduced. However, the multi-hole nozzle is more sensitive than that of the single-hole nozzle. Moreover, decreasing the nozzle hole diameter can reduce the deviation in spray characteristics between the single-hole and multi-hole nozzles. And the multi-hole nozzle spray characteristics are more sensitive to the hole diameter variation.

The comparison in the nozzle internal flow characteristics inside different nozzles was presented in Chapter 5 under the same conditions with the Mie scattering experiments in Chapter 4. The computational results of these two flow configurations reveal that the rate of increasing sac pressure is higher, and the cavitation structure is symmetrical in the single-hole nozzle. However, the swirling motion forms inside the sac and hole of the multi-hole nozzle, which can generate unsymmetrical string-type cavitation and spiral flow. These complex flow patterns also produces a stronger turbulence intensity and larger velocity component at the hole exit. Consequently, the enhanced interfacial instability and wider spray cone angle of the multi-hole nozzle are observed in the Mie scattering images. It is concluded that, different from the single-hole nozzle spray, the sprays from the multi-hole nozzle are dominated by the lower sac pressure, vortex flow in the sac, complex spiral flow structure inside the hole, and Coanda effect between the adjacent spray plumes. However, the distinctions in the internal flow patterns between the single-hole and multi-hole nozzle show different sensitivity under the tiny and normal injection quantity conditions. The deviations of a series of internal flow properties of the multi-hole nozzle between the tiny and normal injection quantity conditions are much more prominent than those of the single-hole nozzle. Moreover, the rail pressure variation can exert more effect on the multi-hole nozzle internal flow under the tiny injection condition. The simulation results also indicate that there are obvious differences in the internal flow and the spray transient around the end and the start of the pilot injections between the single-hole and the multi-hole nozzles. The dribbles of the multi-hole nozzle spray around the end of the pilot injection appear later than that of the single-hole one. It is easier

for the ambient gas to entry into the sac of the single-hole nozzle, which can affect the properties of initial spray jet. The influence of the micro hole diameter on the internal flow and injection processes of the single-hole and multi-hole injectors is prominent. The reduced effective flow area suppresses the cavitation and turbulence flow, alters the injection rate, and prolongs the injection duration. Affected by the lower sac pressure discharge rate and reduced deviation of the internal flow, the difference of the spray properties between single-hole and multi-hole nozzles with micro orifices are reduced significantly.

The simulation study for the single-hole and multi-hole sprays was conducted in Chapter 6. The comparison result can validate the analysis in chapter 4 and Chapter 5. The multi-hole nozzle has lower injection velocity, shorter spray tip penetration, better atomization effect, wider spray propagation, smaller droplet size, and higher flow field turbulent level. As a result, it is necessary to pay more special attention to the practical multi-hole diesel sprays.

The spray evaporation characteristics of single-hole and multi-hole nozzle were investigated in Chapter 7. Comparing the spray under the evaporating condition between the single-hole and multi-hole nozzles, the multi-hole nozzle spray has shorter spray tip penetration and lower evaporation speed. It is believed that the ambient gas entrainment of the multi-hole nozzle spray is insufficient compared with that of the single-hole nozzle spray. There are ten spray plumes under the multi-hole condition, and the ambient gas between the spray plumes can enter into the spray, simultaneous, which create the low pressure region between the spray plumes. The ambient gas downstream will come into the low pressure region, where the countercurrent is observed. Moreover, the lower injection velocity and shorter penetration of multi-hole nozzle is also not beneficial for the gas entrainment. Different ambient gas entrainment properties can alter the fuel evaporation process. Therefore, the different ambient gas flow and entrainment characteristic mainly contribute to this issue. When decreasing the hole diameter to the micro level, the deviation between the single-hole and multi-hole nozzle spray evolution processes is also reduced significantly.

After the deviation between the single-hole and multi-hole nozzles were confirmed, it was believed that it is worthwhile to paying more attention to the practical multi-hole nozzles injectors

8.1.2 Non-evaporating Spray Evolution of Multi-Hole Nozzles

The injection processes and non-evaporating spray evolution characteristics of multi-hole nozzles were discussed under different dynamic operation and nozzle geometrical conditions in Chapter 4.

The kaleidoscopic spray morphology and unstable spray behaviors of the practical multi-hole nozzles are characterized in the experiments. The far-field asymmetric and irregular spray profiles, unstable spray angle and spray cone indicate that the spray propagation is dominated by the nozzle internal flow and the interactions between the adjacent spray plumes, simultaneously. The near-field pulsating and perturbed spray instance implies that the spray development is affected greatly by the complex nozzle configuration. Moreover, the injection rate and spray tip penetration have a strong relationship with the pressure increasing rate in the sac and the effective flow area of the nozzles. As a result, it can be concluded that sprays emerging from the multi-hole nozzles are mainly dominated by the sac pressure, vortex flow in the sac, complicatedly spiral and turbulent flow structure inside the hole except for the spray to spray interaction.

The influence of the hole diameter variation on the injection processes and spray development of the multi-hole injectors is prominent. The reduced effective flow area alters the injection rate, increases the sac pressure, and prolongs the injection duration. Overall, with the decreasing of the orifice diameter of the multi-hole nozzle the spray tip penetration and spray width variation are not linear, which is attributed to the different sac pressure. Moreover, the effect of the micro-hole diameter plays different roles in the spray properties (penetration, spray angle and cone angle) of the multi-hole nozzles at different injection stages. The implications of these results have practical significance when considering the diesel fuel spray trajectory within the combustion chamber.

The effects of the hole length of the Diesel multi-hole nozzles on the fuel injection processes and far-and near-field spray behaviors under the constant injection quantity conditions were also clearly demonstrated, relatively. With the decreasing of the hole length, the injection rate and spray tip penetration is reduced, while the spray width is increased.

8.1.3 Internal Flow Characteristics inside Multi-Hole Nozzle

The characteristics of multi-hole nozzle internal flow were paid abundant attention in Chapter 5. The dynamic operation conditions and nozzle geometrical effect are investigated under the same conditions with the Mie scattering experiments. The numerical study about the internal flow patterns inside the multi-hole nozzles reveal that the flow dynamics are dominated mainly by the unstable swirling motion and vortex flow in the sac and the complex spiral flow structure inside the hole. These flow patterns can generate the unstable multi-type cavitation structure, asymmetric and multi-directional injection velocity components, and the fluctuated turbulence kinetic energy distribution on the hole exit. The parameters mentioned above all play significant roles in the

processes of the spray break up and fuel-air mixing. Furthermore, combining with the experimental results, it is concluded that the local injection velocity and the effective flow area are two crucial factors that affect the nozzle injection rate and the spray propagation distance, simultaneously.

The internal flow is more complicated under the tiny injection quantity condition, and the cavitation structure is absolutely disparate between different injection quantity conditions. Moreover, the internal flow properties are more sensitive to the rail pressure variation under the tiny injection quantity condition.

The hole taper ratio, hole inlet roundness, and the hole diameter variation effect on the internal flow patterns are investigated, and the conical hole, smoother inlet edge can increase the injection rate and reduce the cavitation level inside the multi-hole nozzles. The hole diameter variation affects the sac pressure directly. With the increasing of the hole diameter, the cavitation level is increased, while the sac pressure and injection velocity is reduced, which is important for the spray break up.

The nozzle hole length can affect the development of the flow patterns and the local cavitation inside the hole. Consequently, the void fraction, flow turbulent kinetic energy, and the injection velocity components on the hole exits, which are regarded as key mechanism governing the emerging spray properties, change significantly with the variation of the nozzle hole length. It is safe to say that decreasing the nozzle hole length can enhance the level of cavitation and turbulence inside the hole, increase the injection velocity and spray width, and promote the spray perturbation and break up, while it decreases the fuel effective flow area and the spray propagation length, relatively. Moreover, the changes summarized above are not linearly, and different parameters have variable sensitivity to the nozzle hole length variation.

8.1.4 Computational Study of Multi-Hole Nozzle Sprays

The simulation results of multi-hole nozzle spray were introduced in Chapter 6, the internal flow simulation result was inserted into the break up models as the boundary conditions. The effect of rail pressure and hole diameter on the spray evolution is analyzed in detail. The coupling between the internal flow and spray simulation is the best way to reproduce the spray evolution inside the chamber, and this method can provide more detail boundary information to the break up models and take the nozzle geometrical design effect on the spray characteristics into the consideration. As a result, the accuracy of the numerical work can be increased a lot. The multi-hole nozzle spray was observed in three-dimension, and the ten spray plumes are symmetrical. The ambient gas between the spray plumes entrains into the adjacent sprays, simultaneously, which has significant effect on

the mixture formation and fuel evaporation characteristics. Furthermore, increasing the rail pressure can enlarge the injection velocity, spray tip penetration, and the flow field turbulent level, while it can decrease the injection duration and droplet size, and the spray width is also reduced a little by the increase of the rail pressure. The spray properties are very sensitive to the variation of nozzle hole diameter. The micro hole and the normal larger hole can exert very special effect on the spray evolution. The result are coincided with the experimental analysis in Chapter 4. There is overlap trend in the spray tip penetration and flow field turbulent level, while the droplets size decreases, and the injection velocity increases monotonously with the reduction of the hole diameter.

8.1.5 Mixture Formation Characteristics of Multi-Hole Nozzle Sprays

The spray evolution processes of the multi-hole nozzles under the evaporating conditions were discussed in Chapter 7. Firstly, the possibility of the application of LAS technic on the evaporating spray of multi-hole nozzle, which is always implemented under the single-hole nozzle spray condition, is confirmed, and the accuracy of the measurement is also evaluated from different views. Furthermore, the multi-hole nozzle spray evaporation characteristics were investigated under different dynamic engine operation conditions and variable nozzle geometry conditions.

With the increasing of the rail pressure, the spray tip penetration is increased, and the deviation between the liquid and vapor phase penetration is reduced. The spray evaporation ratio is also increased under the higher rail pressure condition. Under the tiny injection quantity condition, the liquid phase spray tip penetration is much longer than the vapor phase one, while under the normal quantity condition the deviation in the different phase penetration is reduced a lot. Even though the normalized time-resolved spray evaporation ratio of tiny quantity condition is lower than the normal quantity condition.

The multi-hole nozzle evaporating spray tip penetration is increased with the increasing of the hole diameter. However, the spray evaporating speed is decreased under the larger hole diameter condition. The higher sac pressure and smaller droplet size are mainly contributed to the different evaporation characteristics. On the other hand, adjusting the nozzle hole length can also alter the spray evaporating characteristics. The appropriate injection velocity, spray tip penetration, and spray width, which is emerged from the nozzle with 0.6 mm hole length and 0.101mm hole diameter, has the fastest evaporating performance.

8.1.6 Correlation of Nozzle Geometrical Design, Internal Flow, and Spray Behaviors

The nozzle geometrical design was correlated with the numerical and experimental results under the evaporating and non-evaporation conditions at the end of Chapter 5 and Chapter 7, respectively. When concerning the effect of multi-hole nozzle hole length and diameter, the nozzle hole parameters (diameter and length) were normalized as the ratio of hole length to diameter.

Under the non-evaporating condition, with the increasing of the ratio, the spray cone angle is decreased, and the average turbulent kinetic energy on the hole exit is also reduced. However, it should be note that when considering the hole diameter effect, the multi-hole nozzle presents a kind of special regularity, and the spray cone angle and TKE reach to the highest at the ratio of 8. As explained before, the sac pressure of the nozzles with different hole diameter also plays a significant role in the spray width, because the sac pressure and hole diameter not only affect the turbulent and cavitation, but also control the injection velocity and spray momentum.

Under the evaporating condition, the variation of hole diameter and hole length can exerts distinct effect on the spray evaporation characteristics, because different factors dominate the evaporation processes under different conditions. When the hole length is adjusted, the cavitation and turbulent dominate the break up process, with the increasing of the ratio, the TKE is increased a lot. As analyzed before, the internal flow and the air entrainment processes affect the evaporation, simultaneously. As a result, the ratio of 6 has the fastest evaporation ratio. On the contrary, when the hole diameter is adjusted, the droplet size is the main factor that dominates the evaporation process. With the increasing of the ratio, the droplet size is decreased very much. As a result, the evaporation ratio is also increased a lot.

In a word, the internal flow and the aerodynamics factors can alter the liquid jet break up, spray propagation, and the ambient gas entrainment, simultaneously. Two of the most important factors, hole diameter and hole length, can exerts different effect on the spray evaporation process. When pursuing the optimum geometrical nozzle design, the hole length, hole diameter should be considered from a comprehensive view. Moreover, the injection rate, injection duration, and injection quantity are also dominated by the ratio of hole length to diameter. The durability and manufacture process of the nozzle with special parameter are also significant factors when converting the design to the real products. As a result, all of the factors should be evaluated comprehensively, as well as including the whole engine operation variation and the corresponding control strategies.

8.2 RECOMMENDATIONS FOR FUTURE WORKS

There is much more effort, which can be made in the following study of this field.

For example, the sprays in the current study are all free sprays, hence the spray evolution under the impingement conditions should also be measured in the further. The application of flat wall and 2D cavity may release more practical situations inside the combustion chamber of the engines.

There are no combustion conditions in the current investigation. The detail mechanism of multi-hole nozzle spray combustion characteristics needs to be further explored. As a result, the multi-hole nozzle spray combustion processes under the corresponding conditions should be evaluated in detail in the further.

Although the ambient physical condition implemented in the current study are aiming to reproduce the real engine operation environment, the turbulent, tumble, and squish flow inside the combustion chamber all play significant roles in the mixture formation and combustion process. Therefore, it is recommended to investigate the mixture formation and combustion characteristics of multi-hole nozzles in optical engine as well.

The effect of most basic and important nozzle hole parameters (length and diameter) are investigated in the current experimental study, and some more other geometrical parameters (hole inlet roundness and hole taper ratio) are discussed in the numerical study. However, some more crucial factors, such as the sac volume, hole number, hole position and so on, should also be taken into the consideration when conduction the fuel injection and combustion study of the practical diesel multi-hole nozzle injectors.

REFERENCES

1. **Afzal, H., Arcoumanis, C., Gavaises, M., and Kampanis, N.** (1999) Internal Flow in Diesel Injector Nozzles: Modelling and Experiments. *IMEchE Paper S492/S2/99*.
2. **Alajbegovic, A., Grogger, H., and Philipp, H.** (1999) Calculation of the Transient Cavitation in Nozzle Using the Two-Fluid Model. *Proc. ILASS-Americas'99 Annual Conf.*, pp. 373-377.
3. **Andresen, P., Meijer, G., Schlüter, H., Voges, H., Koch, A., Hentschel, W., Oppermann, W., and Rothe, E.** (1990) Fluorescence Imaging inside an Internal Combustion Engine using Tubular Excimer Lasers. *Applied optics*, 26:2392-2404.
4. **Andriotis, A., and Gavaises, M.** (2009) Influence of Vortex Flow and Cavitation on Near-Nozzle Diesel Spray Dispersion Angle. *Atomization and Sprays*, 19:247-261.
5. **Andriotis, A., Gavaises, M., and Arcoumanis, C.** (2008) Vortex Flow and Cavitation in Diesel Injector Nozzles. *Journal of Fluid Mechanics*, 610:195-215.
6. **Araneo, L., Coghe, A., Brunello, G., and Cossali, G.** (1999) Experimental Investigation of Gas Density Effects on Diesel Spray Penetration and Entrainment, SAE Technical Paper, 1999-01-0525.
7. **Arcoumanis, C., and Enotiadis, A. C.,** (1991) In-Cylinder Fuel Distribution in a Port-Injected Model Engine Using Rayleigh Scattering. *Expts. Fluids* 11: 375-387.
8. **Arcoumanis, C., and Kaminoto, T.** (2009). *Flow and Combustion in Reciprocating Engines*. Berlin Heidelberg, Springer-Verlag.
9. **Arcoumanis, C., Badami, M., Flora, H., and Gavaises, M.** (2000) Cavitation in Real Size Multi-Hole Diesel Injector Nozzles. SAE Technical Paper 2000-01-1249.
10. **Arcoumanis, C., Badami, M., Flora, H. and Gavaises, M.** (2000) Cavitation in real-size multi-hole diesel injector nozzles. SAE Technical Paper 2000-01-1249.
11. **Arcoumanis, C., Flora, H., Gavaises, M., et al.** (1999) Investigation of cavitation in a vertical multi-hole diesel injector. SAE Technical Paper 1999-01-0524.
12. **Arcoumanis, C., Gavaises, M., and French, B.** (1997) Effect of Fuel Injection Processes on the Structure of Diesel Sprays. *SAE Technical Paper* 970799.
13. **Arcoumanis, C., Green, H.G., and Whitelaw, J.** (1985) Velocity and Concentration Measurement in a Model Diesel Engine. *Expts. Fluids* 3:270-276.
14. **Arora, M., Ohl, C. D., and Lohse, D.** (2007) Effect of Nuclei Concentration on Cavitation Cluster Dynamics. *J. Acoust. Soc. Am.*, 121(6), pp. 3432-3436.
15. **Baby, X. and Floch, A.** (1997) Investigation of the In-Cylinder Tumble Motion In a Multi-Valve Engine: Effect of the Piston Shape. *SAE Technical Paper* 971643.
16. **Badock, C., Wirth, R., Fath, A., and Leipertz, A.** (1999) Investigation of Cavitation in Real Size Diesel Injection Nozzles. *Int. J. Heat Fluid Flow*, vol. 20, pp. 538-544.
17. **Baumgarten, C.** (2006) *Mixture Formation in Internal Combustion Engine*. Berlin Heidelberg, Springer-Verlag.
18. **Baumgarten, C., Stegemann, J., and Merker, G.** (2002.) A New Model for Cavitation Induced Primary Break-up of Diesel Sprays. *ILASS-Europe, Zaragoza*.

19. **Benajes, J., Pastor, J. V., Payri, R., and Plazas, A. H.** (2004) Analysis of the Influence of Diesel Nozzle Geometry in the Injection Rate Characteristic. *J. Fluids Eng* 126(1), 63-71.
20. **Bergstrand, P., and Denbratt, I.** (2001) Diesel Combustion with Reduced Nozzle Orifice Diameter. SAE Technical Paper 2001-01-2010.
21. **Bergwerk, W.** (1959) Flow Pattern in Diesel Nozzle Spray Holes, Proceedings of the Institution of Mechanical Engineers, vol.173, pp.655-674.
22. **Bianchi, G. M., Pelloni, P., and Corcione, F. E.** et al. (2001) Modeling Atomization of High-Pressure Diesel Sprays. *Journal of Engineering for Gas Turbines and Power*, vol. 123, pp. 419-427.
23. **Bianchi, G. M. and Pelloni, P.** (1999) Modeling the Diesel Fuel Spray Breakup by Using a Hybrid Model. SAE Technical Paper 1999-01-0226.
24. **Blessing, M., König, G., Krüger, C., Michels, U. , and Schwarz, V.** (2003) Analysis of Flow and Cavitation Phenomena in Diesel Injection Nozzles and its Effects on Spray and Mixture Formation. SAE Technical Paper, 2003-01-1358.
25. **Bower, G. and Foster, D.** (1991) A Comparison of the Bosch and Zuech Rate of Injection Meters. SAE Technical Paper 910724.
26. **BP Energy Outlook** (2016) <http://www.bp.com/en/global/corporate/energy-economics/energy-outlook-2035>
27. **Brennen, E. P.** (1995) Cavitation and Bubble Dynamics. Oxford University Press, Oxford.
28. **Bruneaux, G.** (2001) Liquid and Vapor Spray Structure in High-Pressure Common Rail Diesel Injection. *Atomization and Sprays*, 11: 533-556.
29. **Bruneaux, G.** (2005) Mixing Process in High Pressure Diesel Jets by Normalized Laser Induced Exciplex Fluorescence Part I: Free Jet, SAE Technical Paper 2005-01-2100.
30. **Bruneaux, G.** (2008) Combustion Structure of Free and Wall-Impingement Diesel Jets by Simultaneous Laser-Induced Fluorescence of Formaldehyde, Poly-Aromatic Hydrocarbons, and Hydroxides. *International Journal of Engine Research*, 9: 249-265.
31. **Bruneaux, G., Causse, M., and Omrane, A.** (2011) Air Entrainment in Diesel-Like Gas Jet by Simultaneous Flow Velocity and Fuel Concentration Measurements, Comparison of Free and Wall Impinging Jet Configurations. *SAE Technical Paper* 2011-01-1828.
32. **Bruneaux, G., Verhoeven, D., and Baritaud, T.** (1999) High Pressure Diesel Spray and Combustion Visualization in a Transparent Model Diesel Engine. *SAE Technical Paper* 1999-01-3648.
33. **California Air Resources Board.** (2006, accessed 21 Feb 2016). Low Carbon Fuel Standard Program. <http://www.arb.ca.gov/fuels/lcfs/lcfs.htm>
34. **Castleman, R. A.** (1931) The Mechanism of the Atomization of Liquids. *J. Res. Natl. Bur. Std*, 6: 369-376.
35. **Chaves, H., Knapp, M., Kubitzek, A., et al.** (1995) Experimental Study of Cavitation in the Nozzle Hole of Diesel Injectors Using Transparent Nozzles. SAE Technical Paper No.950290.
36. **Chraplyvy, J., and Karlsson, A.** (1996) Flame Lift-off in Diesel Spray. Symposium (International) on Combustion, 26: 2557-2564.
37. **Colton, B.** (2014) The outlook for energy: A view to 2040, ExxonMobil. <http://corporate.exxonmobil.com/en/energy/energy-outlook>.

38. **Corcione, F. E., and Valentino, G.** (1990) Turbulence Length Scale Measurements by Two-Probe-Volume LDA Technique in a Diesel Engine. *SAE Technical Paper* 902080.
39. **Cossali, G. E., Brunello, G., and Coghe, A.** (1991) LDV Characterization of Air Entrainment in Transient Diesel Sprays. *SAE Technical Paper* 910178.
40. **Cossali, G. E., Gerla, A., Coghe, A., and Brunello, G.** (1996) Effect of Gas Density and Temperature on Air Entrainment in a Transient Diesel Spray. *SAE Technical Paper* 960862.
41. **Cyril, C., Morgan, R., and Heikal, M.,** (2015) Microscopic imaging of the initial stage of Diesel spray formation, *Fuel*, 157:140-150.
42. **Dec, J. E.** (1997) A Conceptual Model of DI Diesel Combustion Based on Laser-Sheet Imaging. *SAE Technical Paper* 970873.
43. **DeJuhasz, K. J.** (1931) Dispersion of Sprays in Solid Injection Oil Engines. *Trans. ASME*, 53: 65-77.
44. **Delale, C. F., Okita, K., and Matsumoto, Y.** (2005) Steady-State Cavitating Nozzle Flows with Nucleation. *J. Fluids Eng.*, 127(4): 770-777.
45. **Dent, J. C** (1971) A Basis for the Comparison of Various Experimental Methods for Studying Spray Penetration. *SAE Technical Paper* 710571.
46. **Desantes, J.M., Payri, R., Salvador, F.J., and Morena, De la, J.** (2010), Influence of Cavitation Phenomenon on Primary Break-Up and Spray Behavior at Stationary Conditions. *Fuel*, 89: 3033-3041.
47. **Dillon, M.E., Wang, G., and Huey, R.B.** (2010) Global metabolic impacts of recent climate warming. *Nature*, vol. 467, pp, 704-706.
48. **Dong, P.B., Inaba, T., Nishida, K., and Daisuke, S.** (2016) Characteristics of the internal flow and the near-field spray of a single-hole injector and a multi-hole injector for diesel engines. *Proceedings of the Institution of Mechanical Engineers, Part D: Journal of Automobile Engineering*, 230(5):632-649
49. **Dong, P.B., Inaba, T., Nishida, K., and Ogata, Y.** (2015) Characterization of small injection amount fuel spray injected by the multi-hole nozzle for diesel engines. In: *ICLASS-2015*, Tainan, Taiwan, August, Paper 066.
50. **Dong, P.B., Inaba, T., Nishida, K., Ogata, Y. et al.** (2015) Characteristics of nozzle internal flow and near-field spray of multi-hole injectors for diesel engines. *SAE Technical Paper* 2015-01-1920.
51. **Dong, P.B., Nishida, K., Inaba, T., and Ogata, Y.** (2016) Characterization of Internal Flow and Spray Behaviors of Hole-Type Nozzle under Tiny and Normal Injection Quantity Conditions for Diesel Engine. *SAE Int. J. Fuels Lubr*, 9(1):125-137
52. **Dumont, N., Simonin, O., and Habchi, C.** (2001) Numerical Simulation of Cavitating Flows in Diesel Injectors by Homogeneous Equilibrium Modeling Approach. *CAV 2001, 4th International Symposium on Cavitation*, California Institute of Technology, Pasadena, California, USA.
53. **Durbin, P.A.** (1991) Near-wall turbulence closure modelling without damping functions. *Theor. Comput. Fluid Dyn*, 3:1-13.
54. **Eagle, W. E., Morris, S. B., and Wooldridge, M. S.** (2014) High-speed imaging of transient diesel spray behavior during high pressure injection of a multi-hole fuel injector. *Fuel*, 116: 299-309
55. **Environmental Protection Agency** (2005, accessed 21 Feb 2016). Light Vehicle Emission Standards - Reference Guide (Tier 1 and Tier 2). <http://www3.epa.gov/otaq/standards/light-duty/index.htm>
56. **Environmental Protection Agency** (2014, accessed 21 Feb 2016). Light Vehicle Emission Standards

- Reference Guide (Tier 3). <http://www3.epa.gov/otaq/tier3.htm>
57. **Environmental Protection Agency.** (2012, accessed 21 Feb 2016) EPA and NHTSA Set Standards to Reduce Greenhouse Gases and Improve Fuel Economy for Model Years 2017-2025 Cars and Light Trucks.
 58. **Espey, C., Dec, J. E., Litzinger, T. A., and Santavicca, D. A.** (1997) Planar Laser Rayleigh Scattering for Quantitative Vapor-Fuel Imaging in a Diesel Jet. *Combustion and Flame*, 109: 65-78.
 59. **European Commission.** (1998, accessed 21 Feb 2016) ACEA Voluntary agreement. http://europa.eu/rapid/press-release_IP-98-734_en.htm?locale=en.
 60. **European Commission.** (1998, accessed 21 Feb 2016) Overview of Directive 98/70 on Fuel Quality. <http://eur-lex.europa.eu/legal-content/EN/TXT/?uri=CELEX:31998L0070>.
 61. **European Commission.** (2009, accessed 21 Feb 2016) Regulation 443/2009 - emission performance standards for new passenger cars. <http://eur-lex.europa.eu/legal-content/EN/TXT/?uri=CELEX:02009R0443-20140408>.
 62. **European Commission.** (2016, accessed 21 Feb 2016) Vehicle emission standards.
 63. **Fajardo, C., and Sick, V.** (2009) Development of a High-Speed UV Particle Image Velocimetry Technique and Application for Measurements in Internal Combustion Engines. *Exp. Fluids*, 46:43-53.
 64. **Fath, A., Fettes, C., and Leipetz, A.** (1998) Investigation of the Diesel Break-up Close to the Nozzle at Different Injection Conditions. *The Fourth Internatinal Symposium COMODIA98*, Kyoto, Japan, pp. 429-434.
 65. **Flynn, P. F., Durrett, R. P., Hunter, G. L., zur Loye, A. O., Akinyemi, O. C., Dec, J. E., and Westbrook, C. K.** (1999) Diesel Combustion: An Integrated View Combining Laser Diagnostics, Chemical Kinetics, And Empirical Validation. *SAE Technical Paper* 1999-01-0509.
 66. **Gao, J., Matsumoto, Y., Nishida, K.** (2007) Effects of group-hole nozzle specifications on fuel atomization and evaporation of direct injection diesel sprays. *SAE Technical Paper* 2007-01-1889.
 67. **Gao, J., Nishida, K., Moon, S., and Matsumoto, Y.** (2009) Characteristics of Evaporating Diesel Spray: A Comparison of Laser Measurements and Empirical/Theoretical Predictions, *SAE Technical Paper* 2009-01-0854.
 68. **Gavaises, M. and Andriotis, A.** (2006) Cavitation inside Multi-Hole Injectors for Large Diesel Engines and Its Effect on the Near-Nozzle Spray Structure. *SAE Trans. J. Engines*, 115-3, pp.634-647, 2006-01-1114.
 69. **Gulder, O. L., Smallwood, G. J., and Snelling, D. R.** (1992) Diesel Spray Structure Investigation by Laser Diffraction and Sheet Illumination. *SAE Technical Paper* 920577.
 70. **Ha, J. Y., Iida, N., Sato, G. T., Hayashi, A. and Tanabe, H.** (1984) Experimental Investigation of the Entrainment into Diesel Spray. *SAE Technical Paper* 841078.
 71. **Hanjalic, K., Popovac, M., and Hadziabdic, M.** (2014) A robust near-wall elliptic-relaxation eddy-viscosity turbulence model for CFD. *International Journal of Heat and Fluid Flow*, 25:1047-1051.
 72. **Hayashi, T., Suzuki, M. and Ikemoto, M.** (2014) Effects of Internal Flow in a Diesel Nozzle on Spray Combustion. *International Journal of Engine Research*, vol.6, pp.646-654.
 73. **Hayashi, T., Suzuki, M., Ikemoto, M.** (2012) Visualization of Internal Flow and Spray Formation with Real Size Diesel Nozzle. ICLASS 2012, Heidelberg, Germany, September 2-6.
 74. **Hayato Yamashita, Naoki Toda, Makoto Mashida.** (2014) Air Entrainment Measurement of High

Pressure Diesel Spray from Multi-hole Nozzle. *The 25th Internal Combustion Engine Symposium*.

75. **He, Z.X., Shao, Z., Wang, Q., Zhong, W.J., and Tao X.C.** (2015) Experimental study of cavitating flow inside vertical multi-hole nozzles with different length–diameter ratios using diesel and biodiesel. *Experimental Thermal and Fluid Science*, 60:252–262
76. **He, Z.X., Zhong, W.J., Wang, Q., Jiang, Z.C., Shao, Z.,** (2013) Effect of nozzle geometrical and dynamic factors on cavitating and turbulent flow in a diesel multi-hole injector nozzle, *International Journal of Thermal Sciences*, 70:132-143.
77. **Heinze, T., and Schmidt, T.** (1989) Fuel-Air Ratios in a Spray, Determined between Injection and Autoignition by Pulsed Spontaneous Raman Spectroscopy. *SAE Technical Paper* 892102.
78. **Heinze, T., and Schmidt, T.,** (1989) Fuel-Air Ratios in a Spray, Determined between Injection and Autoignition by Pulsed Spontaneous Raman Spectroscopy. *SAE Technical Paper* 892102.
79. **Heywood, J. B.** (1988) *Internal Combustion Engine Fundamentals*. New York, McGraw-Hill Science Engineering.
80. **Higgins, B., and Siebers, D.** (2001) Measurement of the Flame Lift-Off Location on DI Diesel Sprays Using OH Chemiluminescence. *SAE Technical Paper* 2001-01-0918.
81. **Hiroyasu, H. and Arai, M.** (1990) Structures of Fuel Sprays in Diesel Engines. *SAE Technical Paper*, 900475.
82. **Hiroyasu, H., Arai, M. and Shimizu, M.** (1991) Break-up Length of a Liquid Jet and Internal Flow in a Nozzle, ICLASS-91, 5th International Conference on Liquid Atomization and Spray Systems, Gaithersburg, Maryland, July.
83. **Hu, B., Musculus, M., and Oefelein, J.** (2010) Large Eddy Simulation of a Transient Air Jet with Emphasis on Entrainment during Deceleration. *SAE Technical Paper* 2010-01-1133.
84. **Huang Jing-chuan and Han Cheng-cai.** (1992) Influences of Gas Nucleus Scale on Cavitation. *Applied Mathematics and Mechanics*, 13(4):359-367.
85. **Huh, K.Y, and Gosman, A.D.** (1991) A Phenomenological Model of Diesel Spray Atomization. *Proceedings of the International Conference on Multiphase Flows*, September 24-27, Tsukuba, Japan.
86. **Inaba, T., Dong, P., Nishida, K., Ogata, Y., Shi, B.L., and Shimo, D.**(2014) Comparison of Spray and Internal Flow Characteristics between Single and Multi-Hole Nozzles for Diesel Engine, *ILASS-Asia 2014, 17th Annual Conference on Liquid Atomization and Spray Systems*, paper 066, Shanghai, China, 26-29 October 2014.
87. **Johnston, S.,** (1979) Precombustion Fuel/Air Distribution in a Stratified Charge Engine Using Laser Raman Spectroscopy. *SAE Technical Paper* 790433.
88. **Kamimoto, T., and Kobayashi, H.** (1991) Combustion Processes in Diesel Engines. *Progress in Energy and Combustion Science*, 17:163-189.
89. **Kamimoto, T., Yokota, H., and Kobayashi, H.** (1989) A New Technique for the Measurement of Sauter Mean Diameter of Droplets in Unsteady Dense Sprays. *SAE Technical Paper* 890316.
90. **Katz, J. and Acosta, A.** (1982) Observations of Nuclei in Cavitating Flows. *Applied Scientific Research*, 38(1): 123-132.
91. **Keller A P.** (1972) The Influence of the Cavitation Nucleus Spectrum on Cavitation Inception, Investigated with a Scattered Light Counting Method. *ASME J. Basic Eng.*, pp. 917-925.

92. **Kim Byong-Seok, Yoon Wook Hyeon, Ryu Sung Hyup, and Ha Ji Soo** (2005) Effect of the Injector Nozzle Hole Diameter and Number on the Spray Characteristics and the Combustion Performance in Medium-Speed Diesel Marine Engines. SAE Technical Paper 2005-01-3853.
93. **Kim, J., Nishida, K., Yoshizaki, T. and Hiroyasu, H.** (1997) Characterization of Flows in the Sac Chamber and the Discharge Hole of a D.I. Diesel Injection Nozzle by Using a Transparent Model Nozzle, SAE Technical Paper, 972942.
94. **Kim, Y., Kim, M., Yeom, J., and Min, K.** (2002) LIEF Measurement and Calculation Analysis of Evaporation Spray. *THIESEL 2002 Conference on Thermo- and Fluid Dynamic Process in Diesel Engines*, Valencia, Spain.
95. **Kompenhans, J., and Kähler, C.** (2002) Particle Image Velocimetry- an advanced Experimental Tool for the Investigation of Turbulent Flow Fields. *Engineering Turbulence Modelling and Experiments*, 79-94.
96. **Koo, J. and Martin, J.K.** (1995) Near-nozzle Characteristics of a Transient Fuel Spray, *Atomization and Sprays*, vol. 5, pp.107-121.
97. **Kosaka, H., Aizawa, T., and Kamimoto, T.** (2005) Two-Dimensional Imaging of Ignition and Soot Formation Process in a Diesel Flame. *International Journal of Engine Research*, 6(1): 21-42.
98. **Kosaka, H., Drewes, V., Catalfamo, L., Aradi, A. A., Iida, N., and Kamimoto, T.** (2000) Two-Dimensional Imaging of Formaldehyde Formed During the Ignition Process of a Diesel Fuel Spray. *SAE Technical Paper* 2000-01-0236.
99. **Kosaka, H., Won, Y.H., and Kamimoto, T.** (1992) A Study of the Structure of Diesel Sprays Using 2-D Imaging Techniques. *SAE Technical Paper* 920107.
100. **Kubitschek, J. P., and Weidman, P. D.** (2008) Helical Instability of a Rotating Liquid Jet. *Physics of Fluids*, 20: 91-104
101. **Kuhnert Steffen, Wagner Uwe, Spicher Ulrich, Haas Simon-Florian, Gabel Klaus, and Kutschera Immanuel** (2010) Influence of Injection Nozzle Hole Diameter on Highly Premixed and Low Temperature Diesel Combustion and Full Load Behavior. SAE Technical Paper 2010-01-2109.
102. **Lacis, A.A., Hansen, J.E. Russell, G.L., Oinas, V., and Jonas, J.** (2013) The role of long-lived greenhouse gases as principal LW control knob that governs the global surface temperature for past and future climate change. *Tellus B*, vol. 65.
103. **Lai, M., Zheng, Y., Xie, X., Moon, S., Liu, Z., Gao, J., Zhang, X., Fezzaa, K., Wang, J.** (2011) and Shi, J., Characterization of the Near-field Spray and Internal Flow of Single-hole and Multi-hole Sac Nozzles using Phase Contrast X-ray Imaging and CFD, SAE Technical Paper, 2011-01-0681.
104. **Laonual, Y., Yule, A.J., and Walmsley, S.J.** (2001) Internal Fluid Flow and Spray Visualizaiton for a Large-Scale VCO Orifice Injector Nozzle. *ILASS-Europe, Zurich*, 2-6 September.
105. **Lecoffre, Y.** (1999) Cavitation Bubble Trackers. Brookfield, VT: A. A. Balkema.
106. **Lee, J., Nishida, K., and Yamakawa, M.** (2002) An Analysis of Ambient Air Entrainment into Split Injection D.I. Gasoline Spray by LIF-PIV Technique. *SAE Technical Paper* 2002-01-2662.
107. **Leng, X., He, Z., Jin, Y., Zhong, W.** et al. (2015) Characterization of Internal Flow of Intersecting Hole Nozzle for Diesel Engines. SAE Technical Paper 2015-01-1860.
108. **Lentinello, R.A.** (2000) *Motoring madness Journal of Mechanical Engineering*, 122 (11): 86-92.
109. **Li K.C.** (2014) Effects of Wall Impingement and Multiple Injection on Mixture Formation and

- Combustion Processes of Diesel Spray. Doctoral dissertation of Hiroshima University.
110. **Li, K., Dong, P., Matsuo, T., Shi, B. et al.** (2014) Characteristics of Diesel Spray Flame under Flat Wall Impinging Condition --LAS, OH* Chemiluminescence and Two Color Pyrometry Results," *SAE Technical Paper* 2014-01-2636, doi:10.4271/2014-01-2636.
 111. **Li, K-C., Nishida, K., Ogata, Y. and Shi, B-L.** (2014) Effect of flat-wall impingement on diesel spray combustion. *IMEchE Part D: J Automob Eng.* Epub ahead of print 18 August.
 112. **Lichtarowicz, A. and Pearce, I.D.** (1974) Cavitation and Aeration Effects in Long Orifices. Cavitation Conference, *Institution Mechanical Engineers*, Edinburgh, Sept. 3-5, pp. 129-144.
 113. **Lichtarowicz, A.K., Duggins, R.K., and Markland, E.** (1965) Discharge Coefficients for Incompressible Non-cavitating Flow through Long Orifices. *J. Mech. Engng Sci.*, 7(2): 210-219.
 114. **Liu, Z. and Brennen, C.E.** (1998) Cavitation Nuclei Population and Event Rates. *Trans. ASME, J. Fluids Eng.*, vol. 120, pp. 728-737.
 115. **Margot, X., García, A., Fajardo, P., and Patouna, S.** (2010) Analysis of the cavitating flow in real size diesel injectors with fixed and moving needle lift simulations, *ECCOMAS CFD Conference*, Lisbon, Portugal, June 14–17.
 116. **Margot, X., Hoyas, S., Fajardo, P., and Patouna, S.** (2011) CFD study of needle motion influence on the spray conditions of single-hole injectors, *Atomization and Sprays*, 21: 31-40.
 117. **Maria van der Hoeven** (2015) Energy and Climate Change, World Energy Outlook Special Report, International Energy Agency.
 118. **Matsumoto, Y., Gao, J., Namba, M., and Nishida, K.** (2007) Mixture Formation and Combustion Processes of Multi-Hole Nozzle with Micro Orifices for D.I. Diesel Engines. SAE Technical Paper, 2007-01-4049.
 119. **Melton, L. A. and Verdieck, J. F.** (1985) Vapor/Liquid Visualization in Fuel Sprays. 20th Symposium (International) on Combustion, 1283-1290.
 120. **Meyer, R.S., Billet, M.L, and Holl, J.W.** (1992) Freestream Nuclei and Traveling Bubble Cavitation. *ASME J. Fluids Eng.*, Vol. 114, pp. 672-679.
 121. **Michele, Battistoni, Carlo, Grimaldi and Francesco, Mariani** (2012) Coupled Simulation of Nozzle Flow and Spray Formation Using Diesel and Biodiesel for CI Engine Applications. SAE Technical Paper 2012-01-1267.
 122. **Montgomery, D. T., Chan, M., Chang, C. T., Farrell, P. V., and Reitz, Rolf D.** (1996) Effect of Injector Nozzle Hole Size and Number on Spray Characteristics and the Performance of a Heavy Duty D.I. Diesel Engine. SAE Technical Paper 1996-10-01.
 123. **Moon ,S., Yuan Gao, Suhan Park, Jin Wang, Naoki Kurimoto, and Yoshiaki Nishijima** (2015) Effect of the Number and Position of Nozzle Holes on In- and Near-Nozzle Dynamic Characteristics of Diesel Injection. *Fuel*, 150(15): 112-122.
 124. **Moon, S., Gao, Y., Wang, J., Fezzaa, K., and Tsujimura, T.** (2014) Near-field Dynamics of High-speed Diesel Sprays: Effects of Orifice Inlet Geometry and Injection Pressure, *Fuel*, vol.133, pp.299-309.
 125. **Moon, Seoksu,, Keisuke, K., Kiyotaka, S., Hideaki, Y. et al.** (2015) Ultrafast X-ray study of multi-hole GDI injector sprays: Effects of nozzle hole length and number on initial spray formation, *Experimental Thermal and Fluid Science*, 68:68-81.

126. **Mulemane, A., Subramaniyam, S., Lu, P-H., Han, J-S., Lai, M-C. and Poola, R.** (2004) Comparing cavitation in diesel injectors based on different modeling approaches. SAE Technical Paper 2004-01-0027.
127. **Musculus, M. and Kattke, K.** (2009) Entrainment Waves in Diesel Jets, *SAE International Journal of Engines* 2(1):1170-1193.
128. **Naber, J. D., and Siebers, D. L.,** (1996) Effects of Gas Density and Vaporization on Penetration and Dispersion of Diesel Sprays. *SAE Technical Paper* 960034.
129. **National Highway Traffic Administration.**(1995) Corporate Average Fuel Economy (CAFE), <http://www.nhtsa.gov/fuel-economy> (1995, accessed 21 Feb 2016)
130. **Nishida, K., Tian, J-P., Sumoto, Y., Long, W-Q.** et al (2009) An experimental and numerical study on Sprays injected from two-hole nozzles for DISI engines. *Fuel*, 88:1634-1642.
131. **Nishimura, A. and Assanis, D.N.** (2000) A Model for Primary Diesel Fuel Atomization Based on Cavitation Bubble Collapse Energy. *ICLASS2000*, Pasadena, CA, July 16-20.
132. **Nurick, W.H.** (1976) Orifice Cavitation and Its Effect on Spray Mixing. *J. Fluids Engng.*, vol. 98, pp.681-689.
133. **O'Rourke, P.J.** (1981) Collective Drop Effects in Vaporizing Liquid Sprays. Ph.D Thesis 1532-T, Princeton University, New Jersey.
134. **Payri, F., Arrègle, J., López, J. J., and Hermens, S.** (2006) Effect of Cavitation on the Nozzle Outlet Flow, Spray and Flame Formation in a Diesel Engine. SAE Technical Paper, 2006-01-1391.
135. **Payri, F., Bermudez, V., Payri, R. and Salvador F. J.** (2004) The Influence of Cavitation on the Internal Flow and the Spray Characteristics in Diesel Injection Nozzles. *Fuel*; 83:419-431.
136. **Payri, F., Payri, R., Salvador, F.J., and Martínez-López, J.** (2012) A contribution to the understanding of cavitation effects in Diesel injector nozzles through a combined experimental and computational investigation, *Computers & Fluids* 58:88-101.
137. **Payri, R., García, J.M., Salvador, F.J., and Gimeno J.** (2005) Using spray momentum flux measurements to understand the influence of diesel nozzle geometry on spray characteristics. *Fuel*, 84(5), Pages 551–561.
138. **Payri, R., Tormos, B., Salvador, F. J., and Araneo, L.** (2008) Spray Droplet and Velocity Characterization for Convergent Nozzles with Three Different Diameters. *J. Fuel*, 87:3176-3182.
139. **Peter, W., Franz, X. M., Roll, D.** et al (2003). Can the technology for heavy-duty diesel engines be common for future emission regulations in USA, Japan and Europe? SAE Technical Paper 2003-01-0344.
140. **Pickett, L.M., Kook, S., and Williams, T. C.** (2009) Visualization of Diesel Spray Penetration, Cool-Flame, Ignition, High-Temperature Combustion, and Soot Formation Using High-Speed Imaging. *SAE Technical Paper* 2009-01-0658.
141. **Pickett, L., Manin, J., Payri, R., Bardi, M.** et al., (2013) Transient Rate of Injection Effects on Spray Development, *SAE Technical Paper* 2013-24-0001.
142. **Pilch, M., and Erdman, C. A.** (1987) Use of Breakup Time Data and Velocity History Data to Predict the Maximum Size of Stable Fragments for Acceleration-Induced Breakup of a Liquid Drop. *Int. J. Multiphase Flow*, 13:741-757.

143. **Qin J R, Yu S T J, Zhang Z C, and Lai M C.** (2001) Transient Cavitating Flow Simulations inside a 2-D VCO Nozzle Using the Space-Time CE/SE Method. SAE Technical Paper 2001-01-1983.
144. **Qu Ying-Dong, Cui Cheng-Song, Chen San-Ben, and Li Jin-Quan** (2005) A fast subpixel edge detection method using Sobel–Zernike moments operator, *Image and Vision Computing*, 23(1) 11–17.
145. **Rabenstein, F., Egermann, J., and Leipertz, A.** (1998) Quantitative Analysis of Vapor Phase Structures in Transient Liquid Fuel Sprays. *COMODIA*, Kyoto, Japan.
146. **Rajalingam, B. V., and Farrell, P. V.** (1999) The Effect of Injection Pressure on Air Entrainment into Transient Diesel Sprays. *SAE Technical Paper* 1999-01-0523.
147. **Ramamurthi, K. and Nandakumar, K.** (1999) Characteristics of Flow through Small Sharp-Edged Cylindrical Orifices. *Flow Measurement and Instrumentation*, vol. 10, pp. 133-143.
148. **Reid, R.C., Pravsnitz, J. M., and Sherwood, T. K.** (1985) *Properties of Gases and Fluids*, 3rd ed. McGraw-Hill, Inc., New York.
149. **Reitz, R. D.** (1987) Modeling Atomization Processes in High-pressure Vaporizing Sprays. *Atomization and Sprays*, vol.3, pp. 309-337.
150. **Reitz, R. D., Diwakar, R.** (1987) Structure of High Pressure Fuel Sprays. *SAE Technical Paper* 870598.
151. **Rhim, D.R., and Farrell, P. V.** (2002) Air Flow Characteristics Surrounding Evaporating Transient Diesel Sprays. *SAE Technical Paper* 2002-01-0499.
152. **Ricou, D. R., and Spalding, D. B.** (1961) Measurement of Entrainment by Axis-Symmetrical Turbulent Jets. *J. Fluid Mech.*, 11:21-32.
153. **Roger, C.** (2015) Fuel requirements for advanced IC engines. Keynote speech from SHELL global group of energy and petrochemical companies. SAE PLF International Conference, Kyoto, Japan.
154. **Roth H, Gavaises M and Arcoumanis C.** (2002) Cavitation Initiation, Its Development and Link with Flow Turbulence in Diesel Injector Nozzles. *SAE Trans. J. Engines*, 2002-01-0214 111-3, pp. 561-580.
155. **Rupe, J. H.** (1953) The Liquid-Phase Mixing of a Pair of Impinging Stream. *Jet Propulsion Lab. Progress Report.20-195*, California Inst. of Technology, Pasadena.
156. **Sawersyn, J. P., Sochet, L., Desenne, D., Crunelle-Cras, M., Grase, F., and Bridoux, M.** (1986) A Study of Spatial Distribution of Molecular Species in an Engine by Pulsed Multichannel Raman Spectroscopy. *Proc. 21st Symposium (International) on Combustion*, 491-496.
157. **Schmalzing, C. O., Stapf, P., Maly, R. R., Renner, G., Stetter, H., and Dwyer, H. A.** (1999) A Holistic Hydraulic and Spray Model- Liquid and Vapor Phase Penetration of Fuel Sprays in DI Diesel Engines. *SAE Technical Paper* 1999-01-3549.
158. **Schmidt, D.P., Rutland, C.J., and Corradini, M.L.** (1997) Numerical Study of Cavitating Flow through Various Nozzle Shapes. SAE Technical Paper 971597.
159. **Schmidt, D.P.** (1997) Cavitation in Diesel Fuel Injector Nozzles. PhD Thesis, University of Wisconsin-Madison, p.69.
160. **Schmidt, D.P., Rutland, C. J., Corradini, M.L., Roosen, P., and Genge, O.** (1999) Cavitation in Two-Dimensional Asymmetric Nozzles. SAE Technical Paper 1999-01-0518.
161. **Schmidt, D.P., Rutland, C.J., and Corradini, M.L.** (1999) A Fully Compressible, Two-Dimensional

- Model of Small, High Speed, Cavitating Nozzles. *Atomization and Sprays*, vol. 6, pp. 255-276.
162. **Schweitzer, P. H.** (1937) Mechanism of Disintegration of Liquid Jets. *Journal of Applied Physics*, 8: 513-521.
163. **Senda, J., Kanda, T., Kobayashi, M., and Fujimoto, H.** (1997) Quantitative Analysis of Fuel Vapor Concentration in Diesel Spray by Exciplex Fluorescence Method. *SAE Technical Paper 970796*.
164. **Senda, J., Tanabe, Y., Fujimoto, H., and Fukami, Y.** (1992) Visualization of Evaporative Diesel Spray Impinging Upon Wall Surface by Exciplex Fluorescence Method. *SAE Technical Paper 920578*.
165. **Seuret, V., Bazile, R., Marchal, M., and Couteau, G.** (2010) Effect of Ambient Density and Orifice Diameter on Gas Entrainment by a Single-Hole Diesel Spray. *Exp. Fluids*, 49:1293-1305.
166. **Seuret, V., Bazile, R., Marchal, M., and Couteau, G.** (2010) Effect of Ambient Density and Orifice Diameter on Gas Entrainment by a Single-Hole Diesel Spray. *Exp. Fluids*, 49:1293-1305.
167. **Siebers, D. L.** (1998) Liquid-phase Fuel Penetration in Diesel Sprays, SAE Technical Paper, 980809.
168. **Siebers, D., and Higgins, B.** (2001) Flame Lift-Off on Direct-Injection Diesel Sprays Under Quiescent Conditions. *SAE Technical Paper 2001-01-0530*.
169. **Skogsberg, M., Dahlander, P., Lindgren, R., and Denbratt, I.** (2005) Effects of injector parameters on mixture formation for multi-hole nozzles in a spray-guided gasoline DI engine. SAE Technical Paper 2005-01-0097.
170. **Smallwood, G. J., and Gülder, Ö. L.** (2000) Views on the Structure of Transient Diesel Sprays. *Atomization and Spray*, 10: 355-386.
171. **Soid, S. N. and Zainal, Z. A.** (2011) Spray and combustion characterization for internal combustion engines using optical measuring techniques-a review. *Energy*, 36: 724-741.
172. **Soteriou, C., Andrews, R., and Smith, M.** (1995) Direct Injection Diesel Sprays and the Effect of Cavitation and Hydraulic Flip on Atomization. SAE Technical Paper 950080.
173. **Sou, A., Hosokawa, S., and Tomiyama, A.** (2007) Effects of Cavitation in a Nozzle on Liquid Jet Atomization. *International Journal of Heat and Mass Transfer*, vol. 50, pp. 3575-3582.
174. **Su T F, Patterson M A, Reitz R D, and Farrell P V.** (1996) Experimental and Numerical Studies of High Pressure Multiple Injection Sprays. SAE Technical Paper 960861.
175. **Suh, H. K., Lee, Park, S. W., and Lee, C. S.** (2007) Effect of Piezo-Driven Injection System on the Macroscopic and Microscopic Atomization Characteristics of Diesel Fuel Spray. *Fuel*, 86: 2833-2845.
176. **Suh, H.K and Lee, C.S.** (2008) Effect of Cavitation in Nozzle Orifice on the Diesel Fuel Atomization Characteristics. *International Journal of Heat and Fluid Flow*, vol. 29, pp. 1001-1009.
177. **Tadokoro, T., Sato, K., Gao, J., Matsumoto, Y., Nishida, K.** (2006) Analysis of evaporation process of non-axisymmetrically wall impinging spray by means of laser absorption scattering technique. *Proceeding of the 15th ILASS-Japan Symposium*, Kanagawa, 101-106.
178. **Tatschl, R., V. Kunsberg, Sarre, C., Alajbegovic, A., and Winklhofer, E.** (2000) Diesel Spray Break-Up Modelling Including Multidimensional Cavitation Nozzle Flow Effects. *16th ILASS-Europe Conf.*, Darmstadt, Germany.
179. **Tree, D. R., and Svensson, K. I.** (2007) Soot Processes in Compression Ignition Engines. *Progress in Energy and Combustion Science*, 33: 272-309.
180. **V. Berg, E., Edelbauer, W, and Alajbegovic, A., et al.** (2005) Coupled Simulations of Nozzle Flow,

Primary Fuel Jet Breakup, and Spray Formation. *Journal of Engineering for Gas Turbines and Power*, Vol. 127(4), pp. 897-908.

181. **Van, Doormaal, J.P., and Raithby, G.D.** (1984) Enhancement of SIMPLE Method for Predicting Incompressible Fluid Flows. *Numerical Heat Transfer*, vol. 7, pp. 147-163.
182. **Wakuri, Y., Fujii, M., Amitani, T. and Tsuneya, R.** (1960) Studies of the Penetration of a Fuel Spray in a Diesel Engine. *JSME* 3(9): 123-130.
183. **Wakuri, Y., Fujii, M., Amitani, T., and Tsuneya, R.** (1959) Studies on the Penetration of Fuel Spray of Diesel Engine. *Trans. JSME* 25: 820-826.
184. **Wallis, G.B.** (1969) *One-Dimensional Two-Phase Flow*. McGraw-Hill, NY.
185. **Winklhofer, E., Kull, E., Kelz, E., and Morozov, A.** (2001) Comprehensive Hydraulic and Flow Field Documentation in Model Throttle Experiments under Cavitation Conditions. *Proceedings of the ILASS-Europe Conference, Zurich, 2-6 September*, pp. 574-579.
186. **Wu, K.J., Su, C.C., and Steinberger, R.L.** et al. (1983) Measurements of the Spray Angle of Atomizing jets. *ASME J. Fluids Eng.*, vol. 105, pp.406-413.
187. **Wu, P. K., and Faeth, G. M.** (1995) Onset and End of Drop Formation along the Surface of Turbulent Liquid Jets in Still Gases. *Phy. of Fluids*, 7 (11): 2915-2917.
188. **Yeh, C., Kamimoto, T., Kosaka, H., and Kobori, S.** (1994) Quantitative Measurement of 2-D Fuel Vapor Concentration in a Transient Spray via Laser-Induced Fluorescence Technique. *SAE Technical Paper* 941953.
189. **Yuan, W., Sauer, J., and Schnerr, G.H.** (2001) Modeling and Computation of Unsteady Cavitation Flows in Injection Nozzles. *Journal of Mechanical Industry*, vol. 2, pp. 383-394.
190. **Zeldovich, Y. B.,** (1946) The Oxidation of Nitrogen in Combustion and Explosions. *Acta Physicochim.* 21:577.
191. **Zhang Wu, Tian Jiang-Ping, and Nishida Keiya** (2011) Effects of Nozzle Hole Diameter and Injection Pressure on Flame Lift-Off and Soot Formation in D.I. Diesel Combustion. *SAE Technical Paper* 2011-01-1813.
192. **Zhang, Y. Y.,** (2001) A Study on Mixture Formation in Diesel Sprays with Split Injection Strategy. *Dissertation*, University of Hiroshima.
193. **Zhang, Y., Nishida, K.** (2004) Imaging of vapor/liquid distributions of split-injected diesel sprays in a two-dimensional model combustion chamber. *Combust. Sci. Technol.* 176: 1465-1491.
194. **Zhao, H., and Ladommatos, N.,** (2001) *Engine Combustion Instrumentation and Diagnostics*. Warrendale PA, USA, Society of Automotive Engineers.